Modeling Flotation from First Principles Using the Hydrophobic Force as a Kinetic Parameter

Mohit Gupta

Dissertation submitted to the faculty of Virginia Polytechnic Institute and State University in partial fulfillment of the requirements for the degree of

Doctor of Philosophy
In
Chemical Engineering

Roe-Hoan Yoon, Chair
William A. Ducker, Co-Chair
Richey M. Davis
Christopher A. Noble
Kaiwu Huang

February 15, 2024
Blacksburg, Virginia

Keywords: Flotation modeling, coarse particles flotation, thin liquid films, hydrophobic forces, thermodynamics

Modeling Flotation from First Principles Using the Hydrophobic Force as a Kinetic Parameter

Mohit Gupta

ABSTRACT

Flotation is regarded as the best available separation method for the recovery of valuable minerals such as chalcopyrite ($CuFeS_2$), sphalerite (ZnS), *etc.*, from mined ores. Practically all metals humans use today are produced by flotation. The process relies on controlling the stability of the thin liquid films (TLFs) of water formed between minerals and air bubbles (wetting film), air bubbles (foam film), and mineral particles (colloid films). In flotation, a desired mineral is rendered hydrophobic by surfactant coating as a means to destabilize the TLFs, so that they can be attached to the hydrophobic air bubbles. A TLF ruptures when the disjoining pressure (or surface forces per unit area) of the film becomes negative, *i.e.*, $\Pi < 0$. Thermodynamically, a wetting film can rupture when the contact angle (θ) of a mineral surface is larger than zero. It would, therefore, be reasonable to consider the roles of the surface forces to better understand the fundamental mechanisms involved in flotation. The surface forces considered in the present work included the electric double layer (EDL), van der Waals (vdW), and attractive hydrophobic (HP) forces.

A flotation model has been developed by using the hydrophobic force as a kinetic parameter, which made it possible to track the fates of mineral particles of different of size, surface liberation, and contact angle to predict both recovery and grades for the first time. The model has been validated against the plant survey data obtained from an operating copper flotation plant. The simulation results obtained using the first principles model have been utilized to address the limitations of current flotation practices. One such limitation is the presence of slow-floating target minerals present in the cleaner-scavenger tails (CST) that are routinely recycled back to the rougher flotation bank as circulating loads (CLs) to allow longer retention times for the slow-floating particles for additional recovery. The simulation results show also that opening a flotation circuit by treating the CST streams separately in an advanced circuit can substantially improve the plant performance.

One of the major limitations of flotation is that the coarse particles in a feed stream are difficult to recover due to the low hydrophobicity associated with poor surface liberation. A new flotation model developed in the present work suggests various ways to address the problem. One is to increase the hydrophobicity of the composite (poorly liberated) particles using the Super Collectors that can increase the contact angles to 150 -170^o. Simulation results obtained using the model developed in the present work show significant financial benefits of using Super Collectors.

Flotation is controlled by surface forces as noted above. As particle size becomes larger than ~150 μm, however, the gravitational force comes into the picture and can override the surface forces. A new flotation cell has been developed to mitigate the effects of the extraneous force by decreasing the effective specific gravity (SG) by attaching air bubbles to facilitate levitation and by creating a pulsation to allow particles to move according to SGs independent of particle size, which should help increase the upper particle size limit of flotation.

Surface forces in foam and oil-in-water emulsion films have been measured at different temperatures to determine the changes in thermodynamic properties of the thin liquid films (TLFs) of water confined between two bubbles and two oil drops. The results show that the films are destabilized by the attractive hydrophobic forces created during the course of building H-bonded structures in confined spaces, which entails decreases in enthalpy ($\Delta H < 0$) and entropy ($T\Delta S < 0$), the second term representing the thermodynamic cost of building the structures.

Modeling Flotation from First Principles Using the Hydrophobic Force as a Kinetic Parameter

Mohit Gupta

GENERAL AUDIENCE ABSTRACT

Flotation is a kinetic process designed to separate valuable minerals from mined ores. This process depends on several hydrodynamic and surface chemistry parameters making it hard to model. A U.S. patent was awarded to Sulman and Picard in 1905 for using air bubbles to selectively collect hydrophobic particles from the aqueous phase, leaving hydrophilic particles behind. Since then, the separation process known as *flotation* has been used to produce practically all metals humans use. Many investigators developed flotation models using hydrodynamic parameters, *e.g*., particle size, bubble size, energy dissipation rate, *etc*., but without a reference to particle hydrophobicity. Therefore, the models were successful in predicting recoveries but not product grades. Derjaguin and Dukhin (1961) were the first to model flotation using surface forces but without due consideration of the role of hydrophobic force in flotation. Therefore, it also failed to predict product grades.

In the current work, a new flotation model has been developed using the hydrophobic force as a kinetic parameter. This approach made it possible to predict both recoveries and grades for the first time. The model has been reduced to a simple form mimicking the Arrhenius equation so that it can be used to delineate the different conditions required for optimizing coarse and fine particle flotation. The model has been derived by considering the surface forces in the thin liquid films (TLFs) of water confined between bubbles, and bubbles and particles. It has been found that the hydrophobic force plays a decisive role in destabilizing a wetting film and inducing bubble-particle attachment. The surface forces measured in the present work show that the hydrophobic interactions in macroscopic scales are controlled by enthalpy rather than entropy, which is contrary to the nanoscale hydrophobic interactions. The model has been validated against a full-scale plant operation and demonstrated predictive capabilities. The simulation results have been analyzed to determine the limitations of the current flotation practices. It was found that coarse particle flotation is difficult either due to the presence of composite particles reducing the particle contact angle or due to their poor hydrodynamic properties. Utilizing the insights from the model, various methods of alleviating these limitations have been developed and presented in the current work.

References

Derjaguin, B.V., Dukhin, S.S., 1961. Theory of flotation of small and medium-size particles. *Inst. Min. Metall*. 241–267.

Sulman, H.L., & Kirkpatrick-Picard (1905). *U.S. Patent No. 793,808.*

ACKNOWLEDGMENTS

I would like to start by expressing my most sincere gratitude towards my advisor, Dr. Roe-Hoan Yoon, for his guidance, inspiration, and words of encouragement throughout my Ph.D. tenure at Virginia Tech. His passion for fundamental studies and efforts to tackle real-world problems has been truly inspiring. His wisdom and optimistic attitude to face any challenge will stay with me forever.

I would also like to thank Dr. William Ducker, Dr. Richey Davis, and Dr. Aaron Noble for serving on my committee. I am grateful for their constructive criticism and suggestions to improve the quality of my research work. I would especially like to extend my thanks to Dr. Kaiwu Huang for serving on my committee and for being such a great mentor during the course of my Ph.D. I want to thank him for teaching me how to conduct the disjoining pressure measurements and the flotation simulations. He has been an inspiration for me during this work. I learned a lot due to the stimulating discussion we had about my research.

I would like to acknowledge my colleagues and fellow lab-mates, Dr. Oznur Onel, Dr. Wei Liu, and Kris Strickland for their immense support and constant motivation during my tenure at Virginia Tech. I would also like to acknowledge the staff of the Chemical Engineering department as well as the Mining and Minerals Engineering department for their constant support and help in all the administrative work. I would also like to acknowledge Patrick Finley from the Materials Characterization Lab supported by the Institute for Critical Technology and Applied Science (ICTAS) for training me on the optical tensiometer.

I am grateful to the Department of Energy (DOE) and Minerals Refining Company (MRC), Richmond, Virginia for funding my Ph.D. research work.

Finally, I want to extend my love and gratitude to my parents, my sister, my brother-in-law, and my friends for their constant support and encouragement. Without them, this wouldn’t have been possible.

Table of Contents

List of Figures

List of Tables

Attributions

Chapters 2, 3 and 4 have been published as peer-reviewed journal papers.

Chapter 2: “Gupta, M., Huang, K., & Yoon, R. H. (2022). Predicting the recovery and grade of a rougher flotation circuit from liberation data. Minerals Engineering, 188, 107853.” I was responsible for the model modification, data analysis and manuscript composition. Dr. Kaiwu Huang developed the flotation model. Dr. Roe-Hoan Yoon was the supervisory author and was involved in conceptualization and manuscript composition.

Chapter 3: “Gupta, M., Huang, K., Noble, A., & Yoon, R. H. (2023). Improving the performance of a low-grade porphyry copper ore flotation plant using a simulator that can predict grade vs. recovery curves. Minerals Engineering, 202, 108243.” I was responsible for flotation model development for circuit analysis, data analysis, and manuscript composition. Dr. Kaiwu Huang and Dr. Aaron Noble were involved in the flotation model development. Dr. Roe-Hoan Yoon was the supervisory author and was involved in conceptualization and manuscript composition.

Chapter 4: “Gupta, M., Yoon, R. H. (2024). Maximizing the recovery and throughput of a rougher flotation bank by improving the recovery of composite particles. Minerals Engineering, 207, 108545.” I was involved in conceptualization, data curation, model modification, data analysis, conducting experiments, and manuscript composition. Dr. Roe-Hoan Yoon was the supervisory author and was involved in conceptualization and manuscript composition.

Chapters 5 and 6 are submitted for publication as peer-reviewed conference articles.

Chapter 5: “Gupta, M., Lim, H., Noble, A., & Yoon, R.H. (2024). Simulation of flotation circuits using a model derived from first principles. XXXI International Mineral Processing Congress, Washington DC, October, 2024”. I was involved in conceptualization, flotation model development for circuit analysis data curation, data analysis, conducting experiments, and manuscript composition. Holden Lim was involved in the development of the flotation model based user-friendly simulator. Dr. Aaron Noble was involved in the flotation model development. Dr. Roe-Hoan Yoon was the supervisory author and was involved in conceptualization and manuscript composition.

Chapter 6: “Gupta, M., Yoon, R.H. (2024). “Improving coarse particle flotation by control of surface and hydrodynamic forces, XXXI International Mineral Processing Congress, Washington DC, October, 2024”. I was involved in conceptualization, design, data curation, data analysis, conducting experiments, and manuscript composition. Dr. Roe-Hoan Yoon was the supervisory author and was involved in conceptualization and manuscript composition.

Chapters 1, 7, 8, and 9 are not published.

Chapter 1. Introduction

1.1 General

Froth flotation is a fine particle separation process, in which the target mineral particles suspended in water are hydrophobized so that they can selectively attach to air bubbles rise out of the aqueous phase, while other minerals remain unattached. In 1905, Sulman and Picard were awarded a U.S. patent (No. 793,808) for this process. Practically all metals humans use today are being produced by flotation, and it is still regarded as the best available method of separating mineral fines ~120 years later. It has also been commended; "*perhaps the greatest single metallurgical improvement of the modern era*" (Mouat, 1996; Wills and Finch, 2016).

Flotation separation is based on exploiting the differences in the surface properties of minerals to be separated from each other in an aqueous phase. The differences can be due to either the minerals' natural or modified surface properties. The primary surface property that controls the separation process is hydrophobicity or the degree of water-repelling tendency.

In a typical low-grade ore, the target mineral particles are interlocked with unwanted or gangue minerals, creating a barrier to its floatation separation. Mineral particles can be present either as fully liberated, partially locked with some fraction of the mineral exposed to the surface, or as fully locked without any surface exposure. These finely disseminated mineral surfaces should be made free or liberated before the use of any surface-altering reagents to promote the action of flotation. The process of grinding is used to "liberate" a target mineral to be chemically modified and subsequently attach to air bubbles. Thus, liberation is essential for hydrophobization and subsequent bubble-particle attachment (Clarke *et al.*, 2005; Jameson, 2012).

Prior to flotation, ore is finely ground to 10-100μm to achieve an optimum mineral liberation required for bubble-particle attachment in the pulp phase of a flotation cell (Guadin, 1931). The bubbles preferentially attach to the hydrophobic mineral surface, while the hydrophilic gangue particles are discharged as tailings. In the froth phase, bubble-coalescence leads to the drop-back of less hydrophilic particles in the pulp phase, thereby, producing higher-grade concentrates at higher separation efficiencies.

Along with the surface liberation, froth flotation is controlled by a series of variables that can be classified into surface parameters such as contact angle, surface or zeta potentials, surface tension, *etc.*, physical parameters such as particle size, density, *etc*., and hydrodynamic parameters such as energy dissipation rate, air flowrate rate, bubble size, *etc.* (Huang *et al.*, 2022) Essentially, it is analogous to a fire triangle, where chemical, physical, and the characteristics of the flotation cell controls the flotation efficiency (Wang and Liu, 2021).

A flotation cell is generally characterized by two zones: pulp phase and froth phase. In the pulp phase, flotation kinetics is governed by probabilities of three processes: bubble-particle collision (P_c), attachment (P_a), and detachment (P_d). Bubble-particle interaction is initiated by bubble-particle collision that depends on fluid hydrodynamics and the particles and bubble's size and their number densities (Sutherland, 1948, Gaudin, 1957, Collins and Jameson, 1977, Weber and Paddock, 1983, Abramson, 1975, Schubert, 1999). Collided bubble and particle can undergo attachment if the time taken to rupture the wetting film, known as the induction time, is less than the particle sliding time on the bubble (Dobby and Finch, 1986, 1987, Luttrell and Yoon, 1992, Albijanic *et al.*, 2010, Ralston *et al*., 1999, Pyke *et al.*, 2003). Bubble-particle can get detached due to the combination of hydrodynamic factors including inertial forces, pulp turbulence, the impact of particles in the pulp, and bubble surface oscillations (Yoon and Mao, 1996, Wang *et al.* 2016).

Bubble-particle aggregates that are unaffected by the detachment process in the pulp phase rise to the froth phase. In a froth phase, the bubbles coalesce together reducing the surface area available for the particles to attach, therefore, the less hydrophobic particles detach giving selectivity to the flotation process and improving the final product or concentrate grade (Park *et al.*, 2018).

Current commercial models such as Aminpro, JK SimFloat, UsimPac, *etc*. (Yianatos *et al.*, 2012), account only for the hydrodynamics parameters and rely on rigorous lab testing or historical plant data hence their application is constrained. Therefore, a model based on fundamentals of flotation such as one used in this study, is imperative to eliminate the cumbersome testing or data analysis. The major challenge for devising an efficient empirical model is the fact that contact angle, a major driving force for bubble-particle attachment, is a thermodynamic parameter, and therefore it's a challenge to include it in determining the kinetics of flotation.

A new flotation simulator based on the first principles has been developed to resolve this issue and incorporate the chemistry parameters to accurately predict the flotation kinetics (Yoon *et al.*, 2016; Park *et al.*, 2018; Huang *et al.*, 2022). To accurately incorporate the effect of chemical parameters in the determination of flotation kinetics, the knowledge of surface forces is paramount. These surface forces essentially consist of the van der Waals (vdW) force, electrical double layer (EDL) force and hydrophobic forces. This first-principles-based flotation model has been modified and used during this dissertation for conducting various simulations using plant data. The model as stated solely depends on the flotation physics which is described at length below.

In the next section, the surface forces are first briefly introduced followed by the subprocess of flotation. The last part of the next section describes the details of surface force measurements conducted on foam films which essentially is froth phase that is free of solid particles. This study is then extended to determine the thermodynamics of hydrophobic forces in foam and emulsion films.

1.2 Literature Review

1.2.1 Surface Forces Present in the Thin Liquid Films

Flotation is driven by the thinning of the thin liquid films (TLFs) present between different interfaces in close proximity to each other. When two macroscopic interfaces are brought closer, a TLF is formed between them. There are three types of TLF in flotation, based on the different types of interfaces involved namely, colloid films (solid/liquid/solid), foam films (air/liquid/air), and wetting films (air/liquid/solid) (Huang, 2020).

For a particle to attach to a bubble and "float" out of the flotation cell, the wetting film must rupture or in other words, the thin film of water between the air bubble and solid must drain. In the froth phase, the TLF confined between two air bubbles is drained for the bubbles to coalesce to provide a mechanism for the less hydrophobic particles to detach thereby, improving the grade of the product (Yoon and Luttrell, 1989). The stability of these TLFs defines the recovery and product grades, respectively.

When two macroscopic interfaces approach each other, the initial thinning rate of the liquid film is dictated by the changes in the curvature also known as the capillary pressure, P_c. Once the film is thinned to ~250 nm, the disjoining pressure (Π) or the sum of surface forces per unit area controls the rate of thinning and therefore, TLF's stability. The term disjoining pressure was first coined by Derjaguin (1939), stating it as the difference between the pressure of the liquid in the bulk and that of the thin liquid film. Thermodynamically, Π can be defined as the change in the excess free energy per unit surface area (G/A) with respect to the film thickness (h) at constant temperature (T), pressure (P), and chemical potential of solute (μ_s),

$$\Pi = -\left(\frac{\partial(G/A)}{\partial h}\right)_{P,T,\mu_s} \qquad [1.1]$$

For the TLF to rupture, Π should be negative while the film remains stable when Π is positive (Derjaguin, 1989). Disjoining pressure (Π) as mentioned before, is the sum of surface forces acting in the thin liquid films. As per the Derjaguin-Landau-Verwey-Overbeek (DLVO) theory, the disjoining pressure is equal to the sum of van der Waals (vdW) force and the electrical double layer force (EDL) (Derjaguin,

1939; Derjaguin and Landau, 1941; Verwey and Overbeek, 1955). The structural forces were considered to be zero. According to the DLVO theory,

$$\Pi = \Pi_d + \Pi_e \quad [1.2]$$

where, Π_d is the contribution due to the vdW forces and Π_e is the disjoining pressure due to the EDL forces.

This theory was valid in some cases where the TLF is formed between two similar phases such as colloids and foam films. In these TLFs, the vdW force is always attractive. But in the cases where the resulting vdW force can act repulsive, such as in wetting films, the DLVO theory failed to explain the kinetics of film rupture. The DLVO theory was extended to include the structural forces such as hydrophobic force (Laskowski and Kitchener, 1969; Blake and Kitchener, 1973), steric force (Israelachivili, 2011), and hydration force (Yoon and Vivek, 1998) to accurately predict the stability of any thin liquid film (Chaurev, 1995; Pan and Yoon, 2010; Israelachivili, 2011). For the presented work in this thesis, three major components have been considered,

$$\Pi = \Pi_d + \Pi_e + \Pi_h \quad [1.3]$$

where, Π_h is due to the hydrophobic force.

1.2.1.1 van der Waals (vdW) Force

In 1873, Johannes van der Waals (van der Waals, 1873) suggested that the deviation of the behavior of real gases from the ideal gases may be related to the intermolecular interactions and the forces generated due to that. This postulation led to the finding of the origins of the molecular forces which are now commonly known as vdW forces.

vdW force is the sum of forces originating due to the three different molecular interactions, namely, the induction (Debye) forces, orientation (Keesom) forces, and dispersion (London) forces (Debye, 1920; Keesom, 1921a,b; London, 1930, 1937; Israelachivili, 2011). Debye forces are induced due to the polarization of molecules in the presence of a permanent dipole. Keesom forces are present between two permanent dipoles and are generated when the dipoles orient themselves to attract each other. These two types of forces are significant in the case of polar molecules although, for the non-polar gases or molecules, these forces can't explain the attraction between them.

Dispersion forces, unlike the other components of attractive intermolecular forces, originate due to the instantaneous charge fluctuations in an atom or a molecule leading to the generation of an instantaneous induced dipole moment. These induced dipoles when come in proximity to another uncharged dipole of an atom or molecule, polarize it. This leads to a mutual interaction between 2 bodies and is attractive in nature (London, 1930, 1937). London found the pair potential ($U(r)$) to reduce with the increasing distance between the atoms or molecules (microscopic bodies) and inversely proportional to the distance (r) as,

$$U(r) = -\frac{C}{r^6} \quad [1.4]$$

where, C is the London constant which depends on the polarizability of interacting atoms or molecules.

In the case of macroscopic objects, the interaction forces give rise to an analogous vdW force between the bodies located at a small distance from one another. This interaction energy was determined by a simple pairwise addition of the interatomic interaction energy assuming that there is no retardation due to the interference of the electric fields of neighboring atoms. This novel summation was introduced by Kallmann and Willstratter (1932) and was further worked on by others (Bradley, 1932; de Boer, 1936). Hamaker (1937) considered the bodies to be spherical and evaluated the Hamaker constant (A),

$$A = \pi^2 C \rho_1 \rho_2 \quad [1.5]$$

in which ρ_1 and ρ_2 are the number density of atoms in the two interacting objects.

Lifshitz (1955) worked around the problem by considering the macroscopic properties of the interacting objects instead of the microscopic properties of the atoms. He treated the objects to be a continuous medium and used the dielectric constant (ε) and refractive indices (n) of each medium to determine the non-retarded Hamaker Constant (A_{132}) as the following,

$$A_{132} \approx \frac{3}{4}kT\left(\frac{\varepsilon_1-\varepsilon_3}{\varepsilon_1+\varepsilon_3}\right)\left(\frac{\varepsilon_2-\varepsilon_3}{\varepsilon_2+\varepsilon_3}\right) + \frac{3h_p v_e}{8\sqrt{2}}\frac{\left(n_1^2-n_3^2\right)\left(n_2^2-n_3^2\right)}{\left(\left(n_1^2+n_3^2\right)^{0.5}\left(n_2^2+n_3^2\right)^{0.5}\right)\left[\left(n_1^2+n_3^2\right)^{0.5}+\left(n_2^2+n_3^2\right)^{0.5}\right]} \quad [1.6]$$

here, k is the Boltzmann Constant, T is the temperature in K, h_p is the Plank's constant, v_e is the electronic adsorption frequency. Here, the first term on the right gives the zero-frequency contribution *i.e*. the Keesom and Debye interactions. The second term denotes the dispersion energy when the electronic adsorption frequency is assumed to be the same for all the three media.

The Hamaker constant for the interaction between one macroscopic medium/body (1) with other (2) in a medium (3) was defined by combining the Hamaker constants of each medium involved. The combining rule for Hamaker constant for 2 macroscopic bodies interacting in a medium was predicted by Israelachivili (1972) as follows,

$$A_{132} = (\sqrt{A_{11}} - \sqrt{A_{33}})(\sqrt{A_{22}} - \sqrt{A_{33}}) \quad [1.7]$$

where A_{11}, A_{22}, and A_{33} are Hamaker constants for each medium in vacuum. The vdW forces contribution to the disjoining pressure can then be calculated,

$$\Pi_d = -\frac{A_{132}}{6\pi h^3} \quad [1.8]$$

h is the separation distance.

For symmetrical thin liquid films such as colloidal and foam films, the Hamaker constant is always +ve making the vdW force to be attractive. But unlike the symmetrical TLF such as in the wetting film (air (**1**)/water (**3**)/solid (**2**)), the vdW forces can be repulsive as $A_{11} < A_{33} < A_{22}$.

1.2.1.2 Electrical Double Layer (EDL) Force

Most substances can be charged in the aqueous medium due to various mechanisms such as interfacial adsorption, association or dissociation of the surface groups, or ion exchange (Frumkin, 1924; Yoon and Yordan, 1986; Quast and Readett, 1987; Labib, 1988). Once the surface is charged, it leads to an emanating electric field with a surface potential (ψ_0) which ultimately leads to the migration of the oppositely charged counterions towards the surface. These counterions can be bound to the surface creating a Stern or Helmholtz layer followed by the diffuse layer. Grahame equation shows the relationship between surface charge density (σ) with the ψ_0. Under the assumption of low surface potentials (<25 mV) (Grahame, 1947),

$$\sigma = \varepsilon\varepsilon_0\kappa\psi_0 \quad [1.9]$$

where, ε and ε_0 are the permittivity of the medium and vacuum, respectively. κ is the inverse of Debye length and is a characteristic of the electrolyte concentration. Solving the Poisson-Boltzmann equation under the assumption of constant ε, one can determine ψ,

$$\varepsilon\varepsilon_0\frac{\partial^2\psi_0}{\partial x^2} = -e\sum z_i n_i(\infty)\exp\left(\frac{-ez_i\psi}{kT}\right) \quad [1.10]$$

where x is the distance from the charged surface, z is the valency of the i species of electrolytes, e is the elementary charge, and $n_i(\infty)$ is the electrolytes' number density. The diffuse layer thickness or the Debye length (κ^{-1}) is then calculated as,

$$\kappa^{-1} = \left(\frac{\varepsilon\varepsilon_0 kT}{e^2 \sum z_i^2 n_i(\infty)} \right)^{0.5} \quad [1.11]$$

To solve the Poisson-Boltzmann equation, different boundary conditions (BC) can be used. The solution to Eq. [1.10] leads to the determination of EDL forces between two charged surfaces. This force is caused by the overlapping of the electric field of the surfaces. Two types of BCs can be used, constant surface potentials and constant surface charge. In the course of this work, the boundary condition of constant surface potentials (HHF approximation) will be used which leads to the EDL forces contribution to the disjoining pressure (Π_h) to be equal to,

$$\Pi_e = -\frac{\varepsilon\varepsilon_0 \kappa^2}{2\sinh(\kappa h)} \left[\left(\psi_1^2 + \psi_2^2 \right) \cos ech(\kappa h) - 2\psi_1\psi_2 \coth(\kappa h) \right] \quad [1.12]$$

in which, ψ_1 and ψ_2 are the surface potentials of two charged surfaces coming in close proximity to each other. In the case of wetting films, these represent the surface potentials of air bubbles and solid mineral particles, respectively.

1.2.1.3 Hydrophobic Force

Although DLVO theory was found to be very effective in understanding the mechanisms of symmetrical TLFs, such as colloid and foam films, it was unable to explain the kinetics of thinning of wetting film responsible for the process of bubble-particle attachment in flotation (air/liquid/solid) (Pan and Yoon, 2010, 2016). In such a case, the vdW forces are repulsive in nature as explained in the previous sections, leaving no attractive term in DLVO theory. Therefore, the DLVO theory was extended by many researchers to include an attractive structural force term, known as hydrophobic force.

The hydrophobic force was first postulated by Laskowski and Kitchener (1969) as they described various Frumkin-Derjaguin isotherms for silica interacting with air bubbles. These investigators found that the disjoining pressure was negative for the most hydrophobic silica surface leading to TLF rupture, while the TLF with hydrophilic silica was stable. They related the instability of the TLFs to the decrease in the H-bonding of the water molecules near the hydrophobic surfaces leading to higher chemical potentials in the TLFs than in the bulk water.

The term "hydrophobic force" was first coined by Blake and Kitchener (1972). They found that the wetting film formed with the silylated silica surface was metastable due to the combination of EDL and attractive hydrophobic forces. The HB forces were illuminated when the double layer was compressed by using a highly concentrated electrolyte solution (8.6×10^{-3}M potassium chloride solution), and the wetting film ruptured at a critical thickness of 64 nm.

Israelachvili and Pashley (1982) were the first to determine the hydrophobic force experimentally using surface force apparatus (SFA). The force measurement was conducted between two hydrophobic mica surfaces. An exponential force term (F_h) was used to fit the measured force,

$$\frac{F_h}{R} = C \exp\left(-\frac{h}{D} \right) \quad [1.13]$$

where C is the force constant and denotes the strength of hydrophobic force while D denotes the hydrophobic force decay length. h is the separation between two hydrophobic surfaces. Israelachivili and Pashley found that the hydrophobic force with ~1 nm of decay length while later research saw a longer decay length for colloidal surfaces. Ducker *et al.* (1991) were the first to modify the atomic force microscope to directly measure the surface forces in the wetting film between an air bubble and a silica surface.

Although hydrophobic force is widely recognized, the range of its decay length is shown to vary anywhere between a few nanometers to hundreds of nanometers (Claesson *et al.*, 1986; Zhang *et al.*, 2005;

Shi *et al.*, 2014). To separate the short-range and long-range hydrophobic force, the force is described by two exponential terms as the following,

$$\frac{F_h}{R} = C_1 \exp\left(-\frac{h}{D_1}\right) + C_2 \exp\left(-\frac{h}{D_2}\right) \quad [1.14]$$

Where C_1 and C_2 are the strength and, D_1 and D_2 are the decay lengths of short- and long-range hydrophobic forces, respectively. According to the literature, D_1 ranges from 2.1-2.4 nm while the long-range can be anywhere between 28-45 nm for wetting films (Pan and Yoon, 2018). Disjoining pressure associated with hydrophobic force depends on the geometry of surfaces in contact and can be determined using Derjaguin's approximation (Derjaguin, 1934).

$$\Pi_h(h) = \frac{C_1}{2\pi D_1}\exp\left(-\frac{h}{D_1}\right) + \frac{C_2}{2\pi D_2}\exp\left(-\frac{h}{D_2}\right) \quad [1.15]$$

The hydrophobic force can also be represented in the form of power law as follows (Rabinovich and Derjaguin, 1988),

$$\frac{F_h}{R} = -\frac{K_{132}}{6h^2} \quad [1.16]$$

where K is the hydrophobic rate constant. The disjoining pressure can then be determined by the following expression,

$$\Pi_h = -\frac{K_{132}}{6\pi h^3} \quad [1.17]$$

This form is analogous to the vdW disjoining pressure term (Eq. [1.8]) and hence makes it easier to use in the flotation modeling.

Combining Eq. [1.8], [1.12] and [1.15], the overall disjoining pressure can be written as,

$$\begin{aligned}\Pi(h) &= \Pi_d(h) + \Pi_e(h) + \Pi_h(h) \\ &= -\frac{A_{132}}{6\pi h^3} - \frac{\varepsilon\varepsilon_0\kappa^2}{2\sinh(\kappa h)}\left[\left(\psi_1^2 + \psi_2^2\right)\cos ech(\kappa h) - 2\psi_1\psi_2\coth(\kappa h)\right] - \frac{K_{132}}{6\pi h^3}\end{aligned} \quad [1.18]$$

The origin of long-ranged hydrophobic force is still a topic of debate. Some of the theories include mobility or diffusion of electrically charged particles leading to an attractive electrostatic force, and the presence of nanobubbles on the hydrophobic surfaces. It has also been shown that the structure of water changes in the thin liquid film (Eriksson *et al*., 1989) leading to the formation of higher H-bond number structures similar to water clathrates or ice-cages. To confirm the existence of more structured water structures. Wang *et al.* (2011) and Li and Yoon (2014) measured the thermodynamic parameters for hydrophobic or solvophobic forces in water and ethanol, respectively and showed that the excess entropy and enthalpy reduces as the TLF formed between hydrophobic surfaces due to the structuring of water molecules.

1.2.2 Flotation Thermodynamics and Kinetic Modelling

As an air bubble approaches a mineral surface, it starts displacing the water, eventually creating a thin film of liquid in between. The film rupture is thermodynamically controlled by the interfacial tensions of the various phases involved. As the film is ruptured a contact angle (θ) is formed between the air bubble and the surface and is given by Young's equation,

$$\cos\theta = \frac{\gamma_{SV} - \gamma_{SL}}{\gamma_{LV}} \quad [1.19]$$

in which the numerator represents the wetting film tension and is the difference of the surface tension of solid (γ_{SV}) and interfacial tension between solid and liquid (γ_{SL}). The denominator γ_{LV} is the surface tension of water. The interfacial tensions can be determined using the acid-base theory (van Oss, 2006).

The change in the free energy (ΔG) involved in bubble-particle attachment is given by the Young-Dupre equation as,

$$\Delta G = \gamma_{LV}\left(\cos\theta - 1\right) \qquad [1.20]$$

So thermodynamically, if $\theta > 0$, the bubble particle interaction can occur with ΔG becoming more negative with an increase in the θ. Although, for flotation to happen, the bubble and particle hydrodynamics along with their surface chemistry parameters also play a significant role and will be discussed in the next section.

The process of flotation starts with the interaction of an air bubble and a particle in the pulp phase. Taggart (1927) suggested that the bubble precipitated on the surface due to the presence of super gas-saturated zones in a typical flotation cell. However, Gaudin (1931) described flotation to be driven by the collision between a stationary bubble and a falling particle followed by bubble-particle attachment which was later proven by the experimental evidence provided by various researchers (Bogdanov and Filanowski, 1940; Ramsey and Malozemoff, 1941). Derjaguin and Dukhin (1961) provided a three-phase model for describing the flotation theory for small and medium-sized particles. In many senses, this was the first model to be derived from the first principles which considered surface forces as a kinetic parameter. They emphasized that the initiation of flotation or bubble particle interaction is dominated by fluid hydrodynamics but as the bubble and particles are brought closed, the surface forces become the major driving force.

1.2.2.1 Pulp Phase

The interaction of an air bubble and particle in the pulp phase is dependent on three different parameters,

a) The collision of air bubbles and particles which depends on the hydrodynamics of the bubbles, and particles in the present aqueous system.
b) The bubble-particle attachment that primarily depends on the surface chemistry of the particles.
c) The stability of the formed bubble-particle aggregate in the turbulent flow fields of the pulp phase due to the presence of agitated flotation machines.

The kinetics of the pulp phase can be defined by using the Abrahamson (1975) hard-core collision model for extremely turbulent flow conditions (Schubert, 1999),

$$\frac{dN_1}{dt} = -k_p^{'} N_1 \qquad [1.21]$$

$$k_p^{'} = 5.0 N_2 d_{12}^2 \sqrt{\overline{u_1}^2 + \overline{u_2}^2}\, P \qquad [1.22]$$

where, k_p' is the pseudo first order rate constant, N_1 and N_2 are the number densities of the mineral particles and bubbles in pulp phase respectively. d_{12} is the sum of radii of bubble and particle, $\sqrt{\overline{u_1}^2}$ and $\sqrt{\overline{u_2}^2}$ are the root mean square (RMS) velocities of particles and bubbles and P is the flotation probability. As described, flotation is a function of bubble particle interaction and its overall probability can be described as follows,

$$P = P_c P_a (1 - P_d) \qquad [1.23]$$

where, P_c is the collision probability, P_a denotes the attachment probability and P_d signifies the probability of detachment (Schuhmann, 1942; Sutherland, 1948). Here, the particle RMS velocities are calculated by

the following relationship with the specific energy dissipation of the flotation machine and pulp viscosity (Schubert, 1999),

$$\bar{u}_1 = 0.4 \frac{\varepsilon^{4/9} d_1^{7/9}}{\upsilon^{1/3}} \left(\frac{\rho_1 - \rho_3}{\rho_3} \right)^{2/3} \quad [1.24]$$

where, ρ_1 and ρ_3 are the particle and the water densities, respectively while v is the kinematic viscosity of water. The RMS velocities of the bubbles was calculated using the relationship derived by Lee *et al*. (1987),

$$\overline{u_2} = \left(2 \left(\varepsilon d_2 \right)^{2/3} \right)^{1/2} \quad [1.25]$$

1.2.2.1.1 Probability of Collision (P_c)

The theory of collision is the most extensively studied sub-process in flotation. The first expression for P_c was given by Sutherland (1948) using the fluid streamlines under the assumption of potential flow conditions (large Reynolds number) at the bubble surface, and inertia-less particles. He defined a critical radial distance (R_c) of a flow streamline from the center of the bubble and was a function of bubble (d_2) and particle (d_1) radii. If particle follows this streamline, then it will just graze through the bubble surface. P_c was then defined by the area swept under the flow trajectory of such a particle divided by the projected area of the bubble.

$$P_c = 3 \frac{d_1}{d_2} \quad [1.26]$$

Gaudin (1957) derived a model for Stokes flow regime (small Reynolds number) under the assumption of no particle inertial effect. The condition of stokes flow is valid for very small bubbles (d_b < 100 µm; Luttrell and Yoon, 1992). Gaudin's P_c model for the stokes flow regime was,

$$P_c = \frac{3}{2} \left(\frac{d_1}{d_2} \right)^2 \quad [1.27]$$

Flint and Howarth (1971) solved the Navier-Stokes (N-S) equation numerically to derive a collision model for both the potential and Stokes flow regimes to show the following,

$$P_c = \frac{v_1}{v_1 + v_2} \quad [1.28]$$

where, v_1 is given by the particle velocity and v_2 is bubble velocity. The model was then modified by Reay and Ratlciff (1973).

Weber and Paddock (1983) considered the collision between a spherical bubble and particle under the following assumptions: the bubble is sufficiently larger than the particle and particle obeys Stokes' law. The fluid streamlines can be approximated by Taylor's series. It was also assumed that the bubble and particle hydrodynamic interactions were negligible. The collision probability was determined by the ratio of the rate of particles colliding with the bubble to the number of particles that are present under the projected area of the bubble per unit time. For an immobile bubble surface and low Reynolds number, an analytical solution has been provided for the N-S equation and is as follows:

$$P_c = \frac{3}{2} \left(\frac{d_1}{d_2} \right)^2 \left[1 + \frac{3}{16} \left(\frac{\mathrm{Re}}{1 + 0.249\,\mathrm{Re}^{0.56}} \right) \right] \quad [1.29]$$

where *Re* is the bubble Reynolds number. This equation can be accommodated to a wide range of bubble and particle sizes. Many researchers have developed other models to account for different fluid streamlines the inertial effects, the effects of bubble surface mobility (Yoon and Luttrell, 1989; Schulze, 1989; Nguyen-

Van and Kmet, 1994; Dai *et al*., 1998) and therefore, deserve acknowledgment. However, in the current work, Weber and Paddock's model has been used to simulate the collision probability.

The bubble diameter (d_2) can be calculated using the following bubble generation model by Schulze (1984) who determined its relationship with the surface tension and density of the aqueous phase and the specific energy dissipation:

$$d_2 = \left(\frac{2.11\gamma}{\rho_3 \varepsilon_b^{0.66}} \right)^{0.66} \quad [1.30]$$

1.2.2.1.2 Probability of Attachment (P_a)

Once a particle collides with the bubble, it has to form a three-point contact with the bubble to form a bubble-particle aggregate. The probability of attachment has been modeled majorly either based on bubble-particle contact time and induction time or based on bubble-particle attachment energy barrier defined by the surface forces acting in the wetting film.

The time taken for the particle to slide over the bubble surface is known as the contact time while induction time refers to the time taken in wetting film thinning, film rupture, and the time taken by the particle to form a three-point contact with the bubble (Nguyen *et al.,* 1998). For a bubble-particle attachment to occur, the contact time should be larger than the induction time. It has been shown that the time taken for the film rupture is of the order of 10^{-9}s and the time taken to form a contact angle is assumed to be short too, and therefore these are mostly ignored (Luttrell and Yoon, 1989). Hence, the induction time is a function of surface forces. In other words, the induction time increases if the surface hydrophobicity is reduced which is a major step in rejecting the unwanted or hydrophilic minerals.

The energy balance method was derived by considering the bubble-particle attachment to be analogous to a chemical reaction with an energy barrier equaling to the surface forces acting in the wetting film. Luttrell and Yoon (1992) showed that P_a can be determined by the ratio of the energy barrier (E_1) required to be overcome for the bubble-particle attachment, to the kinetic energy of the particles at the critical rupture thickness of the TLF, E_k,

$$P_a = \exp\left(-\frac{E_1}{E_k} \right) \quad [1.31]$$

The energy barrier, E_1 can be calculated using the Derjaguin approximation and the disjoining pressure obtained from Eq. [1.18] (Huang *et al*. 2022). This equation suggests that, as the hydrophobicity of particles increases, the energy barrier reduces leading to an increase in the probability of attachment which agrees well with experimental data (Luttrell and Yoon, 1989; Yoon and Mao, 1996). E_k can be calculated by using the RMS velocity of the particle at the critical rupture thickness.

1.2.2.1.3 Probability of Detachment (P_d)

Once the particle is attached to a bubble, it passes through the pulp phase to reach the froth phase. The stability of the bubble-particle aggregate depends on both the hydrodynamics and the chemical properties associated with the bubble and particle. If the detachment forces are greater than the attachment, the particle will get detached from the bubble surface. The detachment is caused by the following factors (Sherman, 2018),

a) Particle inertia and the action of gravity,
b) Drag and viscous forces,
c) Hydrostatic pressure,
d) Oscillatory motion of bubbles, and
e) Turbulent eddies leading to a centrifugal force on the bubble-particle aggregates.

The detachment force is directly related to the particle size and increases with the increasing d_p. Therefore, for constant surface chemical properties, the probability of detachment, P_d decreases as the particles become coarser due to the reduced mineral liberation of the particles, and increased effect of turbulence as mass increases. Yoon and Mao (1996) suggested that if the kinetic energy present in the cell (E_k') exceeds the sum of work of adhesion (W_a) and energy barrier of bubble-particle attachment (E_1), the aggregate can be de-stabilized. The following form of P_d was derived and has been used for modeling,

$$P_d = \exp\left(-\frac{W_a + E_1}{E_k^{'}}\right) \quad [1.32]$$

1.2.2.2 Froth Phase

In the froth phase, bubbles coalesce to reduce the surface tension acting upon them. Froth is nothing but foam consisting of solid particles. These particles are either attached to the bubble surface or are present in the water present between two air bubbles, depending on their hydrophobicity. The less hydrophobic particles are rejected due to the reduction in the available surface area of the bubbles due to bubble coalescence, which dictates the product grade and the overall recoveries. The froth recovery can be divided into two parts, one that depends on both the surface chemistry and hydrodynamic cell parameters and the second, which just depends on the flow characteristics across the froth phase. The first one is termed the froth attachment recovery and the second, is the froth recovery by entrainment (Ata, 2009; Ata, 2012; Park *et al.* 2018).

1.2.2.2.1 Froth Attachment Recovery ($R_{F,att}$)

A froth phase consists of plateau borders (PB) formed at the junction of three air bubbles. The space between two of these adjacent bubbles is known as lamella which is a thin film of water. As the water drains out of this film, the TLF can rupture leading to bubble coalescence. Park *et al*. (2018) derived a bubble coarsening model under the influence of particles. The rate of thinning of the lamella film can be determined by using Reynold's lubrication theory,

$$\frac{dh}{dt} = -\frac{2h^3 p}{3\mu R_f^{\,2}} \quad [1.33]$$

here, h is the TLF thickness, t is the drainage time, μ is the dynamic viscosity, R_f the film radius and p is the driving force of the process of film thinning and is the sum of capillary pressure (p_c) and attractive disjoining pressure.

$$p = p_c - \Pi \quad [1.34]$$

Π can be determined by Eq [1.18] while p_c depends on the curvature of the bubble (R) and is given by $2\gamma/R$. The initial rate of thinning is controlled by p_c but as the TLF thins to ~150-200 nm, the disjoining pressure starts to govern the rate of thinning. Park *et al.* determined the capillary pressure by considering the local capillary pressure ($p_{c,local}$) due to each particle present in the lamella and calculating the macroscopic pressure (p_c) as,

$$p_c = \frac{\text{overall capillary force}}{\text{film area}} = \frac{(\frac{2\gamma}{R} - p_{c,local})A_I N_{1,film} + \frac{2\gamma}{R}A_{II}}{A_I N_{1,film} + A_{II}} \quad [1.35]$$

where, $N_{1,film}$ is the number of particles present in the lamella, A_I and A_{II} are the area of the curved region in the vicinity to the particle and the flat free film par from it, respectively (Park *et al.* 2018; Denkov *et al.* 1992). $N_{1,film}$ was calculated based on the number of particles reporting to the froth phase and was given by,

$$N_{1,\text{film}} = P_c P_a (1 - P_d) N_{1,\text{seg}} \quad [1.36]$$

$N_{1,\text{seg}}$ is the number of particles reporting to the lamella film at the bottom of the froth phase.

Vrij and his co-workers (Vrij, 1966; Vrij and Overbeek, 1968; Donners and Vrij, 1978) developed a model using the capillary wave motion to describe the critical rupture thickness (H_{cr}) and the time taken for the rupture (t_{cr}). The minimum rupture time (t_m) was defined as the sum of drainage (t_{drain}) and fluctuation time (t_{fluct}) as follows,

$$\left.\frac{dt_{\text{drain}}}{dh}\right|_{h=h_m} + \left.\frac{dt_{\text{fluct}}}{dh}\right|_{h=h_m} = 0 \quad [1.37]$$

$$t_{\text{fluct}} = 144\mu\gamma h^{-3}\left(\left.\frac{\partial\Pi}{\partial h}\right|_{h_m}\right)^{-2} \quad [1.38]$$

Substituting [1.33] and [1.38] in [1.37] one can get the following,

$$-\frac{3h_m^{-3}R_f^{\,2}}{2(p_c-\Pi)}144\gamma + \left\{-3h_m^{-4}\left(\left.\frac{\partial\Pi}{\partial h}\right|_{h_m}\right)^{-2} - 2h_m^{-3}\left(\left.\frac{\partial\Pi}{\partial h}\right|_{h_m}\right)^{-3}\left.\frac{\partial^2\Pi}{\partial h^2}\right|_{h_m}\right\} = 0 \quad [1.39]$$

As the film thinning due to drainage might not be affected by fluctuation and continue to accelerate, the critical rupture thickness (h_{cr}) was assumed to be less than h_m,

$$h_{cr} = 0.845 h_m \quad [1.40]$$

The critical rupture thickness is a major property which depends on the chemical and hydrodynamic parameter of the froth phase. The time taken for two identical bubbles to rise and coalesce will be dependent on the time taken (t_{cr}) in the drainage of the liquid film between them to reach h_{cr}. The t_{cr} can be determined by using Reynold's lubrication theory (Eq. [1.33]) by plugging the disjoining pressure and capillary pressure values and formulating *h vs. t* curves. Using this information, Park *et al*. (2018) derived the following formula for the degree of bubble coalescence which is the ratio of the diameter of bubbles at the top ($d_{2,t}$) and the bottom ($d_{2,b}$) of the froth phase,

$$\frac{d_{2,b}}{d_{2,t}} = \left[\exp\left(-\frac{0.46 n_f h_f}{J_g t_c}\right)\right]^{0.5} \quad [1.41]$$

here, n_f is the number of ruptured faces which ranges from 1-12 as the bubble is considered to be a dodecahedron, h_f is the froth height, J_g is the superficial gas velocity and t_{cr} is the critical rupture time. As can be analyzed from Eq. [1.35], as the number of particles in the lamella film increases, the macroscopic capillary pressure and therefore the driving pressure (p) will be changed, modifying the critical rupture time. The ratio of the bubble sizes at the top and bottom defines the maximum recovery obtained in a froth phase. Gorain *et al*. (1998) related the froth recovery to the froth retention time (τ_f) and showed that as the retention time in the froth increases, the froth recovery is exponentially reduced. Combining this exponential decrease with the maximum froth recovery, one can get the overall froth recovery due to attachment.

$$R_{F,att} = \frac{d_{2,b}}{d_{2,t}}\exp\left(-\alpha\tau_f\right) \quad [1.42]$$

where, α is an empirical parameter which usually ranges between 0.01-0.05 for industrial flotation cells Gorain *et al*., 1998).

1.2.2.2.2 Froth Recovery by Entrainment ($R_{F,ent}$)

The fine particles can also get recovered by being mechanically carried by the froth without being attached to the air bubbles (Trahar 1981, Warren, 1985). Factors affecting froth entrainment recovery includes water recovery, particle shape and size, froth structure, mineral specific gravity and other hydrodynamic properties of a flotation cell (Bisshop and White, 1976; Engelbrecht and Woodburn, 1975; Kirjavainen, 1992; Lynch *et al.,* 1981).

Degree of entrainment is generally defined in terms of water recovery as fine particles are carried along with the water present in the lamella films. Maachar and Dobby (1992) determined an empirical expression for entrainment to relate the water recovery with degree of entrainment,

$$R_{F,ent} = R_{FW} \cdot \exp(-0.0325 \cdot \Delta\rho) \cdot \exp(-0.063 d_1) \quad [1.43]$$

where, R_{FW} is the feed water recovery from the froth, $\Delta\rho$ is the specific gravity difference between the solid and water, and d_1 is particle diameter in μm.

1.2.2.3 Overall Flotation Recovery

The overall flotation cell recovery can be calculated by considering the drop-back of the particles from the froth phase to the pulp phase, which provides them with more opportunity to recover. The overall recovery (R) using pulp phase (R_p) and froth phase (R_p) recoveries comes out to be (Huang *et al*., 2022),

$$R = \frac{R_p R_f}{R_p R_f + 1 - R_p} \quad [1.44]$$

1.2.2.4 Flotation Model Parameters

In overall, the following are the chemical, physical and fitting parameters in the flotation model:

Chemical Parameters:

- Particle contact-angle
- Grade of each size-class of minerals
- Hamaker constants, A_{131} and A_{232}
- Frother Type and Concentration
- Collector Type and Concentration
- Bubble zeta potential
- Particle zeta potential
- Surface tension of water
- Dielectric constants
- Permittivity

Physical Parameters:

- Size-by-class liberation matrix, m_{ij}
- Specific gravity
- Feed rate
- Pulp density (%solids)
- Specific power in a flotation cell
- Superficial gas velocity
- Cell volume
- Air fraction
- Cell Area
- Froth Height

- Liquid Viscosity
- Impeller zone fraction

Fitting Parameters:

- Bubble Coverage to determine the number of particles attached to a bubble.
- Bubble diameter fitting constant to determine the bubble diameter at the tip of impeller.
- Number of lamella faces that are ruptured in the froth phase used in Eq. [1.41].
- Parameter α of Eq. [1.42].
- Locking factor to be used in Cassie-Baxter equation to predict the composite particles contact angles.
- Intensity of agitation near impeller and collection zone to determine particle and bubble velocities and bubble diameter.

1.2.3 Thermodynamics of the hydrophobic interactions in foam films

As discussed in the previous sections, froth drainage helps in determining the final product grade and the overall recovery. To study the froth behavior, it is paramount to understand the foam film characteristics.

Foam is a system where the gas phase is dispersed in the liquid medium. In the case of froth flotation, air bubbles are dispersed in the aqueous solutions. In a 2-D foam, three bubbles meet each other forming a plateau border (PB) while in a 3-D foam, 4 plateau borders meet at an angle of 109°. A thin liquid film of water present between two such air bubbles close to each other is known as foam film which dictates the foam stability (Exerowa and Kruglyakov, 1997; Wang, 2012).

Disjoining pressure across the thin liquid film determines the rate of thinning of this foam film. As mentioned earlier, it is the sum of the surface forces acting on the film. This can be calculated by conducting a thin film pressure balance or the normal stress balance where the external pressure is the difference between the capillary pressure and the repulsive disjoining pressure Eq. [1.34].

Here, P is the external pressure applied on the film and P_c is the capillary pressure due to the curvature of the film. Initially, the film thinning is dictated by the change in radius of curvature, but as the two air/water interfaces are less than 200 nm away from each other, the thinning is driven by the surface forces/disjoining pressure. One can calculate the pressure exerted on the TLF by measuring the rate of film thinning using interferometric techniques and solving Reynold's lubrication theory. In the current work, the local capillary pressure is also considered to account for the local curvature changes in the foam film. The method is analogous to the one used for wetting films.

N-S equation can be used to describe the film-thinning process under the assumption of low fluid velocities. Pan and Yoon (2011, 2016) and Huang and Yoon (2019, 2020) used the spatial-temporal profile derived from the thin film interferometry to numerically determine the disjoining pressure in wetting film. Similarly, foam film interactions can be studied.

In a wetting film, as an air bubble approaches a solid flat surface, the local capillary pressure will change as the thin film for a deformable surface will not have a constant radius of curvature. The change in the film thickness (h) with respect to the time (t) can be described by Reynold's lubrication theory under the assumption of the immobile surfaces as,

$$\frac{\partial h}{\partial t} = \frac{1}{12\mu r}\frac{\partial}{\partial r}\left(rh^3\frac{\partial p}{\partial r}\right) \qquad [1.45]$$

here, r is the radial distance from the center of the film.

The excess pressure can be written as the following,

$$p_c = \frac{2\gamma}{R} - \frac{\gamma}{2r}\frac{\partial}{\partial r}\left(r\frac{\partial h}{\partial r}\right) \quad [1.46]$$

Using the boundary conditions, $p(r \to \infty)=0$ and $\frac{\partial p}{\partial r}|_{r=0} = 0$, the hydrodynamic or excess pressure and therefore, disjoining pressure can be determined using Eqs. [1.45] and [1.46].

$$\Pi = \frac{2\gamma}{R} - \frac{\gamma}{2r}\frac{\partial}{\partial r}\left(r\frac{\partial h}{\partial r}\right) - 12\mu\int_{r=\infty}^{r}\frac{1}{rh^3}\left[\int_{r=0}^{r} r\frac{\partial h}{\partial t}dr\right]dr \quad [1.47]$$

Similar steps have been taken to build a disjoining pressure isotherm by analyzing the spatial-temporal profiles of surfactant-free foam films.

Utilizing the value of Π_h obtained as described in the previous section, one can determine ΔG associated with the hydrophobic interaction between two macroscopic surfaces using the following,

$$\Delta G = -\int_{h=\infty}^{h_0} \Pi_h(h)\,dh \quad [1.48]$$

where h_0 is the thickness of the α-film. Thermodynamically, the excess surface free energy (ΔG) represents the change in the film tension as an infinitely thick film thins to a finite thickness, h. For constant pressure (P), it is given by the Gibbs-Duhem equation,

$$d\Delta G = -\Delta S dT - \Pi dh \quad [1.49]$$

Here, ΔS is the corresponding excess surface entropy. Assuming that the surface force contributions due to the vdW forces, and EDL forces are not sensitive to the temperatures, as A_{232} and ψ_2 don't change significantly, the thermodynamic quantity, ΔS can be related to ΔG, and can subsequently to Π_h at constant temperature (T) and thickness (h) as (Wang *et al*., 2011),

$$\begin{aligned}\Delta S &= -\left(\frac{\partial \Delta G}{\partial T}\right)_{P,h} \\ &= -\frac{C}{2\pi}\exp\left(-\frac{h}{D}\right)\left[\frac{d(\ln C)}{dT} + \frac{h}{D}\frac{d(\ln D)}{dT}\right]\end{aligned} \quad [1.50]$$

In the present work, the temperature dependence of hydrophobic force parameters was found by conducting surface force measurements at different temperatures. Excess surface enthalpies (ΔH) can then be determined using the following,

$$\Delta H = \Delta G + T\Delta S \quad [1.51]$$

where, C and D are the hydrophobic force constant and decay length, respectively.

Thermodynamics of colloidal film has been studied in the past (Wang *et al.*, 2011) and it was found that both ΔS^f and ΔH^f became negative as the two hydrophobic surfaces were brought close to each other indicating the formation of stable structures in the thin liquid film of water in between which was enthalpic in nature. They showed that the number of H-bonds increased with the reducing separation distance. In lieu of the findings, it was proposed that the hydrophobic force is indeed a true structural force and is due to the formation of particle clathrates near the hydrophobic surfaces.

In the current work, the thermodynamics of two macroscopic interactions are studied, emulsion and foam films using the thin-pressure balance techniques where instead of measuring the pressure changes, the light interference patterns are recorded using a microscope to accurately predict attractive (negative) disjoining pressures.

1.3 Research Objectives

The main objective of this research is to modify the above described first-principle based flotation model to enhance its applicability in optimization of full-scale flotation circuits. The other important objective is to evaluate the thermodynamics of foam films to find the origins of hydrophobic forces.

The specific research objectives are as follows:

- Develop and modify a flotation simulator derived from first principles that uses hydrophobic forces as a kinetic parameter to accurately predict the performance of a large-scale copper plant rougher flotation circuit (Chapter 2).
- Develop an analytical solution for the circuit analysis for a large copper plant using the rate constants derived from first principle based flotation model to enlist the kinetics and economic benefits of discarding the cleaner scavenger tails to a separate fine recovery unit. (Chapter 3)
- Develop a new reagent to achieve high mineral particle contact angles and improve flotation kinetics and simulate the improvements in the performance of a large-scale copper plant rougher circuit. (Chapter 4 and 5).
- Develop a new coarse-particle recovery unit to expand the upper particle size limit of mineral flotation. (Chapter 6).
- Conduct disjoining pressure measurements using thin film pressure balance technique to determine the presence of long ranged hydrophobic forces in surfactant free foam films and the thermodynamics of this macroscopic scale interactions. (Chapter 7)
- Conduct disjoining pressure measurements using thin film pressure balance technique to determine the thermodynamics of hydrophobic interactions in surfactant-free emulsion films to understand the macroscopic scale hydrophobic interactions and determine the thermodynamic origin of long-range hydrophobic forces (Chapter 8).

1.4 References

Abrahamson, J., 1975. Collision rates of small particles in a vigorously turbulent fluid. Chemical Engineering Science, 30(11), 1371-1379.Bushell, C. H. G. (1962). Kinetics of flotation. Trans. AIME, 223, 266-278.

Albijanic, B., Ozdemir, O., Nguyen, A. V., & Bradshaw, D. (2010). A review of induction and attachment times of wetting thin films between air bubbles and particles and its relevance in the separation of particles by flotation. Advances in colloid and interface science, 159(1), 1-21.

Ata, S. (2009). The detachment of particles from coalescing bubble pairs. Journal of colloid and interface science, 338(2), 558-565.

Ata, S. (2012). Phenomena in the froth phase of flotation—A review. International Journal of Mineral Processing, 102, 1-12.

B.V. Derjaguin, S.S. Dukhin (1961) Theory of flotation of small and medium size particles, Trans. Inst. Min. Metall. 70. 221246.

Bisshop, J. P., & ME, W. (1976). Study of Particle Entrainment in Flotation Froths.

Blake, T. D., & Kitchener, J. A. (1972). Stability of aqueous films on hydrophobic methylated silica. Journal of the Chemical Society, Faraday Transactions 1: Physical Chemistry in Condensed Phases, 68, 1435-1442.

Bogdanov, O. S., & Filanovski, M. S. (1940). Adhesion of mineral particles to air bubbles. J. Phys. Chem. USSR, 14, 224-227.

Bradley, R. S. (1932). LXXIX. The cohesive force between solid surfaces and the surface energy of solids. The London, Edinburgh, and Dublin Philosophical Magazine and Journal of Science, 13(86), 853-862.

Churaev, N., Contact angles and surface forces. Advances in Colloid and Interface Science 1995, 58 (2-3), 87-118.

Claesson, P. M., Blom, C. E., Herder, P. C., & Ninham, B. W. (1986). Interactions between water—stable hydrophobic Langmuir—Blodgett monolayers on mica. Journal of colloid and interface science, 114(1), 234-242.

Clark, M. E., Brake, I., Huls, B. J., Smith, B. E., & Yu, M. (2005). Creating value through application of flotation science and technology. Centenary of Flotation Symposium, 6-9 June,Brisbane, QLD.

Collins, G. L., & Jameson, G. J. (1977). Double-layer effects in the flotation of fine particles. Chemical Engineering Science, 32(3), 239-246.

Dai, Z., Dukhin, S., Fornasiero, D., & Ralston, J. (1998). The inertial hydrodynamic interaction of particles and rising bubbles with mobile surfaces. Journal of Colloid and Interface Science, 197(2), 275-292.

De Boer, J. H. (1936). The influence of van der Waals' forces and primary bonds on binding energy, strength and orientation, with special reference to some artificial resins. Transactions of the Faraday Society, 32, 10-37.

Debye, P. (1920). Die van der Waalsschen Kohasion-skrafte. Phys. Zs., 21, 178-187.

Denkov, N.D., Ivanov, I.B., Kralchevsky, P.A., Wasan, D.T., 1992. A possible mechanism of stabilization of emulsions by solid particles. J. Colloid Interface Sci. 150 (2), 589–593.

Derjaguin, B. V. (1934). Friction and adhesion. IV. The theory of adhesion of small particles. Kolloid Zeits, 69, 155-164.

Derjaguin, B. V. (1989). Theory of stability of colloids and thin films (pp. 30-30). New York: Consultants Bureau.

Derjaguin, B. V., & Kussakov, M. (1939). Anomalous properties of thin polymolecular films. Acta Physicochim. URSS, 10(1), 25-44.

Derjaguin, B. V., & Landau, L. (1941). Theory of the stability of strongly charged lyophobic sols and of the adhesion of strongly charged particles in solutions of electrolytes. Acta Physicochim. URSS, 14(733-762), 39.

Dobby, G. S., & Finch, J. A. (1986). A model of particle sliding time for flotation size bubbles. Journal of Colloid and Interface Science, 109(2), 493-498.

Dobby, G. S., & Finch, J. A. (1987). Particle size dependence in flotation derived from a fundamental model of the capture process. International Journal of Mineral Processing, 21(3-4), 241-260.
Donners, W.A.B., Vrij, A., 1978. The critical thickness of thin free liquid films. Colloid Polym. Sci. 256 (8), 804–813.
Ducker, W. A., Senden, T. J., & Pashley, R. M. (1991). Direct measurement of colloidal forces using an atomic force microscope. Nature, 353(6341), 239-241.
Engelbrecht, J. A., & ET, W. (1975). The effects of froth height, aeration rate, and gas precipitation on flotation.
Eriksson, J. C., Ljunggren, S., & Claesson, P. M. (1989). A phenomenological theory of long-range hydrophobic attraction forces based on a square-gradient variational approach. Journal of the Chemical Society, Faraday Transactions 2: Molecular and Chemical Physics, 85(3), 163-176.
Exerowa, D., & Kruglyakov, P. M. (1997). Foam and foam films: theory, experiment, application. Elsevier.
Flint, L. R., & Howarth, W. J. (1971). The collision efficiency of small particles with spherical air bubbles. Chemical Engineering Science, 26(8), 1155-1168.
Frumkin, A. (1924). Phasengrenzkräfte und Adsorption an der Trennungsfläche Luft. Lösung anorganischer Elektrolyte. Zeitschrift für Physikalische Chemie, 109(1), 34-48.
Gaudin, A. M. (1931). Effect of particle size on flotation. Technical Publication, 3-23.
Gaudin, A. M. (1957). Flotation. McGraw-Hill.
Gorain, B.K., Harris, M.C., Franzidis, J.P., Manlapig, E.V., 1998. The effect of froth residence time on the kinetics of flotation. Miner. Eng. 11 (7), 627–638.
Grahame, D. C. (1947). The electrical double layer and the theory of electrocapillarity. Chemical reviews, 41(3), 441-501.
Hamaker, H. C. (1937). The London—van der Waals attraction between spherical particles. physica, 4(10), 1058-1072.
Huang, K. (2020). Surface Forces in Thin Liquid Films (Doctoral dissertation, Virginia Tech).
Huang, K., & Yoon, R. H. (2019). Effect of ζ-potentials on bubble-particle interactions. Mining, Metallurgy & Exploration, 36, 21-34.
Huang, K., & Yoon, R. H. (2020). Control of bubble ζ-potentials to improve the kinetics of bubble-particle interactions. Minerals Engineering, 151, 106295.
Huang, K., Serhat Keles, Ian Sherrell, Aaron Noble, and Roe-Hoan Yoon (2022). Development of a Flotation Simulator that can predict grade vs. recovery curves from mineral liberation data. Mineral Engineering, 181, 107510.
Israelachvili, J. N., *Intermolecular and surface forces: revised third edition*. Academic press: 2011.
Israelachvili, J., & Pashley, R. (1982). The hydrophobic interaction is long range, decaying exponentially with distance. Nature, 300(5890), 341-342.
Israelachvili, J.-N. In The calculation of van der Waals dispersion forces between macroscopic bodies, Proceedings of the Royal Society of London A: Mathematical, Physical and Engineering Sciences, The Royal Society: 1972; pp 39-55.
Jameson, G.J. (2012). The effect of surface liberation and particle size on flotation rate constants. Minerals Engineering, 36-38, 132-137.
Kallmann, H., & Willstaetter, M. (1932). Zur theorie des aufbaues kolloidaler systeme. Naturwissenschaften, 20(51), 952-953.
Keesom, W. H. (1921a). The quadrupole moments of the oxygen and nitrogen molecules. Koninklijke Nederlandse Akademie van Wetenschappen Proceedings Series B Physical Sciences, 23, 939-942.
Keesom, W. H. (1921b). The cohesion forces in the theory of van der Waals. Koninklijke Nederlandse Akademie van Wetenschappen Proceedings Series B Physical Sciences, 23, 943-948.
Kirjavainen, V. M. (1992). Mathematical model for the entrainment of hydrophilic particles in froth flotation. International journal of mineral processing, 35(1-2), 1-11.
Labib, M. E. (1988). The origin of the surface charge on particles suspended in organic liquids. Colloids and Surfaces, 29(3), 293-304.

Laskowski, J., & Kitchener, J. A. (1969). The hydrophilic—hydrophobic transition on silica. Journal of Colloid and Interface Science, 29(4), 670-679.
Lee, C. H., Erickson, L. E., & Glasgow, L. A. (1987). Bubble breakup and coalescence in turbulent gas-liquid dispersions. Chemical Engineering Communications, 59(1-6), 65-84.
Li, Z., & Yoon, R. H. (2014). Thermodynamics of solvophobic interaction between hydrophobic surfaces in ethanol. Langmuir, 30(44), 13312-13320.
Lifshitz, E. M. (1955). The theory of molecular attraction forces between solid bodies. Zhurnal Eksperimentalnoi Teoreticheskoi Fiziki, 29, 94-110.
London, F. (1930). Zur theorie und systematik der molekularkräfte. Zeitschrift für Physik, 63(3-4), 245-279.
London, F. (1937). The general theory of molecular forces. Transactions of the Faraday Society, 33, 8b-26.
Luttrell, G. H., & Yoon, R. H. (1992). A hydrodynamic model for bubble—particle attachment. Journal of colloid and interface science, 154(1), 129-137.
Lynch, A. J., Johnson, N. W., Manlapig, E. V., & Thorne, C. G. (1981). Mineral and coal flotation circuits: Their simulation and control.
Maachar, A., & Dobby, G. S. (1992). Measurement of feed water recovery and entrainment solids recovery in flotation columns. *Canadian metallurgical quarterly*, 31(3), 167-172.
Mouat, J. (1996). The development of the flotation process: technological change and the genesis of modern mining, 1898–1911. Australian Economic History Review, 36(1), 3-31.
Nguyen, A.V., Ralston, J., Schulze, H.J., 1998. On modelling of bubble–particle attachment probability in flotation. Int. J. Miner. Process. 53 (4), 225–249.
Nguyen-Van, A., & Kmeť, S. (1994). Probability of collision between particles and bubbles in flotation: the theoretical inertialess model involving a swarm of bubbles in pulp phase. International journal of mineral processing, 40(3-4), 155-169.
Pan, L., & Yoon, R. H. (2010). Hydrophobic forces in the wetting films of water formed on xanthate-coated gold surfaces. Faraday discussions, 146, 325-340.
Pan, L., & Yoon, R. H. (2016). Measurement of hydrophobic forces in thin liquid films of water between bubbles and xanthate-treated gold surfaces. Minerals Engineering, 98, 240-250.
Pan, L., & Yoon, R. H. (2018). Effects of electrolytes on the stability of wetting films: Implications on seawater flotation. *Minerals Engineering*, 122,1-9.
Pan, L., Jung, S., & Yoon, R. H. (2011). Effect of hydrophobicity on the stability of the wetting films of water formed on gold surfaces. Journal of colloid and interface science, 361(1), 321-330.
Park, S., Huang, K., & Yoon, R. H. (2018). Predicting bubble coarsening in flotation froth: Effect of contact angle and particle size. Minerals Engineering, 127, 256-264.
Pyke, B., Fornasiero, D., & Ralston, J. (2003). Bubble particle heterocoagulation under turbulent conditions. Journal of colloid and interface science, 265(1), 141-151.
Quast, K. B., & Readett, D. J. (1987). The surface chemistry of low-rank coals. Advances in colloid and interface science, 27(3-4), 169-187.
R.H. Ramsey, P. Malozemoff, Eng. Mining J. 142 (3) (1941) 45.
Rabinovich Ya. L and Derjaguin. B.V. in Proceedings of the 5th Hungarian Conference on Colloid Chemistry. Balatonfured. Hungary, Lorand Eotvos University. Budapest. 1988.
Ralston, J., Fornasiero, D., & Hayes, R. (1999). Bubble–particle attachment and detachment in flotation. International Journal of Mineral Processing, 56(1-4), 133-164.
Reay, D., & Ratcliff, G. A. (1973). Removal of fine particles with spherical air bubbles. Journal of Chemical Engineering, 51(178), 206.
Schubert, H. (1999). On the turbulence-controlled microprocesses in flotation machines. International journal of mineral processing, 56(1-4), 257-276.
Schuhmann Jr, R. (1942). Flotation Kinetics. I. Methods for steady-state study of flotation problems. The Journal of Physical Chemistry, 46(8), 891-902.
Schulze, H. J. (1984). Physico-chemical elementary processes in flotation. Developments in mineral processing, 4.

Schulze, H. J. (1989). Hydrodynamics of bubble-mineral particle collisions. Mineral Processing and Extractive Metallurgy Review, 5(1-4), 43-76.
Sherman, H. (2018). Hydrodynamic forces on floating particles.
Shi, C., Chan, D. Y., Liu, Q., & Zeng, H. (2014). Probing the hydrophobic interaction between air bubbles and partially hydrophobic surfaces using atomic force microscopy. The Journal of Physical Chemistry C, 118(43), 25000-25008.
Sutherland, K. L. (1948). Physical chemistry of flotation. XI. Kinetics of the flotation process. The Journal of Physical Chemistry, 52(2), 394-425.
Taggart, A. F (1927).: Handbook of Ore Dressing. John Wiley and Sons, Inc., New York. pp. 797-9, 806-8; 1945 edition, Section 12, pp. 52-4.
Trahar, W. J. (1981). A rational interpretation of the role of particle size in flotation. International Journal of Mineral Processing, 8(4), 289-327.
Van der Waals, J. D. (1873). Over de Continuiteit van den Gas-en Vloeistoftoestand (Vol. 1). Sijthoff.
Van Oss, C. J. (2006). Interfacial forces in aqueous media. CRC press.
Van, A. N., & Kmeť, S. (1992). Collision efficiency for fine mineral particles with single bubble in a countercurrent flow regime. International journal of mineral processing, 35(3-4), 205-223.
Verwey, E. J. W., and J. Th G. Overbeek. "Theory of the stability of lyophobic colloids." Journal of Colloid Science 10, no. 2 (1955): 224-225.
Vrij, A., 1966. Possible mechanism for the spontaneous rupture of thin, free liquid films. Discuss. Faraday Soc. 42, 23–33.
Vrij, A., Overbeek, J.T.G., 1968. Rupture of thin liquid films due to spontaneous fluctuations in thickness. J. Am. Chem. Soc. 90 (12), 3074–30
Wang, D., & Liu, Q. (2021). Hydrodynamics of froth flotation and its effects on fine and ultrafine mineral particle flotation: A literature review. Minerals Engineering, 173, 107220.
Wang, G., Nguyen, A. V., Mitra, S., Joshi, J. B., Jameson, G. J., & Evans, G. M. (2016). A review of the mechanisms and models of bubble-particle detachment in froth flotation. Separation and Purification Technology, 170, 155-172.
Wang, J., Yoon, R. H., & Eriksson, J. C. (2011). Excess thermodynamic properties of thin water films confined between hydrophobized gold surfaces. Journal of colloid and interface science, 364(1), 257-263.
Wang, L. (2012). Drainage and rupture of thin foam films in the presence of ionic and non-ionic surfactants. International Journal of Mineral Processing, 102, 58-68.
Warren, L. J. (1985). Determination of the contributions of true flotation and entrainment in batch flotation tests. International Journal of Mineral Processing, 14(1), 33-44.
Weber, M. E., & Paddock, D. (1983). Interceptional and gravitational collision efficiencies for single collectors at intermediate Reynolds numbers. Journal of Colloid and Interface Science, 94(2), 328-335.
Wills, B. A., & Finch, J. A. (2016). Mineral processing technology: An introduction to the practical aspects of ore treatment and mineral recovery. Butterworth Heinemann.
Yianatos, J., Carrasco, C., Bergh, L., Vinnett, L., & Torres, C. (2012). Modelling and simulation of rougher flotation circuits. International Journal of Mineral Processing, 112, 63-70.
Yoon, R. H., & Luttrell, G. H. (1989). The effect of bubble size on fine particle flotation. Mineral Procesing and Extractive Metallurgy Review, 5(1-4), 101-122.
Yoon, R. H., & Mao, L. (1996). Application of extended DLVO theory, IV: derivation of flotation rate equation from first principles. Journal of Colloid and Interface Science, 181(2), 613-626.
Yoon, R. H., & Vivek, S. (1998). Effects of short-chain alcohols and pyridine on the hydration forces between silica surfaces. Journal of Colloid and Interface Science, 204(1), 179-186.
Yoon, R. H., & Yordan, J. L. (1986). Zeta-potential measurements on microbubbles generated using various surfactants. Journal of Colloid and Interface Science, 113(2), 430-438.
Yoon, R. H., Soni, G., Huang, K., Park, S., & Pan, L. (2016). Development of a turbulent flotation model from first principles and its validation. International Journal of Mineral Processing, 156, 43-51.

Zhang, J., Yoon, R. H., Mao, M., & Ducker, W. A. (2005). Effects of degassing and ionic strength on AFM force measurements in octadecyltrimethylammonium chloride solutions. Langmuir, 21(13), 5831-5841.

Chapter 2. Predicting The Recovery and Grade of a Rougher Flotation Circuit from Liberation Data

(Gupta, M., Huang, K., & Yoon, R. H., 2022. *Minerals Engineering*, *188*, 107853.)

2.1 Abstract

A flotation model has been validated against the survey data obtained from a copper rougher flotation circuit with a circulating load. The model was developed using the hydrophobic force as a kinetic parameter, which made it possible to use the contact angles of the free and composite particles as input parameters so that the model can predict both recoveries and grades. The model also recognizes the role of bubble coarsening in determining the froth phase recoveries and grades. The model predictions are in good agreement with the survey data. The size-by-size recovery curve as predicted from the model shows an optimum particle size range that is consistent with most of the operating data reported in the literature. The model suggests that the upper particle size limit may be determined by the instability of the froth phase rather than the turbulence in the pulp phase of a flotation cell.

2.2 Introduction

Flotation is regarded as the best-available separation process for the recovery of fine particles. A mined ore is ground typically to less than ~100 μm to liberate a target mineral from the rest, with the fine particles dispersed in an aqueous (or pulp) phase. A hydrophobizing agent (collector) is added to the pulp phase to selectively render the target mineral hydrophobic. Air bubbles are then introduced to the pulp to collect the hydrophobic particles on the surface, leaving the hydrophilic ones unattached. The bubble-particle aggregates formed in this manner rise in the pulp phase due to increased buoyancy, form a froth phase on top of the pulp phase and float into the launder to be recovered as a concentrate, while the hydrophilic particles leave the cell as tailings. Thus, flotation is essentially a hydrophobic-hydrophilic separation process.

When an air bubble in an aqueous phase approaches a surface, the bubble changes its local curvature, creating a capillary pressure that can cause the intervening liquid (water) to drain and thin. As the film thins to less than ~250-300 nm, the capillary pressure wanes as the film becomes more or less flat, while surface forces become stronger with decreasing film thickness, allowing the film thinning process to be controlled by the disjoining pressure (Π). As the film thins further to a critical thickness (h_{cr}), at which the disjoining pressure becomes negative, *i.e.*, $\Pi < 0$, the film ruptures catastrophically, creating a solid/air interface and forming a finite contact angle (θ) along the three-phase contact line, which is a prerequisite for flotation. Pan and Yoon (2010) measured Π in the thin liquid films (TLFs) formed on the gold surfaces coated with potassium amyl xanthate (KAX) using the Thin-Film Pressure Balance (TFPB) method. The results showed that the film thinning and rupture are controlled by the hydrophobic force, which increased with increasing θ. The same conclusion was drawn from the disjoining pressure measurements conducted on the TLFs of water formed on gold surfaces coated with potassium ethyl xanthate (KEX) (Pan and Yoon, 2016). These measurements were conducted using the Force Apparatus for Deformable Surfaces (FADS), which was more accurate than the TFPB.

Contact angle formation may be viewed as an incipient flotation, in which Π plays a decisive role in determining θ as shown by the Frumkin-Derjaguin isotherm (Frumkin, 1938; Derjaguin, 1940),

$$\Delta G = -\int_{h_\infty}^{h_0} \Pi(h)dh = \gamma_{LV}\left(\cos\theta - 1\right) \qquad [2.1]$$

The disjoining pressure in Eq. [2.1] may be given as the sum of the Π_e, electrical double-layer (EDL), Π_d, van der Waals (vdW), and Π_h, hydrophobic (HP) forces as follows (Yoon and Mao, 1996),

$$\Pi(h) = \Pi_d(h) + \Pi_e(h) + \Pi_h(h) \qquad [2.2]$$

In bubble-particle interactions, the vdW force is always repulsive and so is the EDL force in most cases, while the HP force is always attractive. The HP force can be expressed either as an exponential force law or as a power law. The latter was used in the following form (Rabinovich *et al.*, 1993),

$$\frac{F_h}{R} = -\frac{K_{131}}{6h^2} \quad [2.3]$$

in which F_h is the hydrophobic force, R is the radius of surfaces, h is the closest separation distance between two interacting surfaces, and K_{131} is the hydrophobic force constant between two surfaces **1** in water **3**. It has been shown that the HP constant (K_{132}) between particle **1** and air bubble **2** can be obtained from the following relationship (Yoon *et al*. 1997; Pan and Yoon, 2010),

$$K_{132} = \sqrt{K_{131}K_{232}} \quad [2.4]$$

in which K_{232} is the hydrophobic force constant between two air bubbles in water. It has been shown that K_{131} varies with θ (Pazhianur and Yoon, 2003), while K_{232} varies with electrolyte (and frother) concentrations (Wang, 2012). The best example of contact angles and hydrophobic forces controlling flotation separation may be the work of Jameson (2012), who showed that the flotation rate constant increases exponentially with increasing surface liberation, which in turn controls the contact angles of composite particles in accordance with the Cassie-Baxter equation (1944).

As bubbles rise in a froth phase, they become larger in size due to coalescence, forcing less-hydrophobic particles to drop off the surface due to the limited 'parking' area and the shockwaves created by the coalescence and drop back to the pulp phase. These mechanisms are responsible for the cleaning action of the froth phase (Moys, 1978; Ata, 2012). It would, therefore, be useful to predict bubble coarsening in the froth phase to predict product grades. Park *et al*. (2018) derived a model that can predict bubble coarsening as functions of particle size, hydrophobicity, particle loading, local capillary pressure, superficial gas velocity, *etc*. Huang *et al*. (2022) combined the bubble-coarsening model of Park *et al*. with their pulp phase recovery model to develop a comprehensive flotation model that can be used to predict both recovery and grade. The model has been validated against the mini-plant data reported by dos Santos and Galery (2018a,b).

In the present work, the operational data obtained from the rougher flotation circuit of a large porphyry copper ore processing plant has been used to validate Huang *et. al*.'s flotation model. The input to the simulation was the size-by-class liberation matrix. It is assumed that all of the particles in a given liberation class have the same contact angle, which in turn varies with the particle size as the surface liberation varies with particle size. Once the contact angles of particles are known, the values of K_{132} are determined using Eq. [2.4] and Π using Eq. [2.2], which in turn is used to determine the kinetics parameters, *e.g.*, energy barriers for bubble-particle attachment, and subsequently, the flotation rate constant as functions of particle size, bubble size, liberation, *etc*., as described by Huang *et al*. (2022). The simulation results are in reasonable agreement with the plant survey data and provide new insights to improve the efficiency of flotation.

2.3 Model

2.3.1 Pulp Phase Recovery

Flotation begins with the collision between bubbles and particles in the pulp phase of a flotation cell, followed by attachment. The kinetics of bubble-particle attachment may be represented as first-order rate equation,

$$\frac{dN_1}{dt} = -k_p N_1 \quad [2.5]$$

in which N_1 is the number density of particles in the pulp phase and k_p is the rate constant, which may be given as follows (Huang *et al.* 2022),

$$k_p = 5.0 N_2 d_{12}^2 \sqrt{\overline{u_1}^2 + \overline{u_2}^2}\, P \qquad [2.6]$$

where N_2 is the number density of bubbles in the pulp phase, d_{12} tis the collision radius, which is the sum of the radii of a bubble and a particle of interest, $\sqrt{\overline{u_1}^2}$ and $\sqrt{\overline{u_2}^2}$ are the corresponding RMS velocities. In Eq. [2.6], P is the probability of bubble-particle attachment, which is a product of the probabilities of collision (P_c), attachment (P_a) and not being detached ($1\text{-}P_d$) in the pulp phase, *i.e.*, $P = P_c P_a (1\text{-}P_d)$ (Schuhman, 1942; Sutherland, 1948). Eq. [2.6] is based on the collision model derived by Abrahamson (1975).

In the present work, we used the collision model of Weber and Paddock (1983),

$$P_c = \frac{3}{2}\left(\frac{d_1}{d_2}\right)^2 \left[1 + \frac{3}{16}\left(\frac{\mathrm{Re}}{1 + 0.249\,\mathrm{Re}^{0.56}}\right)\right] \qquad [2.7]$$

in which d_1 and d_2 are the particle and bubble diameters, respectively, and Re is the Reynolds number for streamline collision.

For the probability of attachment (P_a), Luttrell and Yoon (1992) used the following expression,

$$P_a = \exp\left(-\frac{E_1}{E_k}\right) \qquad [2.8]$$

in which E_1 is the energy barrier for bubble-particle attachment and E_k is the kinetic energy of particles in the pulp phase at h_cr. By analogy to the Arrhenius equation, P_a represents the fraction of the particles whose $E_\mathrm{k} = E_1$. Eq. [2.8] suggests that only the particles with $E_\mathrm{k} > E_1$ can be attached to air bubbles. Thus, it is necessary to keep E_1/E_k minimum to maximize P_a.

One can determine E_1 from a free energy isotherm ($G(h)$), which is a function of disjoining pressure,

$$\Pi = -\frac{A_{132}}{6\pi h^3} - \frac{\varepsilon\varepsilon_0\kappa^2}{2\sinh(\kappa h)}\left[\left(\psi_1^2 + \psi_2^2\right)\mathrm{cosech}(\kappa h) - 2\psi_1\psi_2\coth(\kappa h)\right] - \frac{K_{132}}{6\pi h^3} \qquad [2.9]$$

in which A_{132} is the Hamaker constant, ε the permittivity of vacuum, ε_0 the dielectric constant of water, κ the reciprocal Debye length, and ψ_1, and ψ_2 are the surface (or ζ -) potentials of the particles and bubbles, respectively.

Derjaguin approximation (1934) relates the forces of interaction between two macroscopic surfaces of different geometries to the interaction energies. Huang *et al*. (2022) used this relation to derive a relationship between a particle of radius R_1 and an air bubble of radius R_2,

$$\int_{r=0}^{r=\infty} \Pi(h) 2\pi r dr = 2\pi\left(\frac{R_1 R_2}{R_1 + R_2}\right) G(h) \qquad [2.10]$$

in which $\Pi(h)$ and $G(h)$ are the disjoining pressure and free energy isotherms, respectively, and r is the radial coordinate of the TLF. One can derive a functional form of $G(h)$ and determine E_1 as follows,

$$E_1 = \int_{r=0}^{r=\infty} G(h)\big|_{\Pi=0}\, 2\pi r dr \qquad [2.11]$$

which gives the value of energy barrier (E_1) in unit of Joules.

Eq. [2.8] suggests that $P_a = 1$ at $E_1 = 0$. What if the hydrophobic force continues to become stronger beyond this point? The answer should be that flotation kinetics continues to increase by virtue of the increase in the hydrodynamic pressure (p),

$$p = p_c - \Pi \qquad [2.12]$$

which should increase with decreasing Π. If the disjoining pressure becomes more negative by increasing the hydrophobic force using a stronger collector, p will increase and hence facilitate the kinetics of film thinning and bubble-particle attachment. Eq. [2.12] shows also that one can increase p by increasing p_c, which can be accomplished by using smaller air bubbles (Huang and Yoon, 2020).

The detachment probability (P_d) is of the same form as P_a as follows,

$$P_d = \exp\left(-\frac{W_a + E_1}{E_k'}\right) \quad [2.13]$$

where $W_a (= \gamma_{LV}\pi R_1^2(1-cos\theta)^2)$ is the work of adhesion and E_k' is the kinetic energy available for bubble-particle detachment in the pulp phase. In general, $W_a >> E_1$; therefore, one can minimize P_d by increasing θ and by not decreasing the surface tension of water (γ_{LV}) excessively for bubble generation. Thus, Eqs. [2.8] and [2.13] suggest that the higher the contact angle, the higher the P_a and (1-P_d) and hence the higher pulp phase recovery (R_p).

2.3.2 Froth Phase Recovery

Hydrophobicity also plays a critical role in the froth phase of a flotation cell. As bubble surface area decreases due to coalescence, less-hydrophobic particles would drop off the bubbles, providing a froth cleaning mechanism. Bubble coalescence is, of course, the central issue in determining the stability of foams and froths. Froth stability is difficult to predict as particles act as 'solid surfactants' as is the case with Pickering emulsions. Park *et al*. (2018) derived, nevertheless, a model that can predict bubble size enlargement (or coarsening) as follows,

$$\frac{d_{2,b}}{d_{2,t}} = \left[\exp\left(-\frac{0.46 n_f h_f}{J_g t_c}\right)\right]^{0.5} \quad [2.14]$$

in which $d_{2,b}$ and $d_{2,t}$ represent the bubbles at the base and the top of a froth phase, respectively, n_f the number of the pentagonal faces of a bubble that rupture during coalescence, h_f the froth height, and t_c is the critical rupture time of a lamella film. Both n_f and t_c are functions of particle size (d_1), particle hydrophobicity (θ), and the hydrophobic force in lamella films. Therefore, hydrophobicity and hydrophobic force should play a role in determining the grades of froth products.

Park *et al*. derived the froth stability model assuming that the air bubbles coalesce when the disjoining pressure in the lamella film that is free of particles becomes negative, *i.e*., Π < 0. It has been shown that at low surfactant (or frother) concentrations, the hydrophobic force is the major attractive force destabilizing foam films (Yoon and Wang, 2007). Although Eq. [2.14] does not have d_1 as a parameter affecting bubble coarsening, it and particle loading in a lamella film affect the local curvatures of the menisci around the particles and hence the macroscopic capillary pressure (p_c) in the film. During the initial stages of film thinning, its kinetics is controlled by p_c, which can be readily predicted using the Young-Laplace and Reynolds lubrication theories. Thus, the effects of particle size, particle hydrophobicity, and particle loading have been embedded in t_c, which can be predicted from first principles.

Moys (1979) developed a froth phase model to better understand the cleaning action of the froth and predict froth grades. The model was based on the premise that bubble coalescence introduces shocks and reduces bubble surface area, both of which encourage particles to detach from lamella films. He reported that froth grades increase with froth height in support of his premise that weakly attached particles drop off bubbles preferentially, resulting in an increase in froth grades. Lynch *et al*. (1974) also reported the variation in mineral grades with froth height, while Ata (2009) showed that detachment occurs suddenly at the moment of coalescence.

Figure 2-1. The five-cell rougher flotation bank with a circulating load consisting of a cleaner-scavenger tail.

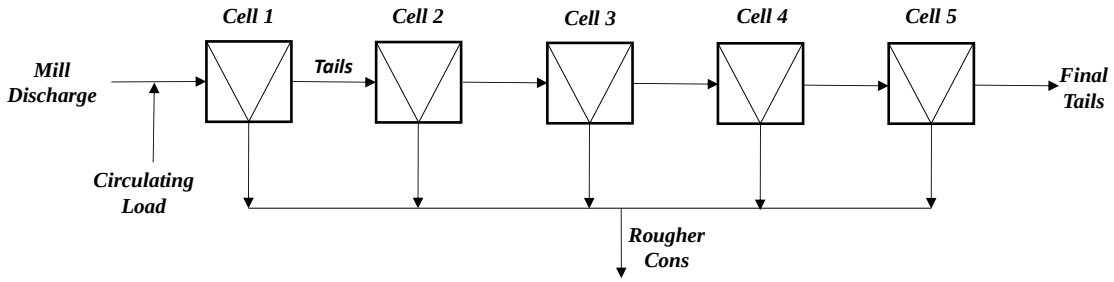

Figure 2-2. The five-cell rougher flotation bank with a circulating load consisting of a cleaner-scavenger tail.

Huang *et al*. (2022) derived a froth-phase recovery (R_f) model,

$$R_f = \frac{d_{2,b}}{d_{2,t}} \exp(-\alpha\tau) \qquad [2.15]$$

in which α is the rate constant of detachment and τ is the retention time of particles in the froth phase. The pre-exponential term effectively represents the maximum carrying capacity of the froth phase. Less hydrophobic particles, *e.g*., composite particles, would have a larger α than the fully-liberated hence more hydrophobic particles. Thus, the separation process in the froth phase relies on selective detachment, while the same in the pulp phase relies on selective attachment. Eq. [2.15] suggests that a higher degree of bubble coarsening should result in a lower froth phase recovery but a higher froth grade. Also, the exponential term suggests that one can produce a higher-grade froth product by simply increasing the froth height.

2.4 Results and Discussion

2.4.1 Liberation Characteristics of Plant Feed

The model predictions have been made on a rougher flotation bank of a large copper flotation plant. The plant has four parallel rougher banks, each consisting of five mechanically-agitated flotation cells, each with a volume of 4,500 ft^3 as shown in *Figure* 2-1. The throughput of the bank was 1,455 tons/hr of feed assaying 0.24 %Cu. The rougher feed included a mill discharge and a cleaner-scavenger tail as a circulating load.

The company provided information on mineral liberation as obtained from the QEMSCAN and ICP-MS analyses. *Figure* 2-2a shows the copper distribution in the form of a 5 x 5 size-by-class matrix, which

Table 2-1. Size-by-class mineral liberation matrix (m_{ij}) for rougher feed

Particle Size, *i* (μm)	Liberation Class, *j* (%)					Total (%)
	0-10	10-30	30-50	50-100	100	
+300	18.63	0.05	0.01	0.02	0.00	18.71
150-300	21.52	0.02	0.03	0.02	0.02	21.60
75-150	18.44	0.03	0.02	0.01	0.11	18.60
20-75	21.95	0.04	0.01	0.02	0.20	22.22
-20	18.62	0.02	0.01	0.01	0.20	18.87
Total	99.18	0.17	0.06	0.07	0.52	100.00

was converted to a mass distribution plot shown in *Figure* 2-2b. The conversion was made by giving 20% more weight to the fully-liberated particles as obtained by using QEMSCAN. This was necessary to match the copper distributions obtained using the 2D analysis with the copper distribution obtained by ICP analysis. The data given in *Figure* 2-2b are also presented in *Table* 2-1 as a size-by-class liberation matrix (m_{ij}), which represented a mass distribution of particles of size ***i*** and liberation class ***j***. The matrix does not include the data for the 0-10% liberation class as the numbers were much too large as compared to those of other liberation classes.

The ore contained chalcopyrite (0.72%) as the major copper-bearing mineral and a small amount (0.01%) of other copper minerals plus molybdenite (0.06%) and pyrite (2.45%). The major silicious gangue minerals included quartz (24.11%), K-feldspar (26.56%), and plagioclase (30.06%). It has been assumed for the purpose of simulation that chalcopyrite had a water contact angle of 70.6° while the gangue minerals have $\theta = 10°$. Under these assumptions, the contact angles ($\bar{\theta}_j$) of composite particles have been calculated as follows,

$$\bar{\theta}_j = \exp\left(a_1 b_1 \ln\theta_1 + a_2 b_2 \ln\theta_2\right) \qquad [2.16]$$

in which a_1 and a_2 are the surface areas of chalcopyrite and silicious gangue minerals exposed on the surface of the sample briquettes prepared for image analysis, respectively, while b_1 and b_2 represent correction factors. The values of b_1 = 1.03 and b_2 = 1 have been used to improve the fit between the size-by-size recoveries obtained at the plant and those obtained by simulation using the composite contact angles obtained using Eq. [2.16]. The approach taken here is similar to using the Cassie-Baxter equation except that the contact angles obtained in this manner represent geometric mean contact angles for composite particles.

2.4.2 Energy Barrier

The energy barrier (E_1) of Eq. [2.8] represents the resistance to film thinning and rupture during the last stages of bubble-particle interaction, which is controlled by the disjoining pressure (or surface forces) in a wetting film. Derjuaguin and Duhkin (1961) suggested that the resistance arises from the repulsive EDL forces in wetting film and that E_1 should vary as ζ^2. The role of ζ-potentials in flotation is well recognized in the literature. Flotation of molybdenite reaches a maximum at a pH where the mineral acquires a zero zeta-potential (Chander and Fuerstenau, 1972). An advantage of using a cationic surfactant for the flotation of the silicious gangue minerals may be to minimize the ζ-potential (Fuerstenau, 1957). Coal can be floated without a collector or frother at high electrolyte concentrations due to double-layer compression (Blake and

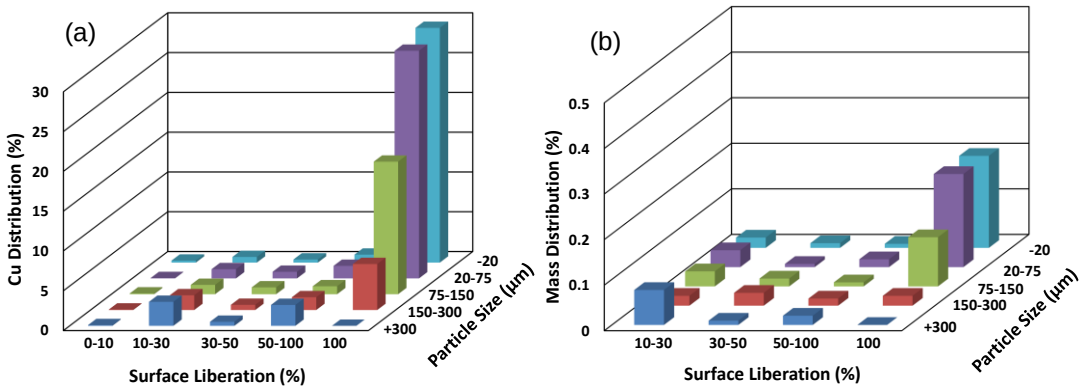

Figure 2-3. (a) the size-by-class copper distribution in the feed to the copper flotation bank, (b) the size-by-class mass distribution (m_{ij}) used for simulation. Data for the materials in the 0-10% liberation class are not shown.

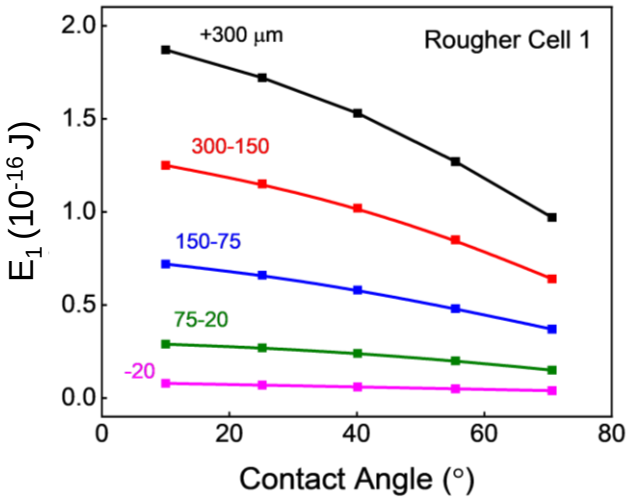

Figure 2-4. Effect of contact angles on the energy barriers (E_1) for the interactions between an air bubble and different sizes of particles as obtained using Eqs. [10] and [11].

Kitchener, 1973). The use of a cationic polymer can greatly decrease the induction time by decreasing the repulsive EDL forces in a wetting film (Huang and Yoon, 2020).

A more common way to reduce E_1 is to increase the hydrophobic force to counterbalance the repulsive EDL forces, which is accomplished by increasing θ using appropriate collectors. In general, the higher the contact angle, the higher the hydrophobic force, which should in turn give rise to lower E_1 and hence higher flotation kinetics and recoveries (Huang *et al*., 2022).

Figure 2-3 shows the values of E_1 obtained using Eq. [2.11] using the ($G(h)$) isotherms

$$G(h) = \frac{1}{2\pi}\left(\frac{R_1 + R_2}{R_1 R_2}\right)\int_{r=0}^{r=\infty} \Pi(h) 2\pi r dr \qquad [2.17]$$

derived from the Derjaguin approximation (Eq. [2.10]). Eq. [2.11] was used at $h = h_{cr}$, where $\Pi = 0$. The values of h_{cr} were obtained using Eq. [2.9] by setting $\Pi = 0$ and using the values of the surface chemistry parameters and the bubble and particle sizes. The results presented in *Figure* 2-3 were obtained using the following parameters: A_{132} = -7.08x10^{-20} J, ψ_1 = -20 mV, ψ_2 = -40 mV, κ^{-1} = 96 nm, and K_{232} = 4.07x10^{-17} J, and R_2 = 0.75 mm. The values of K_{131} were obtained from the $\bar{\theta}_{ij}$ values of the composite particles using the mineral liberation data (m_{ij} matrix) presented in *Table* 2-1 and *Figure* 2-2b as a function of particle size i (=2R_1).

As shown, E_1 decreases with increasing $\bar{\theta}_{ij}$ and decreasing R_1. The decrease in E_1 with increasing contact angle can be attributed to the increase in hydrophobic force (or K_{132}) as has been shown previously as part of validating the flotation model described in the present communication against the experimental data obtained from a mini-plant (Huang *et al*., 2022).

The results presented in *Figure* 2-3 are a manifestation of the Derjiaguin approximation. As Eq. [2.10] shows, a decrease in R_1 should cause a decrease in Π and hence E_1. Between R_1 and R_2, Π is more sensitive to the former as $R_1 << R_2$ in flotation practice. This finding may seem counter-intuitive as P_a and flotation recovery should increase with decreasing particle size. Note, however, that a decrease in particle size should also decrease the kinetic energies (E_k) of particles. In fact, E_k should decrease as R_1^{-3} while Π decreases effectively as R_1^{-1}. The net effect of decreasing particle size should then be an increase in E_a/E_k, which should in turn cause a decrease in P_a. A solution to this problem may be to increase E_k, which can be achieved by increasing the energy dissipation rate or by improving the design of the rotor-stator mechanisms of a flotation cell.

Table 2-2. Effect of particle size on energy barrier and flotation probabilities

d_1	E_1	Flotation Probabilities			
(μm)	(10^{-15} J)	P_c	P_a	1-P_d	P
+300	0.4	0.002	0.567	0.785	0.0007
150-300	1.48	0.023	0.959	0.304	0.0066
75-150	3.68	0.015	0.994	0.103	0.0158
20-75	6.43	0.462	0.999	0.041	0.0188
0-20	9.7	0.823	1	0.015	0.0127

2.4.3 Pulp Phase Recovery

Eq. [2.6] representing the first-order rate constant may be rewritten as

$$k_p = 5.0 N_2 d_{12}^2 \sqrt{\overline{u_1}^2 + \overline{u_2}^2}\, P_c \exp\left(-\frac{E_1}{E_k}\right) \qquad [2.18]$$

in which the pre-exponential term represents the collision efficiency while the exponential term represents in view of the Boltzmann distribution law, the fraction of the particles whose kinetic energies (E_k) is the same or larger than the energy barrier (E_1) to film thinning and rupture. Eq. [2.18] is of the same form as the Arrhenius equation for chemical kinetics,

$$k = A \exp\left(-\frac{E_a}{RT}\right) \qquad [2.19]$$

In this regard, the E_1 of Eq. [2.19] may be regarded as the activation energy (E_a) required for a particle to penetrate a TLF of water and form a contact angle. Some of the particles will be detached and return to the aqueous phase. This important sub-process has been incorporated into Eq. [2.6] as part of the probability of overall flotation (P) in the form of (1-P_d), which represents the probability of a particle not being detached before entering the froth phase.

Flotation is sensitive to particle size and is efficient over the relatively narrow particle size range of approximately 20-150 μm (Wills and Finch, 2016). According to Eq. [2.10], E_1 is more sensitive to particle size (R_1) than to bubble size (R_2), because $R_1 \ll R_2$. In the present work, Eqs. [2.10] and [2.11] were used to determine E_1 for the interactions between fully-liberated chalcopyrite particles of d_1 in the range of 10-300 μm with $\theta = 70.6^o$ and air bubbles with $d_2 = 1.5$ mm. The surface force parameters needed to calculate the $\Pi(h)$ and $G(h)$ isotherms were: $A_{132} = 7.08 \times 10^{-20}$ J, $\psi_1 = -20$ mV, $\psi_2 = -40$ mV, $\kappa^{-1} = 96$ nm, and $K_{232} = 4.07 \times 10^{-17}$ J, and $K_{131} = 5.07 \times 10^{-20}$ J. The results presented in *Table* 2-2 and *Figure* 2-3 show that E_1 decreases with decreasing d_1.

The values of E_1 obtained in this manner were then used to determine P_a and P_d using Eq. [2.8] and [2.13], respectively. The methods of determining E_k and E_k' are described in *Appendix I*. The values of P_c, on the other hand, were obtained using Eq. [2.7] from the particle and bubble sizes involved. *Table* 2-2 and *Figure* 2-4 show the changes in P_c, P_a, (1-P_d), and P. Note here that the values of the overall probability of flotation (P) decrease with decreasing particle size, providing an explanation for the difficulty of floating particles. The main cause for the low P for finer particles was the low probability of collision (P_c) as is well

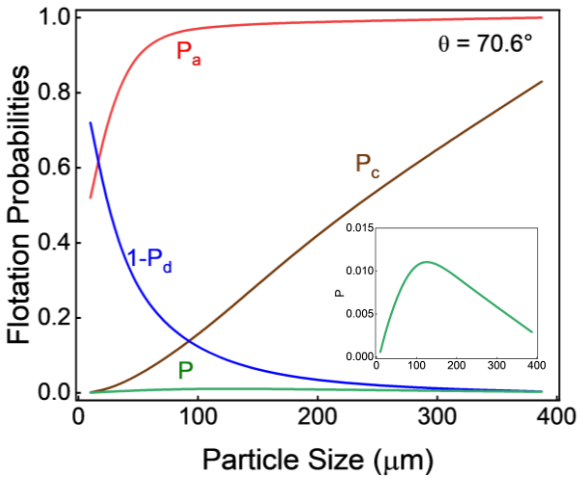

Figure 2-5. The probabilities of bubble-particle collision (P_c), attachment (P_a) and not being detached ($1-P_d$) for fully-liberated chalcopyrite particles in the first rougher cell as obtained using Eq. [7], [8] and [13], respectively.

known. Fine particles follow the streamlines around larger bubbles, resulting in low values of P_c (Luttrell and Yoon, 1992). One way to overcome this problem would be to decrease d_2 to increase $(d_1/d_2)^2$, which was the basis for the microbubble and nanobubble flotation technologies (Yoon *et al*., 1992; Pourkarimi *et al*., 2021; Sobhy *et al*., 2021). Still another way to improve fine particle flotation would be to increase P_a by increasing the kinetic energy E_k by increasing the energy dissipation rate in the pulp phase of a flotation cell as suggested by Eq. [2.8]. A decrease in E_1 by way of using a strong collector should also increase P_a and hence P to improve fine particle flotation. Also shown in *Figure* 2-4 and *Table* 2-2 is that $1-P_d$, representing the probability of not being detached, decreases sharply with increasing particle size, which in turn explains the difficulty in coarse particle flotation.

Figure 2-4 shows that the probability of flotation (P) is very low throughout the entire particle size range considered. As shown, it is due to the low P_c and large P_d at the small and large particle size ranges, respectively. The P *vs*. d_1 plot presented as an inset shows that P reaches a maximum at d_1 = 150 μm, which is actually close to the upper particle size limit observed in copper flotation (Clark *et al*., 2005). The apparent discrepancy between the P *vs*. d_1 plot shown as inset and the usual flotation practice may be due to the fact that the P values represent what happens in the pulp phase, while the upper particle size limit of 150 μm observed in flotation practice is the consequence of what happens in both the pulp and froth phases. This discrepancy suggests that coarse particles are lost in the froth phase rather than in the pulp phase. Park *et al*. (2018) showed indeed that coarse and less hydrophobic particles readily drop off bubbles as the bubble size increases due to coalescence.

2.4.4 Froth Phase Recovery

Two different methods of determining froth phase recoveries (R_f) have been reported in the literature. These include the changing froth depth (CFD) and bubble-load method (BLM) developed by Vera *et al*. (1999) and Seaman *et al*. (2006), respectively. In the former, R_f is determined by dividing the overall flotation rate constant (k) encompassing both the pulp- and froth-phase recoveries by the rate constant (k_p) for the pulp-phase flotation recovery step at a given froth height (h_f), *i.e*.,

$$R_f = \frac{k}{k_p} \qquad [2.20]$$

In this method, k_p is determined by assuming that it is equal to the k at $h_f = 0$, which is determined by extrapolating the values of k obtained at different froth heights. In the latter method, a specially designed probe is inserted vertically into the pulp phase to allow for the bubble-particle aggregates to rise through

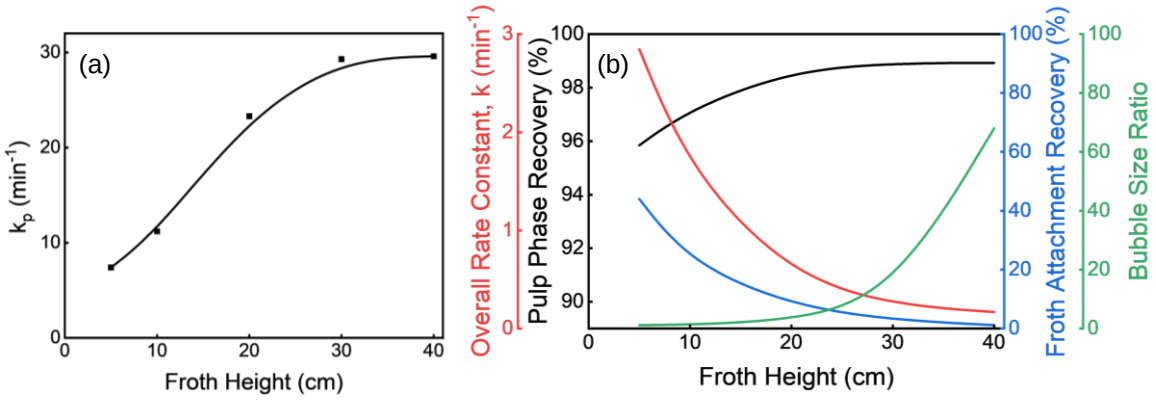

Figure 2-6. Effect of froth height in the first rougher cell on (a) pulp phase rate constant; (b) pulp phase recovery, froth phase attachment recovery, overall rate constant and, bubble size ratio.

the pulp phase and be collected in a separate chamber so that the number of the particles recovered by selective attachment is determined. It has been shown previously that the simulation results are substantially lower than those reported by using the CFD method in the literature but are in reasonable agreement with those determined using the BLM method (Huang *et al.*, 2022).

In the present work, we determined the k_p values using Eq. [2.6] using the RMS velocities and the P_c values calculated from the equations given in *Appendix I*, while the values of P_a and P_d values were calculated using Eqs. [2.8] and [2.13], respectively. The model predictions were made by varying the froth heights from 5 to 40 cm in the first cell of the rougher flotation bank (*Figure* 2-1). The froth phase recovery model (Eqs. [2.14] and [2.15]) are designed such that the particles of lower surface liberation drop off bubbles at a lower h_f where bubble coarsening is less extensive. At a higher h_f, bubble size grows further to the extent that even the particles of higher surface liberation would drop off bubbles due to further limitations in 'parking area.' These constraints will result in an increase in the population of the particles of higher contact angles at a higher froth height, which in turn should give rise to a higher k_p value as shown in *Figure* 2-5a. On the contrary, extrapolating the k_p *vs*. froth height plot to $h_f = 0$, k_p will become small, which will in turn increase R_f in accordance with Eq. [2.20]. Thus, the CFD method overpredicts froth recoveries.

Figure 2-5b further illustrates the various subprocesses taking place in a froth phase. To begin with, bubble size increases with increasing froth height due to coalescence, causing the composite particles of lower surface liberation to drop back first due to their lower contact angles, which in turn causes the pulp phase recoveries (R_p) and hence the k_p to increase as shown. This will also cause the froth phase recoveries due to attachment (R_f) to decrease in accordance with Eq. [2-20]. Since the overall flotation recovery (R) is a product of R_p and R_f, *i.e.*, $R = R_pR_f$, the overall rate constant k should decrease along with the decrease in R_f as shown. On the other hand, a decrease in R_f should increase the froth grade (or the final product grade) – a process known as froth cleaning. Thus, the driving force for froth cleaning, which is the vitally important function of flotation, is bubble coalescence. Although the bubble coalescence causes froth recoveries to decrease, it is an absolute necessity for producing high-grade concentrates.

2.4.5 Size-by-Size Recoveries

Figure 2-6 shows the size-by-class recoveries of the copper-bearing mineral particles present in the rougher flotation bank as predicted using the model described in the foregoing sections. The simulation started with the size-by-class mineral liberation matrix (m_{ij}) presented in *Table* 2-1. The contact angles of

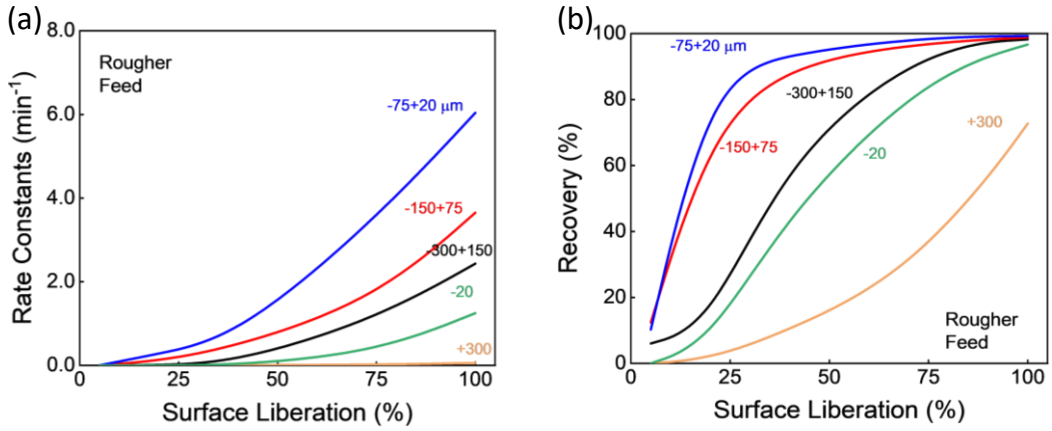

Figure 2-7. Effect of surface liberation in the rougher bank on (a) simulated overall size-by-class rate constants for different particle sizes; (b) overall size-by-class Cu recoveries.

the different liberation classes ($\bar{\theta}_j$) were calculated using Eq. [2.16] assuming that $\theta = 70.6°$ and 10° for the grains of free chalcopyrite and free silicious gangue, respectively. The contact angle data were used to determine the hydrophobic force constant (K_{131}) of Eq. [2.9] and subsequently the $G(h)$ isotherms, which were used to determine the energy barriers (E_1) for bubble-particle interaction using Eqs. [2.10] and [2.11]. The E_1 values obtained in this manner were then used to determine k_p using the following relation,

$$k_p = 5.0 N_2 d_{12}^2 \sqrt{\overline{u_1}^2 + \overline{u_2}^2}\, P_c \left(1 - P_d\right) \exp\left(-\frac{E_1}{E_k}\right) \qquad [2.21]$$

which is equivalent to Eq. [2.18]. The only difference between Eqs. [2.18] and [2.21] is that the former does not have a parameter P_d representing the probability of detachment. Eqs. [2.7] and [2.13] were used to predict the P_c and P_d, respectively. The values of k_p obtained using Eq. [2.21] were then used to predict the pulp phase recovery (R_p) as follows,

$$R_p = \frac{k_p t}{1 + k_p t} \qquad [2.22]$$

for a fully mixed flotation cell. The pulp phase recoveries obtained in this manner were then combined with the froth phase recoveries (R_f) obtained from Eq. [2.15] to determine the overall flotation recovery (R) using the following relation (Dobby and Finch, 1990),

$$R = \frac{R_p R_f}{R_p R_f + 1 - R_p} \qquad [2.23]$$

The overall rate constant (k) was then obtained using Eq. [2.20] from the values of k_p and R_f. Both the k and R values presented in *Figures* 2-6a and -b were obtained using the various operating parameters, *e.g.*, J_g, h_f, and the air holdup (ε_g), *etc.*, collected from the plant survey and the size-by-class liberation data presented in *Table* 2-1.

The various steps described above were repeated for each of the five flotation cells of the rougher bank sequentially to determine the values of k_{ij} and R_{ij} for each element of the m_{ij} matrix given in *Table* 2-1. The bank recovery of the particle size and liberation class (R_{ij}) was calculated using the following relation,

$$R_{ij} = 1 - \frac{t_{ij} T_{ij}}{f_{ij} F_{ij}} \qquad [2.24]$$

in which f_{ij} and t_{ij} are the feed and tails grades of a class, respectively, and F_{ij} and T_{ij} are the feed and tails mass flow rates, respectively. Once the R_{ij} values are known, one can readily obtain the values of k_{ij} assuming that each flotation cell was perfectly mixed.

In *Figures* 2-6a and -b, the values of k_{ij} and R_{ij} obtained in the manner described above are plotted *vs*. surface liberation. As anticipated, both k_{ij} and R_{ij} increased with surface liberation, which can be attributed to the increase in $\bar{\theta}_j$. An increase in contact angle should decrease E_1 as shown in *Figure* 2-3 and hence k_p as Eq. [2.21] suggests. An increase in contact angle should also help improve the coarse particles' recovery in the pulp phase by way of decreasing the probability of detachment (P_d) by virtue of increasing the work of adhesion (W_a), which is a function of contact angle (See Eq. [2.13]). P_d also plays a critical role in the froth phase. Composite particles with lower surface liberations preferentially drop off the air bubbles in the froth phase and return to the pulp phase, which serves as an important mechanism by which froth grades improve. It is interesting to note here that upgrading a mined ore, which is the objective of flotation, relies on selective attachment in the pulp phase and selective detachment in the froth phase, both of which are controlled by contact angles.

The simulation results presented in *Figure* 2-6 show that both the k_{ij} and R_{ij} are the highest at the particle size of -75+20 μm followed by the -150+75 μm size fraction. The particles larger than 150 μm show substantially lower recoveries, particularly for those above 300 μm. Clark *et al*. (2005) reported that copper recoveries fall below 62% at d_1 > 150 μm due to the poor mineral liberation, which drops dramatically at larger sizes. The simulation result shows also that +300 μm particles can be recovered provided that they are sufficiently liberated. The k_{ij} = 0.136 min^{-1} for the fully liberated chalcopyrite particles with d_1 = 300 μm, which is large enough to give a 76% recovery at the retention of 23.28 min. In reality, coarse particles are poorly liberated and hence will have much lower recoveries than simulated.

The -20 μm particles also exhibited low k_{ij} and R_{ij} values as shown in *Figures* 2-6a and -b, respectively. As has already been noted, much of the difficulty associated with fine particle flotation arises from the low collision probability (P_c). It appears, however, that there is another important reason, that is, poor liberation even with the smallest particles present in the rougher feed. According to the size-by-class liberation matrix given in *Table* 2-1, a vast majority (98.7%) of the copper-bearing minerals in the -20 μm size fraction belong to the poorest liberation class of 0-10%. Only 0.2% of the materials are fully liberated. Furthermore, the mass of the particles may be too small to give rise to a high probability of attachment (P_a) and high values of k_{ij} and R_{ij}. Much of the -20 μm particles are recycled back to the rougher flotation circuit as a circulating load, which may or may not be a good practice as will be discussed in the ensuing publication of this series.

2.4.6 Predicting Recovery vs. Grade Curves

Table 2-3 shows the cumulative copper recoveries obtained by simulating the plant operation along the 5-cell rougher flotation bank. Also shown for comparison are the plant survey data. The two sets of data are in reasonable agreement, validating the simulator developed by Huang *et al*. (2022). The data set is also plotted in *Figure* 2-7a, in which the red line represents the simulation results, while the data points represent the plant data.

Also shown in the table are the simulated grades of the froth products from each flotation cell. Unfortunately, the plant survey data did not include the product grades to be compared cell-by-cell with the simulation results. On the other hand, the simulated tailings grade of 0.033 %Cu is very close to the actual tailings grade of 0.035 %Cu.

Both the predicted grades and recoveries given in *Table* 2-3 are plotted in *Figure* 2-7b to construct a recovery *vs*. grade curve. As shown, the rougher cell gives a high-grade froth product but at a low copper recovery. The grades of the froth products from the subsequent flotation cells are lower; however, each cell incrementally adds more copper-bearing minerals most likely in the form of composite particles, to the launder and the rougher concentrate. The net result of operating the 5-cell flotation bank is to produce the final rougher concentrate assaying 3.11 %Cu at a recovery of 86.6% from a low-grade copper ore feed

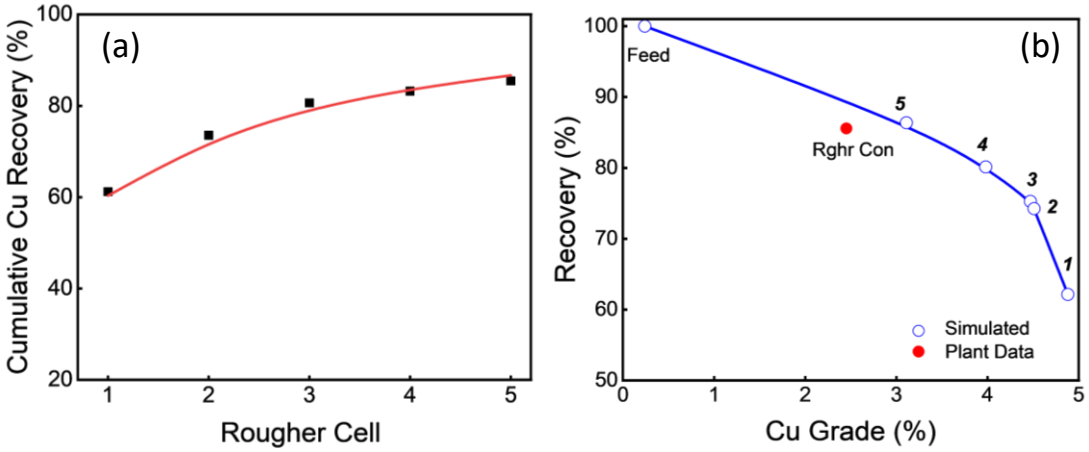

Figure 2-8. (a) Validation of the simulation by (a) the comparison of the simulated (line) and plant (symbol) cumulative cell-by-cell Cu recoveries. (b) simulated grade-recovery curve for the rougher bank. Numbers 1, 2, 3, 4 and 5 represents the simulated cumulative grade and recovery (blue open circle) for the corresponding cell. The plant overall recovery is shown as Rghr Con (red circle).

assaying 0.24 %Cu. These simulation results are in reasonable agreement with the plant survey data: a rougher concentrate assaying 2.46 %Cu at the 85.4% copper recovery. The objective of a rougher flotation bank is to maximize the recovery, which entails the recovery of composite particles.

2.4.7 Effect of Mineral Liberation on Contact Angle

In flotation, particle size and mineral liberation may be the two most important parameters affecting both the recovery and grade. Welsby *et al*. (2010) reported the size-by-class flotation rate constants (k_{ij}) by analyzing the flotation products taken from a pilot-scale test work by means of a mineral liberation analyzer (MLA). Jameson (2012) found that the rate constants (k) reported by Welsby *et al*. can be normalized by the maximum rate constant (k_{max}) at a given size class, that is, the k/k_{max} ratios obtained at different particle sizes in a given liberation class are practically same. The author showed also that the k/k_{max} ratio increased with increasing liberation, reaching unity for fully-liberated particles. These findings simply suggest that the higher the liberation, the higher the flotation rate and hence the recovery and grade as is anticipated.

Table 2-3. Comparison between plant data and simulated values for each rougher cell.

Product	Cu Distribution (%)		Grade (%Cu)	
	Simulated	Plant Data	Simulated	Plant Data
Cell 1	62.9	65.4	4.88	-
Cell 2	11.8	12.6	3.27	-
Cell 3	1.0	1.6	2.62	-
Cell 4	4.8	1.7	1.44	-
Cell 5	6.1	4.1	0.79	-
Rougher Tail	13.4	14.6	0.033	0.035
Rougher Conc.	86.6	85.4	3.11	2.46
Feed	100.0	100.0	0.24	0.24

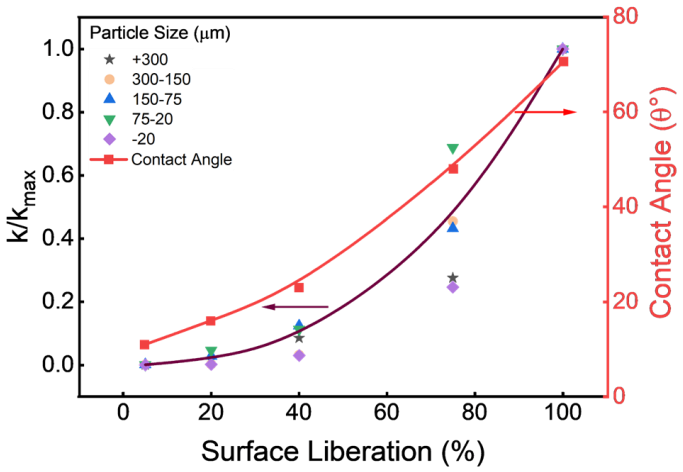

Figure 2-9. Normalized rate constants (k/k_{max}) for the rougher bank vs. degree of surface liberation and contact angle (θ) for different particle sizes.

Figure 2-8 shows a k/k_{max} *vs*. surface liberation plot on the basis of k_{ij} values obtained by simulation and presented in *Figure* 2-6a. Also shown in the figure are the composite contact angles $\bar{\theta}_j$ of the particles in the five different liberation classes, *i.e*., 0-10, 10-30, 30-50, 50-100, and 100% surface liberations, using Eq. [2.16]. Thus, the increase in k/k_{max} is simply a manifestation of increased contact angles at higher surface liberations.

The data presented in *Figure* 2-8 show that the rate constants at the 50-100% surface liberations are not normalized as well as those obtained at the lower and higher degrees of liberation. The simulation data presented in *Figure* 2-6a show that the k values exhibit substantially larger divergence at higher surface liberations or contact angles than at lower surface liberations. It appears that hydrodynamic parameters play more important roles at higher surface liberations or contact angles. Conversely, hydrodynamics would become immaterial in flotation, when the surface chemistry conditions, *e.g*., contact angles in particular, are not properly controlled.

2.4.8 Coarse Particle Recovery

Figure 2-9a shows the size-by-size recoveries (R_i) of copper-bearing minerals for the rougher flotation bank as obtained by simulation. Also shown are the corresponding flotation rate constants (k_i). The recoveries are high at the 10-100 μm particle size range and drop above the optimal size range. The copper recovery predicted at +150 μm is 63%, which is close to what was reported by Clark *et al*. (2005). The authors suggested that the sharp drop in recovery was due to the dramatic decrease in liberation above this particular size for the flotation of porphyry copper ores. The shape of the recovery *vs*. particle size curve shown in *Figure* 2-9a is typical of most mineral flotation practices. The results show that high recoveries of copper can be achieved if the ore can be ground to less than 100 μm. Since grinding is the most energy-intensive unit operation in mineral processing, it would make sense to maximize the recovery at a coarse grind and regrind the low-grade rougher concentrate to improve the liberation and obtain higher concentrate grades.

Many investigators view that the coarse particles drop off air bubbles in the pulp phase of a flotation cell due to the high turbulence created by the rotor-stator mechanisms. The coarse particle flotation machines have been designed to address this problem by using different types of fluidized beds rather than the rotor-stator mechanisms for bubble-particle contacts. Furthermore, coarse particles attached to bubbles rise slower in the pulp phase. Mankosa and Luttrell (2002) developed a method of using a combination of

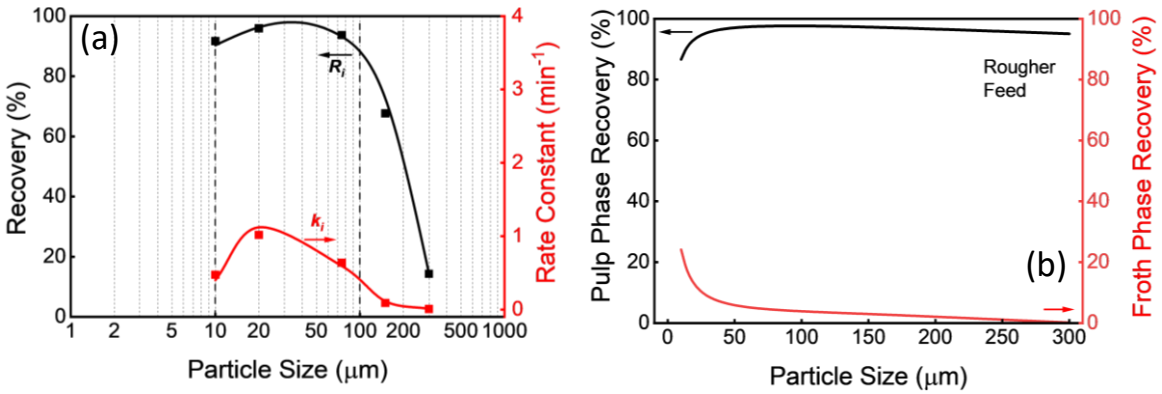

Figure 2-10. a) Size-by-size recoveries and rate constants. The lines represent simulation results, while the points represent the plant survey data; b) effect of particle size on the pulp and froth phase recoveries in the first rougher cell.

air bubbles and upward fluidization to facilitate the transport of coarse hydrophobic particles to the cell weir. Jameson's group developed a novel fluidized bed approach to improve coarse particle flotation (Jameson, 2010, 2018; Jameson and Emer, 2019). More recently, Sutherland *et al*. (2020) developed a flotation machine, in which the segregation of bubbles from unattached particles is facilitated in inclined channels. All of these devices are designed to create quiescent conditions to minimize the probability of detachment.

Figure 2-9b compares the pulp and froth phase recoveries as determined by using the simulator. The pulp phase recoveries decrease with an increase in particle size at d_1 > 150 μm. Note, however, that the froth phase recovery is more sensitive to particle size. At d_1 = 300 μm, the coarse particle recovery approaches zero. The simulation results suggest that the problems associated with coarse particle flotation may be due to the high probability of detachment in the froth phase rather than in the pulp phase.

2.5 Summary and Conclusions

A flotation model developed from first principles has been validated against a rougher flotation circuit with a circulating load. The model has been developed on the basis of the premise that bubble-particle interaction is driven by the hydrophobic force, which in turn made it possible to use contact angle and mineral liberation as model parameters. The model has been converted to a simulator on the basis of the Microsoft Excel VBA platform. The input parameters to the simulator include the size-by-liberation matrix derived from the image analysis of the rougher feed and the various operating parameters such as contact angle, bubble size, retention time, energy dissipation rate, froth height, *etc*. In general, the simulation results are in good agreement with the plant survey data in both recoveries and grades. The recovery-by-particle size curve obtained in the first rougher cell shows a dropoff of particles above 150 μm most probably due to the sharp drops in liberation and froth phase recovery.

2.6 References

Abrahamson, J., 1975. Collision rates of small particles in a vigorously turbulent fluid. Chemical Engineering Science, 30(11), 1371-1379.Bushell, C. H. G. (1962). Kinetics of flotation. Trans. AIME, 223, 266-278

Ata, S. (2009). The detachment of particles from coalescing bubble pairs. Journal of colloid and interface science, 338(2), 558-565.

Ata, S. (2012). Phenomena in the froth phase of flotation—A review. *International Journal of Mineral Processing*, *102*, 1-12.

Blake, T. D., & Kitchener, J. A. (1972). Stability of aqueous films on hydrophobic methylated silica. *Journal of the Chemical Society, Faraday Transactions 1: Physical Chemistry in Condensed Phases*, *68*, 1435-1442.

Camp, T. R., & Stein, P. C. (1943). Velocity gradients and internal work in fluid motion. *J. Boston Soc. Civ. Eng.*, *30*, 219-237.

Cassie, A. B. D., & Baxter, S. (1944). Wettability of porous surfaces. *Transactions of the Faraday society*, *40*, 546-551.

Chander, S., & Fuerstenau, D. W. (1972). On the natural floatability of molybdenite. *Trans. AIME*, *252*, 62-69.

Clark, M. E., Brake, I., Huls, B. J., Smith, B. E., & Yu, M. (2005). Creating value through application of flotation science and technology. *Centenary of Flotation Symposium, 6-9 June*,Brisbane, QLD.

Derjaguin, B. V. (1934). Friction and adhesion. IV. The theory of adhesion of small particles. *Kolloid Zeits*, *69*, 155-164.

Derjaguin, B. V. (1940). Theory of the capillary condensation and other capillary phenomena taking into account the disjoining effect of long-chain molecular liquid films. *Zh. Fiz. Khim*, *14*, 137.

Derjaguin, B. V., & Dukhin, S. S. (1961). Theory of flotation of small and medium-size particles, Institution of Mining and Metallurgy. 241-267.

Do, H. (2010). Development of a turbulent flotation model from first principles (Doctoral dissertation, Virginia Tech).

dos Santos, N. A., & Galery, R. (2018a). Modelling flotation per size liberation class–Part 1–Minimizing the propagation of experimental errors in the estimate of flotation recovery. *Minerals Engineering*, *128*, 254-265.

dos Santos, N. A., & Galery, R. (2018b). Modelling flotation per size liberation class–Part 2–Evaluating flotation per class. Minerals Engineering, 129, 24-36.

Finch, J.A., Dobby, G.S., 1990. Column flotation. Pergamon Press.

Frumkin, A. N., & Gorodetzkaya, A. (1938). On the phenomena of wetting and the adhesion of bubbles. II. The mechanism of the adhesion of bubbles to a mercury surface. *Acta Physicochim. URSS*, *9*, 327.

Fuerstenau, D. W. (1957). Correlation of contact angles, adsorption density, zeta potentials, and flotation rate. *Trans. AIME*, *208*, 1365-1367.

Huang, K., & Yoon, R. H. (2020). Control of bubble ζ-potentials to improve the kinetics of bubble-particle interactions. *Minerals Engineering*, *151*, 106295.

Huang,K., Serhat Keles, Ian Sherrell, Aaron Noble, and Roe-Hoan Yoon (2022). Development of a Flotation Simulator that can predict grade vs. recovery curves from mineral liberation data. *Mineral Engineering*, 181, 107510.

Jameson, G. J. (2010). New directions in flotation machine design. *Minerals Engineering*, *23*(11-13), 835-841.

Jameson, G. J. (2018). *U.S. Patent No. 10,040,075*. Washington, DC: U.S. Patent and Trademark Office.

Jameson, G. J., & Emer, C. (2019). Coarse chalcopyrite recovery in a universal froth flotation machine. *Minerals Engineering*, *134*, 118-133.

Jameson, G.J. (2012). The effect of surface liberation and particle size on flotation rate constants. *Minerals Engineering*, 36-38, 132-137.

Jowett, A. (1980). Formation and disruption of particle-bubble aggregates in flotation. *In Fine particle processing: Proceedings of International symposium on fine particles*. SME.

Lee, C. H., Erickson, L. E., & Glasgow, L. A. (1987). Bubble breakup and coalescence in turbulent gas-liquid dispersions. *Chemical Engineering Communications*, *59*(1-6), 65-84.

Luttrell, G. H., & Yoon, R. H. (1992). A hydrodynamic model for bubble—particle attachment. *Journal of colloid and interface science*, *154*(1), 129-137.

Lynch, AJ, Johnson, NW, McKee, DJ & Thorne, G. C. (1974). The behaviour of minerals in sulphide flotation processes, with reference to simulation and control. Journal of the Southern African Institute of Mining and Metallurgy, 74(9), 349-361.

Mankosa, M. J., & Luttrell, G. H. (2002). *U.S. Patent No. 6,425,485*. Washington, DC: U.S. Patent and Trademark Office.

Moys, M. H. (1978). A study of a plug-flow model for flotation froth behaviour. *International Journal of Mineral Processing*, *5*(1), 21-38.

Moys, M. H. (1979). *A study of processes occurring in flotation froths* (Doctoral dissertation).

Pan, L., & Yoon, R. H. (2010). Hydrophobic forces in the wetting films of water formed on xanthate-coated gold surfaces. *Faraday discussions*, *146*, 325-340.

Pan, L., & Yoon, R. H. (2016). Measurement of hydrophobic forces in thin liquid films of water between bubbles and xanthate-treated gold surfaces. Minerals Engineering, 98, 240-250.

Park, S., Huang, K., & Yoon, R. H. (2018). Predicting bubble coarsening in flotation froth: Effect of contact angle and particle size. *Minerals Engineering*, *127*, 256-264.

Pazhianur, R., & Yoon, R. H. (2003). Model for the origin of hydrophobic force. *Mining, Metallurgy & Exploration*, *20*(4), 178-184.

Pourkarimi, Z., Rezai, B., Noaparast, M., Nguyen, A. V., & Chelgani, S. C. (2021). Proving the existence of nanobubbles produced by hydrodynamic cavitation and their significant effects in powder flotation. *Advanced Powder Technology*, *32*(5), 1810-1818.

Rabinovich, Y. I., Guzonas, D. A., & Yoon, R. H. (1993). Role of chain order in the long-range attractive force between hydrophobic surfaces. *Langmuir*, *9*(5), 1168-1170.

Schubert, H. (1999). On the turbulence-controlled microprocesses in flotation machines. *International journal of mineral processing*, *56*(1-4), 257-276.

Schuhmann Jr, R. (1942). Flotation Kinetics. I. Methods for steady-state study of flotation problems. *The Journal of Physical Chemistry*, *46*(8), 891-902.

Schulze, H. J. (1984). Physico-chemical elementary processes in flotation. *Developments in mineral processing*, *4*.

Seaman, D. R., Manlapig, E. V., & Franzidis, J. P. (2006). Selective transport of attached particles across the pulp–froth interface. *Minerals Engineering*, *19*(6-8), 841-851.

Sobhy, A., Wu, Z., & Tao, D. (2021). Statistical analysis and optimization of reverse anionic hematite flotation integrated with nanobubbles. *Minerals Engineering*, *163*, 106799.

Sutherland, J. L., Dickinson, J. E., & Galvin, K. P. (2020). Flotation of coarse coal particles in the Reflux™ Flotation Cell. *Minerals Engineering*, *149*, 106224.

Sutherland, K.L. (1948). Physical Chemistry of Flotation. XI. Kinetics of the flotation process. *The Journal of Physical Chemistry*. 52(2), 394-425.

Vera, M. A., Franzidis, J. P., & Manlapig, E. V. (1999). Simultaneous determination of collection zone rate constant and froth zone recovery in a mechanical flotation environment. *Minerals Engineering*, *12*(10), 1163-1176.

Wang, L. (2012). Inter-bubble attractions in aqueous solutions of flotation frothers. *Separation Technologies for Minerals, Coal, and Earth Resources*, 35-45.

Weber, M. E., & Paddock, D. (1983). Interceptional and gravitational collision efficiencies for single collectors at intermediate Reynolds numbers. *Journal of Colloid and Interface Science*, *94*(2), 328-335.

Welsby, S.D.D., Vianna, S.M.S.M., Franzidis, J.-P., 2010. Assigning physical significance to floatability components. International Journal of Mineral Processing 97, 59–67.

Wills, B. A., & Finch, J. A. (2016). Mineral processing technology: An introduction to the practical aspects of ore treatment and mineral recovery. Butterworth Heinemann.

Yoon, R. H. and Wang, L. (2007). Hydrophobic Forces in Foam Films. *Colloid Stability: The Role of Surface Forces*. Edited by Tharwat F. Tadros. Weinheim: Wiley-VCH Verlag.161-186.

Yoon, R. H., & Mao, L. (1996). Application of extended DLVO theory, IV: derivation of flotation rate equation from first principles. *Journal of Colloid and Interface Science*, *181*(2), 613-626.

Yoon, R. H., Adel, G. T., & Luttrell, G. H. (1992). *U.S. Patent No. 5,167,798*. Washington, DC: U.S. Patent and Trademark Office.

Yoon, R. H., Flinn, D. H., & Rabinovich, Y. I. (1997). Hydrophobic interactions between dissimilar surfaces. *Journal of colloid and interface science*, *185*(2), 363-370.

2.7 Appendix

Root mean square (RMS) velocities of particles and bubbles

The RMS velocities of the particles were calculated using the following relationship given by Schubert (1999):

$$\overline{U}_1 = 0.4\frac{\varepsilon^{4/9} d_1^{7/9}}{\upsilon^{1/3}}\left(\frac{\rho_1 - \rho_3}{\rho_3}\right)^{2/3} \qquad [2.A.1]$$

where, d_1 is the particle diameter, ρ_1 and ρ_3 are particle and water densities, respectively, ε is the energy dissipation rate and, v is the kinematic viscosity of water.

The RMS velocities of the bubbles was obtained using the following relation (Lee *et al.* 1987)

$$\overline{U}_2 = \left(C_0\left(\varepsilon d_2\right)^{2/3}\right)^{1/2} \qquad [2.A.2]$$

here, C_0 (=2) is a constant and, d_2 represents the bubbe diameter predicted from a bubble generation model (Schulze, 1984),

$$d_2 = \left(\frac{2.11\gamma}{\rho_3 \varepsilon_b^{0.66}}\right)^{0.66} \qquad [2.A.3]$$

where γ is the surface tension, and ε_b is the energy dissipation rate at the bubble generation zone.

Kinetic energy of particles for bubble-particle attachment

The kinetic enegy of particles at the critical rupture thickness of the wetting film, E_k is given by:

$$E_k = \tfrac{1}{2} m_1 \left(\overline{U}_{1,h_{cr}}\right)^2 \qquad [2.A.4]$$

where, m_1 is the mass of the particle, $\overline{U}_{1,h_{cr}}$ is the RMS velocity of the particle at the critical rupture thickness (h_{cr}) of the wetting film.

Kinetic energy of particles for bubble-particle detachment

E_k' is the detachment kinetic energy due to turbulence in the pulp phase. Do (2010) considered the particle detachment due to the eddies formation in the turbulent flow (Jowett, 1980; Schulze, 1984) to derive the following relationship for E_k'.

$$E_k^{'} = \tfrac{1}{2} m_1 \left(\left(d_1 + d_2 \right) \sqrt{\varepsilon / \nu} \right)^2 \qquad [2.A.5]$$

in which $\sqrt{\varepsilon/\nu}$ is the shear rate in a vortex (Camp and Stein, 1943).

Chapter 3. Improving the Performance of a Low-grade Porphyry Copper Ore Flotation Plant Using a Simulator That Can Predict Grade vs. Recovery Curves

(Gupta, M., Huang, K., Noble, A., & Yoon, R. H., 2023. *Minerals Engineering*, *202*, 108243.)

3.1 Abstract

A large porphyry copper flotation plant has been simulated using a flotation model developed from first principles using the hydrophobic force as a kinetic parameter (Huang *et al*., 2022; Gupta *et al*., 2022). The input to the simulation was the size-by-class liberation matrix (m_{ij}) of a flotation feed, which was essential for predicting the size-by-class flotation rate constants (k_{ij}) and hence a grade *vs*. recovery curves for the flotation bank. The model can be used to predict the performance of a flotation circuit provided that m_{ij} matrices are available for the feeds to the flotation banks in the circuit. With limited information on feed characteristics, we carried out a circuit simulation of the plant with some simplifying assumptions. The results suggest that significant financial benefits can be gained by recovering the slow-floating particles from the cleaner-scavenger tails that constitute the circulating load using an advanced separation technology in a separate copper recovery unit. With this approach, it is possible to substantially increase the throughput while maintaining copper recoveries and concentrate grades.

3.2 Introduction

Flotation may be the most important separation process used in the minerals industry. Its objective is to produce a salable concentrate from a mined ore with desired grade at a maximum recovery and throughput. In the minerals industry, air bubbles are used to collect hydrophobic particles selectively on the surface. In general, selectivity arises from the control of particle hydrophobicity. In dissolved air flotation (DAF), recovery is the prime objective by collecting all particulate materials indiscriminately on the surface of microbubbles *via* electrostatic interaction (Han *et al*., 2006).

In a special symposium honoring his contributions to flotation science, Sir Ian Wark (1984) stated that contact angle is the only practicable measure of the strength of bubble-particle adhesion, which is the most important step in flotation. Since then, many investigators learned how to measure the forces rather than the energies involved in bubble-particle interaction (Pan and Yoon, 2016; Huang and Yoon, 2019). In modeling flotation, which is a kinetic process, disjoining pressure (P) of a wetting film, given in units of N/m^2, serves as a useful criterion for contact angle formation. In principle, a wetting film should rupture spontaneously when $P < 0$ in the presence of the hydrophobic force (Churaev, 1995; Pan and Yoon, 2016; Huang and Yoon, 2020). Bubble-particle attachment can also occur at $P > 0$. It is necessary, however, to provide activation energy to overcome the energy barrier (E_1) to film rupture. Derjaguin and Dukhin (1961) used the DLVO theory to derive a relation that E_1 should increase as the square of particle V-potentials, which corroborated well with an earlier work of Fuerstenau (1957).

It has been shown more recently that E_1 can be determined as follows (Gupta *et al*., 2022),

$$E_1 = -\int_{\infty}^{h_{cr}} \Pi(h)dh \qquad [3.1]$$

in which h_{cr} is the critical rupture thickness. As discussed above, h_{cr} occurs at the film thickness at which $P = 0$. It has also been shown that a further decrease in P below the point of $E_1 = 0$ should accelerate the process of film thinning and hence greatly increase the flotation kinetics (Huang and Yoon, 2020). Thus, the role of hydrophobic force in flotation is to decrease E_1 and create a negative disjoining pressure to facilitate the kinetics of bubble-particle attachment and hence increase the recovery and grade.

The authors of the present investigation developed a flotation model using the hydrophobic force as a kinetic parameter (Hung *et al*., 2022; Gupta *et al*., 2022). The model can predict grade *vs*. recovery curves using the size-by-liberation (m_{ij}) matrix of a flotation feed as input. The m_{ij} matrix is then converted to a

size-by-class contact angle matrix (q_{ij}) using a modified Cassey-Baxter equation and is subsequently transformed to a size-by-class flotation rate constant (k_{ij}) matrix using the flotation model. As expected, k_{ij} is found to increase with q_{ij}, which in turn increases with mineral liberation. Thus, the model predicts that particles with a higher degree of liberation should float first and produce higher-grade concentrates in a bank of flotation cells.

The model has been validated against a set of experimental data obtained with a mini-plant and the rougher flotation bank of a large porphyry copper-moly flotation plant. In the present work, we used the model to optimize a flotation plant, which consists of a rougher flotation bank, a coarse cleaner bank, flotation columns, and a cleaner-scavenger bank. At present, the plant is recycling the cleaner scavenger tail (CST) to the rougher flotation bank as a circulating load (CL) to give longer retention times for the slow-floating particles. Circulating loads in general can potentially help increase both the recovery and grades but at a significant loss of recoveries (Wills and Finch, 2016). According to Paakkinen and Penttila (1977), a closed-circuit operation at a nickel flotation plant entailed a 20-30% loss of throughput. In the present work, possibilities of recovering copper directly from the CST in a separate circuit will be explored to increase both the recovery and throughput.

3.3 Model

3.3.1 Rate Equations

3.3.1.1 Pulp Phase Recovery

In the pulp phase of a flotation cell, mineral particles **1** collide with air bubbles **2** to allow the latter to selectively collect hydrophobic particles on the surface and rise to form a froth phase. The rate of the hydrophobic particles being collected by air bubbles may be represented as

$$\frac{dN_1}{dt} = -Z_{12}P \qquad [3.2]$$

in which Z_{12} is the frequency of bubble-particle collision and P is the probability of flotation. Abramson (1975) derived an equation to predict Z_{12} under highly turbulent conditions,

$$Z_{12} = 5.0 N_1 N_2 d_{12}^2 \sqrt{\overline{u_1}^2 + \overline{u_2}^2} \qquad [3.3]$$

in which N_1 and N_2 are the number densities of particles and bubbles, respectively, d_{12} collision radius, and $\sqrt{\overline{u}_1^2}$ and $\sqrt{\overline{u}_2^2}$ are RMS velocities. P is the product of probabilities of collision (P_c), attachment (P_a), and of not being detached ($1-P_d$) in the pulp phase (Sutherland, 1948).

Eqs. [3.2] and [3.3] may be combined to obtain a second-order rate equation,

$$\frac{dN_1}{dt} = -k_p N_1 N_2 \qquad [3.4]$$

with k_p being the rate constant,

$$k_p = 5.0 d_{12}^2 \sqrt{\overline{u_1}^2 + \overline{u_2}^2} P \qquad [3.5]$$

Eqs. [3.4] and [3.5] may be combined by assuming that N_2 stays constant during flotation,

$$\frac{dN_1}{dt} = -k_p' N_1 \qquad [3.6]$$

in which case the first-order rate constant becomes

$$k_p' = 5.0 N_2 d_{12}^2 \sqrt{\overline{u_1}^2 + \overline{u_2}^2} P \qquad [3.7]$$

which is widely used to model flotation. In practice, however, N_2 decreases with time in a flotation bank, making it difficult to model flotation as a first-order rate process. The decrease in N_2 may be due to the depletion of frothers and the decrease of N_1 with time. As is well known, particles act as solid surfactants and hence control the bubble sizes in both the pulp and froth phases of a flotation cell (Ata, 2012; Binks, 2002; Katpay, 2006; Park *et al*., 2018).

3.3.1.2 Froth Phase Recovery

Bubble-particle aggregates formed in a pulp phase enter the froth phase, in which less hydrophobic particles drop back into the pulp phase, a phenomenon that is critical for improving the grades of froth products. The drop-back mechanism is attributed to bubble coarsening (Moys, 1978) and film drainage. Park *et al*. (2018) developed a bubble-coarsening model by considering the role of particles in froth stability, while Huang *et al*. (2022) derived a model that can predict the froth phase recovery (R_f) as follows,

$$\begin{aligned} R_f &= R_{att} + R_{ent} \\ &= \frac{d_{2,b}}{d_{2,t}} \exp\left(-\alpha\tau\right) + R_w \exp\left(-0.0325\Delta\rho - 0.063 d_1\right) \end{aligned} \quad [3.8]$$

in which the first term represents the recovery due to bubble-particle attachment (R_{att}) and the second term represents the recovery due to entrainment (R_{ent}). The first term of Eq. [3.8] is based on the work of Gorain *et al*. (1998) who showed experimentally that the froth phase rate constant decays exponentially with residence time (t) with the parameter α being a fitting parameter. The preexponential term represents the ratio of the bubble sizes at the top ($d_{2,t}$) and bottom ($d_{2,b}$) of a froth phase that are related to the maximum capacities of the bubbles of different sizes carrying particles upward. Park *et al*. (2018) derived a model that can predict the bubble size ratio as follows,

$$\frac{d_{2,b}}{d_{2,t}} = \left[\exp\left(-\frac{0.46 n_f h_f}{J_g t_c} \right) \right]^{0.5} \quad [3.9]$$

in which h_f is the froth height, J_g is the superficial gas velocity, n_f is the number of bubble faces coalescing in a froth phase, and t_c is the critical rupture time of a lamella film. The second term of Eq. [3.8] suggests simply that the ultrafine and low-SG particles can be recovered indiscriminately in proportion to the fraction of water recovered to froth phase (R_w) (Maachar and Dobby, 1992).

One can readily derive the following relation to determine the overall flotation rate constant (k), encompassing the rate constants for the processes occurring in the pulp and froth phases of a flotation cell as follows (Finch and Dobby, 1990; Huang *et al.* 2022).

$$k = k' R_f \quad [3.10]$$

3.3.1.3 Particle and Bubble Size Effects

When a mineral particle collides with an air bubble, the intervening water film (wetting film) must thin and rupture to form a finite contact angle (q). The kinetics of film thinning is the most critical and decisive step in determining the kinetics of bubble-particle interactions. Under quiescent conditions, film thinning is driven by the capillary pressure (p_c) associated with the changes in local curvature. Under turbulent conditions, inertia forces may play a significant role. As the film thins to ~250 nm, film thinning is controlled by the disjoining pressure (P) created by surface forces. In principle, a wetting film should rupture at the critical rupture thickness (h_{cr}) at which P = 0.

Eq. [3.11] represents the extended DLVO theory that can be used to predict P,

$$\Pi(h) = -\frac{A_{132}}{6\pi h^3} - \frac{\varepsilon\varepsilon_0\kappa^2}{2\sinh(\kappa h)}\left[\left(\psi_1^2 + \psi_2^2\right)\text{cosech}(\kappa h) - 2\psi_1\psi_2 \coth(\kappa h)\right] - \frac{K_{132}}{6\pi h^3} \quad [3.11]$$

which gives the sum of the van der Waals (vdW), electrical double-layer (EDL), and hydrophobic (HP) forces (Yoon and Mao, 1996; Pan and Yoon, 2016); A_{132} is the Hamaker constant for the interaction between mineral **1** and air bubble **2** in water **3**; y_1 and y_2 are the EDL potentials, and K_{132} is the HP constant; e, e_0 and k are the dielectric constant of water, permittivity of air, and the reciprocal Debye length, respectively. Once the film ruptures, the film retreats rapidly to create a solid/air interface, resulting in the formation of a finite contact angle.

In flotation, the vdW force is repulsive as $A_{132} < 0$, which implies that energy is required to displace the water from hydrophobic surfaces. The EDL force is also repulsive as minerals and air bubbles are both negative under most flotation conditions. The EDL force is a longer-range force than the vdW forces; therefore, EDL forces are responsible for creating significant energy barriers (E_1) for bubble-particle interactions.

Huang *et al.* (2022) developed a method of determining E_1 from the free energy isotherm (G(h)) as a function of disjoining pressure isotherm (P(h)), particle radius (R_1), and bubble radius (R_2) as follows,

$$\begin{aligned} G(h) &= \frac{1}{2\pi}\left(\frac{R_1+R_2}{R_1R_2}\right)\int_{r=0}^{r=\infty}\Pi(h)2\pi r dr \\ &= \gamma_{LV}\left(\cos\theta - 1\right) \end{aligned} \qquad [3.12]$$

which is obtained by combining the Frumkin-Derjuaguin isotherm (Frumkin, 1938; Derjaguin, 1940) and the Derjaguin approximation (1932). One can then determine E_1 by integrating $G(h)$ over the bubble-particle contact area as follows,

$$E_1 = \int_{r=0}^{r=\infty} G(h)\big|_{\Pi=0}\, 2\pi r dr \qquad [3.13]$$

Thus, E_1 is a function of particle size, bubble size, and the various surface chemistry parameters that determine P(h) (Eq. [3.11]). It has been shown that E_1 decreases with decreasing bubble size, explaining the benefits of using smaller air bubbles for flotation, and with decreasing particle size (Huang *et al*., 2022). Once E_1 is known, one can predict the probability of bubble particle attachment (P_a) using the following relationship (Luttrell and Yoon, 1992),

$$P_a = \exp\left(-\frac{E_1}{E_k}\right) \qquad [3.14]$$

which determines flotation selectivity.

3.3.2 Key Parameters

3.3.2.1 Surface Forces

A distinguishing feature of the model presented in the foregoing section is that the HP force is used as a kinetic parameter controlling the speed at which a wetting film thins, ruptures, and retracts to form a contact angle. The EDL force has long been recognized as a kinetic parameter in flotation (Fuerstenau, 1957; Derjaguin and Dukhin, 1961). That the vdW force is repulsive as has been noted above is a detriment to flotation. In two-liquid flotation (TLF), in which oil drops rather than air bubbles are used to collect hydrophobic particles, the vdW force is attractive, however. Therefore, oil drops form substantially larger contact angles than air bubbles and hence give rise to faster kinetics of dewetting (Huang and Yoon, 2019). It has been shown indeed that the TLF process is superior to air bubble flotation for fine particle recovery (Mellgren and Shergold, 1966; Lai and Fuerstenau, 1968).

The use of HP force allows one to use q effectively as a kinetic parameter in modeling flotation. One can obtain the values of the hydrophobic force parameters (K_{132}) for bubble-particle interaction from contact angles as described by Huang *et al*. (2022). The relationship between these two parameters is akin to the relationship between the surface charge density and z-potentials in colloid chemistry.

Gupta *et al*. (2022) determined the contact angles to different classes of composite particles present in a flotation feed using a modified Cassey-Baxter equation. The contact angle matrix (q_{ij}) obtained in this manner was then used to determine the first-order flotation rate constants (k'_{ij}) using the model equations presented in the foregoing section. The size-by-class rate constant should vary with particle size (*i*), degree of liberation (*j*), and various other operating parameters.

3.3.2.2 Bubble Number Density

As a mill discharge enters a rougher flotation bank, fully liberated particles would float first, yielding the highest-grade concentrates in the first cell of a rougher bank (Gupta *et al*. 2022); however, the recovery in the first cell is low as the number of-fully liberated particles are limited. As materials flow through subsequent flotation cells, recoveries increase as composite particles begin to float with a concomitant decrease in product grade. The recovery *vs.* grades curves predicted from the model using the contact angles (q_{ij}) of composite particles are in reasonable agreement with those obtained in mini- and full-scale plant operations (Huang *et al.*, 2022; Gupta *et al*., 2022). As the materials continue to move along the rougher bank, bubble size becomes larger due to the depletion of frothers and particles of higher degree of liberation, causing N_2 and hence k'_{ij} to decrease. The materials that are most prone to this problem would be those with low degrees of liberation and finer particles. These materials represent the slow-floating particles that are present in the cleaner-scavenger tails (CST).

One way to improve the recovery of the slow-floating particles will be to increase the bubble number density (N_2). Many investigators tested this concept and obtained promising results (Jameson, 2010, Dickinson *et al*., 2014, Battersby *et al*., 2003, Jordan, 1993 and Firth *et al*., 1999; Jameson and Elmer, 2019). These and other investigators developed novel flotation cells, in which bubble-particle interactions occur under conditions of high N_2 by generating ultra-fine bubbles (Dalhke *et al*., 2005; Jameson, 2010). In the air-sparged hydro-cyclone (ASH), bubble-particle interactions occur under conditions of high $N_2$and centrifugal force fields to improve the kinetics of bubble-particle interactions and substantially reduce the flotation time (Miller *et al.*, 1988). Controlling N_2 to improve the recovery of slow-floating particles may be best represented by the second-order flotation (SOF) concept (Eqs. [3.4] and [3.5]).

3.3.2.3 Circulating Load

The most common approach to addressing the issues associated with CST is to send it back to the grinding and/or directly to the rougher flotation bank as a circulating load (CL). The slow-floating particles are effectively given longer retention times under plug-flow conditions so that they can be more readily collected by air bubbles. This approach works but at a cost of reduced throughput. When processing sulfide ores, one must also consider superficial oxidation, which can reduce contact angles and floatability.

3.3.2.4 Contact Angle

Flotation separation in the minerals industry is based on controlling the hydrophobicity of the particles to be collected by air bubbles. Grinding is in effect to increase the contact angles of particles to be floated by virtue of liberation. Coarse particle flotation is difficult due to the low contact angles associated with low degrees of liberation. Thus, many of the difficulties associated with the slow-floating particles in CST can be addressed by using stronger collectors. In general, the contact angles of the minerals recovered by flotation are in the range of 60 to 80^o. The contact angles can be increased up to 90^o using non-ionic surfactants with low HLB numbers of less than 15 and hydrophobic polymers (Yoon US Patent 6,871,743; 10,144,012).

Another way to address the problems associated with the low contact angles may be to use the two-liquid flotation (TLF) process. This process has been further developed by using recyclable hydrophobic liquids, e.g., pentane, hexane, and iso-hexane, so that spent solvents can be readily recycled (Yoon, 9,518,241). The process is highly selective and has practically no lower particle size limit. The process is akin to solvent extraction which is designed to separate molecules. The process known as hydrophobic-hydrophilic separation (HHS) is being used to recover ultrafine coal particles. An ancillary advantage of

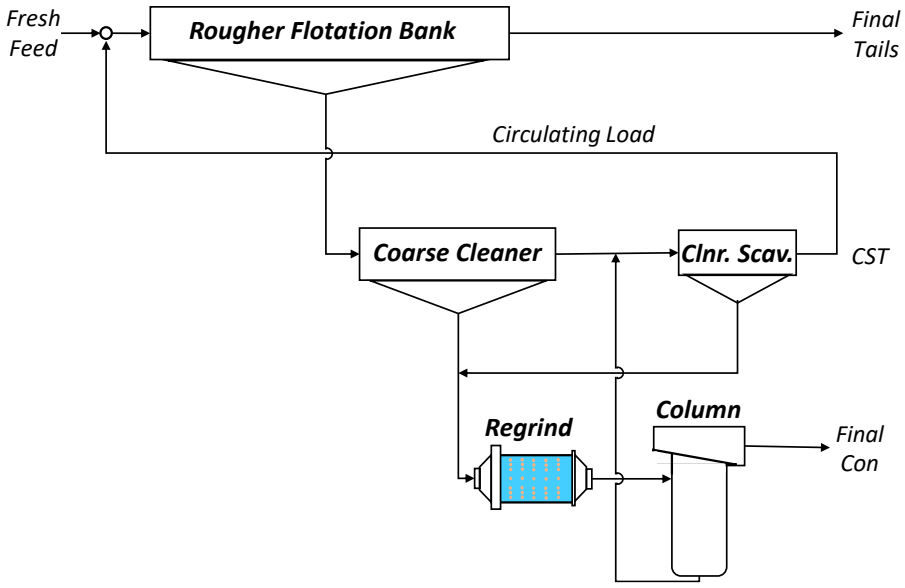

Figure 3-1. A flowsheet for the processing of a low-grade porphyry copper ore. The slow-floating CST is recycled as a circulating load.

the process is that its products are practically dry and water consumption is substantially lower than in flotation.

3.4 Simulation

3.4.1 Feed Characteristics

The model equations presented in the foregoing section have been used to simulate a porphyry copper flotation circuit with the objective of maximizing recovery, grade, and throughput. *Figure* 3-1 shows the circuit in which a copper ore feed is upgraded first in a rougher bank, consisting of five mechanically agitated flotation cells, each with a volume of 127.4 m^3. The froth product is further upgraded in the coarse cleaner bank, with its concentrate being reground and subjected to column flotation to obtain a copper-molybdenite concentrate.

Porphyry copper deposits represent the largest source of copper. In 2018, the mining industry produced 21 million metric tonnes (Mt) of refined copper, most of which (82%) was extracted from low-grade porphyry-type copper ores with the rest extracted from the ores of sedimentary origin. Most of the porphyry copper deposits are located along the Pacific coasts of South and North Americas, Southeast Asia, and Oceana along the Pacific Ring of Fire. The median grade of the porphyry copper deposits is 0.44 %Cu while the grade of the deposits in lower 10 percentile is 0.24 %Cu (Singer *et al*., 2008). Porphyry copper ores can produce important byproducts such as molybdenite and free gold. The major copper mineralization is chalcopyrite with small amounts of chalcocite, bornite, and covellite. Pyrite is a major gangue mineral that is depressed during copper flotation. The flotation circuit shows that the column tail is subjected to cleaner-scavenger flotation jointly with the coarse cleaner tail to recover the copper-bearing minerals that are not sufficiently hydrophobic as they are not sufficiently liberated and/or too small in size to be recovered in the column cell. The cleaner-scavenger tail (CST) consisting of the slowest-floating particles in the circuit is recycled back to the rougher flotation bank as circulating load (CL).

Thus, the feed to the rougher bank is a blend of the fresh and CST feeds. The grades of the rougher and CST feeds are 0.24 and 0.32 %Cu, respectively, while the volumetric and mass flow rates of the CST feed

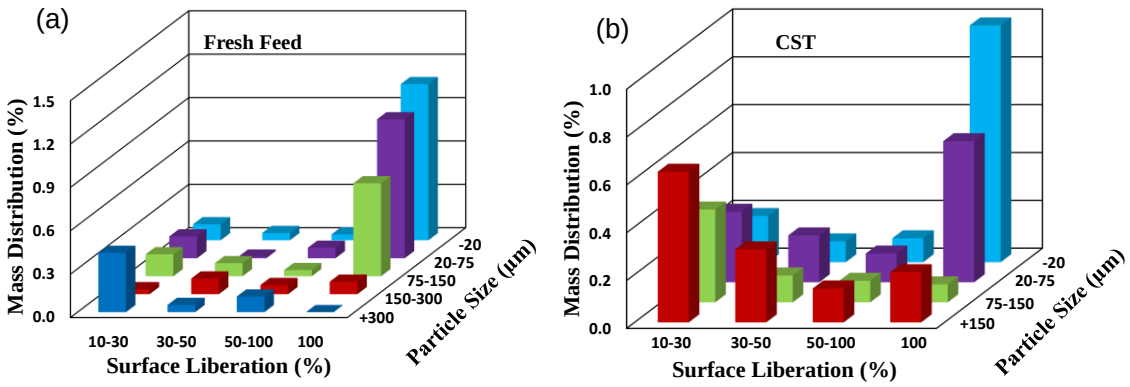

Figure 3-2. Size-by-class mass distribution (mij matrix) of particles in a) fresh feed and in b) CST. The % distributions 0-10% surface liberation are not shown as they are out of scale.

are 22 and 11.6 %, respectively. One can then back-calculate the grade of the freshly mined copper ore to be 0.23 %Cu from mass balance.

Figure 3-2 and *Tables* 3-1 and 3-2 represent the liberation matrices (m_{ij}) of the materials in the fresh feed and CL (or CST) streams. According to the matrix of the fresh feed, 40% of the particles in the feed stream are in the -150+20 µm size range, which may be considered the optimum size range. Of the rest, 16.4% are finer than 20 µm and 43. 6% are coarser than 150 µm. It is interesting to note that >20% of the coarse particles belong to the 0-10% liberation class, which may be the main reason for the difficulty in floating coarse particles (Clark *et. al*., 2005). Note also that 64% (0.39 out of 0.61%) of the fully liberated copper-bearing minerals are lost to CST due to their small particle size, *i.e*., < 20 mm.

Table 3-1. Size-by-class liberation (m_{ij}) matrix for the fresh feed to the rougher circuit.

Particle Size, *i* (µm)	Liberation Class, *j* (%)					Total (%)
	0-10	10-30	30-50	50-100	100	
+300	20.90	0.09	0.01	0.02	0.00	21.02
-300+150	22.50	0.01	0.02	0.01	0.02	22.57
-150+75	18.77	0.03	0.02	0.01	0.12	18.95
-75+20	20.84	0.03	0.002	0.02	0.20	21.10
-20	16.16	0.02	0.01	0.01	0.18	16.37
Total	99.18	0.17	0.06	0.07	0.52	100.00

Table 3-2. Size-by-class liberation (m_{ij}) matrix for Cleaner Scavenger Tails (CST).

Particle Size, *i* (µm)	Liberation Class, *j* (%)					Total (%)
	0-10	10-30	30-50	50-100	100	
+150	13.62	0.09	0.04	0.02	0.03	13.80
-150+75	15.69	0.06	0.02	0.01	0.01	15.80
-75+20	30.92	0.09	0.06	0.04	0.18	31.30
-20	38.56	0.08	0.03	0.04	0.39	39.10
Total	98.81	0.32	0.16	0.11	0.61	100.00

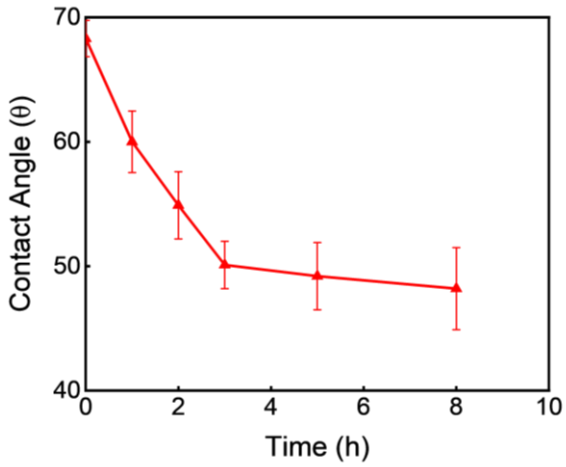

Figure 3-3. Effect of aging on the contact angles of chalcopyrite in water.

Gupta *et al*. (2022) used a modified Cassie-Baxter equation to determine the effective contact angles ($\overline{\theta}_{ij}$) of composite particles of particle size *i* and liberation class *j*. The calculations were made assuming that q = 72° for chalcopyrite and q = 10° for silicious gangue. The authors showed that flotation rate constants increase with $\overline{\theta}_{ij}$, demonstrating the importance of contact angles in flotation. It appeared that grinding has dual objectives: improve surface liberation and increase contact angles, both contributing to increased grades of froth products.

It is possible that the contact angles of the particles in CST decrease while being recirculated particularly for the particles smaller than ~20 mm, whose first-order rate constants in the pulp phase (k'_P) are small due to the low collision probabilities. In an effort to estimate the extent of contact angle decrease during recirculation, a polished chalcopyrite specimen was placed in a $5x10^{-3}$ M PAX solution at the natural pH for 15 min without agitation. As shown in *Figure* 3-3, its contact angle decreased from 68.3° to 40° in 8 hrs. The contact angle measurements were conducted using the captive bubble method at pH 11 using a Ramé-Hart Goniometer.

3.4.2 Rougher Circuit

Based on the $\overline{\theta}_{ij}$ values obtained from the m_{ij} matrix, the first-order flotation rate constants ($k'_{p,ij}$) in the pulp phase have been predicted using Eq. [3.7] and [3.11]-[3.14] for each cell in the rougher bank. The flotation rate constants determined in this matter were then used to obtain the size-by-class recoveries ($R_{p,ij}$) using the following relation,

$$R_{p,ij} = \frac{k'_{p,ij}t}{1+k'_{p,ij}t} \qquad [3.15]$$

which is applicable for fully mixed flotation cells.

The froth phase recoveries ($R_{f,ij}$) of the particles of different sizes and surface liberation can be predicted using Eq. [3.8]. The recoveries due to entrainment have also been calculated in the same manner as described previously (Huang *et al*., 2022). From the pulp and froth phase recoveries, the overall cell-by-cell recoveries (R_{ij}) for different particles of size (*i*) and liberation (*j*) classes can be obtained using the following relationship,

$$R_{ij} = \frac{R'_{p,ij}R_{f,ij}}{R'_{p,ij}R_{f,ij}+(1-R^f_{ij})} \qquad [3.16]$$

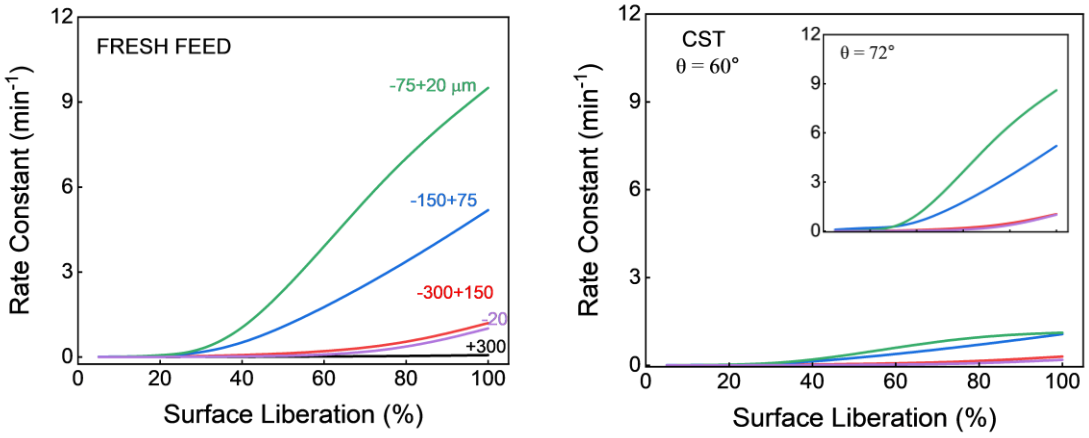

Figure 3-4. Effects of surface liberation on the size-by-class flotation rate constants (k_{ij}) for a) fresh feed (θ = 72°) and b) CST (θ = 60°). The inset shows the effects of increasing the contact angles of CST particles to 72°. The k_{ij} values represent the bank rate constants.

The simulations were carried out for three different feed streams: i) fresh feed, ii) CST feed, and iii) rougher feed which is a combination of the two.

The cell-by-cell recoveries obtained as described above were then used to construct the cumulative recovery *vs*. grade curves for particles of different sizes and liberation classes, which were then used to obtain bank recoveries (R_{ij}) and bank rate constants (k_{ij}) as described previously (Gupta *et al*., 2022). *Figure* 3-4 compares the bank k_{ij} values plotted for the different particle size and liberation classes present in the fresh and CST feeds. As shown, the CST feeds exhibited substantially lower k_{ij} values than the fresh feeds.

For the fresh feed, the -75+20 mm size fraction represented the fastest floating particles, followed by the -150+75 mm and -300+150 mm fractions. This order corresponds to the order by which the population of the fully-liberated particles decreases in the three different size fractions (see *Figure* 3-2a and *Table* 3-1). Loss of the free copper minerals is the highest for the -20 mm fraction, which may be attributed to the unfavorable hydrodynamic condition, *i.e.*, low probability of collision. On the other hand, the poor recovery of the +300 mm fraction may be due to the low surface liberation and hence the high probability of detachment associated with low $\overline{\theta}_{ij}$ values. It has been shown previously that the $\overline{\theta}_{ij}$ = 15° for the composite particles with 5% surface liberation (Gupta *et al*., 2022). However, coarse particles can also have distinct patches of hydrophobic material (*e.g*., chalcopyrite) of high local grades. In this regard, the slow kinetics observed with coarse particles may also be attributed to the low probability of bubbles finding the right spots for fast attachment and the low probability of detachment.

The reasons for the poor recoveries predicted for the CST feed are more complex. *First*, significant amounts of copper are associated with the +150 mm size fraction that is not well liberated, as shown in *Figure* 3-2b. *Second*, most of the copper is associated with the -20 mm particles that are difficult to be recovered for hydrodynamic reasons. Both reasons can give rise to low k_{ij} values for the copper-bearing mineral particles in CST. It appears that the CST feed represents a collection of the slowest-floating particles in the flotation circuit. An obvious solution to the problem will be to give the slower-floating particles longer retention times by returning them to the rougher-scavenger circuit as a circulating load, which is a common practice in the minerals industry.

The approach to extending the retention time may create a different problem. Sulfide minerals are unstable and hence can be readily oxidized to form sulfur oxide species, *e.g*., SO_4^{2-}, $S_2O_3^{2-}$, *etc*., that render the surface hydrophilic and cause contact angles to decrease as shown in *Figure* 3-3. A solution to this

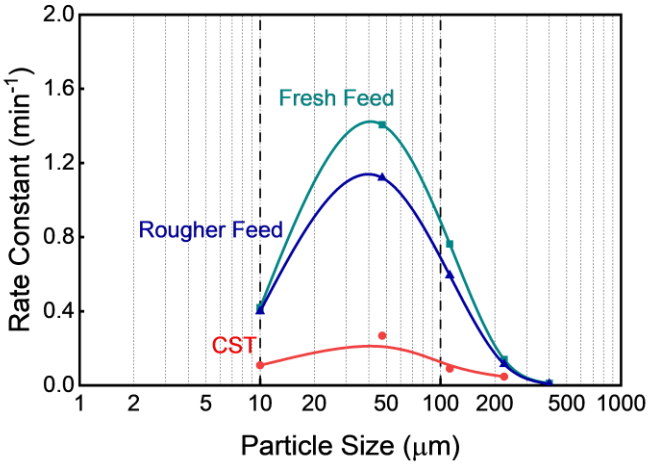

Figure 3-5. Size-by-size flotation rate constants for materials in fresh feed, rougher feed, and CST.

problem may be to use hydrophobizing agents to counter the detrimental effect of superficial oxidation. To explore this possibility, simulations were conducted by increasing the contact angle of the chalcopyrite portion of the composite particles in CST from θ = 60° to 72° as shown in the inset of *Figure* 3-4b. As shown, a relatively small increase in contact angle greatly increased k_{ij}.

3.4.3 Cleaner Circuit with Circulating Load

Recycling CSTs from a cleaner circuit to a rougher bank as a circulating load (CL) is a common practice in mineral flotation plants (*Figure* 3-1). *Figures* 3-4b and 3-5 show that the values of k_{ij} for the copper-bearing materials in CST are substantially lower than those in fresh feed due to i) incomplete liberation, ii) small particle size, and iii) superficial oxidation. It would, therefore, be reasonable to give them longer retention times to compensate for the low k_{ij} values. It is generally believed that building up CLs should

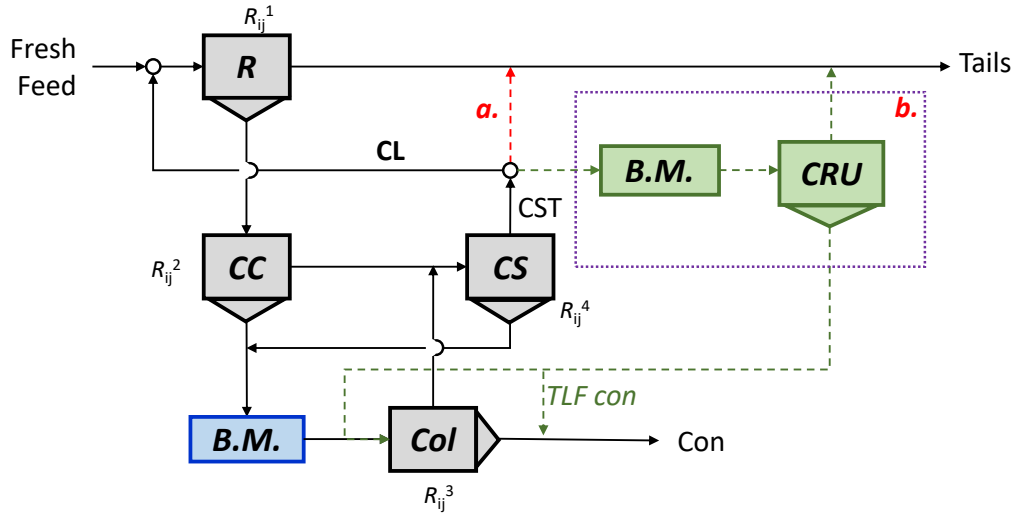

Figure 3-6. The flotation circuit that was used for simplified studies. The R_{ij}^1, R_{ij}^2, R_{ij}^3 and R_{ij}^4 are the size-by-class recoveries of rougher, coarse cleaner, column, and cleaner scavenger cells, respectively. The circuit analyses were carried out by varying the fraction (C) of CST being recycled as CL from 0 to 1. At C = 0, the CST was discarded in its entirety to tails as shown by arrow a. When C ≠ 0, the CST was ball-milled and processed in the CRU circuit (b) to recover the copper-bearing minerals using advanced separation technologies: i) flotation with a strong collector, ii) SOF, and iii) TLF.

help increase both recovery and separation efficiency (Wills and Finch, 2016; Lynch *et al*, 1981). The simulation results reported by Loveday and Marchant (1972) showed a 0.6% increase in copper recovery by increasing CL.

Figure 3-6 represents a flotation circuit of a large porphyry copper flotation plant that has been simulated in the present work. The feed to the rougher (*R*) bank consists of fresh feed and the CST (or CL) from the cleaner circuit. The performance of the rougher bank was simulated using the model developed by Huang *et al*. (2022) and Gupta *et al*. (2022). For these simulations, the m_{ij} matrices of both the fresh (*Table* 3-1) and CST (*Table* 3-2) feeds were available. Therefore, it was possible to obtain the size-by-class recoveries (R_{ij}) and rate constants (k_{ij}) for each cell along the bank.

Unfortunately, the m_{ij} matrices were not available for the feeds to the flotation banks and columns operating in the cleaner circuit. Therefore, we predicted the recoveries of the overall flotation circuit, including the rougher and cleaner banks using the linear circuit analysis (LCA) concept. Meloy (1983) suggested that a feed (*F*) splits into a product (*P*) as *RF*, in which *R* is a selection function and that *R* is independent of *F*, which is known as the linearity assumption. The LCA concept can then be used to determine circuit recoveries using an algebraic approach. In the present work, we assumed that the performance of each flotation bank can be represented by a large single flotation cell of known k_{ij}^{a} and R_{ij}^{a} values, in which the superscript *a* represents the different banks in the circuit. With this simplifying assumption, one can readily derive an analytical formula for the circuit recovery (R_{ij}^{c}),

$$R_{ij}^{c}=\frac{R_{ij}^{3}A}{B-C\left(1-R_{ij}^{4}\right)\left(\left(1-R_{ij}^{3}\right)A+R_{ij}^{1}\left(1-R_{ij}^{2}\right)B\right)} \qquad [3.17]$$

in which

$$A=R_{ij}^{1}R_{ij}^{2}+R_{ij}^{1}R_{ij}^{4}\left(1-R_{ij}^{4}\right) \qquad [3.18]$$

and

$$B=1-\left(1-R_{ij}^{3}\right)R_{ij}^{4} \qquad [3.19]$$

In these equations, the superscripts a = 1, 2, 3, and 4 represent the rougher, coarse-cleaner, column, and cleaner-scavenger banks, respectively; and *C* represents the fraction of the CST that is being recirculated.

The following equation was used to determine the R_{ij}^{a} values of the fictitious single flotation cell representing the rougher flotation bank,

$$R_{ij}^{a}=1-\exp(-k_{ij}t_{a}) \qquad [3.20]$$

in which k_{ij} is a size-by-class matrix determined by the cell-by-cell simulations using the m_{ij} matrix for the fresh feed and t_a is the retention time of the particles. The bank recovery (R^{a}) of the copper-bearing minerals can, therefore, be determined by the following relation,

$$\begin{aligned} R^{a} &= \sum \phi_{ij}^{a} R_{ij}^{a} \\ &= 1-\sum \phi_{ij}^{a} \exp(-k_{ij}t_{a}) \end{aligned} \qquad [3.21]$$

which is analogous to the rate equation derived by Chander and Polat (1994). In Eq. [3.21], φ_{ij}^{a} is essentially a distribution function of the rate constants, which is equivalent to the size-by-class mass fraction of the particles,

$$\phi_{ij}^{a}=\frac{m_{ij}^{a}}{\sum m_{ij}^{a}} \qquad [3.22]$$

Table 3-3. Size-by-class flotation rate constants (k_{ij}) and recoveries (R_{ij}) for the materials in the closed-circuit configuration.

Particle Size *i* (μm)	Liberation Class *j* (%)									
	0-10		10-30		30-50		50-100		100	
	k_{ij} (min^{-1})	R_{ij} (%)	k_{ij} (min^{-1})	R_{ij} (%)	k_{ij} (min^{-1})	R_{ij} (%)	k_{ij} (min^{-1})	R_{ij} (%)	k_{ij} (min^{-1})	R_{ij} (%)
+300	0.0	0.0	0.00	0.0	0.007	0.1	0.023	3.8	0.136	93.9
-300+150	0.004	0.1	0.008	0.1	0.005	20.7	0.231	99.5	0.904	100.0
-150+75	0.009	0.8	0.057	31.7	0.825	100.0	2.382	100.0	4.351	100.0
-75+20	0.002	0.0	0.027	3.8	0.503	100.0	4.972	100.0	8.935	100.0
-20	0.00	0.0	0.002	0.0	0.015	0.6	0.088	69.1	0.834	100.0

Table 3-3 shows the R_{ij} matrix obtained using Eq. [3.20]. The R_{ij} values in this table should give the same grade *vs*. recovery curves as may be obtained using the real flotation bank consisting of five 127.4 m^3 flotation cells.

In the absence of m_{ij} matrices that could have been used to determine the k_{ij} and R_{ij} matrices by cell-to-cell simulations for the cleaner flotation circuit, an assumption was made that the k_{ij} values of the copper-bearing particles were one-half of the particles in the fresh rougher feed. A rationale for using this assumption was that much of the middlings are purposely dropped back to the pulp phase to obtain a desired product grade, *e.g*., 25 Cu%. With this assumption, it was possible to determine the retention times for the coarse cleaner (t_2), column cells (t_3), and cleaner-scavenger cells (t_4) by solving Eqs. [3.17]-[3.19] iteratively. The boundary conditions for solving them included the circuit recovery of 85.4% copper, CST grade of 0.32 %Cu, final concentrate grade of 25.68 %Cu, and C = 1 for which CL accounts for 11.6% by weight (or 20% by volume) of the rougher feed.

It was necessary to solve a large number of equations simultaneously. For a given k_{ij} matrix, it was necessary to solve a 5x5 size-by-class matrix, and there were four k_{ij} matrices representing four different flotation banks in the entire flotation circuit. It was found also that the boundary condition of CL of 11.6% by weight of the rougher feed, which was obtained from the plant survey, was unreasonably high. An iterative solution of Eqs. [3.17]-[3.19] suggest a value of CL = 7.1% by weight would be more reasonable. The iterative solutions also gave the values of t_2 = 15 min for the coarse cleaner, t_3 = 24 min for flotation columns, and t_4 = 6 min for cleaner scavengers. These were the retention times of the fictitious single large flotation cells that can approximate the performances of the coarse cleaner, columns, cleaner scavenger banks of the cleaner circuit that can produce 25.68 %Cu concentrate at a 85.4% copper recovery in a closed circuit configuration shown in *Figure* 3-6.

3.4.4 Open-Circuit

In a closed-circuit configuration, CST contributed 20% of the total volumetric flow to the rougher bank. The simulations were conducted by varying the circulating load factor (C) from 0 to 1 where C = 0 represents the fully-open circuit configuration, while C = 1 represents the case where the whole of the CST was recycled. The simulation results presented in *Figure* 3-7 and *Table* 3-6 show that discarding the entire CST flow consisting of mostly the slowest-floating particles to a tailings pond and replacing it with fresh feed can increase the throughput by 24.8% as shown by the black solid line with a corresponding revenue increase from $605.7 million to $743.9 million at $3.85/lb Cu. The large increase in throughput and financial gains entailed a decrease in copper recovery from 86.65 to 85.3% as shown by the dotted black line in *Figure* 3-7. The loss of recovery may be difficult to accept psychologically in view of the significant investments made at the upstream processes. We have, therefore, explored the possibility of recovering the

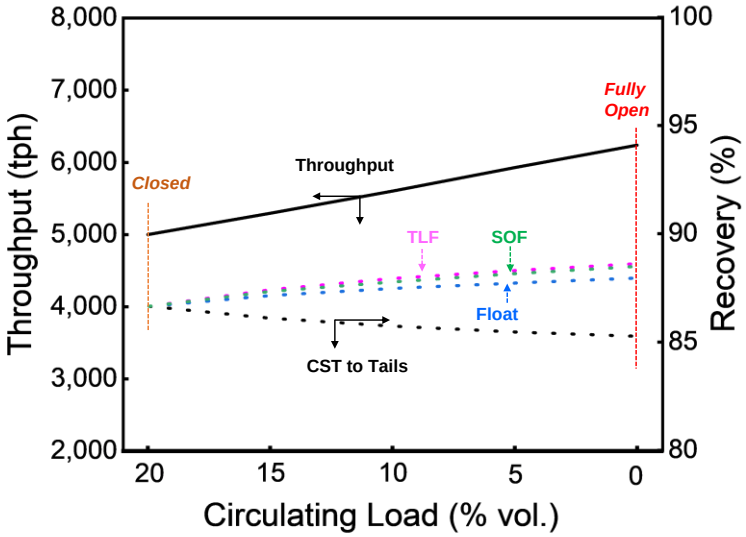

Figure 3-7. Effects of decreasing circulating load to increase the throughput (black lines), which entails losses of copper recovery (black dashed line). The dotted lines in color show that copper recovery can be increased by processing CST in the copper recovery unit (CRU) using flotation with a strong collector, SOF, or TLF.

copper directly from the CST in a separate copper recovery unit (CRU) using a novel separation process as depicted in *Figure* 3-6b as an inset. This approach should allow the plant operators to take advantage of increasing the throughput by replacing the CST flow to the rougher bank as a CL by increasing the flow rate of the fresh feed.

3.4.5 Open Circuit with Copper Recovery Unit

We have considered several different approaches that may be useful for the recovery of the slow-floating particles separately from CST in the CRU circuit. As shown in *Figure* 3-6, the CRU circuit includes

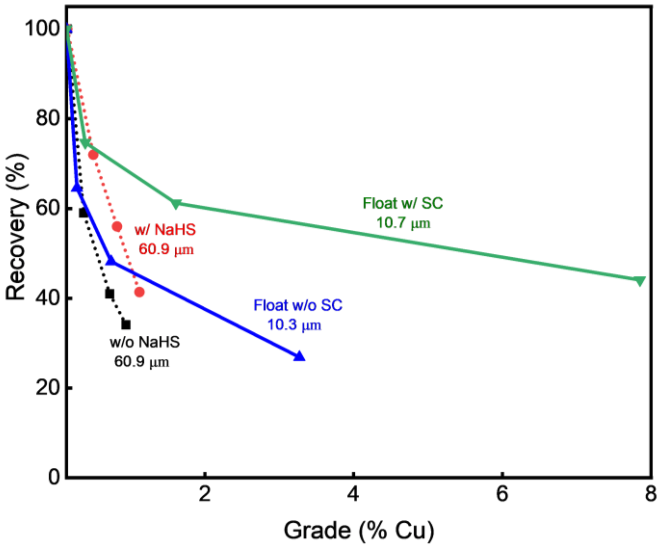

Figure 3-8. Effects of removing oxidation products from the surface of copper-bearing minerals present in CST by using NASH (dotted lines) and by grinding prior to flotation (solid lines). Super collector (SC) was effective for copper recovery from the mill product.

a ball (or a stirred) mill to decrease the population of composite particles in CST and to overcome the harmful effects of superficial oxidation.

The first approach was to address the problem associated with superficial oxidation by treating a CST sample (d_{80} = 60.9 mm) from an operating porphyry copper flotation plant with NaHS prior to a set of laboratory scale flotation tests. In one test, 100 g/t potassium amyl xanthate (KAX) was used as collector without using the reducing agent. The flotation test conducted after the pretreatment step produced a copper concentrate with a grade of 1.12 %Cu with a 41.4% copper recovery as compared to a grade of 0.94 %Cu with a copper recovery of 34.1%. These results suggest that superficial oxidation may indeed be a problem, which can be addressed using a reducing agent to remove the oxidation products from the surface of the copper-bearing minerals.

In another test, the CST sample was wet ground in a stirred mill to d_{80} = 10.3 μm and treated with a strong hydrophobizing agent, known as a super collector (SC), for flotation. In another, the mill product was floated with KAX as a collector but without the SC. The results obtained using SC produced substantially better results as shown in *Figure* 3-8. The test conducted using the SC produced a froth product with 1.54% Cu at a recovery of 56.2% as shown in *Table* 3-4. Thus, using a stronger hydrophobizing agent may be useful for the recovery of copper from CST.

Still another method of recovering copper from CST may be the concept of second-order flotation (SOF) as represented by Eq. [3.4]. Most engineers use Eq. [3.6], the first-order rate equation, which is valid when N_2 is constant is much larger than N_1 and stays constant during flotation. In reality, however, N_2 decreases along the bank of flotation cells where only the slow-floating particles are left. An obvious way to address this issue will be to increase N_2 downstream, which can be costly. A better solution may be to use a specially-designed flotation cell known tentatively as second-order flotation (SOF) cell. In this process, microbubbles are generated in a static mixer under highly turbulent conditions. A stream of CST is injected into the mixer so that bubble-particle attachment occurs under conditions of high-kinetic energies. Fine particles have low inertia, which makes it difficult for them to overcome the tension in the TLF of water formed between them, which is known as wetting tension (γ_{SV}-γ_{SL}). The bubble-particle aggregates formed under these conditions are then separated in a centrifugal field created in a hydro-cyclone. *Table* 3-4 shows the results of a laboratory-scale tests conducted on a CST sample with d_{80} = 38.8

Table 3-4. Laboratory test results obtained with a CST sample using flotation, SOF, and TLF processes.

Stream	Flotation		SOF		TLF	
	Grade (%Cu)	Rec. (%)	Grade (%Cu)	Rec. (%)	Grade (%Cu)	Rec. (%)
Conc.	1.54	56.2	1.46	64.4	30.36	64.9
Tail	0.076	43.8	0.065	35.6	0.093	35.1
Feed	0.165	100.0	0.165	100.0	0.265	100.0

Table 3-5. Circuit simulation results obtained at different circuit configurations.

Stream	Closed		Fully Open					
			Float		SOF		TLF	
	Grade (%Cu)	Rec. (%)	Grade (%Cu)	Rec. (%)	Grade (%Cu)	Rec. (%)	Grade (%Cu)	Rec. (%)
Conc.	25.68	86.65	27.15	87.95	27.14	88.49	27.20	88.62
Tail	0.0305	13.35	0.0276	12.05	0.0264	11.51	0.0261	11.38
Feed	0.227	100.0	0.227	100.0	0.227	100.0	0.227	100.0
	5,000 tph		6,239 tph (24.8% increase)					

μm using a laboratory-scale SOF test. As shown in *Table* 3-4, a froth product assaying 1.46 %Cu was obtained at a 64.4 % recovery. The retention time required for SOF test was only 1.1 sec. The laboratory Denver cell flotation test, the results of which is also given in *Table* 3-4, required a 60 sec of retention time.

Lastly, we subjected a CST sample with d_{80} = 12 μm to a laboratory-scale two-liquid flotation (TLF) test, with the results given in *Table* 3-4. As shown, a 30.6 %Cu concentrate was obtained at a recovery of 64.9 % from a feed assaying 0.265 %Cu. The feed assay was higher than those of the other tests as the sample was taken at a different time. In the TLF test, oil drops rather than air bubbles were used to collect hydrophobic particles. It is easier for an oil drop to collect hydrophobic particles simply because oil drops can form higher contact angles than air bubbles. An advantage of using the TLF process over the other two processes is that its concentrate can directly sent to the copper-moly separation plant, while the other concentrates should be sent to the cleaner flotation circuit for further upgrading.

3.5 Discussion

A series of simplified circuit analyses (SCA) were carried out for the entire flotation circuit including the copper recovery unit (CRU) to recover copper-bearing minerals directly from CST. Simulations were carried out by considering employing three different advanced separation processes as options for CRU. These included i) conventional flotation using a stronger collector, ii) an SOF unit for fast flotation of ultrafine particles, iii) a TLF unit to produce high-grade concentrates. The simulations were carried out under the assumption that all flotation banks and CRUs were single cells for mathematical simplicity. The high-grade TLF concentrate was sent directly to the final concentrate sump, while the flotation and SOF products were directed to the cleaner circuit to be further upgraded.

The feeds to the CRUs were the CSTs ground in a ball mill as shown in *Figure* 3-6. It was assumed that the top size of the mill products was 75 μm and that mill discharge was fed to flotation columns. It was assumed also that the copper recoveries and the mass pulls were the same as those obtained in the laboratory tests. The k_{ij} values of the mill product were assumed to be the same as those of other composite particles in the cleaner circuit. Lastly, it was assumed that the m_{ij} matrix of the CRU product was such that the columns could produce desired product grade and recoveries.

The simulation results presented in *Figure* 3-7 and *Table* 3-5 show that processing CST in CRU circuits increased throughput without losing recoveries. Interestingly both recoveries and concentrate grades increased over the case of closed-circuit configuration. The three dotted lines plotted in color in *Figure* 3-7 show that all three advanced separation technologies tested in the CRU circuits increased copper recoveries well above those obtainable using both the closed and open circuit configurations while maintaining substantial gains in throughput. Furthermore, the new approach suggested in the present work increased concentrate grades by 1.46-1.52 %Cu as shown in *Table* 3-5, while the recovery increases were in the range of 1.3-1.97 %. Two reasons for the increased grades may be given. *First*, the fresh feed consists of higher population of liberated particles than those in the CST flow as can be seen in *Tables* 3-1 and 3-2.

Table 3-6. Comparison of the financial benefits obtained from using different options for handling CST.

	Closed[1]	Fully Open			
		Pond[2]	Float[3]	SOF[4]	TLF[5]
Throughput (tph)	5,000	6,239	6,239	6,239	6,239
Cu Recovery (%)	86.65	85.30	87.95	88.49	88.62
Conc Grade(%Cu)	25.68	26.84	27.15	27.14	27.20
Revenue (10^{6})[6, 5]	605.7	743.9	767.1	771.8	772.9

Second, the fine grinding of the CST in the CRU circuit should increase the population of liberated particles in the column product.

The economic benefits of the proposed approach have been summarily presented in *Table* 3-6. As shown, the open circuit configuration can greatly increase the throughput without losing recoveries. In fact, both the recoveries and grades increased significantly. As a result, the financial benefits that can be brought about were in the range of $99.2 million to $167 million, representing 16.7 to 27.6% increases in revenue over the case of employing conventional closed-circuit operations. These improvements are due to the use of advanced separation processes in the CRU circuit, which will save energy, require significantly less water, and generate less tailings. It appears that the choice of advanced separation technologies will depend on the operator's preferences and environmental considerations.

It was possible to carry out the simulations including economic benefits simply because our model can predict grade vs. recovery curves for the first time. The primary objective of flotation is to produce concentrate grades, which has been made possible by recognizing that flotation is a kinetic process and that the kinetics is determined by the driving force for flotation, that is, hydrophobic force. Particles and bubbles cannot move to each other without force. According to Newton's law, force is zero in the absence of acceleration. We have shown in our surface force measurements that the hydrophobic force increases exponentially in the thin liquid films of water formed between particles and mineral surfaces.

3.6 Summary and Conclusion

Circulating loads are commonly used in the flotation industry to recover slow-floating particles by providing extended retention times. It has been shown that building up circulating loads improves recovery and grade but at the cost of reduced throughput. A computer simulation carried out on a large porphyry copper flotation plant using a flotation model developed from first principles suggests that significant financial and environmental benefits can be realized by opening the circuit and recovering the copper-bearing minerals from the circulating load in a separate circuit using an advanced separation process. Three different advanced separation technologies have been tested by simulation, all suggesting substantial financial benefits.

The flotation model can predict the grade *vs*. recovery curves by predicting the size-by-class flotation rate constants using the size-by-liberation class matrix of a flotation feed. Since the liberation matrices were not available for all the feeds in a complex flotation circuit. It was, therefore, necessary to carry out circuit simulations using simplifying assumptions. Nevertheless, the simulation results can predict reasonable recoveries and separation efficiencies as the simulation was based on size-by-class rate constants rather than flat recoveries along a flotation bank.

3.7 References

Abrahamson, J. (1975). Collision rates of small particles in a vigorously turbulent fluid. *Chemical Engineering Science*, *30*(11), 1371-1379.

Ata, S. (2012). Phenomena in the froth phase of flotation—A review. *International Journal of Mineral Processing*, *102*, 1-12.

Battersby, M. J. G., Brown, J. V., & Imhof, R. M. (2003). The Imhoflot G-Cell--An Advanced Pneumatic Flotation Technology for the Recovery of Coal Slurry from Impoundments. *Aufbereitungs Technik-Mineral Processing*, *44*(9), 14-19.

Binks, B. P. (2002). Particles as surfactants—similarities and differences. *Current opinion in colloid & interface science*, *7*(1-2), 21-41.

Chander, S., and Polat, M., 1994, "In quest of a more realistic flotation kinetics model," in Flotation Proc. of IVth meeting of Southern Hemisphere on Mineral Technology and IIIrd Latin American Congress of Froth Flotation, Chile, Vol. II, pp. 481-500.

Churaev, N. V. (1995). Contact angles and surface forces. *Advances in colloid and interface science*, *58*(2-3), 87-118.

Clark, M. E., Brake, I., Huls, B. J., Smith, B. E., & Yu, M. (2005). Creating value through application of flotation science and technology. In: Centenary of Flotation Symposium, 6-9 June, Brisbane, QLD.

Dahlke, R., Gomez, C., & Finch, J. A. (2005). Operating range of a flotation cell determined from gas holdup vs. gas rate. *Minerals Engineering*, *18*(9), 977-980.

Derjaguin, B. V. (1934). Friction and adhesion. IV. The theory of adhesion of small particles. *Kolloid Zeits*, *69*, 155-164.

Derjaguin, B. V. (1940). Th eory of the capillary condensation and other capillary phenomena taking into account the disjoining effect of long-chain molecular liquid films. *Zh. Fiz. Khim*, *14*, 137.

Derjaguin, B. V., & Dukhin, S. S. (1961). Theory of flotation of small and medium-size particles, Institution of Mining and Metallurgy. 241-267.

Dickinson, J. E., & Galvin, K. P. (2014). Fluidized bed desliming in fine particle flotation–part I. *Chemical Engineering Science*, *108*, 283-298.

Finch, J. A., & Dobby, G. S. (1990). Column flotation. *Flotation Science and Engineering*, 291-329.

Firth, B. (1999). Turbo flotation: faster, cleaner, cheaper fine coal recovery. *The Australian Coal Review*.

Frumkin, A. N., & Gorodetzkaya, A. (1938). On the phenomena of wetting and the adhesion of bubbles. II. The mechanism of the adhesion of bubbles to a mercury surface. *Acta Physicochim. URSS*, *9*, 327.

Fuerstenau, D. W. (1957). Correlation of contact angles, adsorption density, zeta potentials, and flotation rate. *TRANSACTIONS OF THE AMERICAN INSTITUTE OF MINING AND METALLURGICAL ENGINEERS*, *208*(7), 1365-1367.

Gorain, B. K., Harris, M. C., Franzidis, J. P., & Manlapig, E. V. (1998). The effect of froth residence time on the kinetics of flotation. *Minerals Engineering*, *11*(7), 627-638.

Gupta, M., Huang, K., & Yoon, R. H. (2022). Predicting the recovery and grade of a rougher flotation circuit from liberation data. *Minerals Engineering*, *188*, 107853.

Han, M. Y., Kim, M. K., & Ahn, H. J. (2006). Effects of surface charge, micro-bubble size and particle size on removal efficiency of electro-flotation. *Water science and technology*, *53*(7), 127-132.

Hood, G. D., & Jordan, C. E. (1993). In-line static mixer rapid flotation system for improved flotation kinetics. *Mining, Metallurgy & Exploration*, 10(4), 182-187.

Huang, K., & Yoon, R. H. (2019). Surface forces in the thin liquid films (TLFs) of water confined between n-alkane drops and hydrophobic gold surfaces. *Langmuir*, *35*(48), 15681-15691.

Huang, K., & Yoon, R. H. (2020). Control of bubble ζ-potentials to improve the kinetics of bubble-particle interactions. *Minerals Engineering*, *151*, 106295.

Huang, K., Keles, S., Sherrell, I., Noble, A., & Yoon, R. H. (2022). Development of a flotation simulator that can predict grade vs. Recovery curves from mineral liberation data. *Minerals Engineering*, *181*, 107510.

Jameson, G. J. (2010). Advances in fine and coarse particle flotation. *Canadian Metallurgical Quarterly*, *49*(4), 325-330.

Jameson, G. J., & Emer, C. (2019). Coarse chalcopyrite recovery in a universal froth flotation machine. *Minerals Engineering*, *134*, 118-133.

Kaptay, G. (2006). On the equation of the maximum capillary pressure induced by solid particles to stabilize emulsions and foams and on the emulsion stability diagrams. *Colloids and Surfaces A: Physicochemical and Engineering Aspects*, *282*, 387-401.

Lai, R. & Fuerstenau, D. (1968). Liquid-liquid extraction of ultrafine particles. *Trans. AIME 241*, 549-556

Loveday, B.K. & Marchant, G. (1972). Simulation of multicomponent flotation plants. *Journal of the Southern African Institute of Mining and Metallurgy*, *72*(11), 288-294.

Luttrell, G. H., & Yoon, R. H. (1992). A hydrodynamic model for bubble—particle attachment. *Journal of colloid and interface science*, *154*(1), 129-137.

Lynch, A. J., Johnson, N. W., Manlapig, E. V., & Thorne, C. G. (1981). Mineral and coal flotation circuits: Their simulation and control.

Maachar, A., & Dobby, G. S. (1992). Measurement of feed water recovery and entrainment solids recovery in flotation columns. *Canadian metallurgical quarterly*, *31*(3), 167-172.

Mellgren, O., & Shergold, H. L. (1966). Method for recovering ultrafine mineral particles by extraction with an organic phase. *Trans. Inst. Min. Metall*, *75*, C267-C268.

Meloy, T. P. (1983). Analysis and optimization of mineral processing and coal-cleaning circuits—Circuit analysis. *International Journal of Mineral Processing*, *10*(1), 61-80.

Miller, J. D., Ye, Y., Pacquet, E., & Baker, M. W. (1988). The air-sparged hydrocyclone for fine coal flotation. *Proceedings of MINExpo International*, *88*.

Moys, M. H. (1978). A study of a plug-flow model for flotation froth behaviour. *International Journal of Mineral Processing*, *5*(1), 21-38.

Paakkinen, U., & Penttila, H. (1977). Open circuit in flotation. *Preprint of AIME Annual Meeting*, 77-B-67

Pan, L., & Yoon, R. H. (2016). Measurement of hydrophobic forces in thin liquid films of water between bubbles and xanthate-treated gold surfaces. Minerals Engineering, 98, 240-250.

Park, S., Huang, K., & Yoon, R. H. (2018). Predicting bubble coarsening in flotation froth: Effect of contact angle and particle size. *Minerals Engineering*, *127*, 256-264.

Shergold, H. L., & Stratton-Crawley, R. (1981). Extraction of titanium dioxide into oil from anionic surfactant solutions. *Colloids and Surfaces*, *3*(3), 253-265.

Singer, D. A., Berger, V. I., & Moring, B. C. (2005). Porphyry copper deposits of the world: database, map, and grade and tonnage models. US Geological Survey open-file report, 1060(9).

Sutherland, K. L. (1948). Physical chemistry of flotation. XI. Kinetics of the flotation process. *The Journal of Physical Chemistry*, *52*(2), 394-425.

Wark, I. W. (1984). Principles of Mineral Flotation: the Wark Symposium. Australasian Institute of Mining and Metallurgy.

Wills, B. A., & Finch, J. A. (2016). Mineral processing technology: An introduction to the practical aspects of ore treatment and mineral recovery. Butterworth Heinemann.

Yoon, R. H. (2005). *U.S. Patent No. 6,871,743*. Washington, DC: U.S. Patent and Trademark Office.

Yoon, R. H. (2016). *U.S. Patent No. 9,518,241*. Washington, DC: U.S. Patent and Trademark Office.

Yoon, R. H. (2018). *U.S. Patent No. 10,144,012*. Washington, DC: U.S. Patent and Trademark Office.

Yoon, R. H., & Mao, L. (1996). Application of extended DLVO theory, IV: derivation of flotation rate equation from first principles. *Journal of Colloid and Interface Science*, *181*(2), 613-626.

3.8 Appendix

Two Liquid Flotation (TLF)

Sivamohan (1990) reviewed various methods of recovering very fine particles in mineral processing in general, out of which surface-based methods, ii) magnetic and electrostatic methods, and iii) gravity concentration. Of these, the first group was considered the most promising, simply because surface property gains its importance with decreasing particle size (d_p) as d_p^{-2}, while gravity loses its importance as dp-3. In these regards, it is not surprising that flotation has been used in the minerals industry as the primary method of separating fine particles.

In flotation, a particle collides with an air bubble, causing the latter to deform, which in turn creates a capillary pressure (p) in the wetting film of water, formed between the two macroscopic surfaces. Since $p > 0$, the water in the film drains, and the film thins. If the film thins to $h < 250$ nm, the film thinning begins to be controlled by the disjoining pressure (Π), which is created by the surface forces, e.g., electrical double-layer (EDL), van der Waals (vdW), and hydrophobic (HP) forces. In flotation, both the EDL and vdW forces are repulsive (Pan and Yoon, 2016; Huang and Yoon, 2019). Thus, flotation will occur when the attractive HP force becomes stronger than the sum of the EDL and vdW forces.

That the vdW force is repulsive for bubble-particle interactions is a major disadvantage of flotation, in which air bubbles are used to selectively collect hydrophobic particles. If oil drops rather than air bubbles are used for the same purpose, the vdW force becomes attractive (Huang and Yoon, 2019). Therefore, it takes much less energy for oil drops to attach themselves to hydrophobic surfaces and form larger contact angles. For example, an oil drop (n-dodecane) forms a contact angle of 171° with a thiol-coated gold surface, while an air bubble forms a contact angle of 91°. As is well known, the higher the contact angle, the higher the flotation recovery. Therefore, oil drops are superior collectors for hydrophobic particles. Also, the higher the contact angle, the stronger the hydrophobic forces (Yoon and Ravishankar, 1996; Huang and Yoon, 2019). Therefore, the kinetics of flotation is much faster with oil drops than with air bubbles.

The possibility of collecting fine particles from the aqueous phase using oil drops rather than air bubbles was explored in the 1960s by Lai and Fuerstenau (1968). They used iso-octane to recover 0.1 μm alumina (Al2O3) particles using alkyl sulfonate as a hydrophobizing agent for the colloidal particles. In this process, also known as the two-liquid flotation (TLF) process, hydrophobic particles are collected as oil-in-water (o/w) emulsion droplets, with the particles acting as a solid emulsifier. Thus, the process has no lower particle size limit in fine particles' recovery. One of the authors further developed the process by developing a method of removing entrained water and hydrophilic impurities to produce high-grade concentrates with very low surface moisture (Yoon, 2016).

In the TLF process, a recyclable oil is added to an ore slurry to allow small oil droplets to selectively collect hydrophobic particles and form o/w emulsion drops, while hydrophilic gangue minerals are rejected. The o/w emulsion droplets (or agglomerates) move to a specially designed device known as a Morganizer, in which additional oil may be added to induce phase inversion and form water-in-oil (w/o) emulsion drops. The w/o emulsion is then destabilized by applying a gentle mechanical force so that hydrophobic particles are dispersed in the oil phase and thereby liberate the water droplets into the oil phase. The water droplets liberated in this manner coalesce with each other and form larger drops, settle to the bottom, and are discharged. When the water droplets are removed in this manner, hydrophilic gangue mineral particles dispersed in them are also removed, which is the basis for eliminating entrained hydrophilic particles. The hydrophobic particles dispersed in the oil phase are then separated from the organic phase by solid-liquid separation and subsequently removed by steam stripping. It has been shown that practically all of the spent oil can be removed and recycled.

Chapter 4. Maximizing the Recovery and Throughput of a Rougher Flotation Bank by Improving the Recovery of Composite Particles

(Gupta, M., & Yoon, R. H., 2024. *Minerals Engineering*, *207*, 108545.)

4.1 Abstract

With decreasing ore grades, the cost of mineral processing has been escalating due to the high costs associated with grinding larger volumes of ores for liberation. To minimize the embodied cost, mined ores are usually coarse ground for rougher flotation, in which much of the waste (or 'dead') rocks are removed before regrinding the rougher concentrate to obtain the final product. Thus, the feed to a rougher flotation bank frequently consists of coarse particles that are poorly liberated and, hence, are not hydrophobic enough to be collected by air bubbles in the pulp phase and survive the froth phase without being detached.

In the present work, we explored the possibility of improving the flotation of composite particles using Super Collectors that can increase the water contact angles (θ) of the copper-bearing mineral grains well above 90°. The efficacy of this approach has been tested in laboratory flotation tests, followed by a series of simulations using a flotation model. The model has been derived from first principles using the surface forces in wetting films as kinetic parameters. The major input to the simulator was the liberation matrix (m_{ij}) of a flotation feed and the various operating parameters. The simulations were carried out to obtain the grade *vs.* recovery curves for a low-grade (0.24 %Cu) porphyry copper ore feed with d_{80} = 288 µm. The simulations were carried out using a Super Collector that can increase θ of the chalcopyrite grains to 150°. The grade *vs*. recovery curves obtained from the simulation showed that the Super Collector can substantially increase the recovery of composite particles over the case of using potassium amyl xanthate (PAX) as a collector at approximately 40% shorter retention times. The simulation results also showed that Super Collectors help minimize bubble coarsening and hence contribute to improving the coarse particle recovery.

4.2 Introduction

Copper is one of the most widely used metals after iron and aluminum to support the growing economies around the world. It was initially used 10,000 years ago for making everything from coins to ornaments. Today, it is widely used for building construction (43%), electrical and electronic products (20%), transportation equipment (20%), consumer and general products (10%), and industrial machinery and equipment (7%). Its demand has been growing by 2.8% annually since 1960, which is slightly below the annual world GDP growth rate of 3.5%. However, it is anticipated that the demand will accelerate when electrical vehicles (EVs) displace internal combustion engine vehicles (ICEVs) and more electricity is generated from renewable resources such as offshore windmills and solar panels.

In 2022, the mining industry produced 22 million metric tonnes (Mt) of refined copper, most of which (>60%) was extracted from low-grade porphyry-type copper ores, with the rest extracted from ores of sedimentary origin. It does not appear that copper will run out in the foreseeable future. The world reserve, based on companies' reported data, is 890 million Mt, while a 2023 USGS report suggested 2.1 billion tons of identified copper resources plus 3.5 billion tons of yet-to-be-discovered resources. While the resource is sizeable, the average grade of the copper ores has been declining, causing the global net cash cost to increase. The major costs in the mining and processing of low-grade ores are due to embodied energy costs. It has also been shown that the embodied energies required for mining and mineral processing increase with declining ore grades, partly because lower-grade ores are often fine-grained and hence require finer grinding for liberation (Norgate and Jahanshai, 2006).

Flotation is the primary separation method used to produce copper concentrates for smelting. As is well known, however, flotation has two major limitations: i) narrow particle size range typically in the 20-150 μm range, and ii) poor selectivity below 20 μm (Wills and Finch, 2016). In a typical mineral processing plant, flotation and pumping each account for 10% of the total energy consumption, while grinding accounts for ~70% of the total (O'Connor, 2019).

For processing low-grade ores, the bulk of the energy is consumed for grinding gangue minerals. Therefore, mill operators have been searching for ways to remove the waste (or 'dead') rocks during the rougher-scavenger flotation stage so that they can reduce the volume of materials to be reground and thereby save energy. For this approach to work, it is necessary to extend the upper particle size limit of flotation, which is a challenge as coarse particles are readily detached from air bubbles in the pulp phase due to the turbulence created in mechanically agitated flotation cells. On the other hand, turbulence is essential for bubble generation and bubble-particle contact. One approach to minimizing turbulence is to use an external bubble generator and a fluidized bed for bubble-particle contact.

At present, three different flotation technologies are commercially available for coarse particle flotation. These include HydroFloat (Mankosa and Luttrell, 2002, US6,425,485), Nova Cell (Jameson, 2018, US10,040,075), and CoarseAIR (Crompton *et al*., 2023). All three technologies are designed to use fluidized beds for bubble-particle contacts to minimize turbulence. Air bubbles produced using external inline bubble generators are injected into the fluidized bed along with pressurized water. In effect, coarse particle flotation cells are gravity separators equipped with external bubble generators to decrease the effective specific gravity (SG) of target minerals, *e.g*., chalcopyrite, by attaching air bubbles. Of course, the target minerals must be hydrophobized *via* appropriate collector coating for bubble-particle interaction.

Clark *et al*. (2005) suggested that liberation of the copper-bearing minerals in the Escondida ore drops dramatically above 150 μm, which corresponds to the upper particle size limit of flotation. As particle size becomes larger, the area of the copper-bearing mineral grain(s) exposed to the particle surface would become smaller, causing a decrease in the work of adhesion (W_a) as follows (Yoon and Mao, 1996),

$$W_a = \gamma_{LV} \pi r_1^2 \left(1 - \cos\theta\right)^2 \qquad [4.1]$$

in which γ_{LV} is the surface tension at the liquid (water)/vapor interface, r_1 is the radius of the exposed grain, and θ is its water contact angle. One way to counter the detrimental effect of decreasing r_1 would be to increase the contact angle.

In the present work, the possibility of extending the upper particle size limit of flotation has been studied using a novel flotation collector that can increase the contact angles of sulfide minerals well beyond the range that can be attained using thiol-type collectors. The new reagent, which is referred to as Super Collector (SC), can increase the contact angles to 150°, has been tested for the flotation of a low-grade porphyry copper ore, and the results are compared with those obtained using potassium amyl xanthate (PAX) as collectors. The performance of the two different reagents has been compared in laboratory flotation tests and by computer simulation. The simulation has been made using a flotation model that can predict both the recovery and grades using a flotation model derived from first principles. The simulation results obtained for a rougher flotation bank showed that coarse particle recovery can be increased substantially using the Super Collector, which is an improved version of the flotation promoters disclosed previously (Yoon, US 6,799,682).

4.3 Flotation Model

4.3.1 Pulp Phase

Flotation begins in the pulp phase, in which air bubbles (*B*) collide with mineral particles (*P*) to form bubble-particle aggregates (*A*). The interaction may be represented as,

$$B + P \rightleftharpoons A \qquad [4.2]$$

in the same manner as the second-order chemical reactions. Some of the particles, *e.g.*, composite particles of low surface liberation, may be readily detached from bubbles in a turbulent flow field. In this regard, bubble-particle interactions may be viewed as a process consisting of forward and backward reactions. One can then determine the equilibrium constant (K) as follows,

$$K = \frac{[A]}{[B][P]} = \frac{k_+}{k_-} \qquad [4.3]$$

where [B], [P], and [A] are the concentrations of bubbles, particles, and bubble-particle aggregates, respectively. In flotation, the concentrations may be represented by number densities. The rate of flotation may then be written as,

$$\begin{aligned} \frac{dN_1}{dt} &= -k_p N_1 N_2 \\ &= -Z_{12} P \end{aligned} \qquad [4.4]$$

in which N_1 and N_2 are the number densities of particles and bubbles, respectively, Z_{12} is the collision frequency, P is the probability of flotation, and k_p is the rate constant. P is a product of three subprocesses, *i.e.*, $P = P_c P_a (1 - P_d)$, in which subscripts represent collision, attachment, and detachment.

Abrahamson (1975) derived an expression for the collision frequency assuming a Stokes number of infinity,

$$Z_{12} = 5 N_1 N_2 d_{12}^2 \sqrt{\left(\overline{u_1^2} + \overline{u_2^2}\right)} \qquad [4.5]$$

in which d_{12} is the collision diameter, and $\sqrt{\overline{u_1^2}}$ and $\sqrt{\overline{u_2^2}}$ are the RMS velocities of particles and bubbles, respectively. It is recognized that Eq. [4.5] overpredict for the bubble-particle collision occurring in a flotation cell. It may be reasonable, therefore, to correct Z_{12} using the collision probabilities (P_c) determined using an interceptional collision model,

$$P_c = \frac{3}{2}\left(\frac{d_1}{d_2}\right)^2 \left[1 + \frac{3}{16}\left(\frac{\mathrm{Re}}{1 + 0.249\,\mathrm{Re}^{0.56}}\right)\right] \qquad [4.6]$$

in which d_1 and d_2 are particle and bubble diameters, respectively, and Re is the Reynolds number (Weber and Paddock, 1983).

From Eqs. [4.4] and [4.5], one obtains,

$$k_p = \frac{Z_{12}^o}{N_1 N_2} P_a (1 - P_d) \qquad [4.7]$$

in which $Z_{12}^o = Z_{12} P_c$. Luttrell and Yoon (1992) suggested a model for P_a,

$$P_a = \exp\left(-\frac{E_1}{E_k}\right) \qquad [4.8]$$

in which E_1 is the energy barrier that can be determined from the surface forces in wetting films (Huang *et al*., 2022; Gupta, *et al*., 2022, 2023), and E_k can be determined from the radial velocity of the fluid at the critical rupture thickness (h_c) of the thin liquid film (TLF) (or wetting film) using the stream function of water around an air bubble.

Mao (1996) suggested a model for P_d,

$$P_d = \exp\left(-\frac{W_a + E_1}{E_k'}\right) \qquad [4.9]$$

In Eq. [4.9], W_a (=$\gamma_{LV}\pi R_1^2(1-cos\theta)^2$) is the work of adhesion for a particle of radius R_1 attaching to an infinitely large air bubble with a contact angle θ, and E_k' is the kinetic energy created from the turbulence in a flotation cell.

Substituting Eqs. [4.8]-[4.9] into Eq. [4.7], one obtains,

$$k_p = \frac{Z_{12}^o}{N_1 N_2}\exp\left(-\frac{E_1}{E_k}\right)\left(1-\exp\left(-\frac{W_a+E_1}{E_k^{'}}\right)\right) \quad [4.10]$$

which may be simplified by Taylor's expansion of the third term,

$$k_p = Z_{12}^* \frac{W_a}{E_k^{'}}\exp\left(-\frac{E_1}{E_k}\right) \quad [4.11]$$

in which $Z_{12}^* = Z_{12}^o / N_1 N_2$. Eq. [4.11] is of the same form as the Arrhenius equation, with the preexponential term representing the product of collision frequency and P_d, while the exponential term represents the fraction of particles with $E_k > E_1$. In coarse particle flotation, the W_a/E_k' ratio is small due to the low θ arising from low surface liberation. According to Eq. [4.11], there are two ways to address the problem associated with high P_d of coarse particles. One is to use a Super Collector that can increase θ and hence W_a, and the other is to decrease E_k' by reducing turbulence.

4.3.2 Froth Phase

The bubble-particle aggregates formed in the pulp phase rise by buoyancy to enter the froth phase, in which bubble size becomes larger *via* coalescence. The bubble coarsening entails a decrease in surface area, which in turn forces some of the less hydrophobic particles to drop off the bubble surface due to the decrease in 'parking' area. The consequence of a series of these events will be a higher-grade froth product, albeit at a lower froth phase recovery (R_f). This mechanism serves as a built-in froth-cleaning mechanism by which product grades are substantially increased.

Park *et al*. (2018) derived a model that can predict bubble coarsening in a froth phase,

$$\frac{d_{2,b}}{d_{2,t}} = \left[\exp\left(-\frac{0.46 n_f h_f}{J_g t_c}\right)\right]^{0.5} \quad [4.12]$$

in which $d_{2,b}$ is the bubble size at the base of a froth phase and $d_{2,t}$ is the same at the top, n_f is the number of the 12 lamella faces of the bubbles formed at the base of a froth that ruptures during coalescence, h_f is the froth height, and t_c is the critical rupture time of a lamella film. Both n_f and t_c vary with particle size (d_1), particle hydrophobicity (θ), and the hydrophobic force in lamella films. It has been shown that bubbles become larger, that is, the $d_{2,t}/d_{2,b}$ ratio increases with increasing particle size due to the decrease in the local capillary pressure in the menisci of the water formed in the vicinity of particles and due to the decrease in particle loading in lamella films.

Gorain *et al*. (1998) showed that R_f decreases exponentially with bubble residence time in a froth phase. Eq. [4.12] suggests, on the other hand, that the maximum froth phase recovery cannot exceed the $d_{2,b}/d_{2,t}$ ratio, which led to a froth phase recovery model (Park *et al*., 2018) as follows,

$$R_f = \frac{d_{2,b}}{d_{2,t}}\exp(-\alpha\tau) \quad [4.13]$$

in which τ is the retention time of air bubbles in a froth phase, and α is the rate constant for particles dropping off the bubble surface. In general, coarse particles drop off more easily due to the low local capillary pressure, low particle loading, and low particle contact angles. Coarse particles can have low contact angles due to incomplete liberation. Therefore, their particle loading is low, which in turn gives rise to an unstable froth.

Based on the pulp phase (R_p) and froth phase (R_f) recoveries as discussed above, one can determine the overall flotation recovery using the following relation,

$$R = \frac{R_p R_f}{R_p R_f + 1 - R_p} \qquad [4.14]$$

4.4 Simulation

In the present work, we used the flotation model developed by Huang *et al*. (2022) to simulate the improvement in the recovery of composite particles by increasing the particle contact angles (θ). Simulations were carried out on a copper rougher flotation bank, in which a low-grade porphyry copper ore was processed with the objective of improving flotation using a Super Collector. The flotation circuit consists of four parallel banks each consisting of five mechanically agitated flotation cells with a volume of 127.4 m^3 each. The throughput to a rougher bank was 1,455 tph. The feed was a blend of the fresh feed (0.24%Cu) from the grinding circuit and cleaner scavenger tails (CST) as the circulating load. The fresh feed consisted of chalcopyrite (0.72%) as the major copper-bearing mineral and silicious gangue minerals. The simulations were conducted using the operating data collected during a plant survey, which included specific power of flotation cells, superficial gas rate, air holdup, froth height, *etc*.

The mineral liberation data was provided by the company in the form of 5x5 size-by-class copper distribution matrix, from which a mass distribution matrix was constructed as described by Gupta *et al*. (2022). The matrix consisted of five different liberation classes, *i.e*., 0-10, 10-30, 30-50, 50-100 and 100%. *Figure* 4-1 shows a 3D plot of the size-by-class mass distribution (m_{ij}) matrix of the feed with d_{80} = 288 µm. The mass distribution of the 0-10% liberation class is not shown, as the numbers were much larger than those of the other classes due to the low-grade nature of the feed material. As shown, the feed consisted of a large fraction of composite particles, especially at d_i > 150 µm.

A major difficulty associated with the flotation of low-grade ores is the recovery of coarse particles. As shown in the liberation matrix, the degree of liberation (which we call surface liberation here) decreases with increasing particle size. Since the area of the copper minerals exposed on the surface decreases with decreasing liberation, the contact angles of the particle would decrease with increasing particle size, making it difficult to float them. Clark *et al.* (2005) reported that the liberation of chalcopyrite in the Escondida ore drops precipitously at particle sizes above 150 µm, and so does the flotation recovery. One way to extend the upper particle size limit would be to use a stronger collector that can increase the contact angle at a given surface liberation. In the present work, a proprietary collector, named Super Collector (SC), has been tested, with the results compared with a common collector, potassium amyl xanthate (PAX).

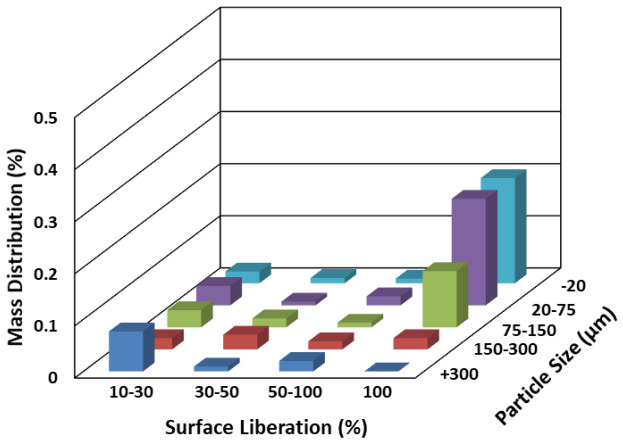

Figure 4-1. A 3D plot of the size-by-class mass distribution matrix (m_{ij}) for the rougher feed (Gupta *et al*., 2022).

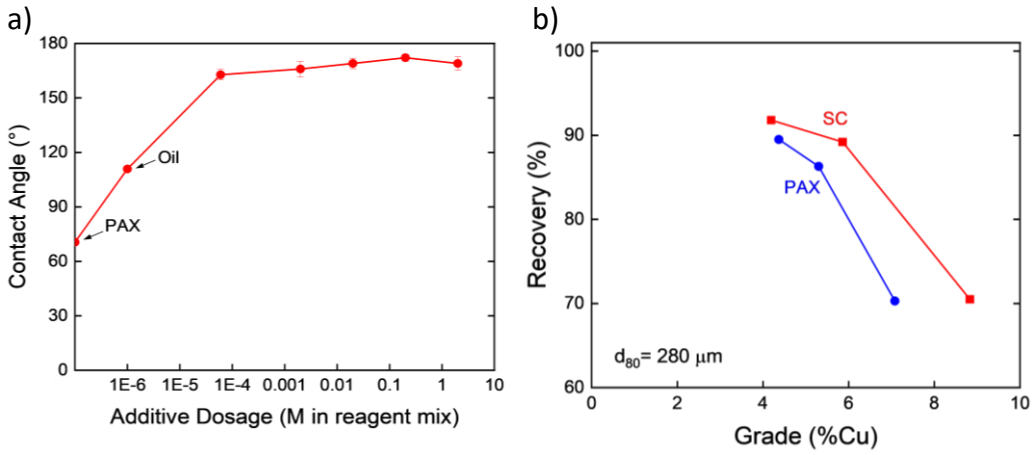

Figure 4-2. (a) Effect of Super Collectors (SC) on the contact angles measured on the polished surfaces of chalcopyrite; (b) Recovery *vs*. grade curves obtained for the laboratory flotation tests conducted using PAX and SC as collectors.

In the present work, a series of contact angle measurements were conducted on a pure chalcopyrite specimen that had been polished using the captive bubble method, and the results are compared in *Figure* 4-2. As shown, the PAX-coated surface exhibited a contact angle of 69.6° at $3x10^{-4}$ M xanthate. The angle increased to 112° in the presence of an extender (diesel). The contact angles measured using different amounts of the Super Collector were in the range of 160 to 170° as shown in *Figure* 4-2a.

The efficacy of using a SC was tested in lab-scale flotation tests on a low-grade porphyry copper ore sample assaying ~0.3%Cu. The tests were conducted in a 2-L Denver laboratory flotation cell using PAX at $3x10^{-4}$ M as a primary collector and MIBC as a frother. The ore sample was ground in a lab-scale rod mill for 10 minutes to obtain a flotation feed with d_{80} = 280 µm. Flotation tests were run at 35 %solids for 5 min, while collecting froth products sequentially at 1, 3, and 5 min. The tests were conducted with and without using SC as an additional collector while keeping the PAX dosage constant. As shown in *Figure* 4-2b, the cumulative recovery after the 5-min flotation time was increased from 88.5 to 91.8%, representing a 3.3% increase in copper recovery at a slightly lower copper grade. The use of SC decreased the tailings grade from 0.039 %Cu to 0.029 %Cu. These improvements may be attributed to the increase in the recovery of the +300 µm composite particles, which accounted for 12.4% by weight of the feed, from 54.3% to 61.8%. This improvement may be attributed to the increase in the contact angles of the composite particles.

Having seen the advantages of using SC in a flotation test, as shown in *Figure* 4-2, we decided to simulate the performance of a copper flotation bank using SC and PAX and compared the results. We used the Cassie-Baxter equation to estimate the contact angles of composite particles as follows,

$$\cos\bar{\theta}_j = a_1 b_1 \cos\theta_1 + a_2 b_2 \cos\theta_2 \qquad [4.15]$$

Table 4-1. Contact angles of composite particles as obtained using PAX and SC as collectors

Contact Angles of Composite Particles (°)				
θ_1	Surface Liberation (%)			
(°)	0-10	10-30	30-50	50-100
70	15.6	31.3	44.8	92.9
150	23.8	48.6	71.2	105.7

where a_1 and a_2 are the surface liberation, given as surface are fractions, θ_1 and θ_2 are contact angles, and b_1 and b_2 are correction factors for chalcopyrite and quartz, respectively. We assumed that b_1 = 0.8, and b_2 = 1.0 to account for the stereographic bias associated with obtaining 3D information from 2D measurements as in liberation analysis. Composite particles can appear as free particles in a 2D measurement, while fully liberated particles always appear as free particles. A value of b_1 = 0.8 means that we are discounting the population of the fully-liberated particles by 20%. For quartz, we assumed that b_2 = 1.0 because most of the gangue minerals in a low-grade ore should appear as free particles.

Under the boundary conditions discussed above, the contact angles of the four different liberation classes ($\overline{\theta}_j$) have been estimated using Eq. [4.15], with the results presented in *Table* 4-1. It was assumed that pure chalcopyrite has θ_1 = 70° when using PAX and θ_1 = 150° when using SC as collectors, while pure quartz would have θ_2 = 2°. The contact angles given in the table were then used to simulate the laboratory flotation test results as a validation of the boundary conditions used for determining the contact angles. Excellent agreements were observed between the predicted and experimental results (not shown in this communication). Based on the encouraging results, the performance of the full-scale rougher flotation bank using PAX and a SC has been predicted using the simulator.

4.5 Results and Discussion

For bubble-particle attachment to occur, the intervening water film, also known as wetting film, should rupture and form a finite contact angle. The rate of film thinning is initially driven by the changes in the local capillary pressure (p_c), which varies with the local curvature of an air bubble. For coarse particles, the inertial forces should also play a role. Once the film thins to ~250 nm, the kinetics of film thinning is controlled by surface forces that create pressure in the wetting film known as disjoining pressure (Π). Bubble-particle attachment should occur when $\Pi \leq 0$. In flotation, the disjoining pressure can be determined using the extended DLVO theory,

$$\Pi(h) = -\frac{A_{132}}{6\pi h^3} - \frac{\varepsilon\varepsilon_0\kappa^2}{2\sinh(\kappa h)}\left[\left(\psi_1^2 + \psi_2^2\right)\text{cosech}(\kappa h) - 2\psi_1\psi_2\coth(\kappa h)\right] - \frac{K_{132}}{6\pi h^3} \qquad [4.16]$$

in which the first term represents the contribution from the van der Waals (vdW) force, which is repulsive, the second term represents the electrical double-layer (EDL) force, and the third term represents the contribution from the hydrophobic (HP) force, which is always attractive and hence serves as a driving force for film rupture (Yoon and Mao, 1996). In Eq. [4.16], A_{132} is the Hamaker constant, ε the permittivity of vacuum, ε_0 the dielectric constant of water, κ^{-1} is the reciprocal Debye length, and ψ_1 and ψ_2 are the surface (or ζ-) potentials of the particles and bubbles, respectively, and K_{132} is the hydrophobic force.

Flotation is a hydrophobic interaction between two hydrophobic entities, *i.e.*, air bubbles and hydrophobic mineral particles. The asymmetric hydrophobic interaction between mineral **1** and air bubble **2** can be determined if the hydrophobic force constant K_{132} can be predicted using the geometric mean combining rule (Yoon *et al.*, 1997),

$$K_{132} = \sqrt{K_{131}K_{232}} \qquad [4.17]$$

where K_{131} is the hydrophobic force constant between two similar surfaces **1** in water **3** and K_{232} is the hydrophobic force constant between two air bubbles **2** in water. It has been shown that K_{131} varies with contact angle (θ) (Pazhianur and Yoon, 2003), while K_{232} varies with frother and electrolyte concentration (Wang and Yoon, 2012). Eq. [4.17] suggests therefore that one can increase the hydrophobic interaction between bubbles and particles or flotation by increasing θ.

Table 4-2. Comparison of E_1 (10^{-17}J) for different size-by-class particles conditioned with PAX and SC

d_1	10-30%		30-50%	
(μm)	PAX	SC	PAX	SC
387.3	23.0	19.2	20.2	13.3
212.1	15.3	12.8	13.4	8.8
106.1	8.8	7.3	7.68	5.0
38.7	3.6	3.0	3.1	2.0
10.0	1.1	0.8	0.8	0.6

That the vdW and EDL forces are repulsive in wetting film results in the formation of an energy barrier E_1 to be overcome for bubble-particle attachment. It has been shown that E_1 is reduced with an increasing hydrophobic force. Huang *et al*. (2022) determined E_1 from a free energy isotherm (G(h)), which in turn can be determined from the disjoining pressure isotherm ($\Pi(h)$) using the Frumkin-Derjaguin isotherm (Frumkin, 1938; Derjaguin, 1940) and the Derjaguin approximation (1934) as follows,

$$G(h) = \frac{1}{2\pi}\left(\frac{R_1 + R_2}{R_1 R_2}\right)\int_{r=0}^{r=\infty} \Pi(h) 2\pi r dr = \gamma_{LV}\left(\cos\theta - 1\right) \quad [4.18]$$

in which R_1 and R_2 are the particle and bubble radii, respectively, and γ_{LV} is the water surface tension. From Eq. [4.18], one can derive the following relation that can be used to determine the energy barriers (E_1) for bubble-particle interactions,

$$E_1 = \int_{r=0}^{r=\infty} G(h)\big|_{\Pi=0}\, 2\pi r dr \quad [4.19]$$

Table 4-2 shows the values of E_1 calculated for the composite particles in the rougher flotation feed. As can be seen from Eq. [4.18] and [4.19], E_1 represents the Gibbs free energy of the wetting film at the critical thickness (h_c) at which the film ruptures, *i.e*., $\Pi = 0$ (Huang *et al*., 2022). As shown by Eq. [4.16], E_1 is determined by the surface forces in the film, which include the vdW, EDL, and HP forces. The first two are repulsive in flotation; therefore, it is necessary to create the hydrophobic force to create a condition that $\Pi \leq 0$. As is well known, the hydrophobic force increases with water contact angle (Yoon and Ravishankar, 1996; Huang, *et al*., 2022). In the present work, we used the Supper Collector to increase the contact angles of the composite particles ($\overline{\theta}_j$) and calculate E_1. We calculated $\overline{\theta}_j$ using the Cassie-Baxter equation (Eq. [4.15]) from the liberation data and the hydrophobic force constant (K_{131}) for particle-particle interactions as described by Huang et al., 2022). Other force parameters used to determine the $\Pi(h)$ isotherm using Eq. [4.16] included: A_{132} = -4x10^{-20} J, ψ_1 =-30 mV, ψ_2 =-20 mV, κ^{-1} = 96 nm, and K_{232} = 4.07x10^{-18} J.

Note in *Table* 4-2 that E_1 increased with decreasing surface liberation and with increasing particle size, both suggesting that the major difficulty associated with coarse particle flotation may be the decreasing surface liberation and the corresponding decrease in $\overline{\theta}_j$. An obvious solution to this problem may then be to find a stronger collector that can increase the contact angles beyond the level that can be achieved using conventional collectors. As *Table* 4-2 shows, the values of E_1 obtained using the Super Collector were substantially lower than those obtained using PAX.

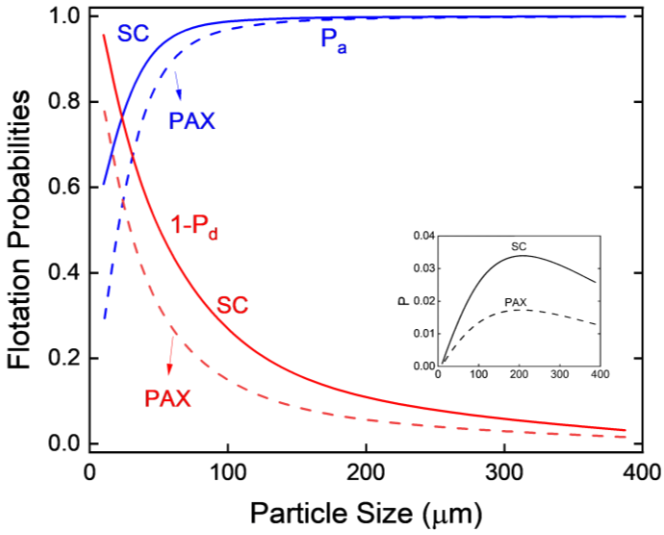

Figure 4-3. The probabilities of bubble-particle attachment (P_a) (blue) and of not being detached (1-P_d) (red) for the fully liberated particles with PAX (dashed line) and SC (solid line) in the first rougher cells. The inset shows the changes in the size-by-size flotation probabilities (P) with SC and PAX. using PAX and SC as collectors.

According to Eq. [4.8], the probability of bubble-particle attachment (P_a) is simply an exponential function of the fraction of mineral particles whose kinetic energies (E_k) are larger than E_1 at h_c. Figure 4-3 shows the changes in P_a as a function of particle size. The calculations were made for fully liberated chalcopyrite particles for simplicity. A set of two calculations was made, one for the case of using a Super Collector and PAX to obtain $\theta = 150^o$ and 70^o, respectively, to calculate P_a using Eq. [4.8]. The results plotted in Figure 4-3 show that P_a increases with particle size owing to the increase in E_k with increasing particle size and that P_a decreases below the particle size of ~150 μm. The latter observation may be attributed to the decrease in E_k. It would, therefore, be able to increase P_a and improve fine particle recovery by decreasing E_1 using a Super Collector, as shown in Figure 4-3. Still another method of improving fine particle flotation would be to increase E_k. The Concorde flotation cell developed by METSO is designed to

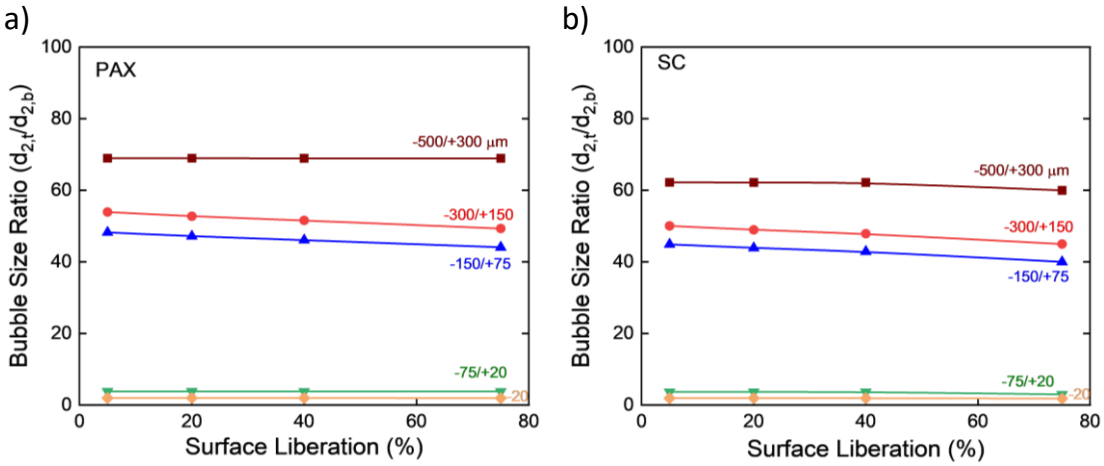

Figure 4-4. Effects of surface liberation and particle size on bubble coarsening for the cases of using (a) PAX and (b) SC as collectors.

improve fine particle recovery by subjecting the aerated slurry to very high shear agitation at supersonic velocities (Jameson, 2010).

Also shown in *Figure* 4-3 are the values of (1-P_d), which represent the probability of not being detached in the pulp phase. The W_a/E'_k ratio of Eq. [4.11], which effectively represents the probability of detachment (P_d), suggests that (1-P_d) can be increased by increasing θ using a stronger collector and, hence, increasing W_a. *Figure* 4-3 shows that the survival probabilities decrease substantially with increasing particle size for both the cases of using the Super Collector and PAX. Nevertheless, the former gives the higher probability of survival.

The two curves given at the inset show the probabilities of flotation, *i.e.*, $P = P_a(1\text{-}P_d)$, which represent the combined effects of controlling P_a and P_d using SC and PAX. Both probabilities should increase by increasing θ. As shown, P reaches a maximum as the particle size reaches ~200 μm due to the increase in P_a. As the particle size becomes larger, P begins to decrease with the continuing increase in E_k. In both cases, Super Collector was more beneficial than PAX. In short, a stronger collector helps improve the recovery of both the fine and coarse particles.

Figures 4-4a and 4-4b show the bubble size ratio ($d_{2,t}/d_{2,b}$) in the first rougher cell in the presence of i) PAX and ii) Super Collector. In general, the bubble size ratio (a measure of bubble coarsening) increases with increasing particle size, which can be attributed to the decrease in the number density of the particles at the bubble surface with increasing particle size. Coarser particles are less hydrophobic due to incomplete liberation; therefore, they are more readily detached from bubbles, causing the bubble size ratio to increase. This observation may be supported by the fact that the bubble size ratio at a given particle size decreases slightly with increasing surface liberation. An important message from the data presented in *Figure* 4-4 is that the extent of bubble size increases is in the range of approximately 2 to 70. Recognizing that the amounts of the particles that can be transported through the froth phase depend on the bubble surface area rather than the bubble size, the large $d_{2,t}/d_{2,b}$ ratios shown in *Figure* 4-4 suggest very low froth phase recoveries, particularly for coarse particles.

The bubble coarsening model represented by Eq. [4.12] was derived on the premise that two air bubbles neighboring each other in a froth phase coalesce due to the breakage of the free films, *i.e.*, the part of a lamella film that is not occupied by particles. The authors and many other investigators found out, however,

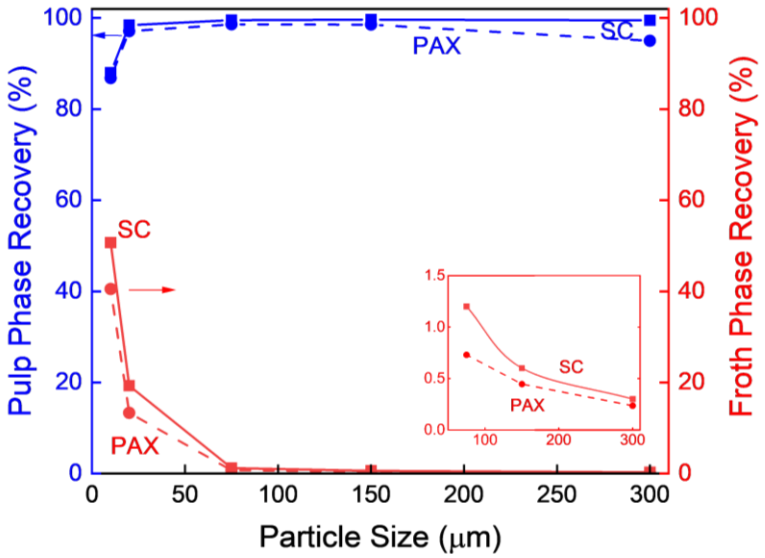

Figure 4-5. Size-by-size recoveries in the pulp (blue) and froth (red) phases of a flotation cell for the cases of using PAX and SC in the first cell of a rougher bank. The inset shows the changes in froth phase recovery at an expanded scale.

that froth stability reaches maxima at θ ~70°, which indicated that lamella films rupture at the solid/liquid interface by dewetting (Garrett, 1993; Pugh, 1996; Ata, 2012). However, the simulation results obtained in the present work did not show bubble coarsening at $\overline{\theta}_j$ > 70°. The apparent discrepancy may be attributed to the fact that the simulation did not consider the rupture mechanism by dewetting. It should be noted here that the laboratory flotation tests conducted on a sample taken from the rougher feed did not exhibit froth instability at $\overline{\theta}_j$ > 70°, which is encouraging for using a stronger collector to improve coarse particle recovery. A possible explanation may be that the composite particles may work as Janus particles that are purposely used to stabilize Pickering emulsions. Binks (2002) noted that colloidal particles consisting of both the hydrophobic and hydrophilic surfaces can act as solid surfactants and can stabilize the fluid-fluid interface (including the air-water interface).

Figure 4-5 shows the size-by-size recoveries in the pulp and froth phases in the first rougher flotation cell. The pulp phase rate constants (k_p) were calculated using Eq. [4.7], while that of the froth-phase recovery process (R_f) was determined using Eq. [4.13]. The froth phase recoveries include those due to bubble-particle attachment and entrainment in the same manner as done previously (Huang *et al.*, 2022; Gupta *et al.*, 2022,2023). As shown, the pulp phase recoveries decrease at particle sizes above 150 µm although the decrease is not substantial. This finding appears contrary to the general perception that coarse particle recovery is difficult due to the turbulence in the pulp phase. Many investigators addressed this problem by finding ways to reduce the turbulence. One way to minimize the turbulence was to use fluidized bed reactors to induce bubble-particle collision and attachment (Mankosa and Luttrell, 2002; Jameson, 2010; Sutherland *et al*., 2020).

What appears rather surprising is that the froth phase recoveries are very low, particularly at particle sizes >150 µm as shown in *Figure* 4-5. This finding is similar to the froth phase recoveries directly measured by Seaman *et al.* (2006). As discussed above, coarse particles readily drop off the bubble surface due to the decrease in the parking area associated with bubble coarsening. The results presented in *Figure* 4-5 show that the froth phase recovery can be increased considerably by using the Super Collector. The recoveries of the -500+300 µm and 150-300 µm fractions were increased from 0.23% to 0.3% and 0.4% to 0.6%, respectively.

Figures 4-6a and 4-6b show the impacts of using the Super Collector on the bank recoveries of the size classes of coarse particles. The simulations were carried out using two different collectors, *i.e.*, PAX and SC, that can render the chalcopyrite grains in composite particles selectively hydrophobic with θ = 70° and

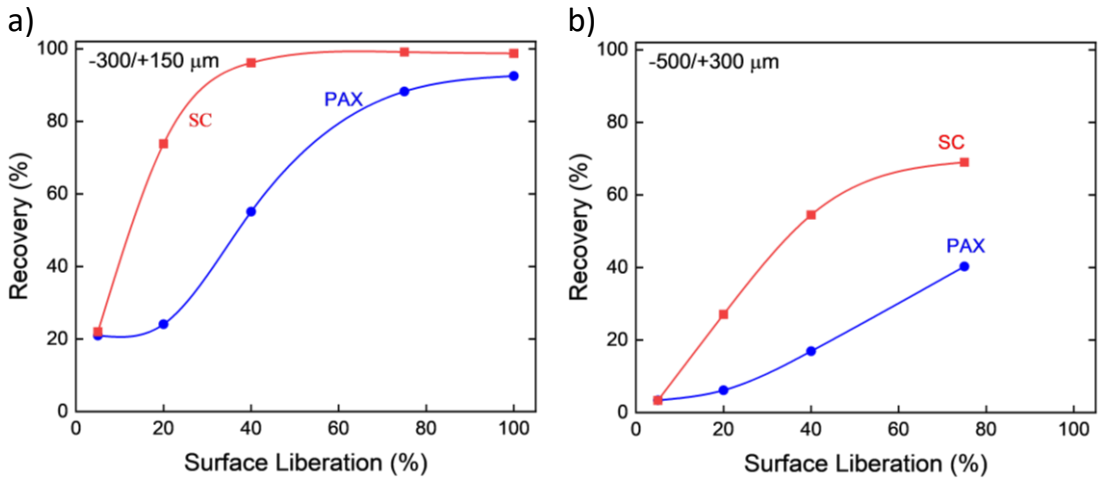

Figure 4-6. Comparison of the size-by-class recoveries obtained for the a) 150-300 µm and b) 300-500 µm size fractions using PAX (blue) and SC (red) as collectors.

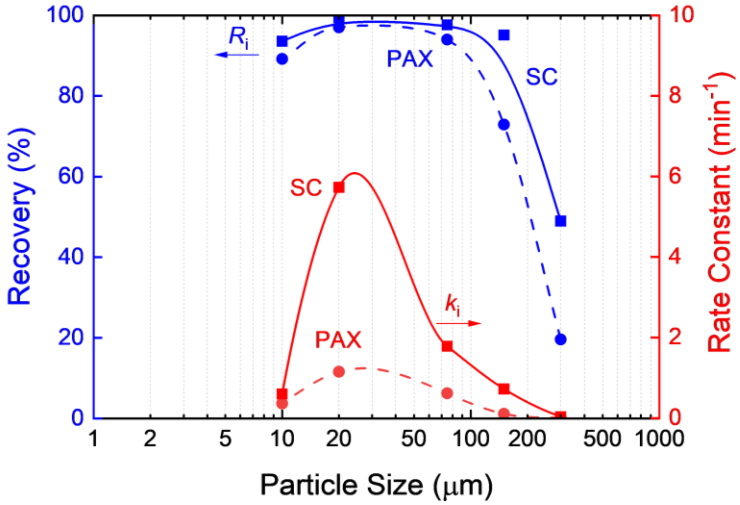

Figure 4-7. Size-by-size bank recoveries (blue) and flotation rate constants (red) as obtained using PAX and SC as collectors.

150°, respectively. As shown, the recoveries of the -300+150 µm fraction were increased by 10-30% by switching the collector from PAX to SC, while those of the -500+300 µm fraction were increased by 30-50%. The greatest impact of using SC was observed at the mid-ranges of surface liberations. The improved pulp phase recoveries observed in the presence of Super Collectors may also be due to the formation of bubble clusters. Ata and Jameson (2005) showed that an increase in θ increased the fraction of air bubbles forming clusters, which should help levitate coarse particles and increase the pulp phase recoveries.

Figure 4-7 shows the size-by-size recoveries obtained by simulation using the m_{ij} matrix constructed from the liberation data presented in *Figure* 4-1. Cell-by-cell simulations were carried out without assuming that each cell has the same recovery for mathematical convenience. The size-by-class recoveries obtained for each cell were used to obtain the cumulative recoveries (R_{ij}) and grades of the concentrate (C_{ij}) and tails (T_{ij}). The bank recoveries were then determined using the following relation,

$$R_{ij} = 1 - \frac{T_{ij}}{F_{ij}} \qquad [4.20]$$

in which F_{ij} is the mass flow rates of different sizes (i) and classes (j) in the feed stream.

The data presented in *Figure* 4-7 show the size-by-size recoveries obtained using PAX and SC as collectors. Note that the use of the stronger collector (SC) shifted the size-by-size recovery curves such that the recoveries of both the coarse and fine particles were improved significantly. Also shown in *Figure* 4-7 are the size-by-size flotation rate constants (k_i) for using PAX and SC. One might wonder why the recovery improvements are not as substantial as observed with the changes in k_i. An answer is that the k_{ij} improvement was manifested in a substantial decrease in retention time requirement to obtain the recoveries shown in *Figure* 4-7. When recoveries are close to maxima, it would be difficult to see the benefits in recovery. Nevertheless, the use of SC increased the recovery from 87.1% at a final concentrate grade of 2.5%Cu to 92.54% at 2.7 %Cu. These improvements were obtained in just 3 flotation cells (382.3 m^3) rather than in 5 cells (637.1 m^3). By virtue of the increased k_{ij}, one can reduce the retention time by 40% or increase the throughput from 1,455 tph to 2,425 tph.

From the bank simulation data presented in *Figure* 4-7, a set of two recovery *vs.* grade curves have been constructed in *Figure* 4-8: one for the case of using PAX as a collector and the other for the case of using Super Collector. The recovery *vs.* grade curves obtained at the higher-grade range appear to be about the same, suggesting that the two different collectors can recover the copper-bearing particles with higher

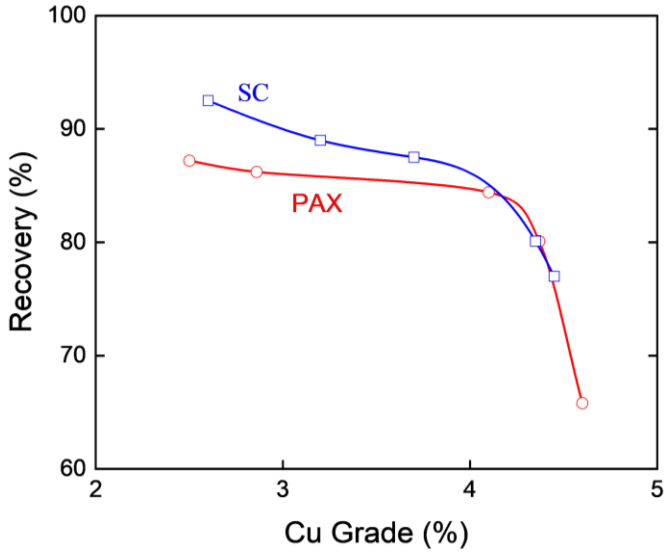

Figure 4-8. Cumulative recovery vs. grade curves of a rougher flotation bank using PAX (red) and SC (blue) as collectors. The use of SC improved the recovery of composite particles in Cells No. 3, 4, and 5.

degrees of surface liberation. The results show also that both collectors can recover composite particles at the expense of significant product grades. On the other hand, the Super Collector gave considerably higher recoveries at a given copper grade. Furthermore, the recovery improvement becomes more significant with decreasing product grade, suggesting that the Super Collector can recover coarser particles with lower surface liberation.

The major difficulty in coarse particle flotation is detachment, which means that the reverse of Reaction [4.2] is faster than that of the forward reaction. Eq. [4.11], which effectively embodies both the forward and backward reactions, may be rewritten as

$$k_p = Z_{12}^{*} \exp\left(-\frac{(E_1 + E_h) - W_a}{E_k^{'}}\right) \qquad [4.21]$$

in which (E_1 + E_h) and W_a represent the energy barriers for the forward and backward reactions of Eq. [4.2]. In Eq. [4.21], E_h represents the hydrodynamic resistance to film thinning during bubble-particle interaction. It can be calculated using Reynold's equation and/or measured directly using the force apparatus for deformable surfaces (FADS) (Pan and Yoon, 2016).

For coarse particles, $E_1 << W_a$ and E_h is negligibly small as compared to the inertia of particles, in which case k_p will be dominated by the work of adhesion. In this regard, the approach taken in the present work, *i.e.*, increasing θ using a Super Collector is justified, as has been demonstrated in both the laboratory scale experiments and in plant simulations. Eq. [4.21] also suggests that at a given θ or W_a, E_k' should be minimized to maximize k_p. A problem with this approach is that we would need high kinetic energies to produce small air bubbles and for efficient bubble-particle contacts. To get around this problem, most coarse particle flotation machines use a combination of an external bubble generator and a fluidized bed contactor. Effectively, they are gravity separators designed to modify the effective SGs of target minerals. For ultrafine particles, E_h may be the major energy barrier for bubble-particle attachment due to their low inertia. The Concorde flotation cell developed by Jameson (2010) has been designed to increase E_k', which can overcome the energy barrier (E_1+E_h) by employing very high-shear agitation.

The size-by-size recoveries obtained for the first flotation cell in the rougher bank show that most of the coarse particles are lost in the froth phase rather than in the pulp phase, as shown in *Figure* 4-5 and reported by Seaman *et al.* (2006). This observation is consistent with the bubble-coarsening data presented

in *Figure* 4-5. Coarse particles destabilize froth, as has been discussed. It has also been shown that Super Collectors can reduce bubble coarsening to some extent and thereby improve coarse particle recovery. If one can develop a way to minimize bubble coarsening, it may be useful to improve coarse particle recovery in a conventional flotation cell.

4.6 Summary and Conclusion

Declining ore grades force mineral processing plants to grind large volumes of mined ores to liberate target minerals for liberation while energy prices are increasing rapidly. One way to address this problem is to obtain preconcentrates at coarse grinds to minimize the volume of the materials to be reground to improve the liberation and obtain higher-grade products. However, coarse particles are difficult to recover by flotation as they are mostly composite particles that are difficult to become hydrophobic using conventional collectors. We addressed this problem by using Super Collectors that can increase the contact angles of the target minerals to 150^{o} to 170^{o}. This approach worked well, as demonstrated in both the laboratory and plant simulations. The results show that Super Collectors can increase the recovery of composite particles significantly at substantially lower retention times. The results obtained in the present work can be substantiated by the mathematical analyses involving the work of adhesion and bubble coarsening. The results of the theoretical analyses suggest ways to further improve coarse particle recovery in the future.

4.7 References

Abrahamson, J. (1975). Collision rates of small particles in a vigorously turbulent fluid. *Chemical Engineering Science*, *30*(11), 1371-1379.

Ata, S. and Jameson, G.A. The Formation of bubble clusters in flotation cells. *Int. J. Miner. Process. 76 (2005) 123-139*.

Ata, S. (2012). Phenomena in the froth phase of flotation—A review. *International Journal of Mineral Processing*, 102, 1-12.

Binks, B. P. (2002). Particles as surfactants—similarities and differences. *Current opinion in colloid & interface science*, 7(1-2), 21-41.

Clark, M. E., Brake, I., Huls, B. J., Smith, B. E., & Yu, M. (2005). Creating value through application of flotation science and technology. *In: Centenary of Flotation Symposium*, 6-9 June, Brisbane, QLD.

Crompton, L. J., Islam, M. T., & Galvin, K. P. (2023). Assessment of the partitioning of coarse hydrophobic particles in the product concentrate of the CoarseAIR™ flotation system using a novel mechanical cell reference method. *Minerals Engineering*, 198, 108088.

Derjaguin, B. V. (1934). Friction and adhesion. IV. The theory of adhesion of small particles. *Kolloid Zeits*, 69, 155-164.

Derjaguin, B. V. (1940). Theory of the capillary condensation and other capillary phenomena taking into account the disjoining effect of long-chain molecular liquid films. *Zh. Fiz. Khim*, 14, 137.

Frumkin, A. N., & Gorodetzkaya, A. (1938). On the phenomena of wetting and the adhesion of bubbles. II. The mechanism of the adhesion of bubbles to a mercury surface. *Acta Physicochim.* URSS, 9, 327.

Garrett, P. R. (1993). Recent developments in the understanding of foam generation and stability. *Chemical engineering science*, 48(2), 367-392.

Gorain, B. K., Harris, M. C., Franzidis, J. P., & Manlapig, E. V. (1998). The effect of froth residence time on the kinetics of flotation. *Minerals Engineering*, 11(7), 627-638.

Gupta, M., Huang, K., & Yoon, R. H. (2022). Predicting the recovery and grade of a rougher flotation circuit from liberation data. *Minerals Engineering*, 188, 107853.

Gupta, M., Huang, K., Noble, A., & Yoon, R. H. (2023). Improving the performance of a low-grade porphyry copper ore flotation plant using a simulator that can predict grade vs. recovery curves. *Minerals Engineering*, 202, 108243.

Huang, K., & Yoon, R. H. (2020). Control of bubble ζ-potentials to improve the kinetics of bubble-particle interactions. *Minerals Engineering*, 151, 106295.

Huang, K., Keles, S., Sherrell, I., Noble, A., & Yoon, R. H. (2022). Development of a flotation simulator that can predict grade vs. Recovery curves from mineral liberation data. *Minerals Engineering*, 181, 107510.

Jameson, G. J. (2010). Advances in fine and coarse particle flotation. *Canadian Metallurgical Quarterly*, 49(4), 325-330.

Jameson, G. J. (2018). *U.S. Patent No. 10,040,075*. Washington, DC: U.S. Patent and Trademark Office.

Luttrell, G. H., & Yoon, R. H. (1992). A hydrodynamic model for bubble—particle attachment. *Journal of Colloid and Interface Science*, 154(1), 129-137

Mankosa, M. J., & Luttrell, G. H. (2002). *U.S. Patent No. 6,425,485*. Washington, DC: U.S. Patent and Trademark Office.

Norgate, T., & Jahanshahi, S. (2006, November). Energy and greenhouse gas implications of deteriorating quality ore reserves. In 5th Australian conference on life cycle assessment: achieving business benefits from managing life cycle impacts.

O' Connor, C. (2019). Global Challenges Facing the Minerals Processing Industry. *In 2019 IMPC Eurasia Conference Proceedings*, 1-10.

Park, S., Huang, K., & Yoon, R. H. (2018). Predicting bubble coarsening in flotation froth: Effect of contact angle and particle size. *Minerals Engineering*, 127, 256-264.

Pazhianur, R., & Yoon, R. H. (2003). Model for the origin of hydrophobic force. *Mining, Metallurgy & Exploration*, 20(4), 178-184.

Pugh, R. J. (1996). Foaming, foam films, antifoaming and defoaming. *Advances in colloid and interface science*, 64, 67-142.

Seaman, D. R., Manlapig, E. V., & Franzidis, J. P. (2006). Selective transport of attached particles across the pulp–froth interface. *Minerals Engineering*, 19(6-8), 841-851.

Sutherland, J. L., Dickinson, J. E., & Galvin, K. P. (2020). Flotation of coarse coal particles in the Reflux™ Flotation Cell. *Minerals Engineering*, 149, 106224.

Weber, M. E., & Paddock, D. (1983). Interceptional and gravitational collision efficiencies for single collectors at intermediate Reynolds numbers. *Journal of Colloid and Interface Science*, 94(2), 328-335.

Wills, B. A., & Finch, J. A. (2016). Mineral processing technology: An introduction to the practical aspects of ore treatment and mineral recovery. Butterworth Heinemann.

Yoon, R.H., & Mao, L. (1996). Application of extended DLVO theory, IV: derivation of flotation rate equation from first principles. *Journal of Colloid and Interface Science*, 181(2), 613-626.

Yoon, R.-H., & Ravishankar, S. A. (1996). Long-range hydrophobic forces between mica surfaces in dodecylammonium chloride solutions in the presence of dodecanol. *Journal of colloid and* interface science, 179(2), 391-402.

Yoon, R.-H., Flinn, D. H., & Rabinovich, Y. I. (1997). Hydrophobic interactions between dissimilar surfaces. Journal of Colloid and Interface Science, 185(2), 363-370.

Yoon, R.-H., Method of increasing flotation rate, U.S. Patent No. 6,799,682, 2004.

Chapter 5. Simulation of Flotation Circuits Using a Model Derived from First Principles

(Submitted to a peer reviewed conference as, Gupta, M., Lim, H., Noble, A., & Yoon, R.H. XXXI International Mineral Processing Congress, Washington D.C., October, 2024)

5.1 Abstract

Fuerstenau (1957) showed that the flotation recovery of quartz reaches a maximum when the collector-coated mineral particles have zero ζ-potentials. A few years later, Derjaguin and Dukhin (1961) developed a model to show that the repulsive electrical double-layer (EDL) forces in wetting films constitute kinetic energy barriers (E_1) for bubble-particle interactions. Thus, these investigators were the first to recognize that the surface forces in wetting films control the kinetics of bubble-particle attachment in flotations. Yoon and Mao (1996) extended the concept by considering the role of attractive hydrophobic forces that can reduce E1 and, hence, increase the kinetics. This approach has been extended further by considering the role of hydrophobic forces in both the pulp and froth phase of a flotation cell to predict the grade vs. recovery curves and to optimize flotation circuits (Huang *et al.*, 2022; Gupta *et al.*, 2023). A user-friendly computer simulator has been developed for practitioners.

5.2 Introduction

Sulman and Picard (1905) were the first to disclose a method of using air bubbles to selectively collect hydrophobic particles on the surface and rise out of an aqueous phase, leaving hydrophilic particles behind (US Patent 793,808). The process known as 'forced air' flotation is recognized as the best available method of separating fine particles to produce high-grade concentrates at high recoveries. In this process, a target mineral (e.g., chalcopyrite) is rendered hydrophobic using a hydrophobizing agent called collector so that the mineral particles can attach themselves to rising stream of air bubbles. Thus, control of particle hydrophobicity is critical for the separation process.

It is difficult, however, to model flotation using hydrophobicity – a thermodynamic property – as a parameter for a kinetic process. It would be better to use the attractive hydrophobic (HP) force to model the movement of hydrophobic particles toward air bubbles in wetting films (Huang *et al*., 2022; Gupta & Yoon, 2024). There are two other forces controlling particle movement, i.e., electrical double-layer (EDL) and van der Waals (vdW) forces. However, these forces are usually repulsive and, hence, are not conducive to bubble-particle attachment. Fuerstenau (1957) was the first to report that flotation recovery reached a maximum under conditions of zero ζ-potentials, which led Derjaguin and Dukhin (1961) to develop a model showing that EDL forces create kinetic energy barriers (E_1) to flotation. Thus, flotation is driven by the HP force, which in turn is closely related to contact angles (θ) – a measure of particle hydrophobicity.

Many investigators took samples from an operating flotation bank and analyzed them using a 2-D mineral liberation analyzer to determine the size (i)-by-class (j) flotation rate constants (k_{ij}) of various composite particles. Results showed that the rate constants increased with surface liberation, which was a simple manifestation of increased contact angles at higher surface liberations (Jameson, 2012; Huang et al., 2022). This finding has a significant implication for the flotation of coarse particles, whose k_{ij} values are low due to low composite contact angles ($\bar{\theta}_{ij}$) (Gupta *et al.*, 2022). A solution to his problem may be to use stronger collectors to increase contact angles.

It is, therefore, the objective of the present investigation to test stronger collectors, known as Super Collectors, developed at Virginia Tech to increase $\bar{\theta}_{ij}$ of composite particles and, hence, to improve the recovery of coarse particles. These reagents are designed to enhance the hydrophobicity of a target mineral (e.g., chalcopyrite) well beyond the level that can be achieved using a conventional collector (e.g., xanthate) alone. The benefits of using the new reagents have been determined using a flotation simulator based on

first principles (Gupta & Yoon, 2024). The simulator allows one to determine flotation rate constants (k_{ij}) of composite particles from the values of $\bar{\theta}_{ij}$ determined from liberation analysis. The k_{ij} values determined in this manner may be referred to as intrinsic rate constants, as opposed to those determined experimentally in laboratory flotation experiments using 10-15 times higher energy dissipation rates ($\bar{\varepsilon}$) but at substantially shorter flotation times. A distinct advantage of using intrinsic kij for plant design is that there is no need to assume scale-up factors. Various design parameters, e.g., retention time, cell volumes and numbers, $\bar{\varepsilon}$, froth height, etc., are input variables for designing a plant by simulation. A user-friendly simulator has been designed to make it easier for process engineers to design a flotation circuit and for plant operators to optimize plant operations by varying both hydrodynamic and surface chemistry parameters as input.

5.3 Model

Flotation begins in the pulp phase where air bubbles are introduced to selectively collect hydrophobic particles and enter the froth phase due to increased buoyancy. The process can be modeled using a second-order rate equation as follows,

$$\frac{dN_1}{dt} = -k_p N_1 N_2 = -Z_{12} P \qquad [5.1]$$

in which, N_1 and N_2 are the number densities of particles and bubbles in the pulp phase, respectively, Z_{12} is the collision frequency, P is the probability of flotation, and k_p is the rate constant. P is the prduct of three sub-processes, i.e., $P = P_c P_a (1 - P_d)$, in which the subscripts c, a, and d represent the collision, attachment, and detachment sub-processes, respectively. Abrahamson (1975) derived an expression for predicting collision frequency (Z_{12}) under extremely turbulent conditions as follows,

$$Z_{12} = 5 N_1 N_2 d_{12}^2 \sqrt{\left(\overline{u_1^2} + \overline{u_2^2}\right)} \qquad [5.2]$$

in which d_{12} is collision diameter, and $\sqrt{\overline{u_1^2}}$ and $\sqrt{\overline{u_2^2}}$ are the RMS velocities of particles and bubbles, respectively.

From Eqs. [5.1] and [5.2], one obtains k_p as follows,

$$k_p = \frac{Z_{12}}{N_1 N_2} P_c P_a (1 - P_d) \qquad [5.3]$$

which may be simplified to obtain,

$$k_p = Z_{12}^* P_a (1 - P_d) \qquad [5.4]$$

The first term of Eq. [5.4], i.e., $Z_{12}^* = Z_{12} P_c / N_1 N_2$, represents the collision frequency normalized by $N_1 N_2$, while the second term, i.e., $P_a(1 - P_d)$, represents a selection function, representing the fraction (P_a) of particles colliding with a bubble and a fraction (1-P_a) of the attached particles not being detached in the pulp phase. P_c (<<1) is effectively a correction factor for Z_{12} which overpredicts collision in a flotation cell.

Substituting the P_a and P_d functions, both in exponential forms (Luttrell and Yoon, 1992; Yoon and Mao, 1996), into Eq. [5.4], one obtains k_p as follows,

$$k_p = Z_{12}^* \exp\left[-\frac{\left(E_1 + E_h\right) - W_a}{E_k^{'}} \right] \qquad [5.5]$$

which is of the same form as the simple Arrhenius equation. In Eq. [5.5], E_1 is the energy barrier for bubble-particle attachment, which can be determined from the surface forces present in wetting films, and E_h is the

hydrodynamic resistance to film thinning. Both E_1 and E_h present significant energy barriers to the particle-bubble attachment step, while W_a ($=\gamma_{LV}\pi r R_1^2(1-cos\theta)^2$) represents the work required to detach a particle of radius R_1 and contact angle θ from an air bubble with a surface tension γ_{LV} (Yoon and Mao, 1996). One can see that W_a should increase substantially with θ, which provides a rationale for using Super Collectors to increase the recovery of coarse particle flotation.

The bubble-particle aggregates formed in the pulp phase of a flotation cell enter the froth phase. The lamella films between two air bubbles drain and rupture at a critical rupture thickness to become a larger bubble, causing less hydrophobic particles to drop off from the bubble due to the limited 'parking' area. Thus, froth phase recoveries can be determined one can predict the bubble coarsening in the froth phase using the following relationship (Park *et al.*, 2018),

$$R_f = \frac{d_{2,b}}{d_{2,t}}\exp(-\alpha\tau) \qquad [5.6]$$

and,

$$\frac{d_{2,b}}{d_{2,t}} = \left[\exp\left(-\frac{0.46 n_f h_f}{J_g t_c}\right)\right]^{0.5} \qquad [5.7]$$

In Eqs. [5.6] and [5.7], $d_{2,b}$ and $d_{2,t}$ represent the bubble sizes at the base and top of a froth phase, respectively, n_f the number of faces of a bubble rupturing during coalescence, h_f the froth height, t_c is the critical rupture time of a lamella film varies with the contact angles of the particles in froth phase.

Substituting Eq. [5.6] into the following relationship (Finch and Dobby, 1990),

$$k = k_p R_f \qquad [5.8]$$

one can determine the flotation rate constant (k) for the pulp and froth phase recovery steps combined in a flotation cell.

Note here that Eq. [5.6] does not include the froth phase recovery due to entrainment, which has been given by Huang *et al.* (2022).

5.4 Results

5.4.1 Laboratory Tests Using Super Collector

Laboratory flotation tests were conducted on a low-grade porphyry copper ore sample assaying ~0.3 %Cu. In each test, 1,000 g sample (-10 mesh) was wet-ground in a rod mill for 10 min to d_{80} = 280 µm. In control tests, the mill products were floated in a 2-L Denver cell with 40-100 g/t potassium amyl xanthate (KAX) as collector and methyl isobutyl carbinol (MIBC) as frother. All tests were conducted for 5 min at 1,000 r.p.m. while taking timed-cut samples at 1, 3, and 5 min. The water contact angles (θ) measured on polished chalcopyrite specimens were in the range of 65-75°. In comparison tests, a Super Collector (SC) was added to the cell after a 2-min conditioning time with 50 g/t KAX, which further increased θ to the 150-160° range.

Figure 1 shows the results of the flotation tests conducted on the porphyry copper ore samples that had been ground to d_{80} = 280 µm in a rod mill. The size-by-size recoveries obtained after the 5-min flotation time obtained using KAX and Super Collector did not appear to show substantial improvements. However, using SC showed significant benefits with the flotation of coarse and fine particles (see *Figure* 1a). On the other hand, the grade *vs.* recovery curves plotted in Figure 1b showed substantial benefits of using SC. As shown, the use of SC substantially improved the selectivity, which can be attributed to the large increase in contact angles. The reason that the size-by-size recoveries did not show significant differences was because

the flotation tests were conducted at a high energy dissipation rate ($\bar{\varepsilon}$) at a long flotation time (5 min). As is well known, flotation rates increase with increasing $\bar{\varepsilon}$ due to increased Z_{12} (see Eq, [5.2]).

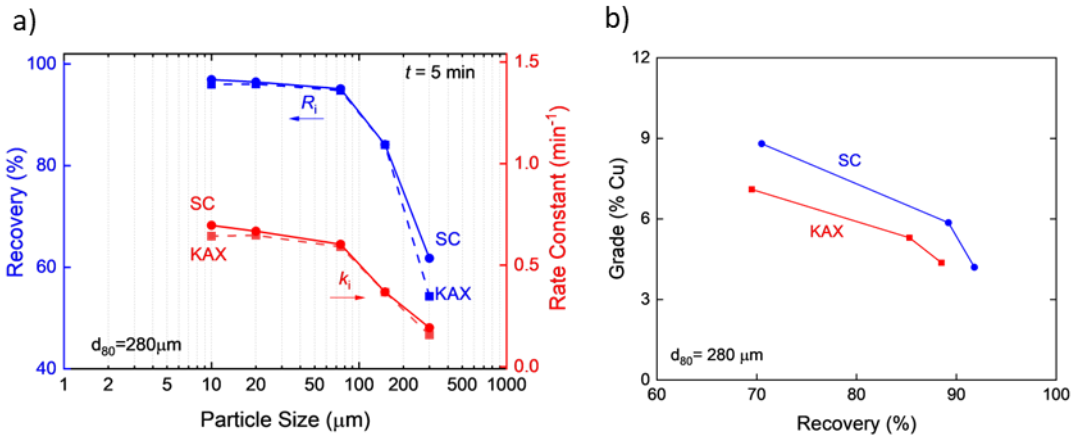

Figure 5-1 a) Size-by-size recovery and b) grade vs. recovery curves obtained in lab tests using SC and KAX as collectors.

5.4.2 Circuit Simulation

Using the model summarily presented in this communication, a flotation circuit has been simulated with and without using SC. Further details of the model equations and simulation have been described previously (Huang *et al.*, 2022; Gupta *et al.*, 2023; Gupta & Yoon, 2024). *Figure* 5.2 shows the flotation circuit, which consists of a rougher flotation bank where a low-grade copper ore is fed to remove most of free gangue minerals. The plant consisted of four rougher banks, each consisting of five 4,500 ft^3 mechanically agitated cells in series. The overall plant throughput was ~5,000 tph. The froth product of the rougher bank was then upgraded in the coarse-cleaners flotation circuit. The coarse-cleaner concentrate was reground to improve liberation, followed by column flotation in the cleaner circuit. The flotation circuit was run in a closed loop so that the cleaner-scavenger tail (CST) was returned to the rougher bank to allow the slow-floating particles to be recovered by giving them longer retention times.

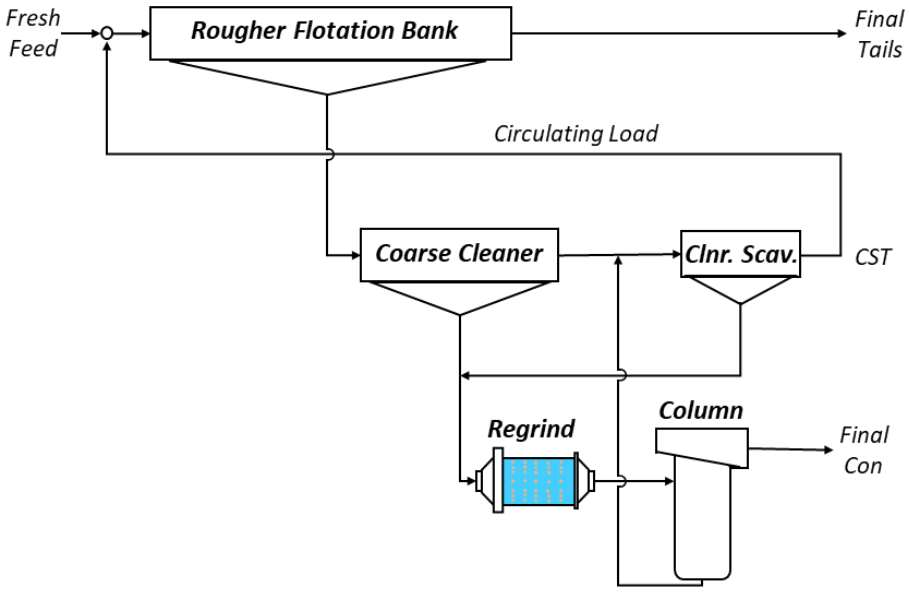

Figure 5-2. A flowsheet for the processing of a low-grade porphyry copper ore. CST is recycled as a circulating load.

Circuit simulations began with the analysis of the mineral liberation (m_{ij}) matrix of the feed to the rougher flotation bank as obtained from a 2-D surface liberation analysis using a TIMA. The liberation data were used to determine the particles of different liberation classes (j) using the Cassie-Baxter equation (1948),

$$\cos\bar{\theta}_j = a_1 b_1 \cos\theta_1 + a_2 b_2 \cos\theta_2 \qquad [5.9]$$

in which a_1 and a_2 are the surface liberation, θ_1 and θ_2 are contact angles of the target and gangue mineral, respectively. and b_1 and b_2 are correction factors. We assumed that b_1 = 0.8, and b_2 = 1.0 to account for the stereographic errors associated with determining locking factors. In determining, we also assumed that θ_1 = 70° and 150° for KAX- and SC-coated target mineral (chalcopyrite), respectively, while θ_2 = 2° for gangue minerals (e.g., quartz). *Table* 5-1 shows the $\bar{\theta}_j$ values determined from the m_{ij} matrix.

Table 5-1.Values of $\bar{\theta}_j$ obtained Using Eq. [5.9]

	Surface Liberation			
	0-10	10-30	30-50	50-100
KAX	15.7	31.5	45.1	63.3
SC	23.8	48.6	71.2	105.7

The values obtained using the Cassie-Baxter equation and presented in Table 5.1 were used to determine the hydrophobic force (F_{hp}) that decays with thickness h of a thin liquid film (TLF) of water formed between two hydrophobic surfaces as follows,

$$\frac{F_{hp}}{r_1} = -\frac{K_{131}}{6h^2} \qquad [5.10]$$

in which K_{131} is a hydrophobic force constant. In the present work, the force constant was determined using a K_{131} *vs.* θ plot established by Pazhianur and Yoon (2003).

The K_{131} values determined from constant angles as described above were then combined with the hydrophobic force constant (K_{232}) between two air bubbles using the combining rule (Yoon et al., 1997),

$$K_{132} = \sqrt{K_{131} K_{232}} \qquad [5.11]$$

to obtain the hydrophobic force constants (K_{132}) between mineral particles **1** and air bubble **2** in water. In using Eq. [5.11], the values of $K_{232} \sim 10^{-17}$ J was used from Wang and Yoon (2009). One can then determine the disjoining pressure (Π) acting in wetting films using the extended DLVO theory as follows (Pan and Yoon, 2016),

$$\Pi(h) = -\frac{A_{132}}{6\pi h^3} - \frac{\varepsilon\varepsilon_0\kappa^2}{2\sinh(\kappa h)}\left[\left(\psi_1^2 + \psi_2^2\right)\mathrm{cosech}(\kappa h) - 2\psi_1\psi_2\coth(\kappa h)\right] - \frac{K_{132}}{6\pi h^3} \qquad [5.12]$$

in which the first term represents the contribution from the repulsive van der Waals (vdW) forces, the second term representing the repulsive electrical double layer (EDL) force, and the third term representing the attractive hydrophobic force. In Eq. [5.12], A_{132} is the Hamaker constant, ε the permittivity of vacuum, ε_0 the dielectric constant of water, κ the reciprocal Debye length, and ψ_1, and ψ_2 are the surface (or ζ-) potentials of the particles and bubbles, respectively.

Substituting the Π(h) isotherm given in Eq. [5.12] into the Derjaguin approximation (1934), one obtains the free energy isotherm, which is a function of particle radius (R_1), bubble radius (R_2), particle contact angle (θ) and surface tension of water (γ_{LV}) as follows,

$$G(h) = \frac{1}{2\pi}\left(\frac{R_1 + R_2}{R_1 R_2}\right)\int_{r=0}^{r=\infty} \Pi(h) 2\pi r dr$$
$$= \gamma_{LV}\left(\cos\theta - 1\right) \qquad [5.13]$$

The value of Gibbs free energy at $\Pi = (\partial G/\partial h) = 0$ will give the energy barrier (E_1) as follows,

$$E_1 = \int_{r=0}^{r=\infty} G(h)\big|_{\Pi=0}\, 2\pi r dr \qquad [5.14]$$

The value of E_1 determined using Eqs [5.14] can then be used to determine k_p using Eq. [5.5], which can be substituted into Eq. [5.8] to obtain the overall flotation rate constant k.

Figure 5.3a shows the size-by-size flotation rate constants (k_i) and recoveries (R_i) plotted for the cases of using i) KAX and ii) SC as collectors. As shown, the use of Super Collector greatly increased both k_i and R_i, demonstrating the benefits of using stronger hydrophobizing agents. It is interesting to note that the differences observed between KAX and SC are much larger in plant simulations than observed in laboratory flotation tests. In general, high energy dissipation rates, typically $\bar{\varepsilon}$ = 10-15 kW/m^3 are used to shorten the flotation times. In plant operations, $\bar{\varepsilon}$ = 0.8-1.0 kW/m^3 were used but at much longer flotation times. In the present work, we used $\bar{\varepsilon}$ = 1 kW/m^3 and 23.7 min of retention time were used for plant simulations.

Figure 5.3b shows the grade *vs*. recovery curves obtained using KAX and SC by plant simulations. Super Collectors gave higher recoveries but at lower copper grades than KAX, suggesting that the former can recover composite particles and, hence, produced lower grade concentrates. This finding also suggests that SC should help improve the recovery of coarse particles. The size-by-size recovery curves presented in *Figure* 5.3a show indeed that coarse particle recoveries were substantially increased by switching to a Super Collector.

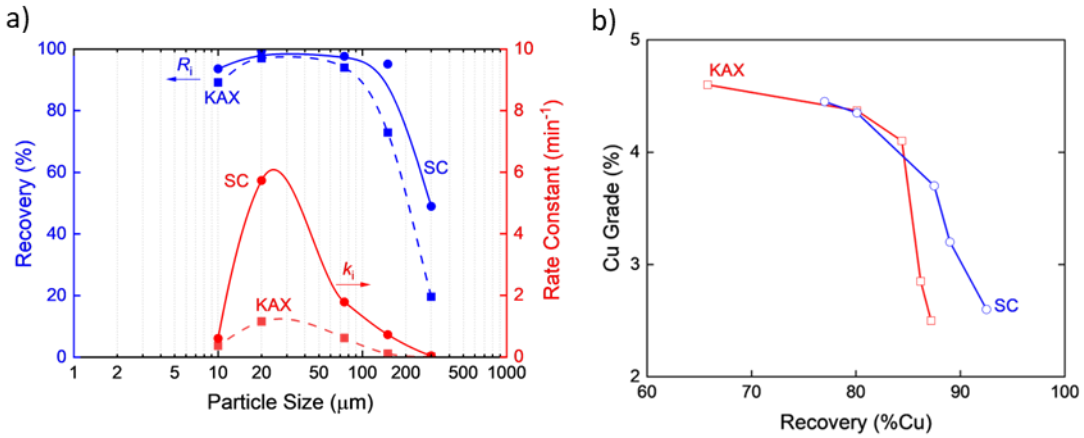

Figure 5-3. a) Size-by-size bank recoveries (blue) and flotation rate constant (red) as obtained using KAX and SC as collectors. b) grade vs. recovery curves obtained from simulation of the rougher flotation bank with KAX (red) and SC (blue).

5.4.3 Improving Throughput and Recovery

In most sulfide mineral flotation plants, the slowest-floating materials congregate in the cleaner-scavenger tails (CSTs), as shown in *Figure* 5.2. The particles are typically < 20 μm in size. Therefore, mill operators return them to the rougher flotation bank as circulating loads (CLs) to help recover the target minerals, e.g., chalcopyrite, by allowing longer retention times. It has been found, however, that much of the target minerals are found as composite particles in a CST stream and/or superficially oxidized while being recirculated repeatedly, both of which would make it difficult to recover them efficiently. In the present work, we conducted plant simulations on a porphyry copper ore flotation plant using a SC and compared the results with those obtained previously using KAX (Gupta *et al.*, 2023).

Table 5.2 shows that a simple substitution of the conventional collector with a SC in a closed-circuit configuration increased the copper recovery from 86.6 to 95.86%. No other changes in operating conditions were necessary to increase the recovery by 9.21%, which can be attributed to the substantial increase in the flotation rate constants (k_i) as shown in *Figure* 5.3a. Of course, the main reason for the increase k_i is the large contact angles brought out from the use of a SC.

Table 5-2. Comparison of plant simulations conducted on a low-grade copper ore flotation plant using KAX and a SC

Reagents	Closed Circuit				Open Circuit			
	Throughput (tph)	Con Grade (%Cu)	Tails Grade (%Cu)	Recovery (%)	Throughput (tph)	Grade (%Cu)	Tails Grade (%Cu)	Recovery (%)
KAX	5,000	25.68	0.0305	86.65	6,239	26.84	0.0325	85.30
SC	5,000	23.72	0.0095	95.86	6,239	25.01	0.0152	93.32

Circulating loads usually account for 20-25% of the volumetric flows through rougher flotation banks. Recognizing that the materials in a CST flow represent the slowest-floating copper-bearing minerals, their flotation rates are much slower than those present in freshly mined ore feeds and, hence, entail a significant decrease in throughput. In this regard, CLs represent a costly exercise in plant operation. With the advent of a series of Super Collectors, it may be worthwhile to open the flotation circuit. The simulation results obtained under open circuit configurations are presented in *Table* 5.2. As shown, the throughput was increased to from 5,000 to 6,239 tph, which represented a 24.8% increase in throughput for the cases of using KAX and SC. When using an SC, copper recovery was increased from 86.65 to 93.32%. These improvements can be translated to an increase in the yearly copper production by 34.4% from 78,658.3 tons to 105,701.2 tons.

With KAX as a collector, opening the rougher circuit increases the throughput similarly but at a loss of copper recovery from 86.65 to 85.3%. Companies are aware of the substantial increase in throughput by opening the circuit but are hesitant to implement the concept due to the loss of copper recovery by 1.35%. When SCs become available commercially, this barrier may be eliminated.

5.5 Summary and Conclusions

A new flotation model has been derived by considering both the forward and backward reactions in bubble-particle interaction. The model can be used to predict the rate constants using a simple Arrhenius-type equation as functions of collision frequency, energy barriers due to surface forces, hydrodynamic resistance, work of adhesion, and energy dissipation rate. It can accurately predict the intrinsic flotation rate constants that can be used to design flotation plants and simulate plant operations without using assumed scaleup factors.

The model has been used to simulate the performance of the super collectors that can create contact angles nearly twice as large as those obtained using conventional collectors. The simulation results show that the super collectors are useful for the flotation of composite particles and hence can improve the recovery of coarse particles. The super collectors are also useful to increase the both throughput and recovery of a copper flotation plant by improving the recovery of the composite particles present in cleaner-scavenger tails.

A user-friendly computer simulator has been developed to make it easier for process engineers to design flotation circuits for different ore types and for plant operators to optimize plant operations by varying both the hydrodynamic and surface chemistry parameters as input.

5.6 References

Abrahamson, J. (1975). Collision rates of small particles in a vigorously turbulent fluid. *Chemical Engineering Science*, 30(11), 1371-1379.

Cassie, A.B.D., Baxter, S., 1944. Wettability of porous surfaces. *Trans. Faraday Soc*. 40,546–551.

Derjaguin, B. V. (1934). Friction and adhesion. IV. The theory of adhesion of small particles. *Kolloid Zeits*, 69, 155-164.

Derjaguin, B. V., & Dukhin, S. S. (1961). Theory of flotation of small and medium size particles. *Trans. Inst. Min. Metall*, 70(5), 221-246.

Finch, J.A., Dobby, G.S., 1990. Column flotation. *Pergamon Press*.

Fuerstenau, D. W. (1957). Correlation of contact angles, adsorption density, zeta potentials, and flotation rate. *Trans. AIME*, 208, 1365-1367.

Gupta, M., & Yoon, R. H. (2024). Maximizing the recovery and throughput of a rougher flotation bank by improving the recovery of composite particles. *Minerals Engineering*, 207, 108545.

Gupta, M., Huang, K., & Yoon, R. H. (2022). Predicting the recovery and grade of a rougher flotation circuit from liberation data. *Minerals Engineering*, 188, 107853.

Gupta, M., Huang, K., Noble, A., & Yoon, R. H. (2023). Improving the performance of a low-grade porphyry copper ore flotation plant using a simulator that can predict grade vs. recovery curves. *Minerals Engineering*, 202, 108243.

Huang, K., Keles, S., Sherrell, I., Noble, A., & Yoon, R. H. (2022). Development of a flotation simulator that can predict grade vs. Recovery curves from mineral liberation data. *Minerals Engineering*, 181, 107510.

Jameson, G. J. (2012). The effect of surface liberation and particle size on flotation rate constants. *Minerals Engineering*, 36, 132-137.

Luttrell, G. H., & Yoon, R. H. (1992). A hydrodynamic model for bubble—particle attachment. *Journal of Colloid and Interface Science*, 154(1), 129-137

Pan, L., Yoon, R.H., 2016. Measurement of hydrophobic forces in thin liquid films of water between bubbles and xanthate-treated gold surfaces. *Minerals Engineering*, 98, 240–250.

Park, S., Huang, K., & Yoon, R. H. (2018). Predicting bubble coarsening in flotation froth: Effect of contact angle and particle size. *Minerals Engineering*, 127, 256-264.

Pazhianur, R., & Yoon, R. H. (2003). Model for the origin of hydrophobic force. *Mining, Metallurgy & Exploration*, 20(4), 178-184.

Rabinovich, Y. I., Guzonas, D. A., & Yoon, R. H. (1993). Role of chain order in the long-range attractive force between hydrophobic surfaces. *Langmuir*, 9(5), 1168-1170.

Sulman, H.L., & Kirkpatrick-Picard (1905). U.S. Patent No. 793,808.

Yoon, R.H., & Mao, L. (1996). Application of extended DLVO theory, IV: derivation of flotation rate equation from first principles. *Journal of Colloid and Interface Science*, 181(2), 613-626.

Yoon RH, Flinn DH, Rabinovich YI. Hydrophobic interactions between dissimilar surfaces. Journal of colloid and interface science. 1997 Jan 15;185(2):363-70.

Wang L, Yoon RH. Effect of PH and electrolyte on the stability of surfactant-free foam films. InSME Annual Meeting and Exhibit and CMA's 111th National Western Mining Conference 2009 2009 Jan 1 (Vol. 2, pp. 810-814).

Chapter 6. Jig Flotation Cell: A Novel Method to Improve Coarse Particle Flotation

(Submitted to a peer reviewed conference as, Gupta, M., Yoon, R.H., Improving coarse particle flotation by control of surface and hydrodynamic forces, XXXI International Mineral Processing Congress, Washington D.C., October, 2024)

6.1 Abstract

Bubble-particle interactions in flotation are controlled by the surface forces in wetting films. The process works well until the particle size becomes larger than ~150 μm, above which gravity forces come into the picture. In the present work, methods of improving coarse particle flotation have been developed by reducing the effective specific gravity (SG) of target minerals by attaching small air bubbles, allowing particle motions to be controlled by SGs independent of particle size, and creating a froth phase to produce higher-grade concentrates.

6.2 Introduction

In 1905, Sulman and Picard were awarded a U.S. patent (No.793,808), which disclosed a method of using air bubbles rather than CO_2 bubbles or oil drops to collect hydrophobic particles from an aqueous phase. The process known as forced air flotation has been used to produce practically all metals humans use today and is regarded as the best available method of separating mineral fines. Despite many successes, flotation is effective over a narrow range of particle sizes of 20-150 μm (Wills and Finch, 2016).

For the flotation of low-grade ores, *e.g*., porphyry copper ores, much of the energy is spent on breaking waste (or dead) rocks. According to Elshkaki (2016), 18% of the energy consumed for producing primary copper goes to mining, 42% to mineral processing, 27% to smelting, 7% to refining, and 3% to tailings disposal. Further, lower-grade ores are often fine-grained and, hence, require finer grinding for liberation (Norgate and Jahanshahi, 2006). In mineral processing, crushing and grinding account for ~70% of the total energy consumption, while flotation and pumping each account for 10% of the total (O'Connor, 2019). One can think about only two ways to achieve significant energy savings; one would be to increase comminution efficiency, and the other to reduce the volume of the materials to be ground.

Clark *et al*. (2005) showed that liberation of the Escondida copper ore drops sharply at particle size (d_p) above 150 μm, which corresponds to the upper particle size limit of flotation. Flotation is a process based on surface properties, which gains its importance with decreasing particle size as d_p^{-2}, while gravity gains its importance as d_p^3. Thus, coarse particle flotation deteriorates more sharply at d_p > 150 μm than fine particle flotation does at d_p < 20 μm, as shown in *Figure* 6-1. One way to overcome the gravity effect would be to reduce the effective specific gravity (SG) of the target minerals by attaching fine particles to their surfaces. Most coarse particle flotation cells have been developed following this approach (Mankosa and Luttrell, 2002; Jameson, 2018; Crompton *et al*., 2023). Due to the poor liberation, coarse particles have low contact angles (θ); therefore, bubbles and particles are contacted in a fluidized bed rather than in a turbulent mixer to minimize the probability of detachment. One other characteristic of the existing coarse particle flotation cells is that they are operated without the froth phase as particles are readily detached at the pulp/froth interface at the pulp/froth interface, which denies the opportunity for less hydrophobic particles to selectively drop off bubble surface to obtain cleaner concentrates.

Ito *et al*. (2019) developed a 'hybrid jig' to enable the separation of PVC and PE, which is difficult because their SGs are close to each other. The problem has been overcome by attaching small air bubbles on PVC to decrease its effective SG to increase the SG differences between the two plastics, which helped increase the separation efficiencies and the top size by orders of magnitude. Despite the use of air bubbles, the hybrid jig remains a gravity separation device rather than a flotation cell. As is the case with coarse particle flotation, no froth phase is formed on top of the pulp phase.

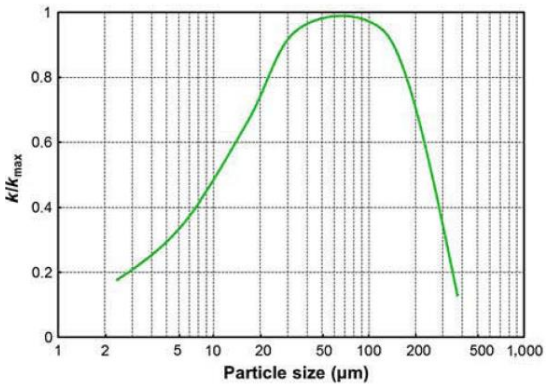

Figure 6-1. Effect of particle size on the relative flotation rate constants; k is the rate constant, and k_{max} is the maximum flotation rate constant (With permission from Wills and Finch, 2016).

In the present work, a new coarse particle flotation cell has been developed by i) reducing the SG of a target mineral by selectively attaching air bubbles, ii) pulsating the liquid in the cell to accelerate the upward movement of coarse particles, and iii) allow bubble-particle aggregates cross the pulp/froth interface during pulsion cycles. Furthermore, appropriate control of the pulsion/suction cycles would particles more according to SGs involved independently of particle size.

Gupta and Yoon (2024) derived an expression for the flotation rate constant (k_p) in the pulp phase of a flotation cell by considering both the forward (attachment) and backward (detachment) steps of bubble-particle interaction,

$$k_p = Z_{12}^{*}\ \exp\left[-\frac{\left(E_1 + E_h\right) - W_a}{E_k^{'}}\right] \qquad [6.1]$$

which is of the same form as the Arrhenius equation. In Eq. [1], Z_{12}^{*} represents the collision frequency normalized by N_1N_2, N_1 representing the number density of particles (**1**) and N_2 representing the number density of air bubbles (**2**); E_1 the energy barrier for bubble-particle attachment; E_h the hydrodynamic resistance to film thinning; W_a ($=\gamma_{LV}\pi r_1^2(1-cos\theta)^2$) the work of bubble-particle attachment, in which g_{LV} is the surface tension at the water/air interface and r_1 is the radius of the target mineral grains (*e.g.*, chalcopyrite); and θ is the contact angle of the particle; and E_k' is the kinetic energy of the particles due to turbulence.

According to Eq. [6.1], k_p can be improved by minimizing E_k' and maximizing W_a by maximizing θ. E_k' can be minimized by allowing bubble-particle contacts under quiescent conditions, *e.g.*, in a fluidized bed. In addition, air, bubbles are created using an external in-line bubble generator. The jig flotation cell developed in the present work is effectively a fluidized bed and uses an external bubble generator. The authors developed Super Collectors (SC) that can increase θ the 150-170^o range, which can greatly increase W_a to decrease the probability of detachment (Gupta and Yoon, 2024). For fine particle flotation, it would be necessary to overcome E_h by increasing the hydrodynamic force as is the case with the Concord cell (Jameson, 2010).

The coarse particle flotation cell developed in the present work has been tested on a sample of coarse particles (212-600 μm) taken from an operating porphyry copper flotation plant. A series of flotation tests were conducted using a small laboratory-scale jig flotation cell to test the new concept on a preliminary basis. All experiments were conducted using potassium amyl xanthate (KAX). The effects of using Super Collectors will be reported in another communication at this conference.

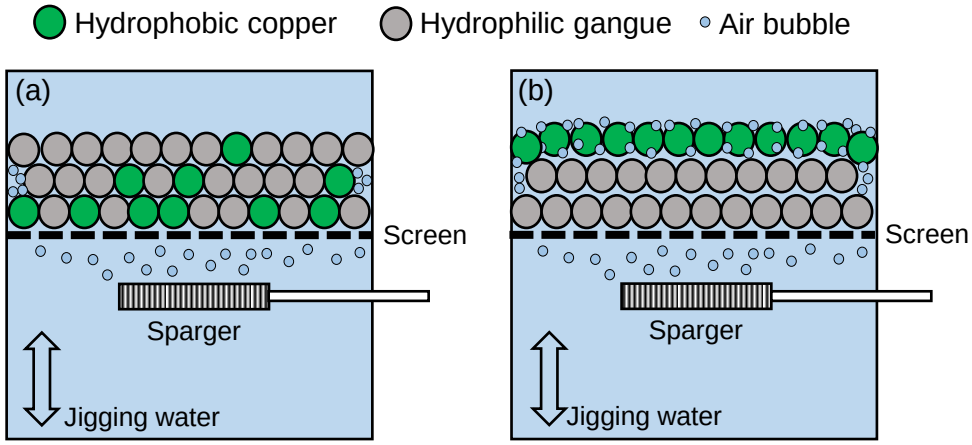

Figure 6-2. A schematic illustration of the separation mechanism of jig flotation. a) Initial stage before jigging action has been initiated, b) the segregation of light hydrophobic-particle-bubble aggregate and gangue particles.

6.3 Theory

In a jig, particles are allowed to move during the initial acceleration period of the pulsion and suction cycles, so that particle motions are determined by acceleration a $(= du/dt)$,

$$a = \left(1 - \frac{\rho_f}{\rho_s}\right) g \qquad [6.2]$$

which is determined by particle density (ρ_s), fluid density (ρ_f), and gravitational acceleration (g). Thus, a jig is designed to separate particles according to particle densities rather than particle size, which is a desired feature for coarse particle flotation. Furthermore, jigs can operate at high pulp densities, which should help increase the separation efficiencies due to the hindered setting effect.

In the present work, a low-grade copper ore sample of 212-600 μm size fraction was fed to a jig flotation cell to separate chalcopyrite ($CuFeS_2$) with $\rho_s = 4.2$ from quartz (SiO_2) with $\rho_s = 2.65$. For this to be possible, a collector (KAX) was added to the feed to render the copper-bearing particles hydrophobic so that air bubble(s) can attach to the mineral surfaces and thereby reduce the effective density of the particles such that its effective density (ρ_s^{Cu}) becomes lower than that (ρ_s^{Si}) of quartz, *i.e.*,

$$\rho_s^{Cu} < \rho_s^{Si} \qquad [6.3]$$

Under this condition, quartz particles will settle on the screen, while the copper-bearing mineral particles settle on top of the quartz particles, forming a stratification. The copper-bearing minerals are removed from the top layer, while the heavier quartz particles are removed at the bottom as shown in Figure 6-2.

The process described above is referred to as jig flotation. However, it is effectively a gravity separation device. As has already been discussed, it is difficult to float coarse particles in a flotation cell, which is

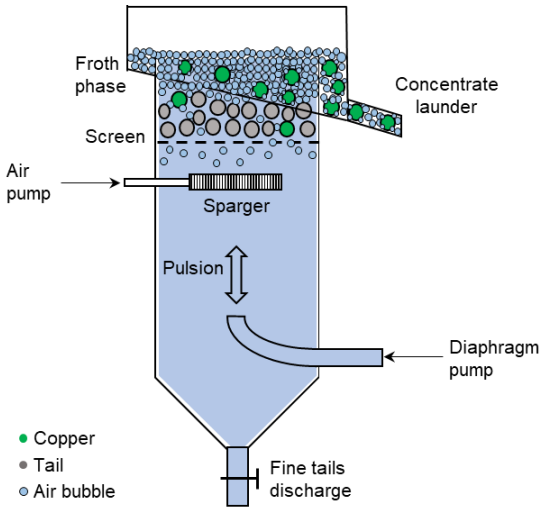

Figure 6-3. Schematics of 1-inch Jig Flotation Cell.

designed to separate particles by control of surface forces, as gravitation force plays a significant role at d_1 > 150 µm.

The particles coated with small air bubbles in the pulp phase of the jig flotation enter the froth phase, in which entrained gangue minerals are removed by the froth-cleaning action to obtain higher-grade concentrates. In most coarse particle flotation cells, hydrophobic particles drop off at the pulp/froth interface, which effectively serves as a barrier. In the jig flotation cell, the bubble-particle aggregates formed in the pulp phase can readily pass through the phase boundary during the pulsion cycle without losing coarse particles. Thus, jig flotation can be operated with a froth phase, in which less hydrophobic particles are dropped off from air bubbles and report to the tailings stream. The target minerals attached to air bubbles are removed from the top while gangue minerals not attached to air bubbles are from the bottom of the particles stratified in accordance with effective SGs.

6.4 Experimental

6.4.1 Sample Preparation

A representative sample was taken from a rougher flotation feed from an operating porphyry copper ore processing plant. The sample was filtered, air-dried, and screened to obtain a 212-600 µm size fraction, which was used as the feed to a series of jig flotation tests.

6.4.2 Equipment and Chemicals Used

A jig flotation cell was fabricated from a 1-inch ID glass tubing at the glassblowing shop at Virginia Tech. The pulsion and suction cycles were created by means of a diaphragm pump, Walchem's IWAKI E-Class Metering Pump. The pump provided a maximum flow rate of 20 gph at stroke rates in the range of 1-360 strokes per minute (spm). Potassium amyl xanthate (KAX) and diesel oil were used as collectors and extenders, respectively, and polypropylene glycol (PPG-425) was used as frother.

6.4.3 Laboratory-Scale Jig Flotation Tests

The schematics of a 1-inch diameter jig flotation cell is shown in *Figure* 6-3. The dimensions of the cell were 1-inch ID x 12-inch height. A 200-mesh screen was placed 2 inches below the overflow lip. A diaphragm pump was used to create jigging motions at different strokes (2.1-4.8 mm) and frequencies 25-150 spm.

In a given experiment, 5-20 g sample was conditioned in a separate vessel with a collector and a frother for 2-3 min before feeding the sample onto the screen. The test began by injecting air bubbles below the screen while at the same time pulsating the aqueous phase by activating the diaphragm pump. After a 2-min flotation time, the weights of the particles reported to the launder and remaining on the screen were measured to determine the weight recovery. The samples were analyzed to determine copper recoveries.

6.5 Results and Discussion

A parametric study was undertaken to optimize the performance of the jig flotation cell. A porphyry copper ore feed with particle sizes in the range of 212-600 µm and grades in the 0.09 to 0.15%Cu was conditioned for 2 minutes with 100 g/t KAX as collector, 50 g/t diesel oil as extender, and 50 ppm PPG-425 as frother. The conditioned sample was subjected to a series of batch tests to establish the optimal operating conditions, e.g., pulp density, air flow rate, and jigging strokes and frequency.

The test results are plotted in *Figure* 6-4 as red triangles. As shown, copper recoveries were in the range of 60-74, and product grades were in the range of 0.51 to 3.65%Cu after single-stage operations in batch mode. Once the optimal operating conditions had been established, a control test was conducted without pulsating the liquid in the flotation cell, with the result presented in *Figure* 6-4 as a green diamond and *Table* 6-1. As shown, the jigging mechanisms incorporated in the flotation cell improved the recoveries substantially but at lower product grades. If the test had been conducted in multiple stages, product grades would have been higher. However, the main objective of coarse particle flotation is to reduce the volume of the materials to be fed to regrind mills for fine grinding, which is energy-intensive.

Due to the declining ore grades, escalating energy costs, and societal pressure for sustainability, the mineral industry is looking for ways to save energy. Coarse particle flotation may be a doable option in the short term with further technological advancements. The work conducted in the present work showed that the difficulty in coarse particle flotation arises from the gravitational force interacting with the surface forces controlling flotation. Methods of mitigating the gravitational force have been explored by adsorbing air bubbles to a hydrophobized target mineral to reduce its effective SG and by pulsating the fluid in a flotation cell to allow particles to move according to SGs independent of particle size. Both of these provisions helped increase the upper particle size limit of flotation. During the pulsion cycle, bubble-particle aggregates formed in the pulp phase can penetrate the pulp/froth interface, forming a froth phase that is conducive to producing higher-grade products.

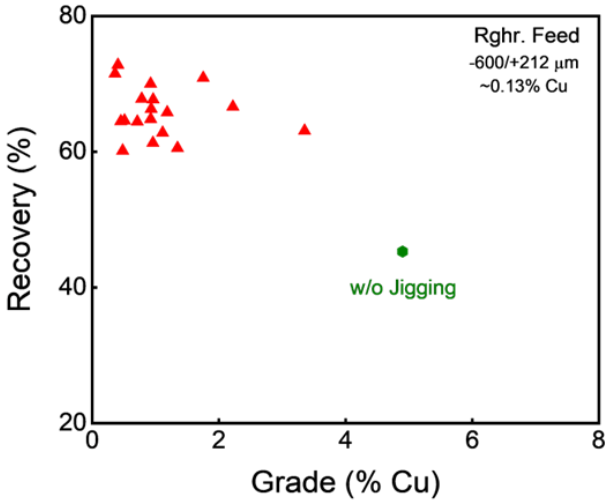

Figure 6-4. Grade *vs*. recovery curve obtained with jig flotation cell using coarse copper ore feed samples.

Table 6-1. Evaluation of the effect of optimized parameters on coarse particles recovery

	Feed (%Cu)	Concentrate (%Cu)	Recovery (%)
w/o jigging	0.15	4.9	45.3
w/ jigging	0.12	1.22	73.6

The team at Virginia Tech is developing a process development unit (PDU) to collect scaleup information by running a series of bench-scale continuous tests. As is well known, Jig is a high throughput device that can take advantage of hindered settling without losing separation efficiencies.

6.6 Summary and Conclusions

A new coarse particle flotation cell named jig flotation cell has been developed to mitigate the effects of the gravitational force that interferes with the surface forces controlling flotation. The new flotation cell has been designed to control the hydrodynamic forces such that particles move according to their SGs independent of particle size, which is conducive to increasing the top size of flotation.

In the jig flotation, bubble-particle aggregates can penetrate the pulp-froth interface during the pulsion cycle without losing particles and form a froth phase, which should help produce higher-grade froth products. A series of laboratory-scale flotation tests have been conducted on a 212-600 μm size fraction assaying 0.09-0.15 %Cu from a low-grade porphyry copper ore. A single-stage jig flotation test produced a 1.22 %Cu concentrate at a 73.6% recovery.

6.7 References

Clark, M. E., Brake, I., Huls, B. J., Smith, B. E., & Yu, M. (2005). Creating value through application of flotation science and technology. Centenary of Flotation Symposium, 6-9 June, Brisbane, QLD.

Crompton, L. J., Islam, M. T., & Galvin, K. P. (2023). Assessment of the partitioning of coarse hydrophobic particles in the product concentrate of the CoarseAIR™ flotation system using a novel mechanical cell reference method. Minerals Engineering, 198, 108088.

Elshkaki, A., Graedel, T. E., Ciacci, L., & Reck, B. K. (2016). Copper demand, supply, and associated energy use to 2050. Global environmental change, 39, 305-315.

Gupta, M., & Yoon, R. H. (2024). Maximizing the recovery and throughput of a rougher flotation bank by improving the recovery of composite particles. *Minerals Engineering*, 207, 108545.

Ito, M., Saito, A., Murase, N., Phengsaart, T., Kimura, S., Tabelin, C. B., & Hiroyoshi, N. (2019). Development of suitable product recovery systems of continuous hybrid jig for plastic-plastic separation. Minerals Engineering, 141, 105839.

Jameson, G. J. (2010). Advances in fine and coarse particle flotation. Canadian Metallurgical Quarterly, 49(4), 325-330.

Jameson, G. J. (2018). U.S. Patent No. 10,040,075. Washington, DC: U.S. Patent and Trademark Office.

Mankosa, M. J., & Luttrell, G. H. (2002). U.S. Patent No. 6,425,485. Washington, DC: U.S. Patent and Trademark Office.

Norgate, T., & Jahanshahi, S. (2006, November). Energy and greenhouse gas implications of deteriorating quality ore reserves. In 5th Australian conference on life cycle assessment: achieving business benefits from managing life cycle impacts.

O' Connor, C. (2019). Global Challenges Facing the Minerals Processing Industry. In 2019 IMPC Eurasia Conference Proceedings, 1-10.

Sulman, H.L., & Kirkpatrick-Picard (1905). U.S. Patent No. 793,808.

Wills, B. A., & Finch, J. A. (2016). Will's Mineral Processing Technology: An introduction to the Practical Aspects of Ore Treatment and Minerals Recovery Eight Edition.

6.8 Appendix

6.8.1 Jig Flotation Cell vs. Denver Cell Flotation

Tests were run with the rougher feed samples with 1-L laboratory Denver flotation cell and compared with the Jig flotation cell to quantify the performance of the newly developed coarse particle recovery unit. For JF cell, coarse rougher feed (212-600 µm) was conditioned at a pH of 10.8 with 100 g/t of KAX as a primary hydrophobizing agent for 5 minutes and 100 g/t of a hydrophobic polymer poly (2-ethyl hexyl) methacrylate (PEHMA) blended with kerosene (33% by *vol*.) as a secondary collector with a conditioning time of 5 minutes. 200 ppm PPG-425 was used as a frother. The conditioned sample was then transferred to the feed screen of a 1-inch jig flotation column and the test was run with a layer of froth (1.5 cm) for 2 minutes. The jigging amplitude and frequency were kept 4.1 mm and 25 spm, respectively with an airflow rate of 1 scfh. Make-up water was added to maintain the slurry level in the cell.

Denver cell flotation tests were also run with the coarse copper rougher feed samples (212-600 µm) to compare with the performance of the jig flotation cell. 200 g of feed was used and conditioned with the same collectors and frother concentration in the cell. The test was run at a low agitation speed of 750 rpm with an airflow rate of 1.7 scfh to reduce the turbulence and with a froth depth of ~1.5 cm. These measures were taken to improve the coarse particle recovery in a conventional flotation cell. The concentrate was collected until the froth phase looked clear, devoid of any particles.

Table A.6-1 shows the comparison of the performance. The jig flotation cell obtained a copper (Cu) recovery of 63.1% at 3.35 %Cu concentrate (con) grade in comparison to the recovery of 52.6% and 3.14 %Cu con grade achieved using the conventional Denver flotation cell. Even after the reduced agitation in a conventional flotation cell or in effect, reduced turbulence, coarse particles were still prone to the low rate constant as given by Eq. [6.1]. It is also widely known that coarse particles consist of composite particles and therefore, have lower particle contact angles reducing the work of adhesion, W_a. This further is detrimental for the rate constants in the pulp phase.

The jig flotation cell helps in improving the bubble-particle hydrodynamics by creating quiescent conditions and reducing the turbulence in the pulp phase and thereby, increasing the rate constant in the pulp phase. One can, therefore, expect to have higher pulp phase recovery of liberated and middling coarse particles. The pulsion stage of jigging motion provides an initial particle acceleration helping the particles penetrate the pulp-froth interface) and thereby, take advantage of the cleaning action of the froth phase. The upward acceleration also helped in optimizing the retention time of these particles in the froth phase and therefore prevented any drop in the recovery while achieving high final upgrade ratios.

6.8.2 Parametric Studies

In the process of optimizing the jig flotation cell performance, a parametric study was undertaken. During these tests, 100 g/t PAX and 50 g/t diesel oil were used as the primary and secondary collectors, respectively. 50 ppm PPG-425 was used as a frother. Duplicate tests were run for 2 minutes and various operating parameters such as jigging strokes or net displacement, frequency, and airflow rate were

Table A.6-2. Comparison of Denver Cell and Jig Flotation cell results with copper ore samples

	PAX (g/t)	PEHMA (g/t)	PPG-425 (ppm)	Feed (%Cu)	Grade (%Cu)	Recovery (%Cu)
Denver Cell	100	100	200	0.11	3.14	52.6
Jig Flotation	100	100	200	0.12	3.35	63.1

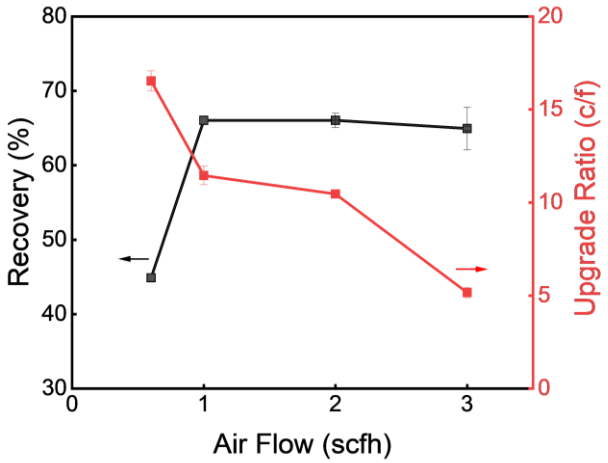

Appendix Figure 6-1. Effects of air flowrate on Jig Flotation recovery and concentrate grade with 212-600 µm copper feed sample. PAX dosage: 100 g/t, diesel: 50 g/t, PPG dosage: 50 ppm, pump stroke: 4.1mm and pump frequency: 25 SPM and residence time: 2 minutes.

conducted. Frother water was manually added from the top of the cell during the tests to maintain the froth depth at 1 cm.

6.8.2.1 Effect of Air flowrate

The series of tests were started by optimizing the air flow rate. Air flow rate can affect the performance by altering the diameter of air-bubble and therefore, the bubble-particle attachment and the apparent specific gravity of bubble-particle aggregate. Although excessive air flow can expand/dilate a particle bed and can lead to flooding conditions causing inefficient gravity separation.

During this set of tests, the other parameters were kept constant, at pulsation amplitude =4.1 mm, pulsation frequency: 25 spm, and pulp density at ~16%. *Appendix Figure* 6-1 shows the effect of changing air flow rates on the final recovery and con grade obtained using a jig flotation cell. The results showed that

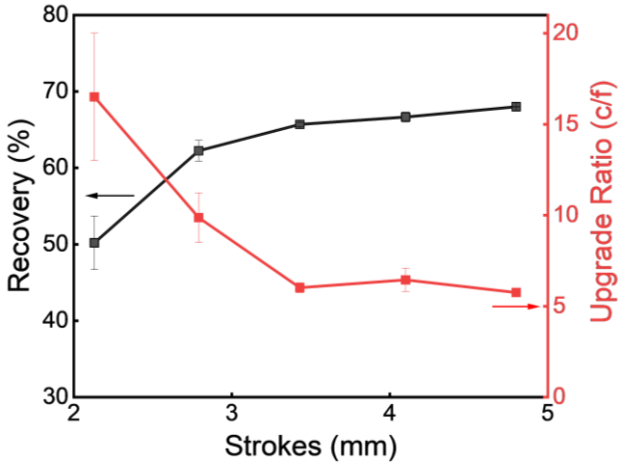

Appendix Figure 6-2. Effects of jigging stroke or displacement on jig flotation recovery and concentrate grade with 212-600 µm copper feed sample. PAX dosage: 100 g/t, diesel: 50 g/t, PPG dosage: 50 ppm, pump freq: 50 SPM and air flowrate: 1 scfh and residence time: 2 minutes.

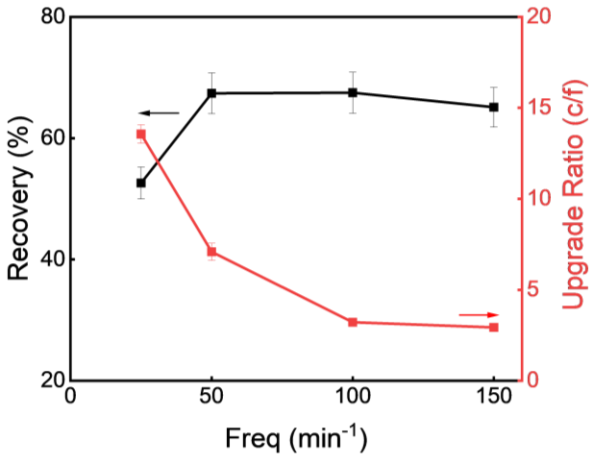

Appendix Figure 6-3. Effects of jigging frequency on jig flotation recovery and concentrate grade with 212-600 µm copper feed sample. PAX dosage: 100 g/t, diesel: 50 g/t, PPG dosage: 50 ppm, pump stroke: 4.1 mm and air flowrate: 1 scfh and residence time: 2 minutes.

an increase in the airflow rate from 0.6 scfh to 1 scfh led to an increase in the final recovery from 44.9% to 66.5%. When the air flow rate was increased further the recoveries tended to remain nearly constant with the final recovery obtained at 3 scfh being equal to 65.0%.

The upgrade ratio (*c*/*f*) on the other hand was reduced as the airflow rate was increased due to the occurrence of flooding conditions in the cell. The upgrade ratio was reduced from 17.1% for 0.6 scfh to 4.9% with 3 scfh. An upgrade ratio of 11.4 was achieved with 1 scfh. Therefore, 1 scfh was considered the optimum air flow rate and was used for the remaining test work.

6.8.2.2 Effect of Pulsation Stroke

In this set of experiments, the stroke in the pulsion stage was varied between 2.1 mm to 4.8 mm. The other parameters were kept constant and were the following, pulsation frequency: 50 spm; air flowrate: 1 scfh and pulp density: 16%. *Appendix Figure* 6-2 shows the effect of jigging stroke.

As shown, as the particles were displaced with a pulsation stroke from 2.1 mm to 2.8 mm, the recoveries increased and remained high even at higher stroke values. With the pulsation displacement of 2.1 mm, it was observed that although particles were suspended in the pulsion amplitude, they did not have enough upward force to get recovered in the froth phase. This requirement was met as the amplitude was increased to 2.8 mm; the suspended particles were able to penetrate the froth phase and were able to be recovered. At 2.8 mm, 73.7% Cu recovery was obtained at an upgrade ratio of 9.9.

As the stroke amplitude was increased further, the recoveries remained the same, although the upgrade ratio (con grade/feed grade) was reduced. The siliceous gangue minerals are less dense than the chalcopyrite-bearing minerals and therefore, require less force to be lifted. When the pulsion displacement was increased, the stronger force helped in the recovery of these hydrophilic particles by reducing their retention time in the froth phase. Therefore, high displacement lowered the final con grade and thus the upgrade ratio. It was found from these tests that the optimum pulsation amplitude for this feed sample was 2.8 mm.

6.8.2.3 Effect of Pulsation Frequency

Jigging frequency determines the duration of the pulsion and suction stages and therefore, can be an important parameter in determining the velocities of the minerals and gangue particles. The pulsation frequency plays a pivotal role in determining the stratification speed by altering the particles' acceleration and velocities. Hence, the effect of pulsation frequency was also studied with the rougher feed samples.

The jigging frequency was varied between 25 to 150 spm to determine the optimum value, while the other parameters were kept constant. The tests were run at a constant amplitude of 4.1 mm, air flowrate of 1 scfh and pulp density of 16%.

Appendix Figure 6-3 shows the effects of pulsation frequency. As shown, with the increase in the frequency, the copper recovery first increased but then reduced slightly. The maximum recovery of 69.5% was obtained at a frequency of 50 spm and the recovery at higher frequency decreased by a small amount to 64.6% at 150 SPM. This reduction might be attributed to the slight decrease in the feed Cu grade (0.14 %Cu *vs*. 0.12 %Cu).

An increase in the pulsation frequency at high strokes can lift and dilate the entire particle bed, even the gangue minerals can escape out of the cell as a concentrate, leading to a reduction in the final con grade and hence the upgrade ratio. This effect was seen in the tests and the upgrade ratio reduced from 13.1 to a mere 2.9 as the frequency was increased from 25 to 150 spm.

Chapter 7. Thermodynamics of the Hydrophobic Interactions in Foam Films

7.1 Abstract

When two air bubbles approach each other in an aqueous phase, a thin liquid film (TLF), also known as foam film, is formed in between. Its stability is controlled by the disjoining pressures (Π) in the film due to the van der Waals, electrical double layer, and hydrophobic forces. A foam film is stable when Π is positive and becomes unstable when it becomes negative. In the present work, a series of disjoining pressure measurements were conducted in the foam films formed in a Scheludko-Exerowa cell. The cell was equipped with a water jacket so that the measurements be conducted at different temperatures. The disjoining pressures were determined by analyzing the spatial-temporal film profiles constructed from the optical fringes recorded using a high-speed camera. The measurements were conducted with surfactant-free foam films at NaCl concentrations in the range of 10^{-3} and 10^{-1} M. The results obtained at different temperatures were analyzed to determine the thermodynamic functions of the bubble-bubble interactions. The results showed that both entropy and enthalpy decreased with film thinning but $|\Delta H| > |T\Delta S|$, suggesting that the film thinning involved enthalpy-entropy compensation. These results are consistent with those observed previously with the colloid films of water confined between macroscopic hydrophobic surfaces. Implications for the results obtained in the present work will be discussed.

7.2 Introduction

A thin liquid film (TLF) is formed when two macroscopic surfaces approach each other in a liquid phase. These TLFs provide a way to study the thermodynamics and kinetic properties of various chemical processes. Foam films are one such kind of TLF which are formed when two air bubbles come close to each other in an aqueous phase. The stability of foam films plays a vital role in various industrial processes such as froth flotation, enhanced oil recovery, personal care products, *etc*. One can tune the stability of these TLFs by adding surfactants that adsorb on the air/water interfaces and thereby, control the film kinetics.

It is believed that the process of foam film thinning is driven by the disjoining pressure which is a function of DLVO forces, *i.e.* the attractive van der Waals (vdW) force, and repulsive electrical double layer (EDL) force. This theory accurately predicts the stability of foam films with high surfactant concentrations but fails to predict fast drainage rates observed at low surfactant concentrations (Verwey and Overbeek, 1948), suggesting that an additional attractive force may drive the process of film thinning and eventual rupture. Some researchers attributed this force to hydrodynamic fluctuations (Ruckenstein and Churaev, 1991), film elasticity (Fruhner *et al*., 2000; Langevin, 2000), or thermal capillary waves (Vrij, 1966; Scheludko, 1967), while others thought that the instability of foam films arises from the hydrophobic (HP) force (Yoon and Aksoy, 1999; Wang and Yoon, 2005).

Israelachvili and Pashley (1982) were the first to directly measure the HP force in colloid films using the surface force apparatus (SFA). The measured forces were represented by a single exponential force law with a decay length of ~1 nm. Many others followed suit and reported the measurement of much longer-ranged hydrophobic forces, which was fitted to a double-exponential force law with decay lengths ranging between 10-26 nm (Yoon and Ravishankar, 1996). Some investigators suggested that hydrophobic forces are of entropic origin in the same manner as the hydrophobic effect (Israelachvili and Pashley, 1984), while others proposed mechanisms involving nanobubbles (Stöckelhuber *et al*., 2004), depletion layer (Lum *et al*., 1999), *etc*. However, the synchrotron x-ray reflectivity measurements conducted at the interface where water meets the methyl-terminated octadecylsilane monolayer with large contact angles did not show any evidence of nanobubbles but rather a depletion layer with a thickness of 0.2-0.4 nm (Poynor *et al*., 2006). Wang *et al*. (2011) and Li and Yoon (2014) showed, on the other hand, that the hydrophobic forces in colloidal films are enthalpy driven, indicating that these forces may originate from enhanced structuring of

the TLFs of confined between hydrophobic surfaces. The thermodynamic cost of building a structure is an entropy decrease.

In the present work, the disjoining pressure measurements were conducted in the surfactant free-foam films using the thin film pressure balance (TFPB) method suing a Scheludko-Exerowa cell. The measurements were conducted at different temperatures in the range of 10-20 ^{o}C to determine the excess thermodynamic properties associated with the hydrophobic interactions of foam films. The results suggested that the film thinning was driven by hydrophobic forces, the strength of which reduces as the temperature is increased. Using the Gibbs-Duhem equation, it was shown that macroscopic hydrophobic interactions entail a decrease in both enthalpy and entropy, in which case $|\Delta H| > |T\Delta S|$, which is the necessary condition for the hydrophobic interaction to be spontaneous. The same thermodynamic relation was found to be the case for the microscopic hydrophobic interactions for colloid films (Wang *et al*., 2011; Li and Yoon, 2014). This finding is the opposite of the cases for the hydrophobic interactions in nanoscale, e.g., micellization. The difference between the two different length scales of hydrophobic interactions arises from the fact that H-bonding is directional highly directional with a bond angle of 104^{o} between two H-bonds. One commonality of the hydrophobic interactions in both the macro- and nano-scale may be that both are effectively solvo-phobic interactions (Li and Yoon, 2014).

7.3 Theoretical Background

7.3.1 Disjoining Pressure Measurements

When two air bubbles approach each other, the liquid between macroscopic surfaces drains due to the changes in bubble curvatures creating the Laplace pressure (p_c) to form a thin liquid film (TLF), also known as foam film. Under the non-slip boundary condition, one can predict the rate of film thinning (or drainage rate) using the Reynolds equation (Pan *et al*., 2011),

$$\frac{\partial h}{\partial t} = \frac{1}{12\mu r}\frac{\partial}{\partial r}\left(rh^3 \frac{\partial p}{\partial r} \right) \qquad [7.1]$$

here, r is the radial distance from the center of the film, μ is the kinematic viscosity of the electrolyte solution and p is the hydrodynamic pressure. By integrating the above equation twice under the boundary conditions, $p_{r\to\infty} = 0$ and $\partial p/\partial r|_{r=0} = 0$, one can determine the hydrodynamic pressure (p) associated with the film thinning,

$$p = 12\mu \int_{r=\infty}^{r} \frac{1}{rh^3}\left[\int_{r=0}^{r} r\frac{\partial h}{\partial t} dr \right] dr \qquad [7.2]$$

Using the normal pressure balance across the film, one may write a relationship between p, capillary pressure (p_c) and the disjoining pressure (Π) as follows,

$$p = p_c - \Pi \qquad [7.3]$$

As the film thickness reduces to < ~200 nm, the film thinning is driven by the disjoining pressure (Π) which is the sum of surface forces acting in the thin liquid film and is given by the extended DLVO theory as (Xu and Yoon, 1989; Pan and Yoon, 2016; Huang and Yoon, 2019),

$$\begin{aligned} \Pi &= \Pi_d + \Pi_e + \Pi_h \\ &= -\frac{A_{232}}{6\pi h^3} - \frac{\varepsilon\varepsilon_0\kappa^2\psi_2^2}{\sinh^2(\kappa h)}\left[1-\cosh(\kappa h)\right] + \frac{C}{2\pi D}\exp\left(-\frac{h}{D}\right) \end{aligned} \qquad [7.4]$$

where, Π_d, Π_e and Π_h are the contributions due to the attractive van der Waals (vdW), repulsive electrical double layer (EDL) and attractive hydrophobic (HP) forces, respectively. A_{232} is the Hamaker constant between two air bubbles (2) in water (3), ε and ε_0 are the permittivity of the medium and vacuum, respectively. κ is the inverse of Debye length and ψ_2 is the surface potential of the air-water interface. In

the present case, hydrophobic force is expressed as a single exponential force and, C and D are the hydrophobic force rate constant and its decay length, respectively. If the disjoining pressure is repulsive ($\Pi > 0$), the film thinning process is slowed and the film reaches an equilibrium thickness (h_e) at $\Pi = p_c$, whereas, the film can catastrophically rupture, if Π (<0) is attractive. In other words, foam films will be unstable if the sum of attractive hydrophobic and vdW forces is greater than the repulsive EDL forces. In the present work, surfactant-free foam films were studied and therefore, other surface forces such as steric forces, were not considered.

The foam film drainage might be accompanied by curvature changes due to the hydrodynamic resistance to thinning. Therefore, in the current work, Young-Laplace equation is used to include the effects of the local film curvature on p_c (Chan *et al*., 2011; Pan *et al*., 2011),

$$p_c = \frac{2\gamma}{R} - \frac{\gamma}{2r}\frac{\partial}{\partial r}\left(r\frac{\partial h}{\partial r}\right) \qquad [7.5]$$

where, R is the film radius of curvature determined from the spatial temporal profiles, and γ is the surface tension of electrolyte solution. Here, the first term on the right is the macroscopic capillary pressure which might be reduced due to the changes in local curvature changes across TLF as denoted by the second term on the right. p_c can be determined by monitoring the spatial-temporal profiles which can then be used to determine the disjoining pressure (Π) as the following,

$$\Pi = \frac{2\gamma}{R} - \frac{\gamma}{2r}\frac{\partial}{\partial r}\left(r\frac{\partial h}{\partial r}\right) - 12\mu\int_{r=\infty}^{r}\frac{1}{rh^3}\left[\int_{r=0}^{r} r\frac{\partial h}{\partial t}dr\right]dr \qquad [7.6]$$

This model is known as Stokes-Reynolds-Young-Laplace model and is valid for a wide range of capillary numbers from 10^{-5} to 10^{2} (Chan *et al*., 2011; Chatzigiannakis *et al*., 2021).

In the current work, the temperature effects on the interaction between surfactant-free air-water interfaces have been studied. At an electrolyte concentration of 10^{-2} M NaCl, the temperature was changed from 10-20 °C to study the foam film thermodynamics. In a separate series of measurements, the electrolyte concentration was also varied in the range of 10^{-3} M - 10^{-1} M NaCl. For all the measurements, we used the value of non-retarded Hamaker constant A_{232} = 3.78x10^{-20} J (Israelachvili, 2011), making Π_d attractive in foam films and therefore, assisting in the film thinning processes. The air-water interfacial potential (ψ_2) and Debye length (κ^{-1}) are functions of electrolyte concentration (Harvey *et al*., 2002; Israelachvili, 2011; Smith *et al*., 2016) and have been modified accordingly. κ^{-1} dependence on temperature has also been accounted for and used in the determination of Π_e. Using these parameters, one can easily determine the contributions of Π_d and Π_e to the disjoining pressure. The values for electrolyte surface tension and viscosity were also modified according to the temperature (Jones and Ray, 1941; Vargaftik *et al*., 1983; Ozbek, 1977).

7.3.2 Thermodynamics of Thin Liquid Films

Utilizing the value of Π_h obtained as described in the previous section, one can determine ΔG associated with the hydrophobic interaction between two macroscopic surfaces using the following,

$$\Delta G = -\int_{h=\infty}^{h_0}\Pi_h(h)\,dh \qquad [7.7]$$

where h_0 is the thickness of the α-film. Thermodynamically, the excess surface free energy (ΔG) represents the change in the film tension as an infinitely thick film thins to a finite thickness, h. For constant pressure (P), it is given by the Gibbs-Duhem equation,

$$d\Delta G = -\Delta S dT - \Pi dh \qquad [7.8]$$

Here, ΔS is the corresponding excess surface entropy. Assuming that the surface force contributions due to the vdW forces, and EDL forces are not sensitive to the temperatures, as A_{232} and ψ_2 don't change

significantly, the thermodynamic quantity, ΔS can be related to ΔG, and can subsequently to Π_h at constant temperature (T) and thickness (h) as (Wang *et al*., 2011),

$$\Delta S = -\left(\frac{\partial \Delta G}{\partial T}\right)_{P,h} = -\frac{C}{2\pi}\exp\left(-\frac{h}{D}\right)\left[-\frac{d(C)}{CdT}+\frac{h}{D^2}\frac{d(D)}{dT}\right] \quad [7.9]$$

In the present work, the temperature dependence of hydrophobic force parameters was found by conducting surface force measurements at different temperatures. Excess surface enthalpies (ΔH) can then be determined using the following,

$$\Delta H = \Delta G + T\Delta S \quad [7.10]$$

7.4 Experimental and Methods

The disjoining pressure measurements were conducted using the Scheludko-Exerowa cell with a pore radius of 0.75 mm using thin film pressure balance (TFPB) method (Scheludko and Exerowa, 1959; Scheludko, 1967). Prior to each test, the cell was cleaned in a Piranha solution consisting of 7:3 by volume of sulfuric acid (H_2SO_4) and hydrogen peroxide (H_2O_2 (30% v/v, Fisher Scientific), at 90 °C for 20 minutes followed by rinsing thoroughly with ultrapure water with resistivity greater than 18.2 MΩ/cm at 25 °C. The cell after cleaning should be rendered hydrophilic. This cleaned cell was kept in the electrolyte solution for approximately an hour for the pores to get completely saturated with the test solution. The electrolyte solutions were prepared using ACS grade sodium chloride (NaCl, Fisher Chemical), which was first heated to 600 °C for 4-5 hours to remove any organic contaminant.

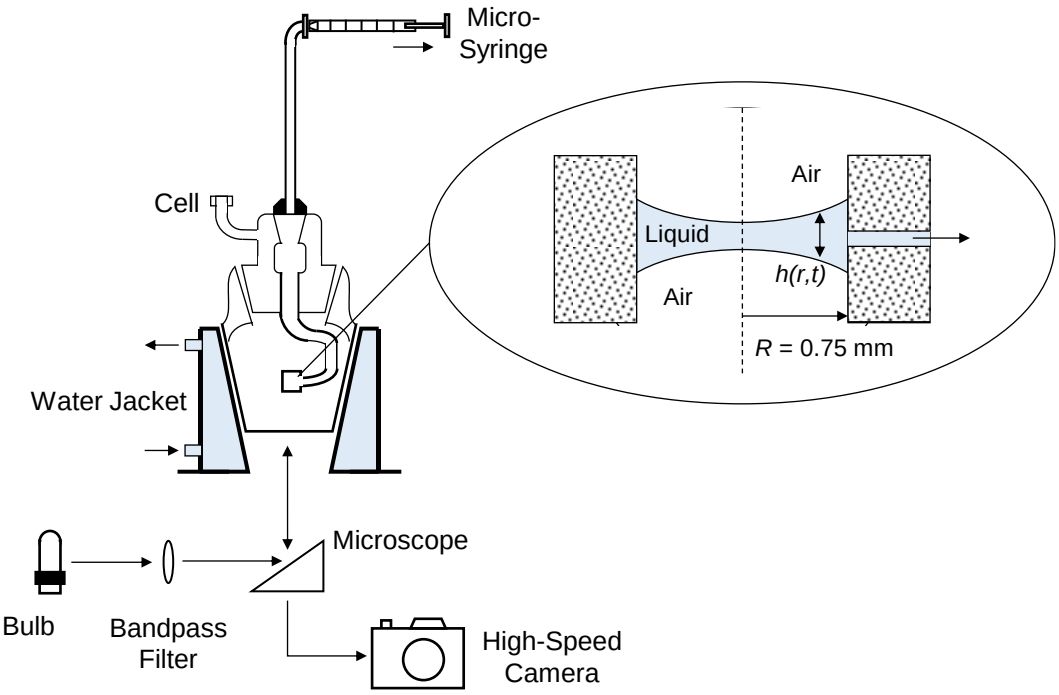

Figure 7-1. Schematic drawing of the experimental set-up used for imaging the spatiotemporal profile using Scheludko-Exerowa cell. The inset shows the bi-concave thin film of water formed in the cell with a hole radius of 0.75 mm.

Figure 7-1 shows the schematic representation of the experimental set-up used to record the spatial-temporal film profiles during the film thinning process. The cell was placed in a water-jacketed chamber so that the measurements be conducted at different temperatures with an accuracy of ± 0.1°C. The set-up included a heater/cooler accessory to run measurements at different temperatures. The chamber was mounted on a tilt stage which was adjusted to form horizontal films. The tilt stage was carefully placed on an inverted microscope (Olympus IX 51) and interference patterns were obtained using a monochromatic light with a wavelength (λ) of 480 nm. This setup was kept on a vibration isolation platform (100BM-1, Minus K Technology), which in turn was placed on a Nexus optical table (T46H, Thorlabs) to isolate the instrument from any ground vibrations. These optical fringes were recorded using a high-speed camera and were analyzed offline using the micro-interferometry technique to construct spatial-temporal film profiles. Foam film was formed by slowly removing the solution using a micro-syringe. As the TLF was thinned to ~3000-4000 nm, the film was allowed to drain freely without additional external pressure. The measured drainage rates after the fringes were illuminated (h~2000 nm) were below 1 µm/s.

7.5 Results and Discussion

In the present work, the spatial-temporal profiles (h(r,t) measurements) were derived for surfactant-free foam films with 10^{-2} M NaCl at 10, 15 and 20 °C. The effect of concentration was also studied by conducting measurements at different electrolyte concentrations ranging from 10^{-3} to 10^{-1} M NaCl. Using this information $p(h)$, $p_c(h)$, and $\Pi(h)$ were determined as per Section 7.3.1 and subsequently, the thermodynamics of hydrophobic interactions was studied according to Section 7.3.2.

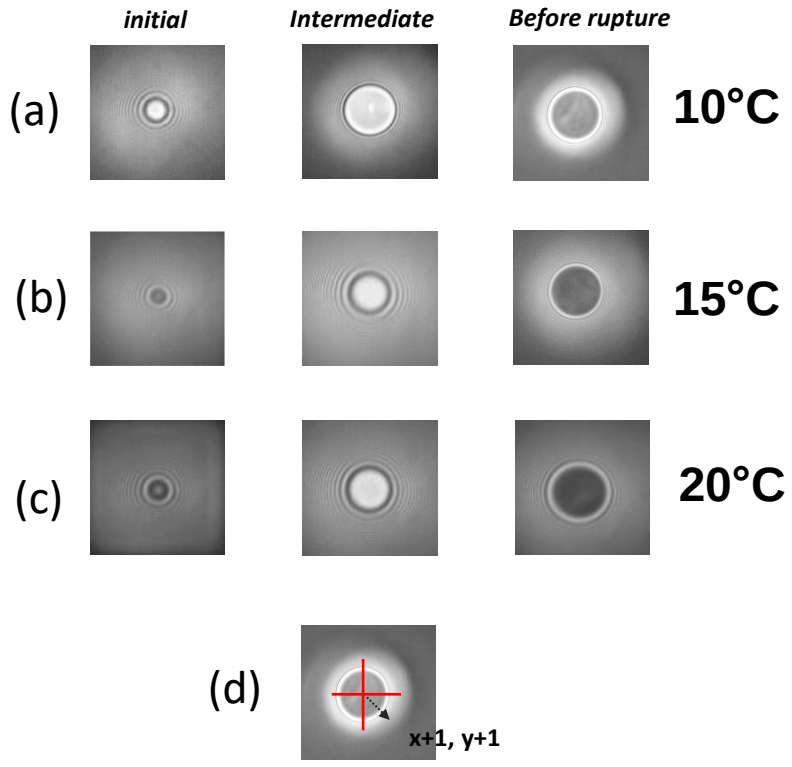

Figure 7-2. Evolution of the interference pattern during the thinning process at a rate of <1 µm/s for foam film formed with 0.01 M NaCl at a) 10°C, b) 15°C and c) 20°C; d) The film thinning process has been determined using Reynold's lubrication theory by analyzing the images by radially outward in the direction x+1, y+1 from the center.

Figure 7-2 shows the evolution of the optical fringes for the film thinning process for 10^{-2} M NaCl at 10°, 15° and 20° C. During the process of film thinning for each measurement, the drainage was accompanied with the formation of a dimple, at an intermediate stage while a common black film (CBF) was observed before the film rupture. The CBF formation at low film thickness (~10-20 nm), is consistent with what has been observed in the literature (Pugh, 1996; Wang, 2006). It was also observed that the film drainage did not look symmetric, so the film was divided into 4 quadrants and drainage was studied in 4 different regions for 10^{-2} M NaCl at 10 °C *i.e.*, x+1, y+1; x+1, y-1; x-1, y-1; and x-1, y+1 (*Figure* 7-2*d*). The surface force parameters obtained, however, remained constant across the film. This finding might be due to the fact that the drainage rate was too slow to impact the film rupture kinetics and therefore, the process of film thinning was pseudo-axisymmetric. Similar observations were also found for the measurements at different temperatures.

Figure 7-3 shows the spatial temporal profile derived from the interference patterns using the thin film interferometry principles at different temperatures. *Figure* 7-3a shows the spatial temporal profile recorded for measurements at 10° C. As can be seen in *Figure* 7-3a, even though the drainage rate was very low, we found that the process of thinning was accompanied by a dimple formation possibly due to the hydrodynamic resistance and the difference in the drainage rates at the center and at the rim (faster rates). This hydrodynamic resistance also reduces the film thinning rate as was observed from the time taken by the film to thin from ~50 nm to ~20 nm at the center. The foam film ruptured at t = 12.25 s at a critical rupture thickness (h_c) of 21.5 nm. *Figures* 7-3b and 7-3c show the spatial temporal film profiles obtained with 10^{-2} M NaCl at 15 and 20 °C, respectively. As shown, a very small dimple formation was also observed at these two temperatures.

We utilized the h(r,t) information obtained from the spatial-temporal profiles to determine the hydrodynamic (p), capillary (p_c) and disjoining pressure (Π). *Figure* 7-4a shows the calculated pressures in the film with 10^{-2} M NaCl concentration at 10 °C. The hydrodynamic pressure was determined using Reynold's lubrication theory as mentioned in Eq. [7.2]. The capillary pressure, p_c was calculated considering the local curvature changes using Young-Laplace Equation (Eq. [7.5]). Although the film thinning was accompanied by a dimple formation, the size of the dimple was relatively small and therefore, the change in film thickness with respect to the film radius was relatively flat, leading to a negligible p_c for h <100 nm. This is also a testament that the p_c doesn't drive the film thinning at very thin films. The disjoining pressure was then determined using Eq. [7.6].

The disjoining pressure (Π) is the sum of surface forces acting per unit TLF area. As the concentration of the electrolyte was fairly large (10^{-2} M), the effect of repulsive EDL forces was diminished. Π became more negative as the film thinned further to <100 nm. The disjoining pressure isotherms or Π *vs*. h shows

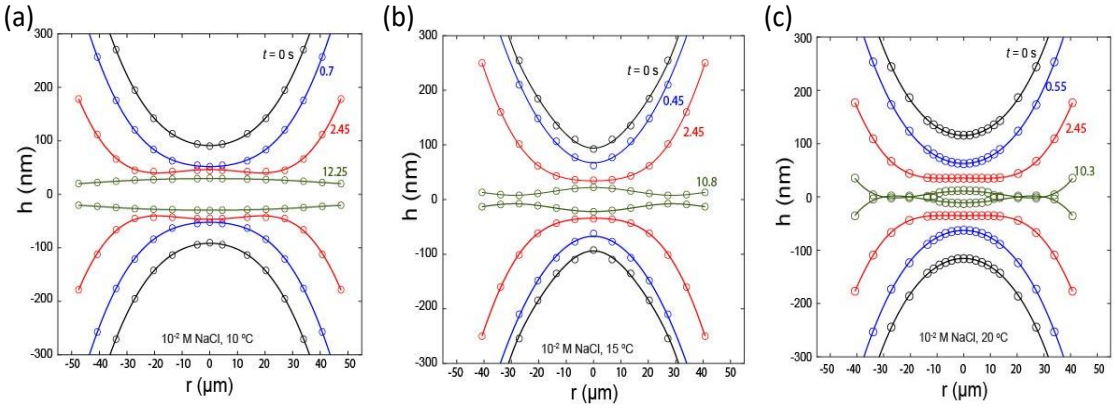

Figure 7-3. Recorded spatial temporal profiles for surfactant-free foam film with 10^{-2} M NaCl solutions at, a) 10 °C, b) 15 °C and, c) 20 °C.

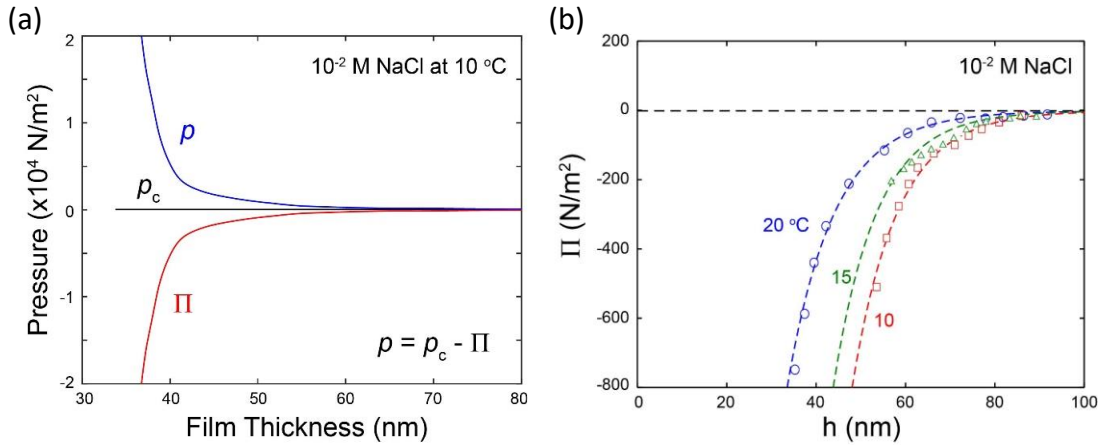

Figure 7-4. a) Hydrodynamic pressure (p), capillary pressure (p_c) and disjoining pressure (Π)determined using the Stokes Reynolds Young Laplace equation, b) Π vs. h determined at different temperatures for 10^{-2} M NaCl

an exponential decrease which might be due to the illumination of the hydrophobic forces. The hydrodynamic pressure (*p*) which represents the kinetics of the film thinning process and is essentially the same in magnitude as Π for thin films, also increased as the thickness was reduced.

The disjoining pressure isotherms Π (h) were determined at different temperatures and fitted with the extended DLVO theory (Eq. [6.4]) as plotted in *Figure* 7-4b. The measured disjoining pressure was negative indicating the presence of net attractive forces that increased as the two interfaces were brought closer. The disjoining pressure became more negative with the reduction in the temperature. For example, at h =60 nm, the disjoining pressure at 10 °C was -236.8 N/m^2 while -69.3 N/m^2 at 20 °C. This trend is similar to the one observed in colloidal films (Wang *et al*., 2011; Li and Yoon, 2014).

The contribution of different surface forces is shown in *Figure* 7-5a. It should be noted that the measured attractive disjoining pressure was substantially more negative and longer-ranged than the contributions from the vdW forces (Π_d) described by the following equation,

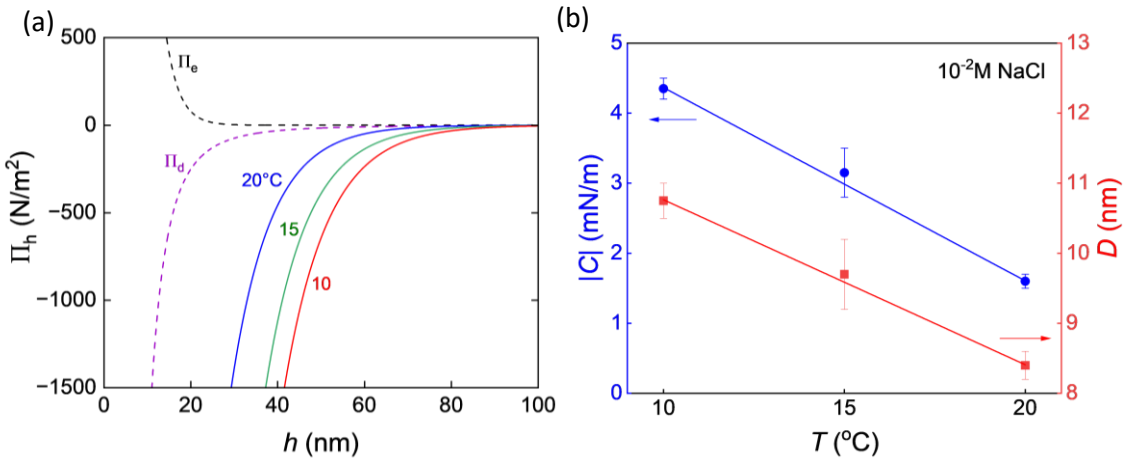

Figure 7-5. a) Π_d *vs*. *h* determined at different temperatures for 10^{-2} M NaCl and, b) the hydrophobic force constant (C) and its decay length (D) determined using the extended DLVO theory.

$$\Pi_d = -\frac{A_{232}}{6\pi h^3} \quad [7.11]$$

where the values of A_{232} = 3.78x10^{-20} J for 10^{-2} M NaCl was found from the literature (Israelachvili, 2011) and did not vary in the temperature range studied. As shown in *Figure* 7-5a, at a high electrolyte concentration of 10^{-2} M NaCl, the EDL forces contributions (Π_e) were also short-ranged due to the screening effect and were described by the following equation,

$$\Pi_e = -\frac{\varepsilon\varepsilon_0\kappa^2\psi_2^2}{\sinh^2(\kappa h)}\left[1-\cosh(\kappa h)\right] \quad [7.12]$$

The Debye length (κ^{-1}) is temperature dependent however, due to the presence of electrolyte, temperature variations did not significantly affect the strength of Π_e. The EDL force parameters *i.e.* the surface potentials (ψ_2) and κ^{-1} were also taken from the literature (Harvey *et al.*, 2002; Israelachvili, 2011; Smith *et al*., 2016) and are tabulated in *Table* 7-1, along with the surface tension (γ) and kinematic viscosity (μ) of the electrolyte solutions for the conditions studied.

Contribution from the hydrophobic force (Π_h) was determined by subtracting the contribution from Π_d and Π_e from Π in accordance to Eq. [7.4]. As can be seen from *Figure* 7-5a, Π_h was substantially more negative and longer-ranged than those due to to the vdW forces suggesting that that the macroscopic-scale film thinning is governed by the HP force which was represented by the single exponential force law

$$\Pi_h = \frac{C}{2\pi D}\exp\left(-\frac{h}{D}\right) \quad [7.13]$$

The HP force parameters, *C* and *D*, determined in this manner are shown in *Figure* 7-5b. It was found that both of these parameters increased in magnitude as the system temperature was reduced. The absolute value of the HP force constant, |C|, denoting its strength increased from 1.6 mN/m to 4.35 mN/m while the decay length, *D*, was extended from 8.4 nm to 10.75 nm as the temperature dropped from 20 to 10 °C. The HP force determined in the present case is weaker than that observed by Wang (2006). This finding might be due to the fact that the local curvature changes were also accounted for in the prediction of HP force (Eq. [7.5] and [7.6]) contrary to the assumption of flat curvature.

In the present work, we determined the excess surface free energy (ΔG) due to the hydrophobic interactions using Eq. [7.7]. The results are plotted as a function of film thickness (h) and temperature (T) in *Figure* 7-6a. ΔG was negative during the process of thinning and its magnitude increased with the reduction in h and T. It should be noted from *Figure* 7-5b that the slope of d|C|/dT and dD/dT were both negative. Therefore using Eq. [7.9], it can be easily derived that ΔS <0 for the hydrophobic interaction between two macroscopic air-water interfaces. *Figure* 7-6b shows the changes in the ΔS *vs.* h at different T. As shown, ΔS became more negative as the film thickness and temperature were reduced indicating a reduction in the degree of freedom or increased ordering due to the formation of new structures in the TLF between two macroscopic interfaces. ΔH was also determined using Eq. [7.10] and plotted as a function of h as shown in *Figure* 7-5c. ΔH also grew more negative as the foam film thickness and temperature was

Table 7-1. Surface force parameters for foam films with 10^{-2} M NaCl solutions at different temperatures

T (°C)	γ (mN/m)	μ (10^{-3} Pa.s)	A_{232} (10^{-20} J)	ψ_2 (mV)	κ^{-1} (nm)	C (mN/m)	D (nm)
10	74.255	1.31	3.78	-30	3.08	-4.35±0.15	10.75±0.25
15	73.525	1.14	3.78	-30	3.05	-3.15±0.35	9.70±0.50
20	72.800	1.01	3.78	-30	3.03	-1.60±0.10	8.40±0.20

reduced suggesting the formation of stable structures in the TLF. These findings are consistent with those presented by Wang *et al*. (2011) and Li and Yoon (2014).

Water can be retained in a confined space between hydrophobic surfaces, for example, inside carbon nanotubes and between two graphene plates (Algara-Siller *et al*., 2015; Cai *et al*., 2019). Water being a highly cohesive liquid, is involved in an enhanced H-bond network at molecular distances, to minimize the disruption of its inherent structure. This increased H-bond lowers the density of water molecules in the confined space. These new-formed structures resemble the ice-like structures found in super-cooled water and are often termed as low-density liquid (LDL) (Roentgen, 1892). Along with the ice-like structure, these LDLs have also been found to exist as pentagonal dodecahedron (Pauling, 1961), clathrate cages (Stillinger, 1980), *etc*. Some researchers have also found evidence of these LDL-like species to exist in the bulk water at ambient conditions (Mallamace *et al*., 2007 a,b; Mallamace, 2009). Sum frequency generation (SFG) spectra for the air-water interface, have also shown that the surface water molecules have lower H-bonds and entail dangling -OH bonds (Du *et al*., 1994; Scatena *et al*., 2001). Therefore, when two such surfaces are brought closer, water molecules can form structures in the TLF to reduce the free energy of the thin water film.

As the foam film was thinned or in other words, the two air-water interfaces were brought towards each other, ΔS and ΔH became more negative indicating the formation of more structures. However, if we look carefully at *Figure* 7-6b, the excess entropy change per unit area of TLF is small (~10^{-6} $Jm^{-2}K^{-1}$), indicating that the number of new structures formed is not large. The entropy reduction for a 5 nm water film that undergoes freezing was estimated to be -6 $mJm^{-2}K^{-1}$ (Eriksson and Yoon, 2007). Nevertheless, this small

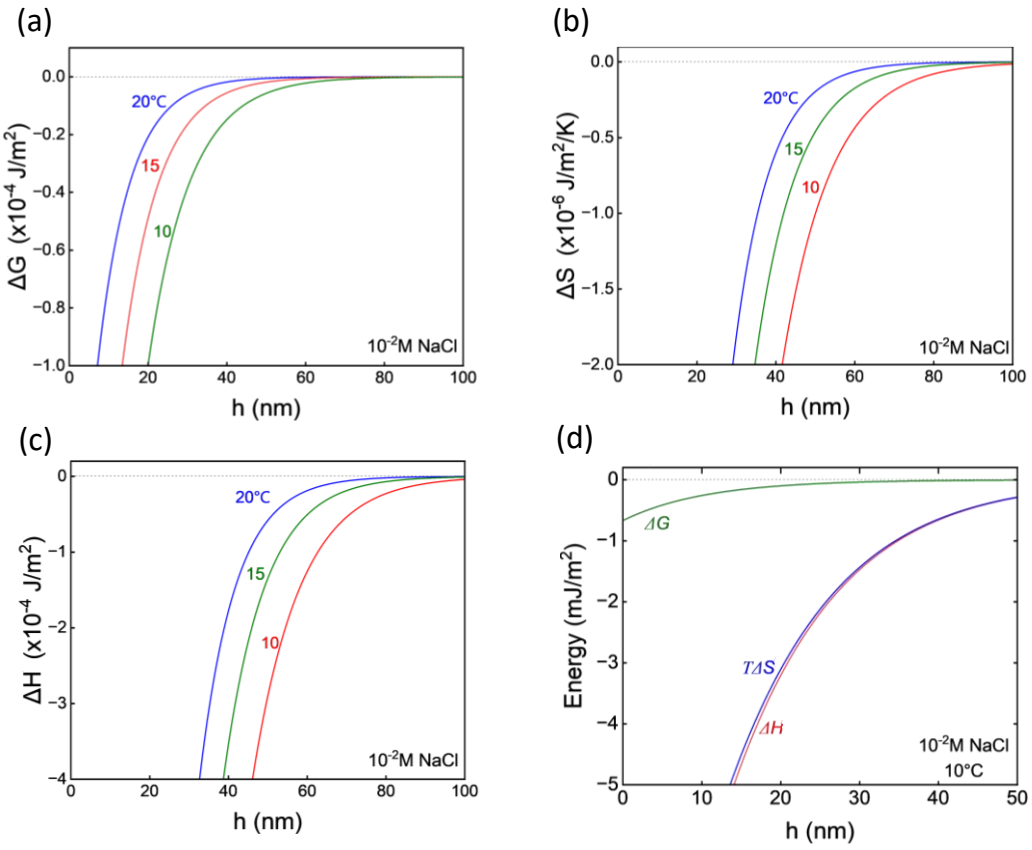

Figure 7-6. Changes in the a). excess surface free energy (ΔG), b). Excess surface entropy (ΔS) and, c). excess surface enthalpy (ΔH) in the surfactant-free foam film with respect to film thickness (h); d) entropy-enthalpy compensation at 10 C.

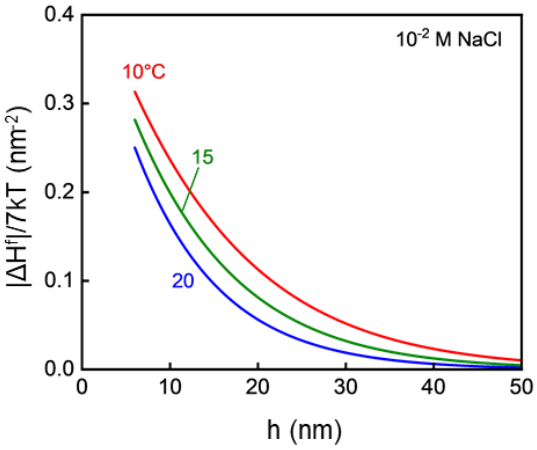

Figure 7-7. Changes in the excess H-bond numbers per unit area vs. film thickness (h) at 10 and 20 °C. The number of H-bonds increase with the decrease in temperature and film thickness.

degree of structuring in the TLF provides evidence that long-ranged hydrophobic interactions are also driven by the structure of water. Molecular Dynamics (MD) simulations have proved the existence of such structural changes at a few molecular distances (Å) although, haven't recognized it at the order of thickness (nm) discussed in this work. Such discrepancy might arise from the fact that the energy changes accompanied during the long-ranged interactions are minute (~10^{-3}-10^{-2} kT/nm^2) whereas, MD has difficulties in accurately quantifying energies below ~0.1 kT/molecule (Eriksson *et al*., 1989).

The thermodynamic quantities *i.e.* ΔG, ΔH, and ΔS were plotted together as shown in *Figure* 7-6d. When both enthalpy and entropy decrease, it is necessary that $|\Delta H| > |T\Delta S|$ for ΔG to be negative for the reaction to be spontaneous. Therefore, it was observed that the hydrophobic interaction between two air-water interfaces was enthalpy-driven. This is contrary to the molecular scale hydrophobic interaction which is rather entropy-driven. It has been pointed out by Chandler (2005) and others (Rajamani *et al*., 2005) that the hydrophobic hydration thermodynamics changes from being entropic to enthalpic with the increase in the length scale of the hydrated molecules due to the reduction in the molecular curvature. Similar might be the case of macroscopic hydrophobic interactions presented in this study.

At the hydrophobic surface, the water molecules are not able to surround the extended surfaces forcing them to re-structure among themselves to minimize free energy loss. This finding can, therefore, be thought to be in similar line with the theory proposed by Stillinger (1980) and Speedy (1984) who attributed the hydrophobic effect to the structuring of water molecules. This hydrophobic force perhaps might be the reason why surfactants, which reduce the hydrophobic forces, are required to form stable foams which otherwise would spontaneously coalesce. The formation of partial clathrates might also lead to a reduction in the rotational entropy which is contrary to what has been seen in the simulations of water in confined spaces (Chakraborty and Chattaraj, 2019), although is consistent with the ordering of the water layer

Table 7-2. Surface force parameters for different electrolyte concentrations at 20 °C

NaCl (M)	γ (mN/m)	μ (10^{-3} Pa.s)	A_{232} (10^{-20} J)	ψ_2 (mV)	κ^{-1} (nm)	C (mN/m)	D (nm)
10^{-3}	72.743	1.003	3.78	-50	9.68	-2.0	11.0
10^{-2}	72.800	1.004	3.78	-30	3.03	-1.5	8.2
10^{-1}	72.950	1.010	3.78	-20	0.91	-1.1	5.5

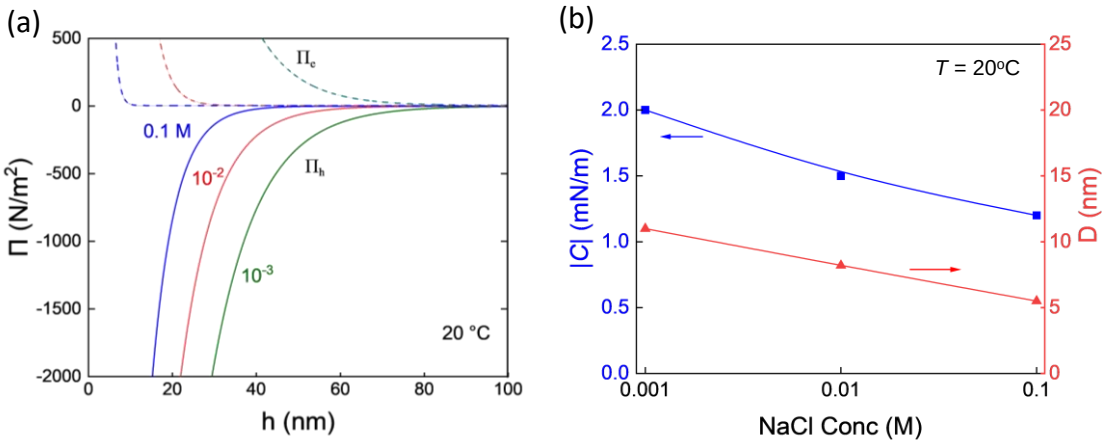

Figure 7-8. (a) The effect of electrolyte (NaCl) concentration on the disjoining pressure isotherm with respect to film thickness (*h*). (b) The effect of electrolyte concentration on hydrophobic forces constant (|*C*|) and decay length (*D*).

confined between hydrophobic surfaces when the layer thickness is less than 2 nm. (Chaplin, 2010). This might be due to the fact that air bubbles are super-hydrophobic in nature, therefore, allowing for higher strength of H-bonding even at nm scale.

Figure 7-6d also shows that the foam film thinning entails high enthalpy-entropy compensation. The enthalpy-entropy compensation occurs due to the loss of entropy when the H-bond number increases. It should be noted that the compensation is more in the foam film as compared to the colloidal film previously studied (Wang *et al.*, 2011). Foam film interaction occurs between two deformable interfaces which might lead to more structuring in the TLF entailing significantly higher entropy cost. *Figure* 7-7 shows that indeed, the foam film interaction even with concentrated electrolyte solution, leads to more H-bonds formation below 50 nm of film thickness. The H-bond number was determined by assuming that the increase in the negative enthalpy is solely due to the formation of H-bonds between water molecules and that the energy of H-bond formation is 7 *kT*. In the present case, the excess H-bonds at a film thickness of 20 nm were 0.054 /nm^2 in comparison to ~0.03 /nm^2 for the colloidal film formed between thiol-coated gold surfaces with a contact angle of 105° (Wang *et al.*, 2011).

It can also be shown from *Figure* 7-7 that, the hydrogen bonds at 20 °C increase once $h < 50$ nm. In the case of colloidal films studied by Wang *et al.*, the structuring was longer ranged. This discrepancy might be due to the following reasons; first, the foam film interactions were measured with concentrated electrolyte solutions (10^{-2} M NaCl) rather than pure water as in the case of colloidal film, which might lead to a reduction in the long-range hydrophobic force. The presence of electrolytes is known to reduce the strength of hydrophobic force as the Cl^- ions can disrupt the H-bond network of water (Raymond and Richmond, 2004).

The effect of electrolyte concentration was also studied in the present work. The NaCl concentration was varied from 10^{-3} M to 0.1 M NaCl. The measurements were conducted at 20 °C and the spatial-temporal profiles were used to determine the disjoining pressure using Eq. [7.1]- [7.6]. The values for the vdW and EDL force constants are presented in *Table* 7-2. Note that with increasing salt concentration, Debye length (κ^{-1}) reduces reducing the extent of repulsive EDL forces. As discussed before, the vdW forces are short range, therefore, we assumed a constant vdW force across all the concentrations studied. Using these force parameters, *C* and *D* values were calculated which are plotted in *Figure* 7-8. As the concentration of NaCl increased, the magnitude of both *C* and *D* values reduced thereby reducing the extent of hydrophobic forces. This is in line with the findings of various other researchers (Wang and Yoon, 2004; Zhang *et al.*, 2005; Tsao *et al.*, 1993).

The dependency of HP force strength on NaCl concentration might indicate that HP force is of an electrostatic nature and can originate due to the presence of large mobile patches of charge species on the interface. However, a similar effect of NaCl concentration was also observed in the wetting films with xanthate-coated gold surfaces where the chemisorbed xanthate formed a uniform layer of neutral and immobile species refuting the electrostatic origin of HP force (Pan and Yoon, 2018). On the other hand, the trend of declining HP forces with salt concentration is coherent with the structural origin of hydrophobic force. As the electrolyte concentration increases, the H-bonded water network is disrupted, reducing the cohesive energy of the water, and making the HP force weaker and shorter-ranged, similar to what was observed in changes in the air-water interface SFG spectra by the addition of H_2SO_4 (Schultz *et al.*, 2003). Raymond and Richmond (2003) found that the NaCl addition reduced the tetrahedrally coordinated H-bonds at the air-water interface which might also be the reason for the results obtained here.

Figure 7-7 shows that the number of H-bonds increases as the film thickness is reduced which is also consistent with the model of Eriksson *et al.* (1989), according to which structuring of water increases with decreasing *h*. Based on the results shown and discussed above, a qualitative model for the interaction of two air-water interfaces has been proposed. This model is similar to the partial clathrate model described by Wang *et al.* (2011). *Figure* 7-9a shows the arrangement of water molecules in a thick foam film.As found from the Sum-Frequency Vibrational Spectroscopic (SFVS) studies (Scatena et al., 2001), , the model shows the presence of dangling OH-groups present at the air/water interface.. The water molecules in the middle of the foam film show the presence of low-density liquid (LDL) clathrates. Mallamace *et al.* (2008) conducted FTIR and Raman spectroscopic studies on confined water molecules to show the formation of LDL species at ambient temperatures (Mallamace, *et al.*, 2007a,b).

As a foam film thins, the population of partial clathrates (or LDLs) should increase as depicted in *Figure* 7-9b. This model provides an explanation for the decrease in -ΔH with decreasing film thickness (*h*) and temperature. Mallamace *et al*. (2007) showed that LDL formation population increases with decreasing temperature.

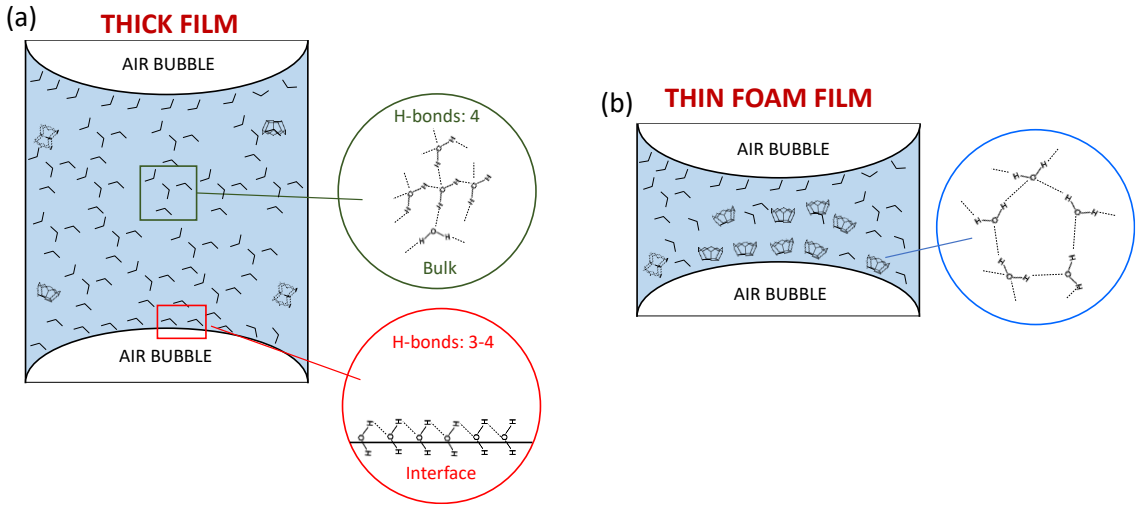

Figure 7-9. A possible mechanism of changes in the water structure during the film thinning process. (a) The H-bond number in the air-water interface in a thick film is less than 4 due to the orientation of H atom towards the water devoid interface. (b) in a case of thin foam film, the LDL is formed where the water structures with the neighboring water molecules increasing the H-bond number driving the film thinning process.

7.6 Summary and Conclusions

A series of disjoining pressure measurements were conducted with surfactant-free foam films formed with electrolyte solutions. These experiments were conducted at different temperatures and at concentrations. The thermodynamic data show that film thinning entails decreases in both enthalpy and entropy, with $|\Delta H| > |T\Delta S|$. This shows that the film thinning is driven by the enthalpy changes associated with the formation of partial clathrates (or LDL), with the entropy decrease representing a thermodynamic costs of building H-bonded structures. It has been found also that both $-\Delta H$ and $-\Delta S$ increases with decreasing film (h) thickness, indicating that it is easier to build H-bonded structures in confined space, while minimizing the entropy costs.

The thermodynamic analysis of the surface force measurements conducted in the present work clearly show that foam films are destabilized by the hydrophobic force, while the conventional wisdom has been that foam films are destabilized by the attractive van der Waals (vdW) force. The results presented in the present work show indeed that the vdW forces are indeed attractive in foam film; however, they are substantially weaker than the hydrophobic forces. It has been found that the hydrophobic forces in foam films become weaker in the presence of NaCl, which may be attributed to the structure breaking role of NaCl.

7.7 References

A. Scheludko, Thin liquid films, *Adv. Colloid Interface Sci.* 1 (1967) 391–464.

Algara-Siller, G., Lehtinen, O., Wang, F. C., Nair, R. R., Kaiser, U., Wu, H. A., ... & Grigorieva, I. V. (2015). Square ice in graphene nanocapillaries. *Nature*, 519(7544), 443-445.

Cai, X., Xie, W. J., Yang, Y., Long, Z., Zhang, J., Qiao, Z., ... & Gao, Y. Q. (2019). Structure of water confined between two parallel graphene plates. *The Journal of chemical physics*, 150(12).

Chakraborty, D., & Chattaraj, P. K. (2019). Bonding, reactivity, and dynamics in confined systems. *The Journal of Physical Chemistry A*, 123(21), 4513-4531.

Chan, D. Y., Klaseboer, E., & Manica, R. (2011). Theory of non-equilibrium force measurements involving deformable drops and bubbles. *Advances in colloid and interface science*, 165(2), 70-90.

Chandler, D. (2005). Interfaces and the driving force of hydrophobic assembly. *Nature*, 437(7059), 640-647.

Chaplin, M. F. (2010). Structuring and behaviour of water in nanochannels and confined spaces. *Adsorption and phase behaviour in nanochannels and nanotubes*, 241-255.

Chatzigiannakis, E., Jaensson, N., & Vermant, J. (2021). Thin liquid films: Where hydrodynamics, capillarity, surface stresses and intermolecular forces meet. *Current Opinion in Colloid & Interface Scienc*e, 53, 101441.

Du, Q., Freysz, E., & Shen, Y. R. (1994). Surface vibrational spectroscopic studies of hydrogen bonding and hydrophobicity. *Science*, 264(5160), 826-828.

Eriksson, J. C., Ljunggren, S., & Claesson, P. M. (1989). A phenomenological theory of long-range hydrophobic attraction forces based on a square-gradient variational approach. *Journal of the Chemical Society, Faraday Transactions 2: Molecular and Chemical Physics*, 85(3), 163-176.

Eriksson, J. C., & Yoon, R. H. (2007). Hydrophobic attraction in the light of thin-film thermodynamics. *Colloid Stability-The Role of Surface Forces*, 99-131.

Fruhner, H., Wantke, K. D., & Lunkenheimer, K. (2000). Relationship between surface dilational properties and foam stability. *Colloids and Surfaces A: Physicochemical and Engineering Aspects*, 162(1-3), 193-202.

Harvey, P. A., Nguyen, A. V., & Evans, G. M. (2002). Influence of electrical double-layer interaction on coal flotation. *Journal of Colloid and Interface Science*, 250(2), 337-343.

Huang, K., & Yoon, R. H. (2019). Surface forces in the thin liquid films (TLFs) of water confined between n-alkane drops and hydrophobic gold surfaces. *Langmuir*, 35(48), 15681-15691.

Israelachvili, J. N., Intermolecular and surface forces: revised third edition. *Academic press*: 2011.

Israelachvili, J., & Pashley, R. (1982). The hydrophobic interaction is long range, decaying exponentially with distance. *Nature*, 300(5890), 341-342.

Jones, G., & Ray, W. A. (1941). The surface tension of solutions of electrolytes as a function of the concentration II. *Journal of the American Chemical Society*, 63(1), 288-294.

Langevin, D. (2000). Influence of interfacial rheology on foam and emulsion properties. *Advances in colloid and interface science*, 88(1-2), 209-222.

Li, Z., & Yoon, R. H. (2014). Thermodynamics of solvophobic interaction between hydrophobic surfaces in ethanol. *Langmuir*, 30(44), 13312-13320.

Lum, K., Chandler, D., & Weeks, J. D. (1999). Hydrophobicity at small and large length scales. *The Journal of Physical Chemistry B*, 103(22), 4570-4577.

Mallamace, F. (2009). The liquid water polymorphism. *Proceedings of the National Academy of Sciences*, 106(36), 15097-15098.

Mallamace, F., Branca, C., Broccio, M., Corsaro, C., Mou, C. Y., & Chen, S. H. (2007). The anomalous behavior of the density of water in the range 30 K< T< 373 K. *Proceedings of the National Academy of Sciences*, *104*(47), 18387-18391.

Mallamace, F., Broccio, M., Corsaro, C., Faraone, A., Majolino, D., Venuti, V., ... & Chen, S. H. (2007). Evidence of the existence of the low-density liquid phase in supercooled, confined water. *Proceedings of the national academy of sciences*, *104*(2), 424-428.

Ozbek, H., Fair, J. A., & Phillips, S. L. (1977). Viscosity of aqueous sodium chloride solutions from 0-150^{o} c (No. LBL-5931). Lawrence Berkeley National Lab. (LBNL), Berkeley, CA (United States).

Pan, L., & Yoon, R. H. (2016). Measurement of hydrophobic forces in thin liquid films of water between bubbles and xanthate-treated gold surfaces. *Minerals Engineering*, 98, 240-250.

Pan, L., & Yoon, R. H. (2018). Effects of electrolytes on the stability of wetting films: Implications on seawater flotation. *Minerals Engineering*, 122, 1-9.

Pan, L., Jung, S., & Yoon, R. H. (2011). Effect of hydrophobicity on the stability of the wetting films of water formed on gold surfaces. *Journal of colloid and interface science*, 361(1), 321-330.

Pashley, R. M., & Israelachvili, J. N. (1984). Molecular layering of water in thin films between mica surfaces and its relation to hydration forces. *Journal of colloid and interface science*, 101(2), 511-523.

Pauling, L. (1961). A Molecular Theory of General Anesthesia: Anesthesia is attributed to the formation in the brain of minute hydrate crystals of the clathrate type. *Science*, 134(3471), 15-21.

Poynor, A., Hong, L., Robinson, I. K., Granick, S., Zhang, Z., & Fenter, P. A. (2006). How water meets a hydrophobic surface. *Physical review letters*, 97(26), 266101.

Pugh, R. J. (1996). Foaming, foam films, antifoaming and defoaming. *Advances in colloid and interface science*, 64, 67-142.

Raymond, E. A., & Richmond, G. L. (2004). Probing the molecular structure and bonding of the surface of aqueous salt solutions. *The Journal of Physical Chemistry B*, *108*(16), 5051-5059.

Rajamani, S., Truskett, T. M., & Garde, S. (2005). Hydrophobic hydration from small to large lengthscales: Understanding and manipulating the crossover. *Proceedings of the National Academy of Sciences*, 102(27), 9475-9480.

Roentgen, W.C. (1892). On the constitution of liquid water. *Annals of Physics*, 281 (1), 91-97.

Ruckenstein, E., & Churaev, N. (1991). A possible hydrodynamic origin of the forces of hydrophobic attraction. *Journal of colloid and interface science*, 147(2), 535-538.

Scatena, L. F., Brown, M. G., & Richmond, G. L. (2001). Water at hydrophobic surfaces: weak hydrogen bonding and strong orientation effects. *Science*, 292(5518), 908-912.

Scheludko, A., & Exerowa, D. (1959). Instrument for interferometric measurements of the thickness of microscopic foam films. *CR Acad. Bulg. Sci*, *7*, 123-132.

Shultz, M. J., Baldelli, S., Schnitzer, C., & Simonelli, D. (2003). Water Confined at the Liquid-Air Interface. In Water in Confining Geometries (pp. 249-273). Berlin, Heidelberg: Springer Berlin Heidelberg.

Smith, A. M., Lee, A. A., & Perkin, S. (2016). The electrostatic screening length in concentrated electrolytes increases with concentration. *The journal of physical chemistry letters*, 7(12), 2157-2163.

Speedy, R. J. (1984). Self-replicating structures in water. *The Journal of Physical Chemistry*, 88(15), 3364-3373.

Stillinger, F. H. (1980). Water revisited. *Science*, 209(4455), 451-457.

Stöckelhuber, K. W., Radoev, B., Wenger, A., & Schulze, H. J. (2004). Rupture of wetting films caused by nanobubbles. Langmuir, 20(1), 164-168.

Tsao, Y. H., Evans, D. F., & Wennerstroem, H. (1993). Long-range attraction between a hydrophobic surface and a polar surface is stronger than that between two hydrophobic surfaces. Langmuir, 9(3), 779-785.

Vargaftik, N. B., Volkov, B. N., & Voljak, L. D. (1983). International tables of the surface tension of water. Journal of Physical and Chemical Reference Data, 12(3), 817-820.

Verwey, E. J. W., & Overbeek, J. T. G. (1955). Theory of the stability of lyophobic colloids. Journal of Colloid Science, 10(2), 224-225.

Vrij, A. (1966). Possible mechanism for the spontaneous rupture of thin, free liquid films. Discussions of the Faraday Society, 42, 23-33.

Wang, J., Yoon, R. H., & Eriksson, J. C. (2011). Excess thermodynamic properties of thin water films confined between hydrophobized gold surfaces. Journal of colloid and interface science, 364(1), 257-263.

Wang, L. (2006). Surface forces in foam films (Doctoral dissertation, Virginia Tech).

Wang, L., & Yoon, R. H. (2004). Hydrophobic forces in the foam films stabilized by sodium dodecyl sulfate: effect of electrolyte. Langmuir, 20(26), 11457-11464.

Wang, L., & Yoon, R. H. (2008). Effects of surface forces and film elasticity on foam stability. International Journal of Mineral Processing, 85(4), 101-110.

Xu, Z., & Yoon, R. H. (1989). The role of hydrophobia interactions in coagulation. Journal of colloid and interface science, 132(2), 532-541.

Yoon, R. H., & Aksoy, B. S. (1999). Hydrophobic forces in thin water films stabilized by dodecylammonium chloride. Journal of colloid and interface science, 211(1), 1-10.

Yoon, R. H., & Ravishankar, S. A. (1996). Long-range hydrophobic forces between mica surfaces in dodecylammonium chloride solutions in the presence of dodecanol. Journal of colloid and interface science, 179(2), 391-402.

Zhang, J., Yoon, R. H., Mao, M., & Ducker, W. A. (2005). Effects of degassing and ionic strength on AFM force measurements in octadecyltrimethylammonium chloride solutions. Langmuir, 21(13), 5831-5841.

Chapter 8. Thermodynamics of the Hydrophobic Interactions in Emulsion Films

8.1 Abstract

When two oil droplets approach each other in an aqueous phase, a thin liquid film (TLF) of water, also known as oil-in-water (o/w) emulsion film, is formed in between. Its stability is controlled by the disjoining pressures (Π) due to the surface forces in the film. The film is stable when $\Pi > 0$ and becomes unstable when $\Pi < 0$. In the present work, a series of disjoining pressure measurements were conducted with surfactant-free films formed between two toluene droplets in water in a Scheludko-Exerowa cell equipped with a water jacket to allow measurements at controlled temperatures. The disjoining pressures (or surface forces per unit area) were measured by analyzing the spatial-temporal film profiles constructed from the optical fringes recorded using a high-speed camera. The optical fringes recorded at different temperatures were analyzed to obtain the pressure balance between the hydrodynamic pressure (p), capillary pressure (p_c), and Π using the Reynolds Lubrication theory, Young-Laplace equation, and extended DLVO theory, respectively. The results show that the driving force in film thinning, and rupture is the hydrophobic force rather than the van der Waals and electrical double-layer forces.

The force measurements conducted at three different temperatures, i.e., 10, 15, and 20°C, were analyzed to determine the changes in the thermodynamic properties of the film with film thickness to find that the thinning and rupture of the o/w films are driven by the hydrophobic forces associated with the decrease in film enthalpy under conditions of $|\Delta H| > |T\Delta S|$. This finding suggests that the hydrophobic force may arise from building H-bonded water structures mimicking the partial clathrates (or low-density liquids) formed in confined spaces in supercooled water, with the entropy change ($\Delta S < 0$) representing a thermodynamic cost of building the structures. This finding is akin to that found with foam films (Chapter 7).

8.2 Introduction

In flotation, air bubbles are used to collect hydrophobic particles from an aqueous phase. The collection mechanism is controlled by the surface forces in the wetting films, which include the van der Waals (vdW), electrical double-layer (EDL), and hydrophobic (HP) forces. In most flotation systems, the first two are repulsive, and the third is attractive, in which case, the third must be attractive to serve as the driving force for the bubble-particle interactions in flotation while the EDL force can present an energy barrier (E_1) for bubble-particle attachment. E_1 can be reduced by controlling the EDL and HP forces, and thereby increase the flotation kinetics.

A fundamental problem associated with flotation is that the vdW force for bubble-particle interaction is repulsive, which gives rise to low contact angles (θ) typically less than 90°. This problem can be overcome by using oil drops rather than air bubbles for flotation. Figure 8-1 compares the contact angles measured on the same substrate (thiol-coated gold) using an air bubble and an oil drop. As shown, the latter formed nearly twice as large a contact angle as the air bubble, which can be attributed to the positive Hamaker constant for the oil-gold interaction. On the other hand, oil is costly to use for flotation. To address the cost issue, methods of using recyclable oils, *e.g.*, pentane, iso-hexane, that can be readily recovered and

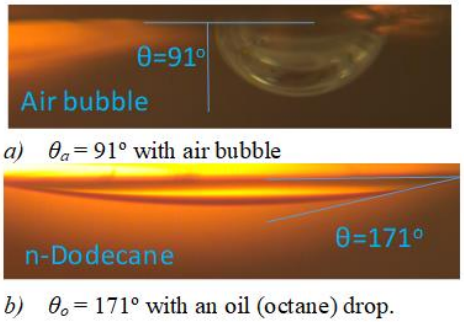

Figure 8-1. Comparison of contact angles of thiol-coated gold using air bubble (90°) and octane drop (171°).

recycled by vaporization/condensation owing to their low vaporization enthalpy. Due to the large oil contact angles, the new flotation process, known as hydrophobic-hydrophilic separation (HHS) and/or two-liquid flotation (TLF), is more efficient than air bubble flotation (Yoon, US Patent 9518241). In effect, these processes are akin to solvent extraction, which is commercially used to separate nano-size materials, *e.g.*, Cu^{2+}, Co^{2+} ions in solution, the HHS and TLF processed do not have lower particle size limits. On the contrary, air bubble flotation becomes inefficient when particle sizes are smaller than ~20 μm.

The objective of the present investigation (Chapter 8) is to study the stability of the thin liquid films of water confined between two oil drops. The investigation began with the measurement of surface forces in the emulsion films using the Scheludko-Exerowa cell in the same manner as described for the study of foam films. In each measurement, two oil drops were pushed against each other while monitoring the curvature to determine the changes in capillary pressure (P_c), hydrodynamic pressure (P), and disjoining pressure (Π) as a function of film thickness (h) using the Young-Laplace, Reynolds, and Extended DLVO theories, respectively. The measurements were conducted at different temperatures to determine the changes in film entropy (ΔS), enthalpy (ΔH) and Gibbs free energies. The thermodynamic data have been used to discuss the origin of the hydrophobic force in emulsion films. All measurements were conducted using toluene as oil phase due to its high reflective index with $n = 1.49$.

The results presented in Chapter 7 showed evidence for the presence of hydrophobic force in foam films, which corroborated well with the results obtained using the vibrational sum frequency spectroscopy (VSFS). Nevertheless, debates are ongoing if air bubbles in water are indeed hydrophobic. On the other hand, no one doubts that oil drops are hydrophobic. In this regard, finding the hydrophobic force in emulsion films may confirm the results obtained with foam films and shed light on finding the origin of the hydrophobic forces in the TLFs of water confined between air bubbles and oil drops.

8.3 Theoretical Background

8.3.1 Disjoining Pressure Measurements

When two deformable macroscopic surfaces approach each other, the liquid in between drains due to the changes in bubble curvatures or Laplace pressure (p_c) and forms a thin liquid film (TLF). If a thin film of water is formed between two deformable oil droplets, the thin film of water is referred to as oil-in-water (o/w) emulsion film. Under the non-slip boundary condition, one can predict the rate of film thinning (or drainage rate) using the Reynolds equation,

$$\frac{\partial h}{\partial t} = \frac{1}{12\mu r}\frac{\partial}{\partial r}\left(rh^3 \frac{\partial p}{\partial r} \right) \qquad [8.1]$$

where r is the radial distance from the center of the film, μ is the kinematic viscosity of electrolyte solution and p is the hydrodynamic pressure. By integrating Eq. [8.1] again under the boundary conditions of $p_{r\to\infty} = 0$ and $\partial p/\partial r|_{r=0} = 0$, one calculate the hydrodynamic pressure (p) as follows,

$$p = 12\mu \int_{r=\infty}^{r} \frac{1}{rh^3}\left[\int_{r=0}^{r} r\frac{\partial h}{\partial t} dr \right] dr \qquad [8.2]$$

A normal stress balance across the film gives a relation between p, capillary pressure (p_c), and the disjoining pressure (Π) as follows,

$$p = p_c - \Pi \qquad [8.3]$$

For a weakly-changing fluid height, i.e., $\partial h/\partial r \ll 1$, the capillary pressure becomes,

$$p_c = \frac{2\gamma}{R} - \frac{\gamma}{2r}\frac{\partial}{\partial r}\left(r\frac{\partial h}{\partial r} \right) \qquad [8.4]$$

R is the radius of oil droplet in the far field, γ is the oil/water interfacial tension. From Eqs. [8.2], [8.3] and [8.4], one obtains the following relation,

$$\Pi = \frac{2\gamma}{R} - \frac{\gamma}{2r}\frac{\partial}{\partial r}\left(r\frac{\partial h}{\partial r}\right) - 12\mu\int_{r=\infty}^{r}\frac{1}{rh^3}\left[\int_{r=0}^{r} r\frac{\partial h}{\partial t}dr\right]dr \qquad [8.5]$$

that can be used to determine Π from $h(r,t)$, which can be derived from the station-temporal film profiles recorded from the measurement.

Once Π is determined in the manner described above, one can determine the force parameters using the extended DLVO theory (Xu and Yoon, 1989),

$$\begin{aligned}\Pi &= \Pi_d + \Pi_e + \Pi_h \\ &= -\frac{A_{232}}{6\pi h^3} - \frac{\varepsilon\varepsilon_0\kappa^2\psi_2^2}{\sinh^2(\kappa h)}\left[1-\cosh(\kappa h)\right] + \frac{C}{2\pi D}\exp\left(-\frac{h}{D}\right)\end{aligned} \qquad [8.6]$$

in which Π_d, Π_e and Π_h are the contributions from the van der Waals (vdW), electrical double layer (EDL), and hydrophobic (HP) forces, respectively. In Eq. 8.6], A_{232} is the Hamaker constant between two oil droplets (**2**) in water (**3**), ε and ε_0 are the permittivity of the water and vacuum, respectively, while κ is the inverse Debye length and ψ_2 the surface potential of the oil-water interface. The last term on the right side denotes the contribution from the hydrophobic forces in a single exponential form, with C and D representing effectively the strength of the hydrophobic force and the decay length, respectively. In principle, an emulsion film should rupture when $\Pi < 0$, a condition when the sum of the vdW and hydrophobic forces exceed the repulsive EDL force.

8.3.2 Thermodynamics of Thin Liquid Films

Utilizing the value of Π_h obtained as described in the foregoing section, one can determine excess surface free energy (ΔG) between two macroscopic surfaces using the following,

$$\Delta G = -\int_{h=\infty}^{h_0}\Pi_h(h)\,dh \qquad [8.7]$$

where h_0 is the thickness of the α-film. Thermodynamically, the excess surface free energy (ΔG) represents the change in the film tension as an infinitely thick film thins to a finite thickness, h. For constant pressure (P), it is given by the Gibbs-Duhem equation as follows,

$$d\Delta G = -\Delta S dT - \Pi dh \qquad [8.8]$$

in which ΔS is the corresponding excess surface entropy. Assuming that the surface force contributions due to the vdW forces, EDL forces are not sensitive to the temperatures, as A_{232} and ψ_2 don't change significantly, we calculated the thermodynamics of hydrophobic interactions using the above equation. In such a case, ΔS can be related to ΔG and subsequently, Π_h at constant temperature (T) and thickness (h) as,

$$\begin{aligned}\Delta S &= -\left(\frac{\partial \Delta G}{\partial T}\right)_{P,h} \\ &= -\frac{C}{2\pi}\exp\left(-\frac{h}{D}\right)\left[-\frac{d(C)}{CdT} + \frac{h}{D^2}\frac{d(D)}{dT}\right]\end{aligned} \qquad [8.9]$$

In the current work, the temperature dependence of hydrophobic force parameters was found by conducting surface force measurements at different temperatures. It should be noted that 0.01 M NaCl solution has been used for conducting these measurements and therefore, the effect of EDL force is in effect screened out making our assumption valid.

Excess surface enthalpies can then be determined using the following,

$$\Delta H = \Delta G + T\Delta S \qquad [8.10]$$

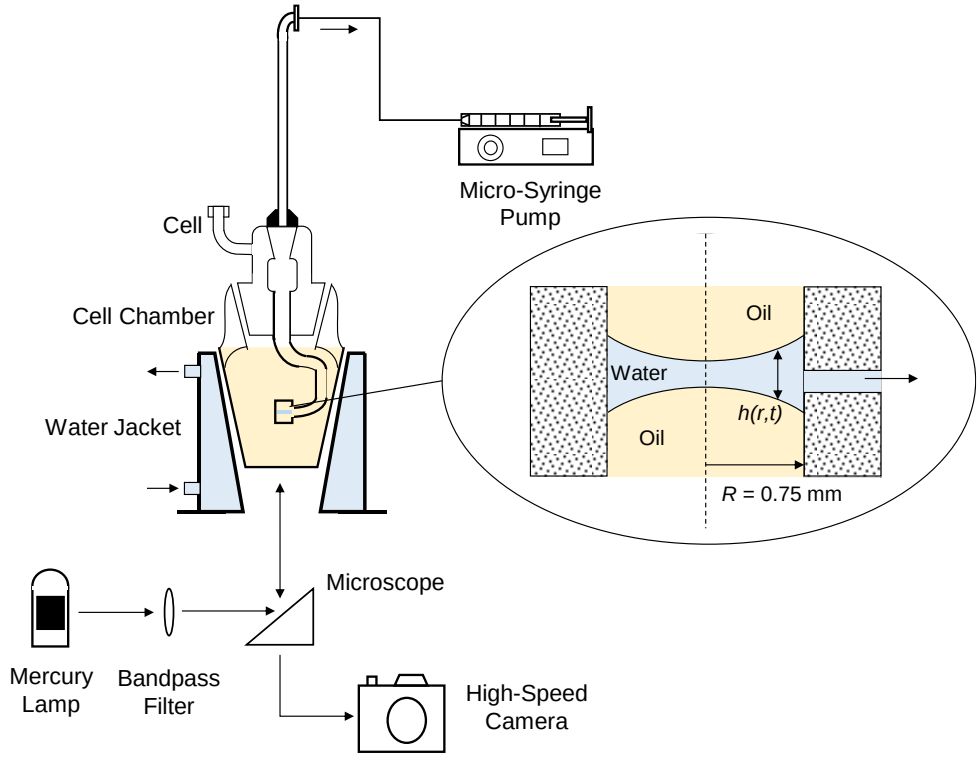

Figure 8-2. Schematic drawing of the experimental set-up used for imaging the spatiotemporal profile using Scheludko-Exerowa cell. The inset shows the bi-concave thin film of water formed in the cell with a hole radius of 0.75 mm.

8.4 Experimental and Methods

Figure 8-1 shows the schematics of the experimental setup used for measuring the surface forces in toluene-water-toluene emulsion films. A Scheludko-Exerowa Cell with a 0.75 mm hole radius was placed in a water-jacketed glass chamber. The cell chamber was filled with toluene (ACS Grade, Fisher Chemicals) while the cell was filled with an electrolyte solution. Prior to each test, the cell was cleaned of any residual organics using mild Piranha solution consisting of 7:3 by volume of sulfuric acid and hydrogen peroxide (30% v/v, Fisher Scientific), at 90 °C for 1 hour while the glass chamber was cleaned with 1:1 v/v iso-propyl alcohol (Fisher Chemical) and sodium hydroxide (30% v/v Fisher Scientific) base solution for 20 minutes. Both the cell and its chamber were washed thoroughly with de-ionized water (resistivity > 18.2 MΩ/cm at 25 °C) after acid and base cleaning, respectively.

The electrolyte solution was prepared using sodium chloride (ACS grade, Fisher Chemical), which was first heated to 600 °C for 5 hours to remove any organic contaminant. The cleaned cell was kept in the electrolyte solution for approximately an hour to get completely saturated with the test solution. A water heater/cooler accessory was used to maintain the temperature with an accuracy of ± 0.1°C. The cell chamber was mounted on an adjustable x-y tilt stage to form horizontal films. A mercury-vapor lamp (USH-103OL, Ushio Inc) was used with a narrow bandpass filter (10 nm bandwidth) to produce a monochromatic light of wavelength, 549 nm. Emulsion films were formed by slowly removing the solution using a micro-syringe pump. Care was taken to ensure free drainage of water (without any external force) before any optical fringes were observed. An inverted microscope (Olympus IX 51) and a high-speed camera were used to observe and record the illuminated interference patterns when the thin liquid film of water was drained to <5000 nm. The recorded patterns were analyzed offline using Scheludko's micro-interferometry technique to construct spatial-temporal film profiles. Special preventive measures were taken to isolate the set-up

from any external vibrations by placing it on a vibration isolation platform (100BM-1, Minus K Technology), which in turn was placed on a Nexus optical table (T46H, Thorlabs).

8.5 Results and Discussion

In the current work, the spatial-temporal profiles (h(r,t) measurements) were recorded for surfactant-free toluene/0.01M NaCl electrolyte solution (o/w) emulsion films at 10, 15, and 20 °C. Using this information $p(h)$, $p_c(h)$, and $\Pi(h)$ were determined as per Section 8.3.1 and subsequently, the thermodynamics of hydrophobic interactions has been studied using the information provided in Section 8.3.2.

Figure 8-3a shows the evolution of the optical fringes for the film thinning process for 0.01 M NaCl at 10 °C. During the process of film thinning for each measurement, the drainage was always accompanied by the formation of a dimple before the film was ruptured. The bright portion in the figures depicts the formation of a dimple. A dimple is formed when the drainage rate is higher at the rim of the film in comparison to its center due to the difference in the magnitude of the radius of curvature. The time to film rupture from an initial thickness of 800 nm varied in the range of 5-7 seconds. Unlike the emulsion film studies with surfactants in the literature, we always had a catastrophic film rupture for the surfactant-free films. *Figure* 8-3b shows the spatial temporal profile derived from the interference patterns using the thin film interferometry principles at 10 °C. The film radius of all the profiles was in the range of 80-140 µm.

The data obtained from the spatial temporal profiles were used to determine the changes in the pressures with respect to the film thickness. Using h(r,t) matrix and Eq. [8.1]-[8.5], we determined the hydrodynamic (p), capillary (p_c), and disjoining pressure (Π) under the immobile interface assumption. *Figure* 8-4a shows one such example. It shows the pressure changes as the film thinned below 100 nm for emulsion films at 10 °C. The change in the capillary pressure was not significant enough to affect the film thinning below

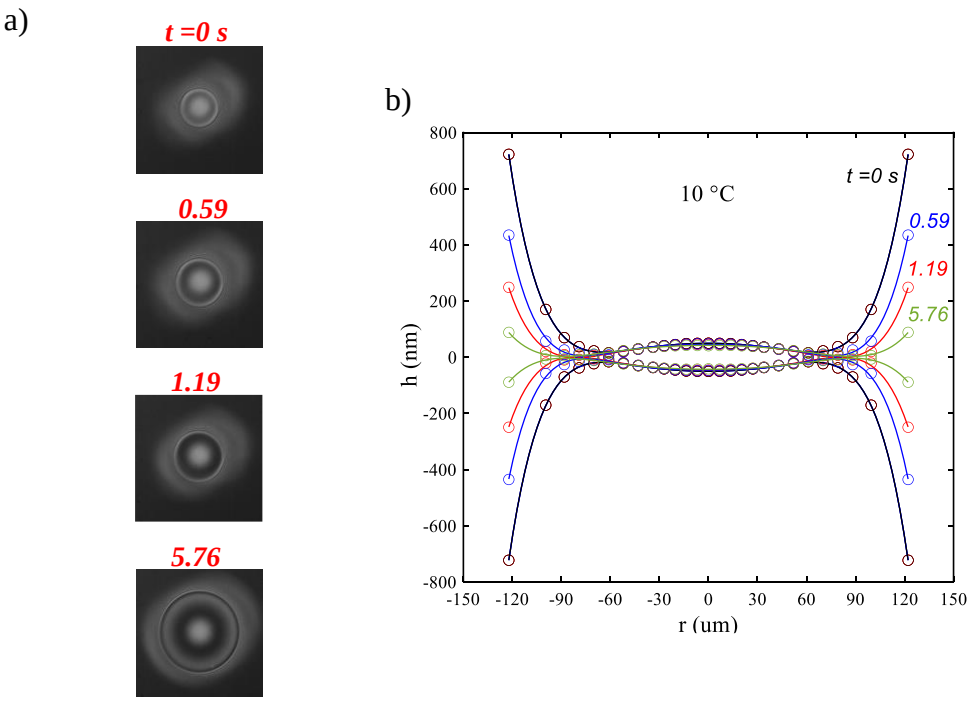

Figure 8-3. a) Observed interference pattern with the drainage of toluene/0.01 M NaCl solutions at 10 °C. b) Spatial temporal profile obtained from the micro-interferometry technique for emulsion film.

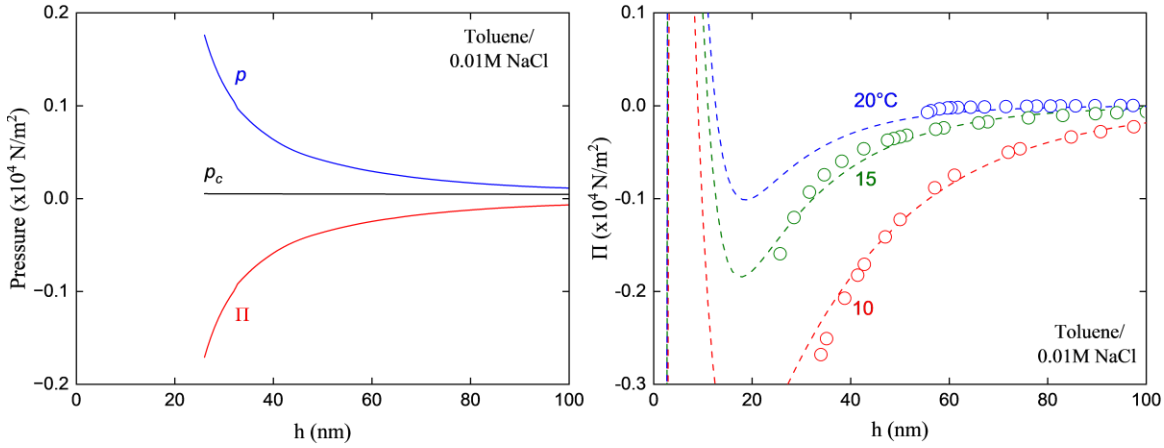

Figure 8-4 a) Hydrodynamic pressure (p), capillary pressure (p_c) and disjoining pressure (Π)determined using Eq.[8.2]-[8.5] at 10 °C, b) Π vs. h determined at different temperatures for Toluene/0.01 M NaCl emulsion film and fitted with extended DLVO theory shown by Eq. [8.6].

100 nm and the film thinning was driven by disjoining pressure. This also shows that the disjoining pressure becomes more negative as the film is thinned indicating the presence of attractive surface force which eventually leads to film rupture.

The surfactant-free emulsion films are thermodynamically unstable, and their instability is described to be due to the presence of attractive vdW forces however, these forces are short-ranged. Therefore, an additional attractive term, the HP force term has been accounted for in the traditional DLVO theory to fit the negative disjoining pressure attained during the experiments at different temperatures. During these experiments, the NaCl concentration was high and therefore, the EDL forces were screened, further destabilizing the emulsion films. At 0.01 M NaCl concentration, the Debye length reduces to ~3 nm reducing the extent of EDL forces. The exponential increase in the negative disjoining pressure, however, may be due to the presence of hydrophobic forces.

With the illumination of HP forces, the hydrodynamic resistance to film thinning increases too, reducing the acceleration of the film thinning. At low thickness *i.e.* h < 200 nm, the capillary pressures usually diminish as the radius of curvature of the film remains relatively flat. Similar findings were observed in the present work, the value of capillary pressure (p_c) was negligible in comparison to the values of other pressures present in the film thinning process. In such cases, hydrodynamic pressure (p) can be thought to be a reaction to the disjoining pressure or essentially hydrophobic forces when the thickness is of the order of 20-100 nm. Below this range, the vdW forces should also contribute to the thinning rate of the emulsion films.

The determined Π(h) isotherms at different temperatures were fitted with the extended DLVO theory. *Figure* 8-4b shows the fitting while accounting for the HP forces as per Eq. [8.6]. As can be observed from the graph, the negative disjoining pressure increases as the temperature is reduced. This trend is similar to what was observed in the previous chapter with foam films and with the colloidal films by Wang *et al.* (2011) and Li and Yoon (2014).

To understand the effect of temperature at length, the contribution of each accounted surface forces has been plotted in *Figure* 8-5a. The effect of temperature on interfacial tension and viscosity was considered as shown in *Table* 8-1. The interfacial tension between 0.01 M NaCl electrolyte solution and toluene was measured using the Biolin Scientific Theta Flow optical tensiometer. The interfacial tension of toluene-0.01 M NaCl water interface at 23.5 °C was measured to be 35.5 mN/m. The effect of temperature was calculated by determining the slope of the *T vs.* γ curve for Toluene-water given by Saien and Akbari

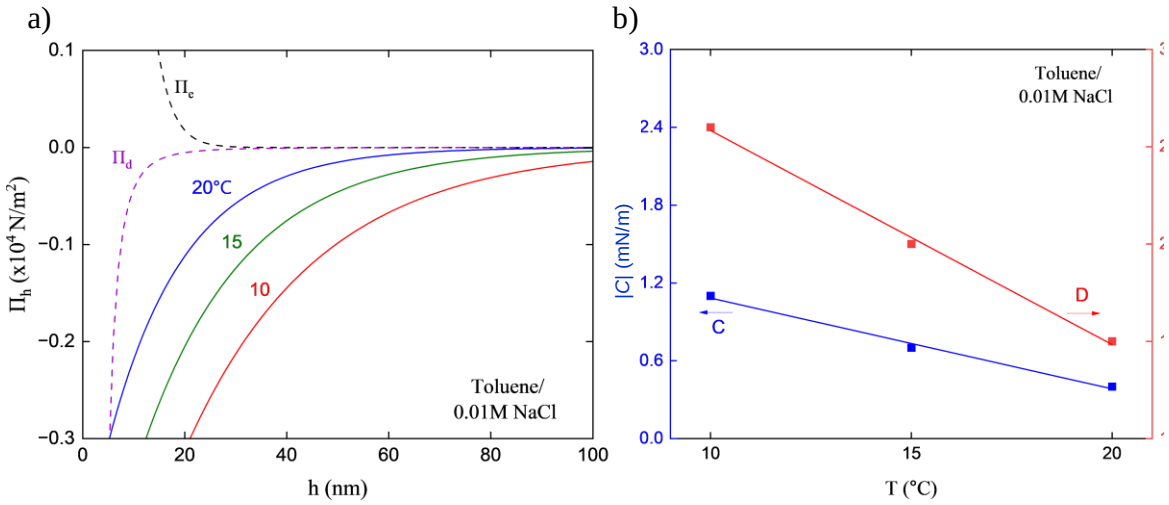

Figure 8-5 a) Π_h vs. h determined at different temperatures using Eq. [6] and, b) the hydrophobic force constant (C) and its decay length (D) determined using the extended DLVO theory.

(2006) and extrapolating it to 10 °C. The surface potential (ψ_2) for the toluene-water interface was assumed to be -35 mV (Shi *et al*., 2016).

Unlike foam films, the temperature might affect the vdW interactions in the oil-water-oil systems. This might be since, in the Lifshitz theory, the zero-frequency term (which is a function of temperature) has a significant contribution to the overall Hamaker constant in the oil phase (Israelachvili, 2011). However, the vdW forces will still be short ranged and a slight variation in the A_{232} wouldn't change their contribution to the overall $\Pi(h)$. Therefore, A_{232} is assumed to be a constant with a value of 0.98×10^{-20}J (Shi *et al*., 2016). Likewise, the effect of temperature on the EDL force would not affect the overall $\Pi(h)$ because 0.01 M NaCl is used for the measurement, the EDL force contribution is also assumed to be constant. The EDL force parameters are tabulated in *Table* 8-1.

Once the vdW and EDL forces' contribution to the disjoining pressure were known, the HP force contribution was back calculated using Eq. [8.6]. From *Figure* 8-5a, the HP force contribution is longer ranged in comparison to other forces. The HP force contribution became more negative as the temperature was reduced similar to what was observed in the foam film in the previous chapter. The following exponential form equation was used to describe HP forces,

$$\Pi_h = \frac{C}{2\pi D}\exp\left(-\frac{h}{D}\right) \qquad [8.11]$$

Here, C and D denote the strength of the HP forces. The values of these HP force parameters were determined by fitting the $\Pi_h(h)$ isotherms in *Figure* 8-5a. The dependency of these parameters on

Table 8-1. Surface force parameters for emulsion films with Toluene and 0.01 M NaCl solutions at different temperatures

T (°C)	γ (mN/m)	μ (10^{-3} Pa.s)	A_{232} (10^{-20} J)	ψ_2 (mV)	κ^{-1} (nm)	C (mN/m)	D (nm)
10	36.30	1.31	0.98	-35	3.08	-1.1	26
15	36.00	1.14	0.98	-35	3.05	-0.7	20
20	35.70	1.01	0.98	-35	3.03	-0.4	15

temperature is shown in Figure 8-5b. As can be seen, both the strength (*C*) and decay length (*D*) of the HP force increased as the temperature was reduced indicating the formation of an increased amount of water structures in the TLF. In this case, the negative values of *C* were increased from -0.4 to -1.1 mN/m while *D* increased from 15 to 26 nm as the temperature reduced from 20 to 10 °C. It is interesting to note here that the strengths of the hydrophobic forces measured in emulsion films are weaker than those measured in foam films at a given electrolyte concentration (*Chapter* 7). The difference may be attributed to the lower interfacial tension at the oil-water interface (~36.0 mN/m) as compared to the air-water interfacial tension (~72 mN/m). The MD simulations conducted by Brown *et al.* (2003) suggested that a small fraction of the dangling OH bonds at the interface could interact strongly with an oil phase which might also be one of the reasons for weaker hydrophobic force in the TLFs of water in the emulsion film as measured by the *C* constant of Eq. 8.11.

Note, however, that the HP force was longer ranged in the emulsion films than in the foam films. Huang and Yoon (2019) found similar results with the wetting films of water formed between an oil drop and a hydrophobic surface. The hydrophobic forces were weaker as measured C constants were weaker than those measured in the wetting films of water formed between an air bubble and a hydrophobic surface. The longer-ranged HP force may be instrumental in increasing the kinetics of film thinning process which is

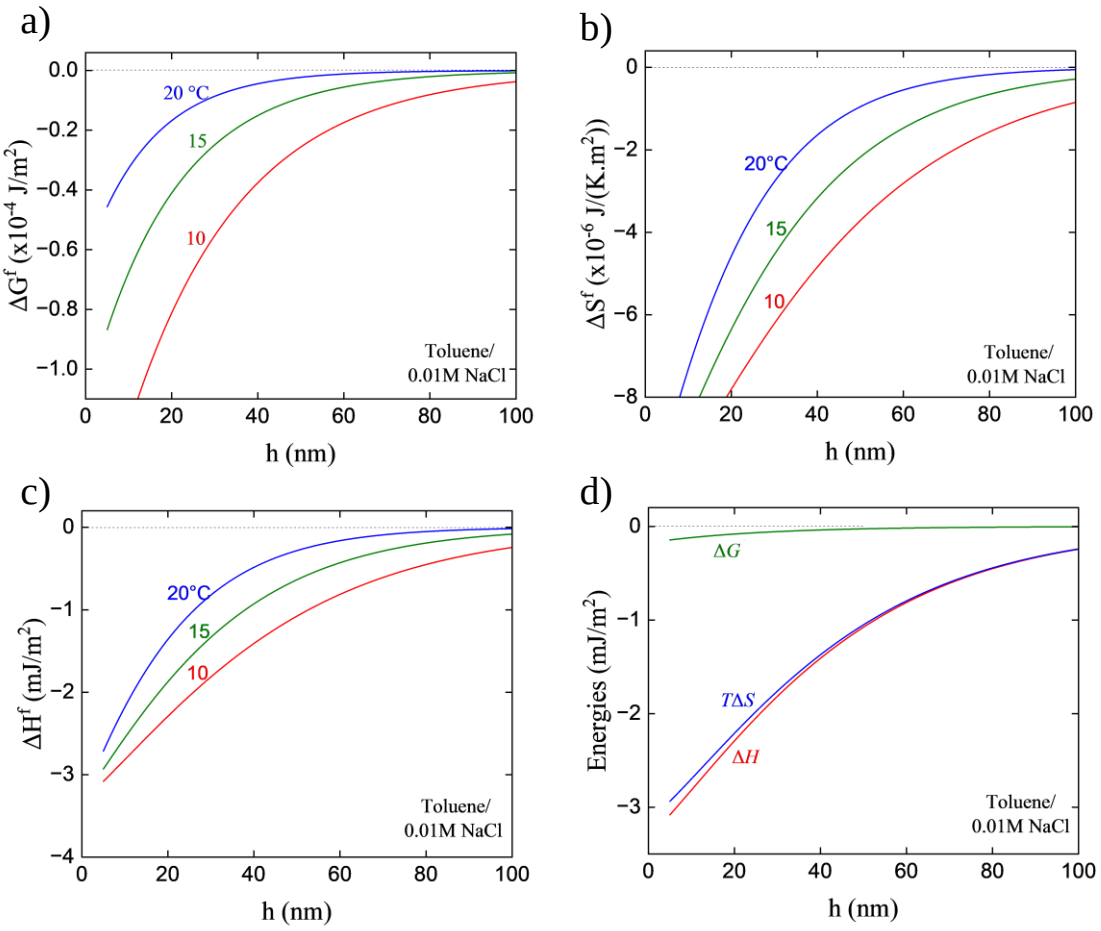

Figure 8-6 Changes in the excess thermodynamics functions, a) excess surface free energy (Δ*G*), b) excess surface entropy (Δ*S*), and c) excess surface enthalpy (Δ*H*) for emulsion film hydrophobic interactions and d) the enthalpy-entropy compensation at 10 °C.

evident from the less time it took to thin and rupture a 200 nm thick emulsion film (4.5 s) than the time (9.8 s) it took thin and rupture a foam film at 20°C).

In the present work, the excess thermodynamic properties were also determined. Once the hydrophobic force parameters were known, the slope of $|C|$ *vs*. T and D *vs*. T were determined. The changes in free energy (ΔG), entropy (ΔS), and enthalpy (ΔH) were calculated using the Eq. [8.7] - [8.10] as shown in Section 8.3.2. *Figure* 8.6 shows the excess thermodynamic properties plotted as a function of emulsion film thickness. As the hydrophobic force isotherms (*Figure* 8-4a) were attractive, it was found that ΔG was negative during the process of thinning and increased in (negative) magnitude as the film thinned. The magnitude of $-\Delta G$ was also increased as the temperatures were reduced. ΔS determined from Eq. [8.9] was also negative indicating the reduction in the degree of freedom possibly due to the increase in the structuring during the thinning of the emulsion films. H was determined using Eq. [8.10] and plotted in *Figure* 8-5c. The increasing magnitude of negative ΔH with emulsion film thinning and reducing temperature suggests the formation of some species or stable structures in the film. Similar trends for the thermodynamic properties were seen in the interactions between different macroscopic hydrophobic surfaces (Wang *et al*., 2011; Li and Yoon, 2014).

In a confined space between hydrophobic surfaces such as carbon nanotubes or graphene sheets, water is retained due to the enhanced H-bonded network in the constricted area (Algara-Siller *et al*., 2015; Cai *et al*., 2019). This improved structuring occurs to minimize the loss of available H-bonding sites in hydrophobic confinement. These newly formed H-bonds usually are longer, lowering the density of water in confined spaces. These low-density liquids (LDL) have water structures that can be similar to the ice-like structures formed in super-cooled water (Roentgen, 1892) or can exist as pentagonal dodecahedrons (Pauling, 1961), clathrate cages (Stillinger, 1980), *etc*. These LDLs have also been found to exist in ambient conditions (Mallamace *et al*., 2008; Mallamace, 2009). Vibrational sum frequency spectroscopy measurements and MD simulations conducted at the air-water interface showed that the surface water molecules have lower H-bonds and entail dangling OH bonds due to the missing water layer at the hydrophobic interface (Du *et al*., 1994; Scatena *et al*., 2001; Sose *et al*., 2022).

As the emulsion film thinned, ΔS and ΔH became more negative indicating the formation of more H-bonded structures. However, the order of ΔS is not large (order of $\sim 10^{-6}$ J), indicating that the extent of structuring was small. Nevertheless, even this small change ins the TLF provides evidence that long-ranged hydrophobic interactions also occur due to the water structuring similar to the origin theory of short-ranged HP forces.

Figure 8-6d shows, ΔG, ΔH and ΔS plotted together. For the free energy to be negative or the process to be spontaneous, it is necessary that the condition, $|\Delta H| > |T\Delta S|$ is satisfied. From the plot, it is evident that the process is enthalpy-driven rather than entropy. This is contrary to the molecular scale hydrophobic interaction which is rather entropy-driven. When macroscopic hydrophobic surfaces come in close proximity, the water molecules at the interfaces are not able to surround the extended surfaces forcing them to re-structure among themselves to minimize free energy loss (Chandler, 2005). This finding is, therefore, thought to be in similar line with the theory proposed by others (Stillinger, 1980; Speedy, 1984) who attributed the hydrophobic effect to the structuring of water molecules. The formation of partial clathrates might also lead to a reduction in the rotational entropy which has been the case when a very thin water layer (~1 nm) is confined between two hydrophobic surfaces (Chaplin, 2010). The longer range of hydrophobic forces measured in the present work might be due to the extended H-bonded network in the TLF of water forming a low-density liquid (LDL), due to the presence of a super-hydrophobic oil-water interface.

Figure 8-6d also shows that the emulsion film thinning process entails high enthalpy-entropy compensation due to the increase in enthalpy but simultaneously paying the penalty in the form of entropy. It should be noted from *Figure* 8-6d that the compensation is more than the colloidal film previously studied. This might be due to the presence of two deformable interfaces leading to more structuring in the TLF similar to the foam film, entailing significantly higher entropy cost.

8.6 Summary and Conclusions

A series of disjoining pressure measurements were conducted with surfactant-free toluene-water emulsion films formed with electrolyte solutions. These tests were run at different temperatures. It was found that the hydrophobic force was a major driving force in destabilizing the emulsion films. The measured hydrophobic forces were weaker as compared to those measured in foam films, suggesting that the air-water interface is more hydrophobic than the oil-water interface. However, the decay lengths of the HP forces for emulsion films were longer than those of the foam films, explaining the experimental observations that the TLFs in oil-in-water emulsions thin faster than those in foams.

That the attractive hydrophobic forces increased with decreasing temperature suggests that hydrophobic force entails structuring of water molecules in confined spaces, resulting in a decrease in enthalpy and entropy interactions depending on the structuring of water molecules in the TLFs with conditions of $|\Delta H| > |T\Delta S|$, the entropy decrease representing the cost of building structures.

8.7 References

Algara-Siller, G., Lehtinen, O., Wang, F. C., Nair, R. R., Kaiser, U., Wu, H. A., ... & Grigorieva, I. V. (2015). Square ice in graphene nanocapillaries. *Nature*, 519(7544), 443-445.

Cai, X., Xie, W. J., Yang, Y., Long, Z., Zhang, J., Qiao, Z., ... & Gao, Y. Q. (2019). Structure of water confined between two parallel graphene plates. *The Journal of chemical physics*, 150(12).

Chandler, D. (2005). Interfaces and the driving force of hydrophobic assembly. *Nature*, 437(7059), 640-647.

Chaplin, M. F. (2010). Structuring and behaviour of water in nanochannels and confined spaces. *Adsorption and phase behaviour in nanochannels and nanotubes*, 241-255.

Du, Q., Freysz, E., & Shen, Y. R. (1994). Surface vibrational spectroscopic studies of hydrogen bonding and hydrophobicity. *Science*, 264(5160), 826-828.

Huang, K., & Yoon, R. H. (2019). Surface forces in the thin liquid films (TLFs) of water confined between n-alkane drops and hydrophobic gold surfaces. *Langmuir*, 35(48), 15681-15691.

Israelachvili, J. N., Intermolecular and surface forces: revised third edition. *Academic press*: 2011.

Li, Z., & Yoon, R. H. (2014). Thermodynamics of solvophobic interaction between hydrophobic surfaces in ethanol. *Langmuir*, 30(44), 13312-13320.

Mallamace, F. (2009). The liquid water polymorphism. *Proceedings of the National Academy of Sciences*, 106(36), 15097-15098.

Mallamace, F., Corsaro, C., Broccio, M., Branca, C., González-Segredo, N., Spooren, J., ... & Stanley, H. E. (2008). NMR evidence of a sharp change in a measure of local order in deeply supercooled confined water. *Proceedings of the National Academy of Sciences*, 105(35), 12725-12729.

Pauling, L. (1961). A Molecular Theory of General Anesthesia: Anesthesia is attributed to the formation in the brain of minute hydrate crystals of the clathrate type. *Science*, 134(3471), 15-21.

Roentgen, W.C. (1892). On the constitution of liquid water. *Annals of Physics*, 281 (1), 91-97.

Saien, J., & Akbari, S. (2006). Interfacial tension of toluene+ water+ sodium dodecyl sulfate from (20 to 50) C and pH between 4 and 9. *Journal of Chemical & Engineering Data*, 51(5), 1832-1835.

Scatena, L. F., Brown, M. G., & Richmond, G. L. (2001). Water at hydrophobic surfaces: weak hydrogen bonding and strong orientation effects. *Science*, 292(5518), 908-912.

Shi, C., Zhang, L., Xie, L., Lu, X., Liu, Q., Mantilla, C. A., ... & Zeng, H. (2016). Interaction mechanism of oil-in-water emulsions with asphaltenes determined using droplet probe AFM. *Langmuir*, 32(10), 2302-2310.

Sose, A. T., Mohammadi, E., Achari, P. F., & Deshmukh, S. A. (2022). Determination of accurate interaction parameters between the molybdenum disulfide and water to investigate their Interfacial properties. *The Journal of Physical Chemistry C*, 126(4), 2013-2022.

Speedy, R. J. (1984). Self-replicating structures in water. *The Journal of Physical Chemistry*, 88(15), 3364-3373.

Stillinger, F. H. (1980). Water revisited. *Science*, 209(4455), 451-457.

Wang, J., Yoon, R. H., & Eriksson, J. C. (2011). Excess thermodynamic properties of thin water films confined between hydrophobized gold surfaces. Journal of colloid and interface science, 364(1), 257-263.

Xu, Z., & Yoon, R. H. (1989). The role of hydrophobia interactions in coagulation. Journal of colloid and interface science, 132(2), 532-541.

Yoon, R. H. (2016). U.S. Patent No. 9,518,241. Washington, DC: U.S. Patent and Trademark Office.

8.8 Appendix

The spatial temporal profiles obtained at 15 °C and 20°C are shown below.

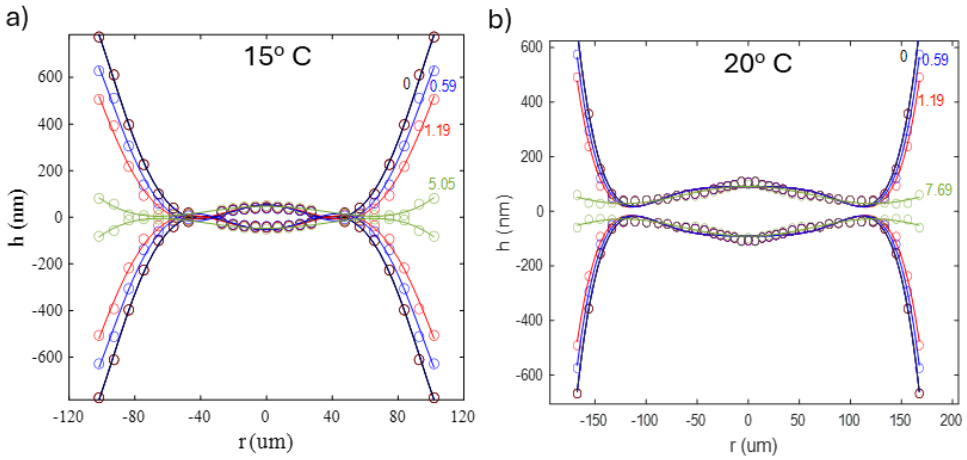

Appendix Figure 8-1. Spatial temporal profile for toluene-water-toluene interactions at a) 15 °C and, b) 20 °C.

Chapter 9. Conclusions and Recommendations

9.1 Conclusions

1. A flotation model has been developed using the hydrophobic force as a kinetic parameter, which made it possible to predict both the recovery and grades for the first time. The major input parameters to the model-based computer simulator include the size-by-class liberation matrix and various chemistry and hydrodynamics parameters. The model has been validated against the plant survey data obtained from an operating copper rougher flotation circuit. The simulation results are in excellent agreement with the plant survey data. The simulator can also predict the size-by-size recoveries, showing a drop-off of recoveries of coarse particles at particle sizes >150 μm due to the sharp decrease in liberation and poor froth phase recoveries. The simulation results also show a direct relationship between flotation rate constants and the contact angles.

2. Circulating loads consisting of the cleaner-scavenger tails (CST) are commonly used in the flotation industry to improve circuit efficiencies. A computer simulator based on the first principle model has been used to determine the size-by-class flotation rate constants for both the fresh feed and CST, which is returned to the rougher flotation circuit as a circulating load (CL). The simulation results show that the CST, which consists of the slowest-floating particles, seriously compromises the throughput of a flotation plant. Simulations have also been conducted for the entire flotation circuit, including the cleaner flotation circuit, to show ways to improve the overall plant performance by treating the CST in a separate circuit using advanced separation processes.

3. Novel reagents known as Super Collectors have been developed that can increase the contact angles of the target minerals to 150^{o} -170^{o}. Both the experimental and simulation results show that the use of Super Collectors can greatly improve the recoveries of the composite particles present in a feed stream at substantially reduced retention times. The improvement can be attributed to the increased contact angles of the composite particles, which in turn can increase the hydrophobic forces and, hence, the flotation rates. An improved recovery of composite particles helps increase the recovery of coarse particles, a large part of which are composite particles. The large contact angles created by using Super Collectors increased the work of bubble-particle attachment and decreased bubble coarsening, both of which help increase coarse particles recovery.

4. A new flotation model has been developed to predict the flotation rate constants using a simple Arrhenius-type equation. The rate constant is a function of normalized bubble-particle collision frequency, energy barrier due to surface forces, work of bubble-particle attachment, hydrodynamic resistance to film thinning, and energy dissipation rate due to turbulence. The model has been used to simulate the performance of a flotation circuit with and without using Super Collectors. The simulation results show that Super Collectors can improve both throughput and recovery of a copper flotation plant by way of improving the composite particles.

5. A new coarse particle recovery unit, called the Jig flotation cell, has been developed to mitigate the harmful effects of the gravitational forces in flotation. This was achieved by decreasing the effective specific gravity (SG) of target minerals to help levitation and by pulsating the aqueous phase to allow particles to settle by SGs independently of particle size. The test results obtained with coarse particles showed promising results.

6. A series of disjoining pressure measurements have been conducted with surfactant-free foam films and emulsion films using the thin film pressure balance (TFPB) method. The micro-interferometric technique was used to construct the spatial-temporal film profiles for the film thinning process. The capillary and hydrodynamic forces are determined by using the Young-Laplace equation and Reynolds

lubrication theory, respectively. The surface forces were then determined using the extended DLVO theory, which included contributions from the van der Waals (vdW), electrical double-layer (EDL), and hydrophobic (HP) forces. The results showed that the hydrophobic forces measured in foam films are stronger than those measured in oil-in-water emulsion films, which may be attributed to the differences in the interfacial tensions involved. On the other hand, the decay lengths of the hydrophobic forces were longer ranged in emulsion films, which corroborates well with the kinetics of air bubble flotation and oil flotation processes.

7. The thermodynamics of hydrophobic interactions in foam and emulsion films have been studied by measuring the disjoining pressures at different temperatures and calculating the excess thermodynamic properties using the Gibbs-Duhem equation. The results show the hydrophobic interactions entail decreases in both enthalpy and entropy, in which case $|\Delta H| > |T\Delta S|$ for the hydrophobic interactions to be spontaneous. This finding suggests that the hydrophobic force may originate from building H-bonded structures in confined spaces to reduce the Free energy of the films ($\Delta G < 0$). The measurements conducted in NaCl showed that hydrophobic forces in foam films decrease in the presence of the electrolyte, possibly due to the structure-breaking role of the electrolyte.

9.2 Recommendations for Future Work

1. In the present work, a flotation model developed from first principles has been used to simulate plant practices. The model consists of analytical equations describing various subprocesses, many of which have been derived by other investigators from first principles. One exemption is the model describing the recovery due to entrainment (Eq. [1.43]), which is an empirical model derived by Maachar and Dobby (1992). It will be beneficial to derive an entrainment model from first principles to complete the derivation of a first principles model.

2. Flotation is a kinetic process involving three phases, i.e., solid, liquid, and gas. Therefore, the model derived from the first principles consists of a series of long equations, which makes it difficult to convey the basic mechanisms involved succinctly. The author of the thesis work is pleased that he came up with an Arrhenius-type model that subdivides the model into collision and attachment subprocesses, which is useful for analyzing the role of various parameters. Further work is necessary to derive a mathematically more rigorous formalism with minimal assumptions.

3. In the present work, the TFPB technique has been used to measure the surface forces in the surfactant-free foam and emulsion films. It may be useful to extend the measurements to more complex soft matter systems to probe the mechanism for demulsification, drug delivery in pharmaceutical industries, etc.

4. The Jig Flotation Cell developed in the present work can be scaled up to a process development unit (PDU) that can be used to generate information, e.g., rate constants, that is necessary to design a pilot plant, which is a necessary step for commercialization. It is also necessary to develop a mathematical model.

9.3 References

Maachar, A., & Dobby, G. S. (1992). Measurement of feed water recovery and entrainment solids recovery in flotation columns. *Canadian metallurgical quarterly*, 31(3), 167-172.